

NATIONAL & KAPODISTRIAN UNIVERSITY OF ATHENS
SCHOOL OF SCIENCE

B.SC. THESIS

**Mineralogical and Geochemical Characterization of
the Mn–paragenesis of Piemontite Schists from
Varnavas area, NE Attica, Greece.**

Student:
Christoforos Zamparas
1114201500030

Supervisor:
Christina Stouraiti
Assistant Professor

*The present thesis is submitted in partial fulfillment for the requirements
of the first **degree***

in the

Faculty of Geology & Geoenvironment

June 1, 2020



ΕΘΝΙΚΟ ΚΑΙ ΚΑΠΟΔΙΣΤΡΙΑΚΟ ΠΑΝΕΠΙΣΤΗΜΙΟ ΑΘΗΝΩΝ
ΣΧΟΛΗ ΘΕΤΙΚΩΝ ΕΠΙΣΤΗΜΩΝ
ΤΜΗΜΑ ΓΕΩΛΟΓΙΑΣ ΚΑΙ ΓΕΩΠΕΡΙΒΑΛΛΟΝΤΟΣ

πτυχιακή εργασία με τίτλο:

**Ορυκτολογικός και Γεωχημικός Χαρακτηρισμός της
Μαγγανιούχου Παραγένεσης των Πιεμοντιτικών Σχιστόλιθων
της Περιοχής του Βαρνάβα, ΒΑ Αττική, Ελλάδα**

του

Χριστόφορου Ζαμπάρα
1114201500030

Επιβλέπουσα: Χριστίνα Στουραΐτη, Επίκ. Καθηγήτρια

ΑΘΗΝΑ, 2020



dedicated to George, Mary, Konstantina & Marianthi

NATIONAL & KAPODISTRIAN UNIVERSITY OF ATHENS
School of Science
Faculty of Geology & Geoenvironment

Abstract

Mineralogical and Geochemical Characterization of the Mn–paragenesis of Piemontite Schists from Varnavas area, NE Attica, Greece.

Christoforos Zamparas

The lower NE Attica Unit consists of a greenschist facies metamorphosed volcanoclastic sequence at its base and an overlying carbonate sequence. Piemontite schists horizons within this unit are associated with calcareous schists and quartz–mica schists. Piemontite–rich quartzitic layers enclose Mn(\pm Fe) ore in nodular forms and thin encrustations. The present B.Sc. thesis deals with the mineral classification, bulk geochemical aspects and mineral chemistry of Mn \pm Fe–nodular and crustal forms in a metamorphosed ferromanganoan metavolcanosedimentary sequence, in Varnavas area, NE Attica. Additionally, it is studied the potential of critical metals in these formations. Detailed investigation combining geochemical (major, trace elements, REE and PGE) and mineralogical (SEM, XRD, Raman) analyses of these Mn– and Fe–oxides allow: a) the identification of the poorly crystallized minerals and b) the definition of the complex manganese paragenesis. The Mn–rich paragenesis consists of metamorphic silicates mainly of piemontite + sursassite + ardennite(–As) + spessartine and Mn–ore mainly of pyrolusite + todorokite + cryptomelane + psilomelane + hollandite + coronadite. The cryptocrystalline nature of the nodules and the laminations requires a multiple–method approach for sufficient data acquisition. We have established that these nodular forms have pyrolusite and todorokite as the dominant manganese oxide intimately intergrown with hollandite and psilomelane. The hematite intercalations are well established with strong X–ray diffraction peaks. These minerals are good scavengers of base, precious metals and REEs. Bulk geochemical analysis of the Mn–rich ore show high Mn/Fe ratios (1.3–5.2), high Ba (2800ppm) and discrimination binary and ternary diagrams suggest a main hydrothermal origin with some contribution of a hydrogenous component. Mineral chemical data and bulk geochemical characteristics are compared with literature data from Mn–deposits of known tectonic environments in order to provide some constraints on the paleogeographic depositional environment of the Mn–rich sedimentary protolith.

Keywords: manganese minerals, Mn–nodules, Fe–Mn–crusts, piemontite, pyrolusite, todorokite, hollandite, metasediments, Varnavas, Attica, Petrography, Raman Spectroscopy

Περίληψη

Η κατώτερη Ενότητα ΒΑ Αττικής αποτελείται από μία ηφαιστειοκλαστική ακολουθία στη βάση και μία υπερκείμενη ανθρακική ακολουθία και έχει μεταμορφωθεί σε συνθήκες πρασινοσχιστολιθικής φάσης. Ορίζοντες πιεμοντιτικών σχιστόλιθων εντός της ενότητας αυτής εναλλάσσονται με ασβεστιτικούς και χαλαζιακούς-μαρμαρυγιακούς σχιστόλιθους. Τα πλούσια σε πιεμοντίτη στρώματα περιλαμβάνουν μεταλλοφορία $Mn\pm Fe$ σε μορφή κονδύλων και λεπτών φλοιών. Η παρούσα πτυχιική εργασία πραγματεύεται τα ορυκτολογικά γεωχημικά και ορυκτοχημικά χαρακτηριστικά των (σιδηρο)μαγγανιούχων κονδυλώδων και φλοιώδων μορφών, που εντοπίζονται εντός της μεταηφαιστειοϊζηματογενούς ακολουθίας πετρωμάτων στην περιοχή του Βαρνάβα, ΒΑ Αττική. Επιπροσθέτως, εξετάζεται το δυναμικό των σχηματισμών αυτών ως προς το περιεχόμενο σε κρίσιμα μέταλλα. Λεπτομερής έρευνα που συνδυάζει γεωχημικές (κύρια στοιχεία, ιχνοστοιχεία συμπεριλαμβανομένων σπάνιες γαίες και μέταλλα της ομάδας του λευκόχρυσου) και ορυκτολογικές (SEM, XRD, Raman) αναλύσεις των Mn-και Fe-οξειδίων επιτρέπει: α) την ταυτοποίηση των φτωχά κρυσταλλωμένων μαγγανιούχων ορυκτών και β) τον προσδιορισμό της περίπλοκης μαγγανιούχου παραγένεσης. Η μαγγανιούχος παραγένεση αποτελείται από μεταμορφικά πυριτικά ορυκτά, κυρίως από πιεμοντίτη + σουρσασίτη + αρδεννίτη(-As) + σπεςσαρτίνη, και μαγγανιούχο μεταλλοφορία, κυρίως από πυρολουσίτη + τοντοροκίτη + κρυπτομέλανα + ψιλομέλανα + ολλανδίτη + κοροναδίτη. Η κρυπτοκρυσταλλική φύση των κονδύλων και των φλοιών απαιτεί μία προσέγγιση με χρήση πολλαπλών μεθοδολογιών, ούτως ώστε να υπάρξει ικανοποιητική λήψη δεδομένων. Οι κονδυλώδεις μορφές αποτελούνται κυρίως από πυρολουσίτη και τοντοροκίτη ως κύρια μαγγανιούχα οξείδια, τα οποία συμφύονται με ολλανδίτη και ψιλομέλανα. Οι ενδιαστρώσεις με αιματίτη ταυτοποιήθηκαν με περιθλασιμετρία ακτίνων-X. Τα οξείδια και υδροξείδια των Fe και Mn είναι συλλέκτες βασικών και πολύτιμων μετάλλων, αλλά και σπανίων γαιών. Ολική γεωχημική ανάλυση της μαγγανιούχου μεταλλοφορίας αποδίδει λόγους Mn/Fe με εύρος 1.3-5.2, υψηλό Ba 2800ppm και δυαδικά και τριαδικά διαγράμματα, κυρίως μη κινητικών ιχνοστοιχείων, υποδεικνύουν κυρίως υδροθερμική πηγή αλλά και συμμετοχή υδρογενετικής προέλευσης. Ορυκτοχημικά και ολικά γεωχημικά δεδομένα συγκρίνονται με βιβλιογραφικά δεδομένα από μαγγανιούχα κοιτάσματα από γνωστά γεωτεκτονικά περιβάλλοντα με σκοπό να δοθούν περιορισμοί ως προς το παλαιογεωγραφικό αποθετικό περιβάλλον του μαγγανιούχου ιζηματογενούς πρωτόλιθου.

Acknowledgements

My admission to the undergraduate program of the Faculty of Geology and Geoenvironment and the followed journey into Geosciences was – tersely – a *gift*, a gift with a dual name. Knowledge and friendship.

From this position I would deeply like to thank *Christina Stouraiti* (Assistant Professor, NKUA), the supervisor of the present B.Sc. thesis, for her unreserved help, both in terms of academic guidance and advice in the substantial understanding of this scientific matter and the methods utilized and in terms of financial support. She was the ideal person to help me organize the amount of data produced by the techniques utilized in the present thesis. I would like also to thank *Konstantinos Soukis* (Research Staff, NKUA) and *Stelios Lozios* (Associate Professor, NKUA) for their assistance on the Geology of Attica and for the final sample selection. Additionally, I would like to thank *Dimitrios Kostopoulos* (Assistant Professor, NKUA) for his advice on the mineralogy and mineral chemistry of manganese-bearing minerals.

I would like also to thank Dr. *Konstantinos Kollias* (Research Staff, School of Mining and Metallurgical Engineering, NTUA), Dr. *Dimitrios Palles* (Institute of Theoretical and Physical Chemistry, NHRF) and *Vassilis Skounakis* (NKUA) for their assistance on the XRF analysis, the Raman Spectroscopy analysis and the SEM-EDS analysis, respectively.

Special thanks are reserved for my fellow students in the Faculty of Geology and Geoenvironment. I would like to thank especially *Dimitrios Latsinoglou*, *Efthimios Vatidis*, *Irini Spilioti* for their assistance on the field and sampling process and, of course, *Petros Papagiannakopoulos*, *Myrto Kyriazi*, *Silvana Keli*, *Adamantios Serafopoulos* and *Antonis Laskos* for our numerous and passionate geoscience-oriented (and not only) discussions. Definitely all of them for their friendship.

I would also want to notably thank my family. My father *George*, my mother *Mary* and my sister *Konstantina* were and are always there for me. I would especially thank my parents for the fact that, when I was a child they never said no for buying me a scientific book, no matter the cost.

Finally, I am deeply grateful to *Marianthi Vaporaki* for being next to me for the last decade in literally every aspect of my life, making her my new family.

I am in debt to my – extended today – family and every real teacher and friend in my life. They and I are responsible for me chasing a utopian perfection, which shall never be accomplished but should motivate us to seek it, at least in everything regarding scientific knowledge and I am grateful for that. Doubt everything written or oral, especially when in class – one day this will be a small brick, the smallest, but in the most important construction.

Christoforos Zamparas
Athens, 2020

Contents

Abstract	iv
Summary (in greek)	v
Acknowledgements	vi
Contents	vii
List of Figures	ix
List of Tables	x
List of Abbreviations	xi
1 Introduction	1
1.1 Thesis' Scope	1
1.2 Literature Review	1
1.2.1 Geological setting	1
An introduction to the Alpine orogenic system and the Hellenides	1
Geology of Attica	4
Previous studies in the sampling area	7
1.2.2 Mineralogy and Geochemistry of manganese and deposit classification	8
Chemistry and geochemistry of manganese	8
Manganese minerals	10
Manganese mineralization in sedimentary environments	10
Classification of manganese formations and deposits	11
Examples of known manganese formations and deposits	14
2 Materials and Methods	16
2.1 Sampling	16
2.2 Optical Microscopy	17
2.3 Analytical Techniques	17
2.3.1 Mineral Characterization Methods and Mineral Chemistry	18
X-Ray Diffractometry	18
Raman Spectroscopy	18
Scanning Electron Microscopy – Energy Dispersive Spectrometry	18
2.3.2 Geochemical Analysis	18
X-Ray Fluorescence	18
Inductively Coupled Plasma – Mass Spectrometry	19
Computational Processing and Statistics	19
3 Results	21
3.1 Petrography	21
3.1.1 Quartz–piemontite schists	21
3.1.2 Mn–Fe–ore	22
3.2 Mineralogy and Mineral Chemistry	23
3.2.1 Ore minerals	25
Main ore minerals	25
Subordinate ore minerals	26
3.2.2 Mn-Silicate minerals	28

3.3	Bulk and Local–Bulk Geochemistry	34
3.3.1	Geochemical Analysis	34
	Metasediments	34
	Ore–rich Samples	38
3.3.2	Normalization Diagrams	39
3.3.3	Binary and Ternary Classification Diagrams	42
3.3.4	Correlation Analysis	45
4	Conclusions and Discussion	48
A	Additional optical microscope photographs	50
B	X–Ray Diffraction data	56
C	MATLAB processed grouped XRD Patterns	67
D	Additional XRD graphs	70
E	Raman Shift Graphs	72
F	SEM–EDS mappings	75
G	Geotectonic Classification Diagrams	78
H	Correlation Matrix	80
	Bibliography	91

List of Figures

1.1	Geotectonic/Terrane map of Greece	3
1.2	Detailed geotectonic map of the Aegean, based on correlations between the neighboring orogens	5
1.3	Part of the Eretria-sheet 1:50000 map and column	6
1.4	Geological map of NE Attica	7
1.5	Mass-age distribution of manganese ore deposits	11
2.1	Section of the quartz-piromontite bearing schist	16
2.2	Sample photographs.	17
3.1	Microphotographs of piemontite schists thin sections (Vrn6, Vrn12), silicate minerals and petrography.	22
3.2	Microphotographs of quartzites thin sections (Vrn14), laminated Fe-mineralization.	23
3.3	Detailed XRD peak identification of selected main ore minerals.	26
3.4	Detailed XRD peak identification of selected subordinate ore minerals.	29
3.5	Detailed XRD peak identification of the Mn-silicate minerals	31
3.6	Back-scatter microphotographs (SEM).	34
3.7	Normalization diagrams of the Varnavas Mn- and Fe-ore samples against Upper Continental Crust.	41
3.8	Normalization diagrams of the Varnavas Mn- and Fe-ore samples against the North Atlantic Shale Composite.	42
3.9	Ternary discrimination diagrams for the ore-samples.	44
3.10	Binary discrimination diagrams.	45
3.11	Similarity dendrogram for the qtz-pmt-schists.	46
3.12	Similarity dendrogram for the ab-quartzites.	47
A.1	Microphotographs (Vrn2), silicate minerals and petrography.	50
A.2	Microphotographs (Vrn6), disseminated Mn-Fe-mineralization.	51
A.3	Microphotographs (Vrn9), veinlet Mn-Fe-mineralization (1).	52
A.4	Microphotographs (Vrn6, Vrn7, Vrn9, Vrn12), veinlet (2) and intergranular Mn-Fe-mineralization.	53
A.5	Microphotographs (Vrn6), nodular massive and spotted Mn-Fe-mineralization.	54
A.6	Microphotographs (Vrn2, Vrn3, Vrn6), Mn-Fe-mineralization.	55
B.1	EVA processed XRD data.	66
C.1	XRD patterns (grouped - major mineral phases).	69
D.1	Detailed XRD peak identification of non-Mn-bearing rock-forming minerals.	71
E.1	Photographs from confocal microscopy and Raman shift graphs (Vrn6, Vrn11).	74
F.1	SEM-EDS elemental mapping.	77
G.1	Binary and ternary geotectonic classification diagrams.	79

List of Tables

1.1	Manganese concentrations in rocks	8
1.2	Manganese minerals in respect to individual mineral classes	10
2.1	A brief description of the analyzed samples.	18
2.2	Lower and upper detection limits for the ICP–MS analysis.	20
3.1	A synopsis of the mineral paragenesis of the analyzed samples.	24
3.2	Groups of the main mineral assemblages in respect to lithotype.	25
3.3	Mineral Chemistry table for the major ore–minerals (I).	27
3.4	Mineral Chemistry table for the major ore–minerals (II).	28
3.5	Mineral Chemistry table for the subordinate ore–minerals.	29
3.6	Mineral Chemistry table for the manganiferous rock–forming minerals.	31
3.7	Major oxide geochemical analysis and Mn/Fe ratio (XRF analysis).	35
3.8	Trace element geochemical analysis (XRF and ICP–MS analysis).	36
3.9	Rare earth element, precious and platinum group metals geochemical analysis and REE indices (XRF, ICP–MS analysis and fire assay fusion).	38

List of Abbreviations

Ch.	Chapter
Sec.	Section
Subs.	Subsection
Par.	Paragraph
Ap.	Appendix
Fig.	Figure
Tab.	Table
XRD	X-Ray Diffractionmetry
XRF	X-Ray Fluorescence
RS	Raman Spectroscopy
ICP	Inductively Coupled Plasma
MS	Mass Spectrometry
SEM	Scanning Electron Microscopy
EDS	Energy Dispersive Spectrometry
REE	Rare Earth Element
PGE	Platinum Group Element

Chapter 1

Introduction

1.1 Thesis' Scope

Manganese is a transition element and base metal, silvery grey in color and brittle. Manganese has numerous applications in metallurgy heavy industry, in construction industry, the energy sector, microelectronics manufacturing, in pharmaceuticals and in dye syntheses [Cannon et al., 2017, Cardarelli, 2017]. As an alloy-component it is used primarily in stainless and high-strength structural steel manufacturing as a deoxidizing and desulfurizing agent and as a factor of increasing malleability [Corathers and Machamer, 2006, Šalák and Selecká, 2012]. Additionally, in metallurgy it is used for creating certain high-strength aluminum and copper alloys [Corathers and Machamer, 2006]. Manganese oxides are used as substitutions in Portland cement clinker phases [Puertas et al., 1989] and in brick coloring [Corathers and Machamer, 2006] as for the construction industry. A particular manganese oxide, initially γ -structured manganese dioxide then as electrolytic manganese oxide and today as lithium-manganese oxide, is especially utilized as a battery cathode [Corathers and Machamer, 2006]. We are closing the series of the examples with the fact that manganese is also used in soft circuitry manufacturing manganese-zinc semiconductors [Cannon et al., 2017].

The element manganese is a transition metal and is commonly found together with iron in minerals in many geological environments and is extensively exploited. The economic significance of manganese-bearing formations is a result of a twofold fact. On the one hand high-grade manganese formations are ideal for high quality extraction of this base metal, while on the other hand a variety of manganese sources tend to host a wide range of metals and non-metals, some defined as critical, strategic and precious ones, due to the scavenging properties of manganese oxides and hydroxides. Some of these metals, along manganese and iron, are cobalt, nickel, copper, zinc, lead, vanadium, titanium, silver, gold, molybdenum, tungsten, lithium, strontium, barium, rare earth elements (scandium, yttrium and the lanthanides), platinum group elements (platinum, osmium, iridium, palladium, ruthenium and rhodium) and some actinides (thorium and uranium). Some non-metals are phosphorus, arsenic and antimony [Baturin, 1988, Graedel et al., 2015, Hein et al., 2020, Pirajno, 2009, Zhang et al., 2012].

The implementation of the present B.Sc. thesis is stemmed from its scope, which is the need **to study further metamorphosed manganese formations**, their mineralogical and geochemical features and from the attempt **to contribute to the study of the complex geology of Attica**. To this end we deal with the mineral characterization and classification, mineral chemistry and the bulk geochemical aspects of manganese nodular and (ferro)manganese crustal forms in a metamorphosed ferromanganese metavolcanosedimentary sequence, in Varnavas area, located in Northeast Attica, Greece. The collateral benefits of the above could be firstly to provide additional constraints on the metamorphic conditions that the protolith underwent as well as, secondly, to provide analogous constraints on the depositional environment physical-chemical conditions of the Mn-rich sedimentary protolith, under a number of assumptions. Comparisons are made on the mineral chemical data and bulk geochemical data of the manganoan formation with literature data from Mn-deposits of known tectonic environments. These could be utilized as paleoenvironmental proxies and the contrasting Mn-deposits or formations can be either contemporary or ancient. Thirdly, in side to the previous additional benefits we could determine the potential of critical metals in these metamorphosed formations.

1.2 Literature Review

1.2.1 Geological setting

An introduction to the Alpine orogenic system and the Hellenides

Greece, and more specifically the Hellenides Orogen, is part of the Alpine-Himalayan Orogenic Belt [Schmid et al., 2008, Schmid et al., 2020, Hinsbergen et al., 2020] that is a multiple-stage orogenic cycle, which is characterized by a series of sedimentary deposits, consecutive subduction, volcanic and suture zones, accretionary belts and metamorphic core complexes [Ring et al., 2010]. It is a discrete structure in the wider Alpine Orogeny, but also serves as the geotectonic

link between Balkanides, Dinarides and Albanides to the North and to Pontides and Anatolides to the East [Melfos and Voudouris, 2017, Schmid et al., 2020].

The Hellenides have been under extensive research since the late half of the 19th century. Both local and regional research contributed to our knowledge, while from the beginning there has been the trend to compare and correlate geological data of different areas. Early syntheses of the data first followed the Theory of Geosynclines and the introduced concept of isopic zones¹, which after their orogenic deformation, were transformed to geotectonic zones across the belt [Aubouin, 1959, Brunn, 1956, Brunn, 1960]. These studies made foundational comparisons of the Hellenides to the Alps, the Penninic mountains, or the North–American West coast mountain belt. The application of the Theory of Tectonic Plates followed and the paleogeography of the Hellenides was revisited [Aubouin et al., 1977, Decourt, 1972, Dewey et al., 1973, Jacobschagen, 1986, Papanikolaou, 1987, Papanikolaou, 1997, Papanikolaou, 2013].

A number of tectonic and paleogeographic models of the Hellenides have been proposed [Jolivet and Brun, 2010, Papanikolaou, 2013, Ring et al., 2010, Schmid et al., 2020, Hinsbergen et al., 2020]. The models proposed involve a different number of oceanic basins along the belt, as well as different geodynamic settings like ophiolites formed within spreading centers along mid–ocean ridges or those formed above supra–subduction zones, as these are the two main representatives of oceanic crust related to our discussion [Papanikolaou, 2009, Papanikolaou, 2013, Stampfli and Borel, 2002, Stampfli and Kozur, 2006]. In contrast to the debate regarding ophiolites the space in between the suture zones is predominantly covered by shallow–water carbonate platforms of Mesozoic to early Cenozoic age or their metamorphic analogues, with some outcrops of pre–Alpine basement rocks of Precambrian or Paleozoic age [Papanikolaou, 2013]. These were thought to represent microcontinents of gondwanic origin in the Tethys ocean [Papanikolaou, 2013, Schmid et al., 2020, Şengör, 1989].

The first model that we shall discuss is the one proposed in [Papanikolaou, 1997], refined in [Papanikolaou, 2009, Papanikolaou, 2013] and thoroughly explained in [Papanikolaou, 2015]. This model briefly asserts that the Hellenides are comprised from nine (tectonostratigraphic) terranes H1–H9, each one of them representing a complex paleogeographic area, as shown in Fig. 1.1. Five of these terranes are considered continental (Hi, i odd number) and four of them oceanic (Hi, i even) in nature. The proposed terranes are divided in units, with each unit representing a distinct isopic zone.

The tectonostratigraphy of the Hellenides, using the previous model, can be organized into the paleogeographic and paleogeodynamic evolution of the mentioned terranes. This evolution comprises three stages. The first stage is the continental rifting in the northern margin of Gondwana, which is characterized by volcanosedimentary sequences of Late Paleozoic to Triassic. The second stage refers to the continental drifting and the contemporaneous oceanic opening of Tethyan basins between the continental terranes of Triassic to Paleogene. This resulted in the formation of shallow–water carbonate platforms or deep–sea basins with pelagic sediments interlayered with and overlying to ophiolites. The third stage is the accretion of the terranes and their units along the Eurasian margin, which is characterized by flysch sedimentation along the trenches from possibly Early Jurassic to Neogene.

The second model we shall discuss is briefly contained in [Nirta et al., 2018] and asserts that the Hellenide orogen evolved through a Permo–Triassic intracontinental rifting stage, which is related to Pangaea break–up; an oceanic spreading stage from Middle Triassic with mid–ocean ridge lithosphere production; an intraoceanic subduction stage in Early to Middle Jurassic along with island arc and back–arc basin formation along the paleo–trench; an intraoceanic thrusting stage associated with high temperature – low pressure (HT–LP) metamorphism since Middle Jurassic; an ophiolite obduction stage since Late Jurassic; a continental collision stage in Cretaceous and ongoing shortening until Middle Eocene; a late orogenic extension stage of the nappe stack, starting in Late Eocene [Bortolotti and Principi, 2005, Brun and Faccenna, 2008, Dilek and Furnes, 2019, Jolivet et al., 2003, Nirta et al., 2018]. The reader can observe the spatial distribution of the ophiolites in [Nirta et al., 2018], which – regardless the model at use – are crucial for any paleogeographic reconstruction and paleogeodynamic setting.

We shall also discuss a third model proposed in [Schmid et al., 2008, Schmid et al., 2020, Hinsbergen et al., 2020], where the Hellenides are presented along the neighboring orogenic unities and considered as components of a larger scheme. A major difference in contrast with the previous model is the absence of any affinity for the Pindos Unit to an oceanic crust, either a mid–oceanic ridge [Papanikolaou, 2009] or a back–arc basin one created from an intraoceanic subduction [Nirta et al., 2018]. The Triassic basalts located at the base of the stratigraphic column of the Pindos Unit are referred as a result of an intracontinental rifting, which characterized the base of a number of columns like the Southern Alpine Unit, the external Dinarides and Hellenides.

The metamorphic rocks of the Hellenides are divided into three groups [Papanikolaou, 1984]. These groups, called the Internal, the Medial and the External Tectonometamorphic Belts, represent the units of the Hellenides that have undergone metamorphic processes. The External is comprised of the Plattenkalk Unit (or Crete–Mani Unit), the Phyllites–Quartzites Nappe (or Arna Unit) and the Siteia Unit and refers to metamorphic rocks in Peloponnese and Crete [Papanikolaou, 2015] and, in a sense, the metamorphic rocks that relate to the Adria microplate (H1). The Internal is formed by the metamorphic rocks that relate to the Rhodope metamorphic core complex and is related to the Pelagonian microplate.

In the present thesis we are interested in the Medial Tectonometamorphic Belt. It refers to metamorphic rocks in Macedonia, Thessaly, eastern Sterea Hellas, Cyclades and Samos. These metamorphic rocks originate from the Pelagonian

¹Specific paleogeographic domains of determined depositional and tectonomagmatic setting.

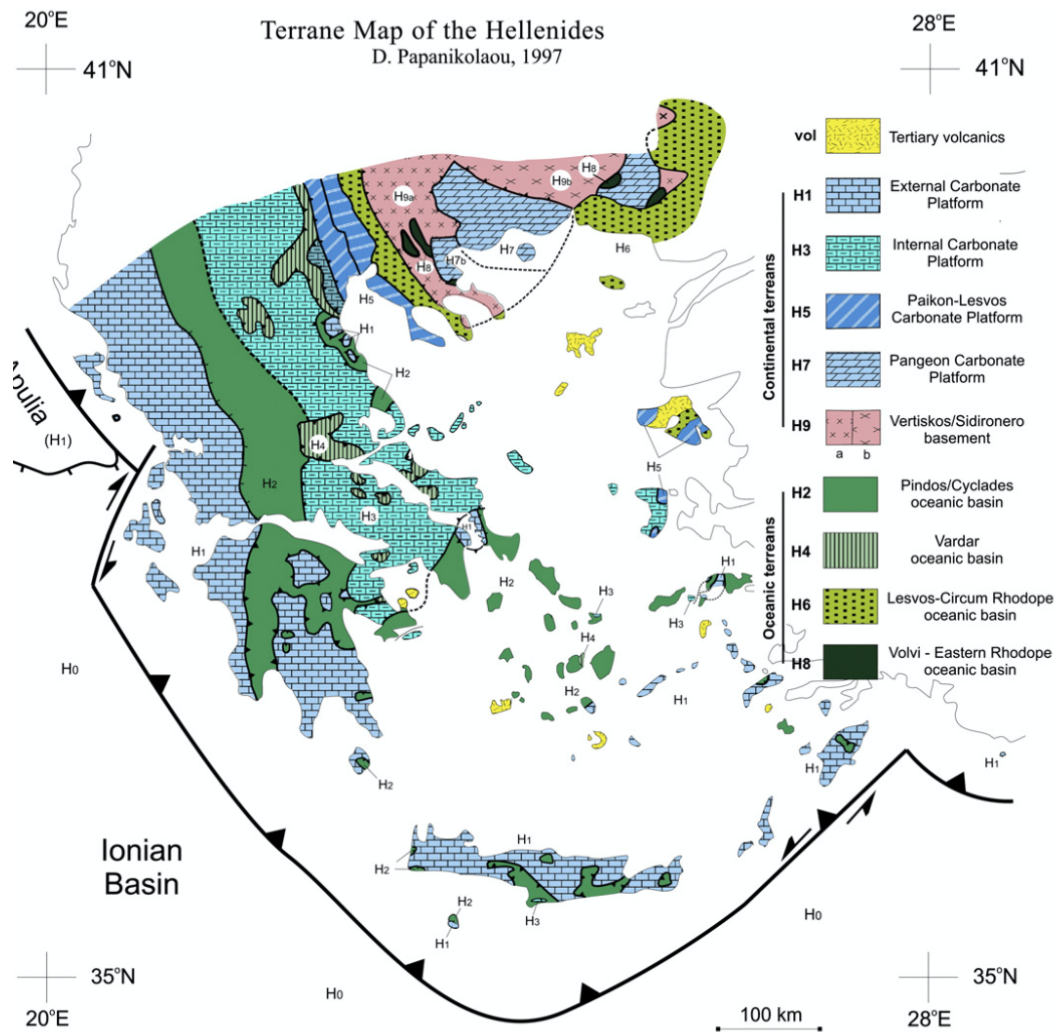


FIGURE 1.1: Geotectonic map of Greece, based on the terranes proposed in [Papanikolaou, 2013].

microplate and the Pindos Ocean [Papanikolaou, 2013] with a debate whether the autochthonous rocks in Attica and the basement rocks in Cyclades are related to the Gavrovo–Tripolitza Unit, thus related to Adria microplate [Jolivet et al., 2013, Papanikolaou, 2013, Papanikolaou, 2015, Scheffer et al., 2016, Schmid et al., 2020]. We are more specifically interested in the metamorphic rocks of the Attic–Cycladic Complex² (ACC), which is a set of units mainly separated into three subsets, namely:

- The Basal Units (BU), which is a general term referring
 - either to the Olympus–Ossa, Almyropotamos, Kerketeas tectonic windows comprised of marbles and metaflysch sequences (Gavrovo–Tripolitza Unit, low–grade metamorphic analogue) in southern Macedonia / northern Thessaly, central Evia and maybe northeastern Attica and Samos and Fournoi Islands, respectively,
 - or the Attica Autochthon comprised of marbles and schists or mélange–type formations in central and south-eastern Attica.
- The Cycladic Blueschist Units (CBU), which is also a general term referring
 - either to the North Cyclades Unit and its homologous units (like the Ampelakia Unit encircling the Olympus–Ossa window, the Pelion/Makrinitza window Unit in Magnisia, the Styra Unit which overlies the Almyropotamos window, the Ampelos Unit in Samos island)
 - or the South Cyclades Unit. The North and South Cyclades Units are distinguished both in terms of paleodeposition of protolith and metamorphic conditions [Papanikolaou, 2013].

²Or Attic–Cycladic Crystalline Complex (ACCC)

- The Upper Unit (UU), which is in fact ophiolites stratigraphically between the Cycladic Blueschist Units and the Upper Plate Units.

Closely related to the CBU are the:

- The upper plate Units, which mainly refer to metamorphic rocks of Pelagonian origin, like the Makrotantalón–Ochi Unit in northern Andros island and southern Evia, the Dryos Unit in Paros island, the Vari Unit in Syros island and the non–metamorphic Cycladic/Sub–Pelagonian Unit.
- The Ios – Cyclades Basement Unit (BU) comprised of gneisses (Gavrovo–Tripolitza Unit, high–grade metamorphic analogue associated with plutonic rocks) in southern Cyclades.
The following references cover the above and provide additional details [Brun and Faccenna, 2008, Gessner et al., 2011, Jolivet and Brun, 2010, Jolivet et al., 2013, Koukouvelas, 2019, Lozios et al., 2019, Perraki and Mposkos, 2001, Papanikolaou, 2013, Papanikolaou, 2015, Ring et al., 2010].

In general, the rocks in the CBU were involved in an Eocene (50–40 Myr) high–pressure (blueschist– to eclogite–facies) event followed by isothermal decompression and a subsequent distinct early Miocene (25–20 Myr) higher temperature greenschist– to amphibolite–facies stage metamorphic event [Jolivet et al., 2013, Papanikolaou, 2013, Papanikolaou, 2015, Ring et al., 2010]. Granitoids were emplaced syn–extensionally, like in Serifos and Mykonos islands. There were also thermal anomalies regarding a Miocene high–temperature metamorphic event, which occurred on the islands of Naxos and Paros, where migmatites formed and it was showed that this amphibolite– to granulite–facies metamorphism occurred during and probably as a consequence of extensional deformation [Ring et al., 2010].

In more detail, we note that for the CBU in Andros and Tinos Islands we have peak P–T conditions of 450 – 500°C and minimum pressure of 10kbar between 55–35Ma. The exhumation is then followed by isobaric heating up to 420°C and 7kbar and then isothermal decompression at 400 – 420°C and 2 – 7kbar. The ductile deformation ends at 21Ma and at 350 – 400°C [Huet et al., 2014, Jolivet and Brun, 2010, Reinecke, 1986]. The Basal Unit (Almyropotamos window) in Evia had peak P–T conditions of 350 – 450°C and 10 – 12kbar.

The geodynamic models discussed earlier are coaligned in the fact that the Cycladic Blueschist Unit is the metamorphic analogue of the pelagic / hemipelagic carbonate and siliciclastic formations of the Pindos Unit, left aside any other attributes Pindos Unit may have, at least for the units which are homologous to the Northern Cyclades Unit. In [Papanikolaou, 2013, Papanikolaou, 2015] the Southern Cyclades Unit and the Cyclades Basement Unit are considered Pelagonian in origin (meaning that they originated from the Internal Carbonate Platform – H₃). On the contrary, in [Schmid et al., 2008, Schmid et al., 2020, Hinsbergen et al., 2020] they are considered, together with the Basal Unit, as metamorphic analogues of the Gavrovo–Tripolitza Unit (Fig. 1.2). In [Schmid et al., 2008, Schmid et al., 2020, Hinsbergen et al., 2020] there is no a one–to–one correspondence of the Northern and Southern Cyclades Units to the Pindos and the Gavrovo–Tripolitza paleogeographic areas, respectively, as they are not mentioned as such.

We should, finally, note that the metamorphic core complex of the ACC was exhumated³ due to orogenic collapse and isostatic uplift as a result of the slab retreat and back–arc extensional regime (increase in the subduction angle).

Geology of Attica

The complex geology of Attica has long been under debate. The first detailed map is attributed to [Lepsius, 1893]. The following researchers tried to correlate its metamorphic rocks to possible precursors in the Hellenides or other metamorphic rocks in the ACC [Katsikatsos, 1976, Kober, 1929, Lekkas and Lozios, 2000, Lozios, 1993, Lozios et al., 2019, Marinis and Petrascheck, 1956, Philippson, 1898, Spanos, 2012].

The area of Varnavas is located in the NE Attica, Greece, and is part of the ACC. This belt hosts a rather wide variety of mineralization styles, either of base and precious metal or industrial rock, relative to its geographical distribution. The mineralization styles include those of porphyry and epithermal, intrusion–related, skarn, metamorphogenic and metamorphic style. The ACC is considered a quite densely mineralized region of the Hellenides Orogenic System. Some mineralized areas in the ACC region are deposits of economic significance and have been exploited viably since antiquity, while others are occurrences that have profound petrological, geochemical, paleoenvironmental or contemporary environmental significance [Melfos and Voudouris, 2017].

Attica can be divided in two parts. The northwestern part is occupied by the upper plate unmetamorphosed to low–grade metamorphic formations of the Sub–Pelagonian Unit. The eastern and southeastern part comprises lower plate metamorphic rocks, that represent the northwestern part of the ACC. The contact between those two upper– and lower–plate domains is covered by the Neogene formations of Athens – Agios Stefanos – Kapandriti Basin. Along the margins of the ACC and within the basin, two more tectonic units can be observed. Firstly, the very low–grade Alepovouni Unit that covers tectonically the northwestern margin of ACC and the mélange type «Athens Schists», which tectonically overlies both the

³Significant work on exhumation of oceanic blueschists and eclogites can be found in [Agard et al., 2009].

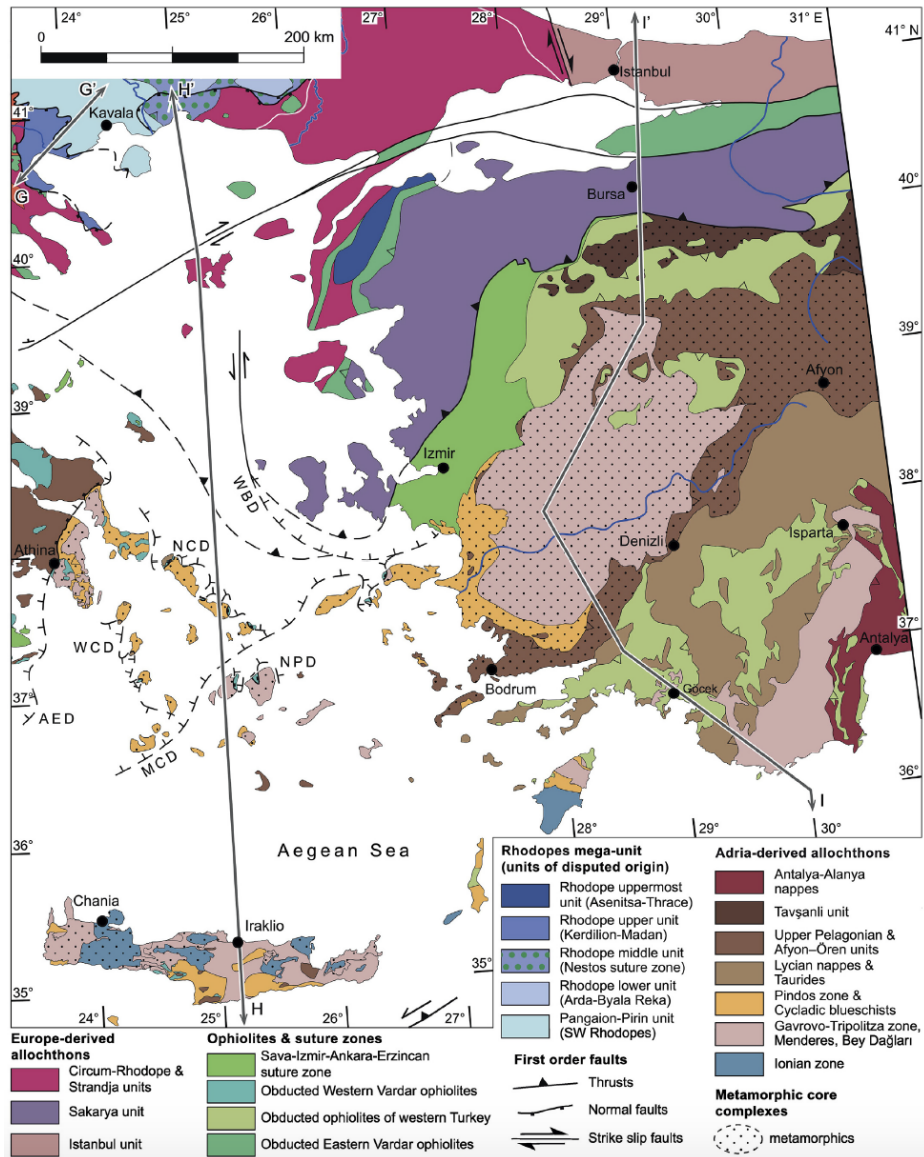


FIGURE 1.2: Detailed geotectonic map of the Aegean, based on correlations between the the Dinarides, Albanides, Balkanides and Taurides of the Alpine Orogen (NCD North Cycladic Detachment, WCD West Cycladic Detachment, NPD Naxos – Paros Detachment, MCD Mid-Cycladic Detachment, AED Attica – Evvia Detachment), from [Schmid et al., 2020].

southeastern margin of the Sub-Pelagonian Unit as well as the northwestern margin of the ACC and the Alepovouni Unit [Lozios et al., 2019].

The tectonostratigraphic column of Attica that [Marinos and Petrascheck, 1956] proposed for Lavrion peninsula includes a Lower and an Upper Unit. The Lower Unit comprises a Lower and an Upper Marble and a schist formation, with a blue-grey metachert marble layer in between, known as the Kessariani Schists. The base of the Lower Marble is partially dolomitic and / or with distinctive schist layers. A low-angle fault has been identified in Hymittos Mt. that juxtaposed the dolomitic lower part against the overlying calcitic part of the Lower Marble. In [Lekkas and Lozios, 2000] it is proposed that this lower part constitutes a different unit, which is named as Vari – Kirou Pira Unit. The Upper Unit represents a more heterogenous formation including schists, quartzites, blocks of mafic and ultramafic rocks and a thicker marble sequence at the top [Lozios et al., 2019].

The area of Northeastern Attica is bordered by Southern Evoikos Gulf (North and East borders), Athens basin and Hymittos Mt. (South border) and Agios Stefanos – Kapandriti basin (West border). The pre-Miocene basement of NE Attica consists of HP metamorphic rocks, which can be subdivided in two tectonic units, a lower and an upper one. The lower NE Attica Unit (NEAU) consists of marble, schists with distinctive blue-grey or metachert marble layers, quartzite, metabasite, acid metavolcanics and sparse serpentinite blocks and occupies most of the mountainous area from Penteli

Mt. to Southern Evoikos Gulf. More specifically, the lower NE Attica Unit consists of a greenschist facies metamorphosed volcanoclastic sequence at its base and an overlying carbonate sequence. Piemontite schists horizons within this unit are associated with calcareous schists, and quartz–mica schists. In contrast, the upper Agios Georgios Unit (AGU), appears in the form of relic outcrops along the eastern margin of Agios Stefanos – Kapandriti basin, mainly in the area close to the artificial Marathon Lake [Lozios, 1993, Lozios et al., 2019].

There are lithological differences between the two units (NEAU and AGU). The dominant foliation of NEAU is formed by typical greenschist–facies mineral assemblages. The high–pressure minerals are only found as relict inclusions in albite. On the contrary, blue amphiboles in AGU are abundant and glaucophane is a well–preserved mineral forming the main foliation [Lozios, 1993, Lozios et al., 2019]. According to [Baziotis et al., 2009, Baziotis et al., 2019], the NEAU underwent a HP/LT metamorphic event with a P–T peak at 9–11kbar and approximately 370°C, followed by decompression at 5–6kbar and a temperature increase during the exhumation, leading to the strong overprint of blue amphiboles by the greenschist mineral assemblages. A different P–T path is given for the AGU, where the mineral assemblages in metabasic rocks record a HP/LT event with a lower P–T peak at approximately 9kbar and an approximate temperature range of 350 – 370°C, followed by continuous cooling during the exhumation. It has been pointed out that, although the P–T conditions for NEAU are similar with those of the Basal Unit in Evia [Shaked et al., 2000], the P–T path is different since the latter is characterized by decompression cooling [Baziotis et al., 2009, Baziotis et al., 2019].

Geodynamic phenomena during the Triassic in the Aegean area are largely controlled by subduction of the Paleotethys ocean and opening of the Neotethys oceans. Triassic volcanosedimentary sequences, like these exposed in Varnavas area, have a complex composition in many cases, reflecting both subduction and rifting setting. A geodynamic model of rift formation in the active continental margin of Pelagonia is proposed to explain the transition from a subduction– to an extension–related magmatic activity in the Late Permian to Triassic time in the broader region of NE Attica and central Evia [Stouraiti et al., 2020]. A comment on the tectonomagmatic setting that set the volcanic input into the studied rocks is in Ap. G.

The Eretria–sheet published map refers to these formations as part of the later called Attic–Cycladic Crystalline Complex, as mainly muscovitic – quartzose – epidotic – carbonate – schists with marble and cipoline intercalations. Part of this map is in Fig. 1.3 [Katsikatsos, 1993]. Analogous formations continue to the South, northern to the Pentelikon mountain [Katsikatsos, 2002].

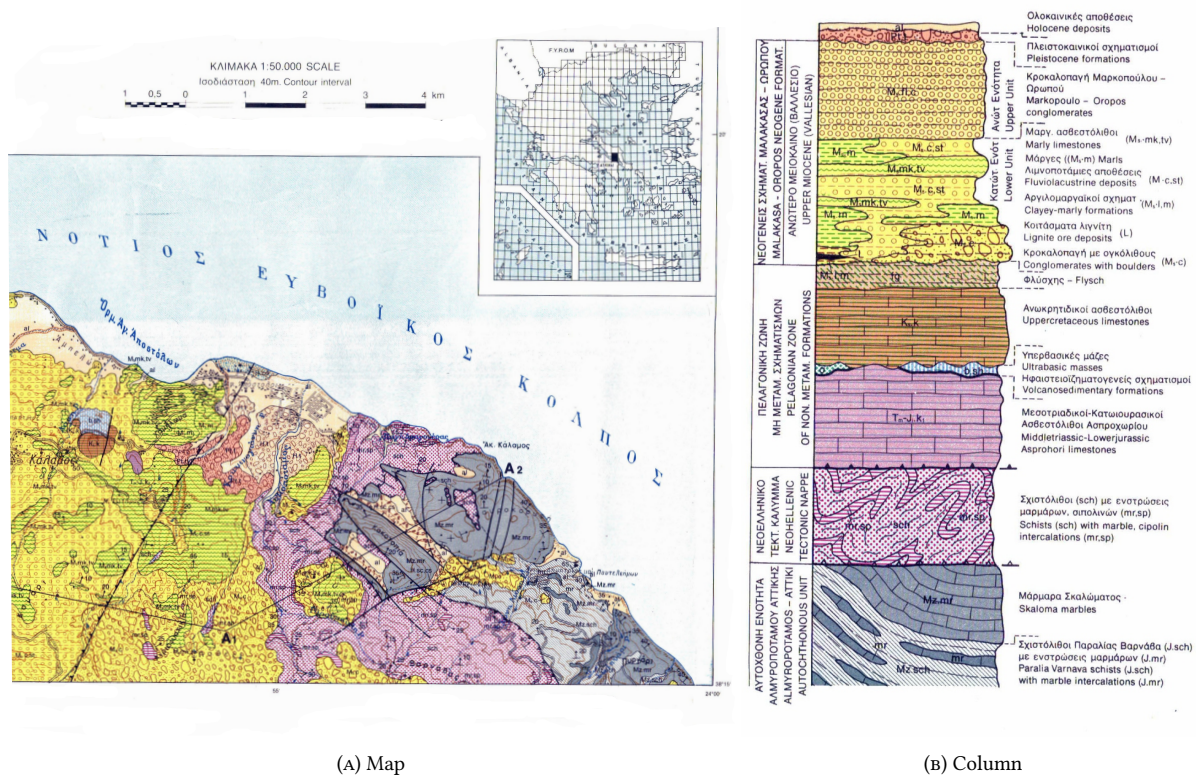


FIGURE 1.3: Part of the Eretria–sheet 1:50000 map and column (the Neohellenic Tectonic Nappe is an older name for the Attic–Cycladic Crystalline Complex), modified from [Katsikatsos, 1993].

The map that we accept in the present B.Sc. thesis regarding NE Attica is in Fig. 1.4 and regarding the regional geotectonic setting the one in Fig. 1.2.

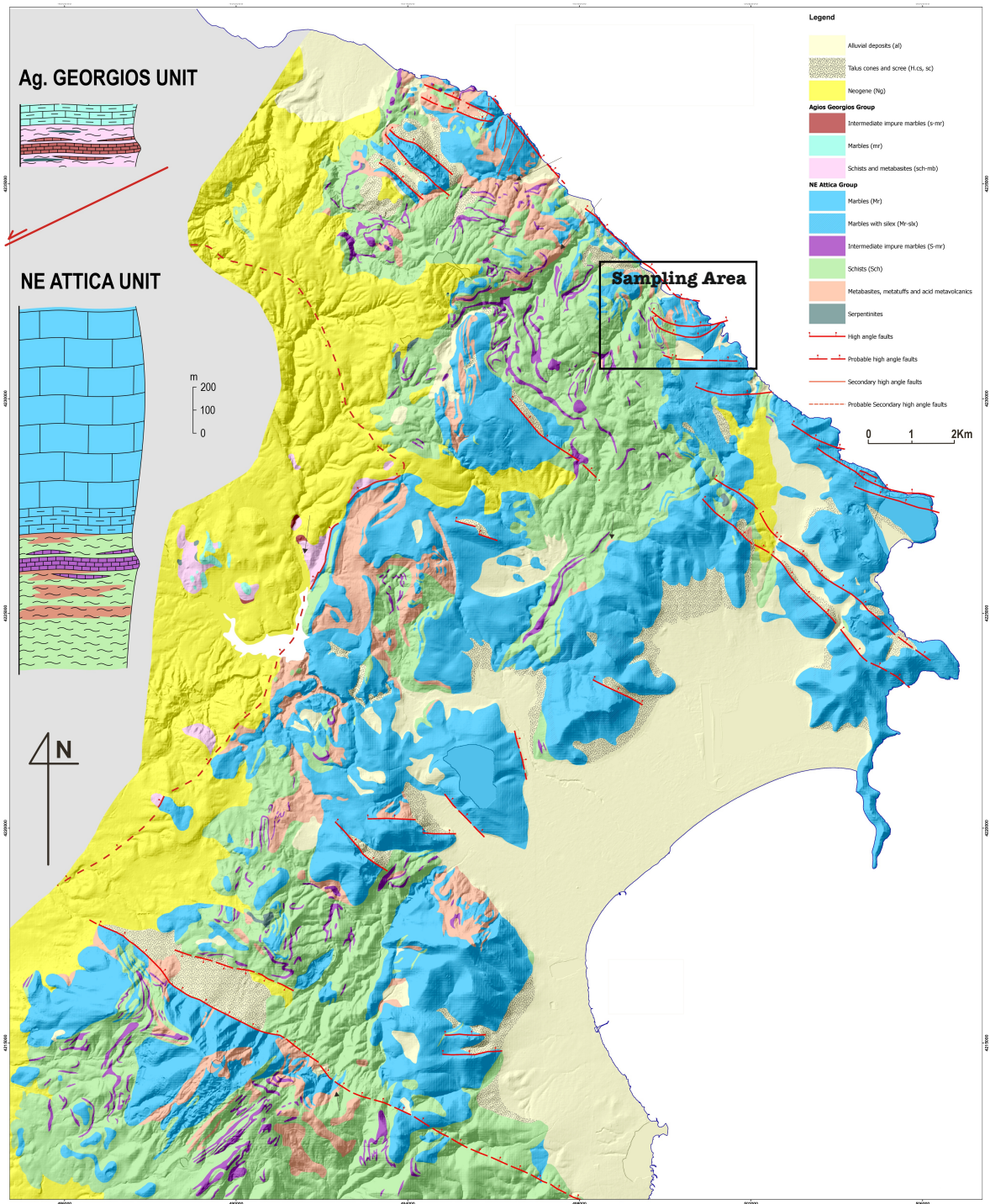


FIGURE 1.4: Geological map of NE Attica. Modified from [Lozios, 1993, Lozios et al., 2019].

Previous studies in the sampling area

Manganoan mineral phases were found and briefly described in [Lozios, 1993] in the areas of Mavrokoryfi and Aghios Georgios, in the relatively autochthonous unit. These Mn-bearing formations are classified into a more general micaceous – chloritic – epidotic schists and quartzites petrological type and are described as an isolated formation that is intercalated between other metasediments. They are mostly defined by piemontite, which has a special pinkish color, and by braunite, which is characterized as the opaque mineral that completes the manganese mineral assemblage. It has to be noted that in the present B.Sc. there has been found only sparse braunite through the quartz–piemontite–schist samples from Aghios Georgios area, Varnavas.

In 2008 a bachelor thesis [Galanopoulos and Charmatzis, 2008] was conducted at the same area. The mineralogy proposed was that of quartz + paragonite + muscovite + phengite + piemontite + epidote + spessartine + sursassite + Mg-celadonite + todorokite. The muscovite–paragonite solvus provided a 506°C temperature, provided muscovite saturation and greater than 10kbar pressure [Blencoe et al., 1994]. The proposed temperature is consider high in comparison with the results in [Baziotis et al., 2019].

1.2.2 Mineralogy and Geochemistry of manganese and deposit classification

Chemistry and geochemistry of manganese

Manganese, as mentioned in the beginning of this Chapter, is a transition metal, which is IUPAC–symboled as ${}_{25}\text{Mn}$, its average atomic weight is 54.938 and has a $[\text{Ar}]3d^54s^2$ fundamental–state electronic configuration. It is represented in nature by only one isotope, ${}^{55}\text{Mn}$. Manganese is also the tenth most abundant element in the Earth’s Crust, with an average concentration of roughly 1000ppm [Sarbas and Topper, 1993, Cardarelli, 2017, Kuleshov, 2017, Taylor and McLennan, 1985]. More details on manganese concentrations in individual rock types are presented in Table 1.1.

TABLE 1.1: Manganese concentrations in rocks, from [Sarbas and Topper, 1993].

Rocks/Sediments	Mean Mn content (ppm)
ultrabasic rocks	1050
basic rocks (basalt)	1390
intermediate rocks (diorite)	1200
intermediate rocks (syenite)	850
acidic rocks (Ca–rich)	540
acidic rocks (Ca–poor)	390
granites	260
graywackes	690
quartzitic sandstones	170
shales	600
shales (low in organic–C)	450
carbonate rocks	550
deep–sea sediments (clays)	5700
deep–sea sediments (carbonates)	1100

It is geochemically a quite strong lithophile element, but with some chalcophile character. In the upper Lithosphere, it is oxyphile and also shows a biophile tendency. Its biophile tendency makes it an element essential to both plants and animals⁴. Manganese is lithophile in most of the stony meteorites, but in the highly reduced enstatite chondrites, it is largely or entirely chalcophile⁵. It has little or no siderophile affinity and regarding other meteorite types, may be concentrated in iron meteorites⁶ [Sarbas and Topper, 1993].

The known valence states of manganese in inorganic compounds range from -3 to $+7$, but only the $+2$, $+4$, and more rarely $+3$ states are common in nature, with more than one valence state occasionally occurring in a single mineral phase⁷ [Kuleshov, 2017]. This behavior is useful as an indicator of depositional variables such as temperature, oxygen fugacity, Eh, and pH. The geochemistry of Mn in magmatic rocks is entirely dominated by the Mn^{2+} ion, whereas amounts of Mn^{3+} or Mn^{4+} in any magmatic rock or mineral are products of secondary oxidation. Oxidation of Mn^{2+} to Mn^{4+} is one of the most important geochemical process occurring in sediments, which is accompanied by precipitation of oxidate Mn compounds. This precipitation happens from solutions with relatively low pH values, even when extremely low concentrations of Mn are involved. A return of all or part of the Mn to the divalent state occurs – mainly – during metamorphism [Sarbas and Topper, 1993], although there exist a number of exceptions [Dasgupta et al., 1989, Dasgupta et al., 1990, Kuleshov, 2017, Roy, 1992].

We should note that for the trivalent state of manganese there are some interesting facts. Mn^{3+} is a metastable ion, which means that the reactions



⁴A factor in plant growth and an enzyme activator as examples, respectively.

⁵Being present in oldhamite, probably in troilite, and alabandite.

⁶Being present in accessory chromite but is virtually excluded from troilite.

⁷For example hollandite supergroup, todorokite/romanèchite.

and



are both favored to the right side of the chemical equations (1.1) and (1.2). However, this ion is stabilized when it enters the lattice of certain minerals, like piemontite, thulite, viridine and kanonaite among others [Burns, 2005, Keskinen and Liou, 1987, Langer et al., 2002]. This stabilization in epidotes, like piemontite, is due to the compressed acentric structure of the M₃ position, in contrast to the M₁ and M₂ of Fe³⁺ and Al³⁺, which behave as centrosymmetric. This electronic chemical-bond distortion is called Jahn–Teller Effect and is crucial in Mn³⁺–mineralization, because is the reason for the striking pleochroism of such minerals⁸, among other mineral phenomena [Bonazzi and Menchetti, 2004, Burns, 2005, Dollace, 1969].

Manganese is the most lithophile element, and has the largest ionic radius of the iron group of elements. It has a crystal–chemical position between Ca²⁺, Mg²⁺ and Fe²⁺. This results in a somewhat varying behavior with respect to its partitioning between coexisting Ca and Fe–Mg rock–forming minerals. The partitioning is dependent on the lattice crystal type, the coordination number and the chemical composition. Extensive details are based on examples regarding aluminosilicates, titanates and carbonates, among others. In addition, the divalent cations of Sr, Ba and Pb in Ca–minerals hinder the entry of Mn²⁺. Ni²⁺ does the same, but to a lesser extent, in Mg–minerals, whereas Fe²⁺ in an Mg–mineral favors the entry of Mn [Sarbas and Topper, 1993].

Although manganese resembles iron in many respects, as far as its manner of occurrence is concerned, there are also important fundamental differences between the two elements. This leads to a separation of Mn during geochemical processes, because of the different character of the ferric and manganic hydroxide colloids or by the action of solutions containing ferrous or ferric sulfate⁹ on Fe– and Mn–bearing carbonates or oxidate sediments. Compared with Fe, by far the greatest part of Mn present in igneous rocks is captured in the structures of rock–forming minerals, and becomes concentrated as separate minerals (oxides, phosphates, silicates) in late magmatic products, i.e. pegmatites and pneumatolytic–derived rocks.

During weathering, and because of differences in solubility and stability for Mn and Fe compounds, Mn may become enriched under favorable conditions as a bicarbonate¹⁰. In such weathering solutions manganese may be deposited under high redox potentials as manganic oxides and hydroxides, which are often accumulated in economical ore deposits. During the weathering process manganese is normally readily depleted from igneous and metamorphic rocks. It is quite mobile in the acid, highly organic weathering profiles of subarctic and temperate zones. In more alkaline soils of the humid tropics manganese, like iron and aluminum, is less mobile and may be concentrated in residual laterites or bauxites. In arid desert regions manganese may be concentrated as a thin surface oxide–film.

Manganese is also precipitated as a carbonate like rhodochrosite or hydroxide when CO₂ is removed from the bicarbonate by the action of (chemolithotrophic) bacteria or by oxidation, which is usual in modern Mn–rich sedimentary environments. The manganese precipitated quantitatively by the processes discussed often occurs as concretions, nodules, or slabs in the host sediment.

During metamorphic processes, the oxides or hydroxides of manganese are only rarely converted to hausmannite (Mn₃O₄) they usually result in silicates, chiefly rhodonite and, in the presence of an ample supply of Al, spessartine [Sarbas and Topper, 1993].

The most important controls on the chemical deposition of Mn from natural solutions include:

- equilibrium controls, which is predominate in igneous, metamorphic, and hydrothermal activity and influence diagenetic behavior of manganese during marine and lacustrine sedimentation;
- adsorption kinetics and colloid chemistry, which becomes most important in the deposition of marine ferromanganese crusts and nodules of Mn–oxides, that are also important scavengers of trace metals in soils and in marine or freshwater sedimentary environments;
- biogenic effects, which are caused by bacteria and other microorganisms which additionally catalyze deep–sea ferromanganese precipitates and these biogenic controls may preponderate in many lacustrine deposits [Sarbas and Topper, 1993].

The number of minerals containing manganese as the essential element is not quite large and the set is composed of mainly oxides and hydroxides [Post, 1999], the two rare sulfides alabandite and häüerite, the abundant carbonate mineral rhodochrosite, and the silicates braunite, tephroite, rhodonite / pyroxmangite, spessartine and piemontite, along with many other Mn–rich silicates. Present in great numbers are, however, minerals that contain manganese as a diadochic¹¹ component for other essential elements. These minerals are of great importance as a source of manganese, which is liberated

⁸The polarization colors, in Mn–silicates and –carbonates, are due to the fact that Mn is a transition metal, left aside the Jahn–Teller Effect [Bonazzi and Menchetti, 2004, Ghose et al., 1986, Langer et al., 2002].

⁹These are derived from the weathering of Fe–sulfides.

¹⁰Or named as hydrogen carbonate anion, HCO₃[–].

¹¹The reader is encouraged to search the notion of diadochic substitution in lattice structures [Hori, 1954].

during alteration or decomposition of rocks, and subsequently becoming concentrated in ore deposits. Ore-grade accumulations of manganese have been restricted in both space and time to a relative few metallogenic eras and provinces [Sarbas and Topper, 1993].

Manganese minerals

Nearly all mineral groups of petrological importance contain a manganese constituent which, sometimes, is found as an independent mineral. The Mn-minerals are only seldom formed as primary constituents of igneous rocks during the main stage of crystallization, for manganese does not become enriched enough to be able to form independent minerals, except in cases where the melt has an exceptionally high Mn-content. The Mn-minerals are generally constituents of metamorphic¹² and sedimentary rocks [Sarbas and Topper, 1993, Nicholson, 1992, Roy, 1968, Roy, 1992, Roy, 2006]. Out of the Mn-mineral species the following numbers in Tab. 1.2 belong to the referred individual mineral classes.

TABLE 1.2: Manganese mineral phases in respect to individual mineral classes, from [Sarbas and Topper, 1993].

Mineral Classes	Quantity
native elements	1
alloys	4
silicides, carbides etc	4
simple sulfides	7
arsenides	1
complex sulfides, arsenides etc	4
halogenides, oxyhalogenides	3
oxides	52
hydroxides	13
arsenites	6
tellurites	5
nitrates	1
carbonates	16
sulfites	1
borates	15
sulfates	14
phosphates	65
arsenates	34
vanadates	5
nesosilicates	7
nesosubsilicates	18
sorosilicates	25
cyclosilicates	7
inosilicates	21
phyllosilicates	31
tectosilicates	1
unclassified and/or unnamed silicates	62
organic compounds	1

Manganese mineralization in sedimentary environments

The global manganese sedimentary record is strictly correlated to the Earth's geological and stratigraphic history. The concentration of manganese in solution and its precipitation in inorganic systems are primarily redox-controlled. The increase in atmospheric photosynthetic O₂ with a CO₂ decrease, the increase in organic matter deposits, the increase in weathering rates and the glaciation cycles due to the supercontinent formations, a progressive Mantle oxygenation during the Archean till the Archean-Proterozoic transition are connected to the manganese sedimentary record [Roy, 2006]. Figure 1.5 shows the mass-age distribution of manganese ore deposits.

Two models of sedimentary manganese mineralization are proposed. Both models suggest that manganese is solubilized in deep-water sediments under anoxic conditions and precipitated at the point where the redox interface impinges on the seafloor. The first is called the euxinic basin model and asserts that anoxia is caused in a basin that is isolated from the open ocean and that has free H₂S in the bottom water. The second is called the oxygen minimum zone model. In this model

¹² Altered rocks, also.

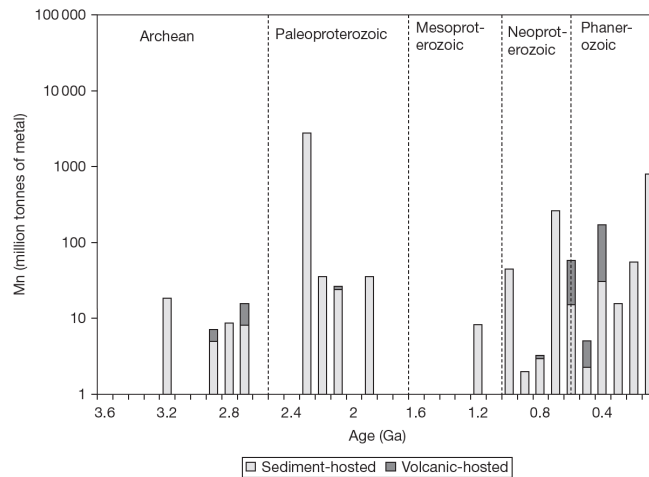


FIGURE 1.5: Mass-age distribution of manganese ore deposits, from [Maynard, 2014].

anoxia is caused by overloading the system with organic carbon from high primary productivity, typically occurring beneath upwelling nutrient-rich areas [Maynard, 2014].

Classification of manganese formations and deposits

According to [Varentsov, 1996] we have the following classification for rock-hosted ores:

- Weathering crusts:
 - Residual accumulations: either in situ or as products of local redeposition. These are in the form of laterites, with shallow or deep leaching processes that may or may not be followed by redeposition. The manganese ores of this type are usually developed after initially Mn-poor accumulations get affected by (sub-)tropical weathering. This type of manganese ore is considered as high-quality ore and is composed of oxide minerals, like cryptomelane, pyrolusite, manganite, lithiophorite, nsutite, todorokite and others.
 - Karst and infiltration accumulations: mostly oxide-mineral ores localized in filling cavities of paleokarst. They are generally composed of braunite, bixbyite, hausmannite, jacobsite and others.
- Sedimentary:
 - Exogenic: an exogenic sediment source like non-local redeposition of weathering crusts, wash-out sediments of the source area or underwater leaching. The commercially significant ore deposits of this sub-type are composed of pyrolusite, manganite, romanèchite, cryptomelane, rhodochrosite, manganocalcite, among others.
 - Endogenic: a hydrothermal-sedimentary source such as hydrothermal solutions in basins or exhalative formations. This is mostly represented by stratified manganese or iron-manganese formations. There are also lithological relations with cherty formations. The associations of Fe-Mn and Ba-Pb-Zn mineralizations are characteristic. They are composed of braunite, hausmannite, hollandite-group minerals, while in oxidation zones of this type todorokite / romanèchite and vernadite varieties can be found.
- Volcanogenic¹³
 - Hydrothermal.
 - Metasomatic.

These two cases have mineral assemblages like the hydrothermal-sedimentary case, either stratabound or vein-like.
- Metamorphosed: mostly referring to regional metamorphism of the above types. Typical oxide ores are braunite, bixbyite, hollandite-group and jacobsite.

For sediment-hosted ores, according to [Varentsov, 1996], the classification is as follows:

¹³No commercial significance.

- Metalliferous sediments: of (amorphous) Fe–Mn–oxohydroxides and heavy–metal sulfides, either proximal or distal to a hydrothermal source.
- Fe–Mn–nodules and crusts: described by concentric radial or laminated characteristics, respectively, defined by mineral successions of Fe– to Mn–oxohydroxides. They are geochemically discriminated as hydrogenous, diagenetic or hydrothermal.

A second manganese–oxide deposit classification according to [Nicholson, 1992] states that depending on the formation process and the depositional environment we have:

- Supergene:
 - Terrestrial:
 - * Bogs and soils, which refers to all accumulations of manganese oxides found in soil profiles, including swamp or bog deposits.
 - * Fresh water, which refers to cements and coatings on stream or lacustrine sediments, like lacustrine nodules, lacustrine coatings, oxide coatings and veins from fresh groundwater. The positive correlations of elements with manganese in supergene fresh water is **Mn** – Ag – **Ba** – Ca – Cd – Ce – **Co** – **Cu** – Fe – **K** – La – Li – **Mg** – Mo – Na – Nb – Ni – P – **Sr** – **Zn**¹⁴.
 - * Weathering, which refers to surface crusts and coatings formed by weathering, dendrites, desert varnish and laterites. The positive correlations of elements with manganese in weathering deposits is Mn – Ag – Ba – Ca – Ce – Co – Cr – Cu – K – La – Mo – Na – Nb – Sr – V – Zn – Zr
 - * Dubhites, which is the manganese–rich equivalent of a gossan. The positive correlations of elements with manganese in dubhite deposits is **Mn** – Ag – Ba – Ce – **Co** – Cr – Cu – La – Mo – **Ni** – **Pb** – Sb – Sr – V – Y – **Zn**.
 - Marine:
 - * Crusts.
 - * Coatings.
 - * Nodules.
 - * Sediments.
All of the above are morphological terms, that each can be further classified as continental run–off, hydrogenous, diagenetic and hydrothermal, with a further discrimination as those of continental shelf, shallow marine and marine. The positive correlations of elements with manganese in supergene marine deposits is **Mn** – Ba – **Co** – Cr – **Cu** – K – Mg – Mo – **Ni** – V – **Zn**.
- Hydrothermal:
 - Terrestrial:
 - * Hot spring, which refers to direct oxide–deposits from geothermal waters and pools. The positive correlations of elements with manganese in hydrothermal hot spring deposits is Mn – Ag – As – Cr – La – Mo – Ni – Zn.
 - * Vein, which only includes the primary precipitates and the supergene mineralization in an upper oxidized sequence.
 - Marine:
 - * Sedimentary exhalative, which refers to bedded manganese–rich sediments of exhalative origin. The positive correlations of elements with manganese in hydrothermal sedimentary exhalative deposits is Mn – As – Ba – Cu – Mo – Sr – V.

This classification does not give account to the metamorphosed analogues or metamorphic in origin manganese oxide deposits.

Mineralogy as a tool in characterizing the genetic origin of manganese deposits has been used occasionally, but diagnostic mineralogical signatures have not been rigorously defined [Nicholson, 1992]. However, according to [Nicholson, 1992, Roy, 1968] there are some qualitative criteria, in which some dominant minerals may contribute to the genetic origin characterization of a manganese–rich formation. To this end, bixbyite, braunite, hausmannite, huebnerite, jacobsite and pyrochroite are mostly of hydrothermal origin, whereas chalcophanite, coronadite, crednerite, vernadite, groutite, hollandite, lithiophorite, manganite, nsutite, quenselite, romanèchite, ramsdellite and woodruffite are mostly supergene in nature [Nicholson, 1992]. This mineralogical discrimination refers to un–metamorphosed formations.

¹⁴**Bold** letters refer to higher positive correlations.

An interesting classification in terms of distribution of manganese minerals in relation to different genetic types can be found in [Roy, 1968]. The four main classes are:

- Minerals in veins formed in hypogene processes. These mostly include pyrolusite, cryptomelane, psilomelane (oxides / hydroxides), rhodochrosite (carbonates), rhodonite / pyroxmangite (silicates) and alabandite (sulfide).
- Minerals formed in sedimentary conditions. These mostly include pyrolusite, cryptomelane, psilomelane, birnessite, todorokite (oxides / hydroxides) and rhodochrosite (carbonate).
- Minerals formed due to metamorphism. These mostly include manganite, bixbyite, braunite, hollandite, hausmannite, jacobite, vredenburchite (oxides / hydroxides), rhodochrosite (carbonate), rhodonite / pyroxmangite, spessartine, tephroite and juddite (silicates).
- Minerals formed by supergene processes. These mostly include pyrolusite and cryptomelane (oxides / hydroxides).

Metamorphosed manganese-rich (volcano-)sedimentary rocks occur widely in different geological settings. The rocks display variable mineral assemblages derived from manganese-rich precursor rocks of diverse bulk composition and through metamorphic reactions of various grades [Dasgupta et al., 1990]. A theoretical study of the mineral reactions in manganese oxide rocks based on pressure, temperature, Mn-content and oxygen fugacity is in [Dasgupta et al., 1989], while in [Roy, 1968] the temperature-related mineral transformations are studied mainly through petrography of a quite wide range of geological settings. Substantial work regarding manganese-rich metapelites and metapsammities based on experimental data coupled with thermodynamic calculations is that of [White et al., 2014]. A classification scheme proposed in [Dasgupta et al., 1990] for metamorphosed manganese-rich formations is the following:

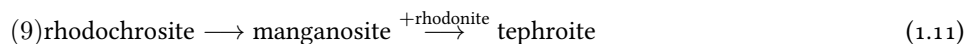
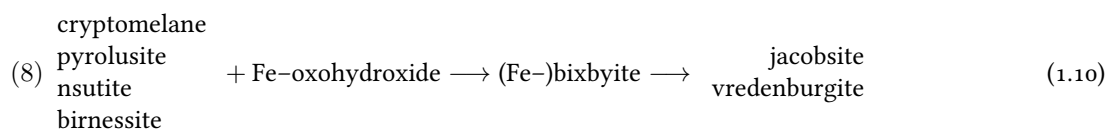
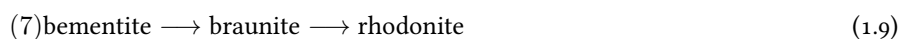
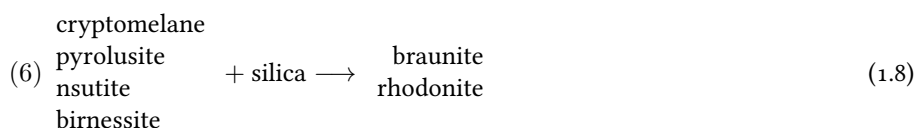
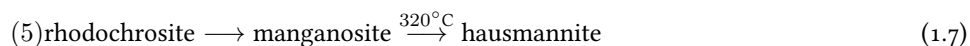
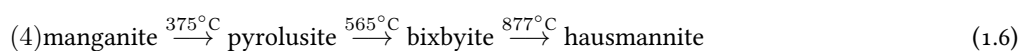
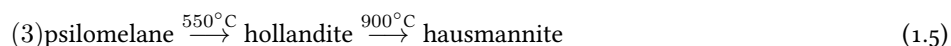
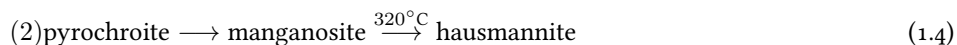
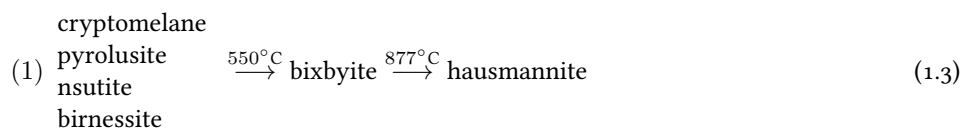
- **Type I:** Manganese-oxide rocks (ore) containing quartz. In Type I assemblages we have braunite and hausmannite, which may intergrow with jacobite. Pyrolusite can be found as recrystallized in greenschist or higher-grade facies. Type I can be further classified as
 - hollandite-bearing or
 - hollandite-free, which is a criterion for the formation to have undergone upper amphibolite facies with hausmannite replacing both hollandite and bixbyite.

When present braunite and hollandite show preferred orientation and braunite is formed in expense of bixbyite.

Type I precursor rocks may resemble what ferromanganese nodules in modern basins are, or diagenetically modified not carbonated sediments. There may be a relation to shallow-marine sediments or seamount sediments and not necessarily those of deep-sea. The precursor mineralogy may be mainly of todorokite, birnessite and vernadite.

- **Type IIA:** Manganese-silicate rocks with minor Mn-oxides. The Type IIA assemblages are dominated by spessartine-rich garnet and quartz, whereas the dominant pyroxenoid is pyroxmangite and not rhodonite. Type IIA precursors are considered as problematic, because the absence of carbonates in the metamorphosed formation does not necessarily imply a non-carbonate precursor. A viable proposition is that of quartz-rich (clayey) mudstone also rich in Fe-Mn-oxohydroxides.
- **Type IIB:** Manganese-oxide-dominated rocks interbanded with Type IIA and containing minor silicates. In Type IIA and IIB assemblages garnet, quartz, pyroxmangite and the (Fe-)Mn-oxides display sharp mutual boundary relations in a granoblastic fabric. Jacobite and pyroxmangite show symplectitic intergrowth. Higher Mn-oxides in nodules and crusts associated with pelagic sediments may be the precursor of Type IIB rocks.
- **Type IIIA:** Manganese-silicate-carbonate rocks with or without minor Mn-oxides. The Type IIIA assemblages have a strong possibility that the premetamorphic sediments to be Mn-Mg-Ca-Fe carbonates, admixed with Si-Al-minerals.
- **Type IIIB:** Manganese-oxide-dominated rocks interbanded with Type IIIA and containing minor Mn-carbonates. In these assemblages rhodochrosite and quartz coexist only at very low metamorphic grades, which is the case also for tephroite. Spessartine replaces Mn-chlorite in greenschist-facies. High-grade assemblages contain knebelite instead of tephroite. These pairs exhibit sharp mutual boundary texture. In high-temperature assemblages garnet, pyroxmangite / rhodonite, Mn-cumingtonite and Mn-olivine show similar texture. Generally, coexisting carbonate and silicate minerals also demonstrate equilibrated fabric. In higher temperature, i.e. in granulite facies, there is rhodonite, johannsenite or hedenbergite granoblastic texture. Type IIIB rocks are probably a result of metamorphic reactions in a mixed carbonate-oxide sediment, which means a high oxidizing seabed near the CCD, at a specific chronostratigraphic era.

The mineral transformations, regarding Mn–minerals, occurring in metamorphic reactions in rising temperature are [Roy, 1968]:



Examples of known manganese formations and deposits

Contemporary manganese-rich sediments are a crucial iron, manganese and generally polymetallic source. The Kara Sea ferromanganese nodules are an important example, with 7 and 10Å–manganite and goethite mineralogy [Vereshchagin et al., 2019]. A distinctly significant example is the Fe–Mn–nodule Clarion–Clipperton Zone, Pacific Ocean, with a Fe–Mn–REE–Cu–Ni–Co–Zn–Mo enrichment and a birnessite and 10Å–phyllo-manganate mineralogy [Hein et al., 2020, Reykhart and Shulga, 2019]. A hydrogenetic example in the Southern Atlantic Ocean refers that there is a PGE accumulation and a buserite, asbolane, birnessite, goethite, (Fe–)vernadite mineralogy [Berezhnaya et al., 2018]. A manganese deposit with a particularly strong hydrothermal component is that of Izu–Bonin–Mariana volcanic arc, with birnessite and todorokite [Usui and Glasby, 1998].

Sedimentary–rock manganiferous formations and deposits are the majority, regarding the genetic origin. An important example is the hydrothermal in origin Baby Bare seamount in the Northeastern Pacific Ocean (2.7 – 0.5Ma), with 10Å–manganite and pyrolucite as the dominant manganese mineralogy [Fitzgerald and Gillis, 2006]. Another important example is the submarine diagenetic / exhalative Cambrian Mn–deposit in Harlech, North Wales, in quartz–spessartine–rich graywackes and mudstones [Bennett, 1987]. The Groote Eylandt manganese–oxide deposit is an important example of supergene alteration processes Mn–mineralization, with proof of a vernadite, romanèchite, pyrolusite and todorokite primary sedimentation, pyrolusite–forming diagenetic reactions, cryptomelane– and lithiophorite– forming supergene processes

and pedogenetic processes in favor of birnessite and chalcophanite [Ostwald, 1988]. An other significant type of hydrothermal sedimentary Mn–mineralization with Mn–Ag enrichment, is the Baja California coastal / intertidal hydrothermal springs with an acanthite, native silver, pyrite, todorokite, romanèchite, aragonite, high–Mg–calcite and barite mineralogy [Salas et al., 2008, Rodríguez-Díaz et al., 2018]. A special sedimentary category is the black–shale–related manganese deposits, like the Úrkút deposit, Hungary, with a Mn–carbonate, 7Å–phyllo-manganate, celadonite, goethite mineralogy with strong biomineralization geochemical signatures or like the Nanhuan Datangpo Formation, China, composed analogously [Polgari et al., 2012, Xiao et al., 2017]. Two other examples of un–metamorphosed volcanosedimentary manganese–rich formations spatially associated with ophiolite sequences are those of Othrys and Perachora, Greece, consisting of pyrolusite, braunite, cryptomelane, manganite, hollandite, vernadite, birnessite and only purolusite, respectively [Panagos and Varnavas, 1984]. Milos Island, Cyclades, Greece is a special example of Quaternary manganese–barite deposit, composed of quartz, K–feldspar, vernadite, pyrolusite, ramsdellite, jacobsonite, barite, hollandite, franklinite and pyroxene [Hein et al., 2000].

Metamorphosed Mn–rich formations are not quite often, such as sedimentary are. An important example are the Devonian Magnitogorsk paleovolcanic belt in Southern Urals, Russia, which is a metamorphosed hydrothermal volcanosedimentary sequence that has undergone regional prehnite – pumpellyite facies metamorphism, consisting of quartz, hausmannite, rhodochrosite, tephroite, ribbeite, pyroxmangite, caryopillite, calcite, kutnahorite, spessartine, rhodonite and clinocllore [Brusnitsyn, 2006, Brusnitsyn, 2010, Brusnitsyn and Zhukov, 2012]. Another important example is piemontite–rich hematitic ore deposit in Tokoro Belt, Hokkaido Island, Japan, which is a metamorphically low–grade radiolarian chert [Akasaka et al., 1988, Choi and Harita, 1992]. The Bald Knob Manganese Deposit is also a metamorphosed one, which has experienced a blueschist–facies event and having a rhodochrosite – kellyite mineralogy [Flohr, 1992]. A significant example is that of the piemontite–bearing quartzose and quartzofeldspathic schists from Arrow Junction, Western Otago, New Zealand, with albite, epidote, piemontite, spessartine and hematite [Coombs et al., 1985]. The Lienne Valley manganese deposit is a Variscan–orogeny Lower Devonian example, with spessartine, Ce–piemontite, pennantite, Mn–thuringite, kutnahorite and allanite [Schreyer et al., 1986]. An amphibolite–facies metamorphosed example is that of Hidaka Mountains, Hokkaido Island, Japan, with quartz, white mica, (Mn–)tourmaline, magnetite, spessartine, epidote, piemontite, viridine and Ti–Mn–hematite [Grapes and Hashimoto, 1978]. A braunite–rich medium– to high–grade metamorphism ore deposit in Southern Apennines, Italy, is composed of braunite, neltnerite, piemontite, cryptomelane, hollandite, todorokite, birnessite, Sr–piemontite [Sinisi et al., 2018]. A manganese formation with significant similarities to metamorphosed Mn–rich formations in Greece is in St. Marcel, Piedmont, Italy, composed of Mn–omphacite, braunite, quartz, albite, piemontite, diopside, microcline, hollandite, Sr–calcite, apatite, Mn–phengite, Mn–phlogopite [Brown et al., 1978]. Fe–Mn–metasediments have also been studied in Kythnos Island, Cyclades, Greece, with hematite or mica–bearing quartzites and garnet–bearing amphibole schists, composed of hematite, magnetite, quartz, calcite, albite, tourmaline, micas, braunite and hausmannite [Chrysanthaki and Baltatzis, 2003]. Additionally, in Tinos Island, Cyclades, Greece, we have a hydrothermal metaconglomerate, composed of calcite, Mn–phengite, Mn–aegirine/jadeite, microcline, albite, quartz, braunite and hollandite [Altherr et al., 2013].

A quite distinct case of a metamorphosed ferromanganese formation is in Andros Island, Cyclades, Greece, which has been exploited since 20th century. Additionally, extensive work has been done in terms of research, regarding the ferromanganese formations, which have undergone a prograde blueschist– to a greenschist– / amphibolite–facies retrograde metamorphic events and being composed of quartz, albite, muscovite, phlogopite, Mg–chlorite, epidote, piemontite, spessartine, ardennite, sursassite, pumpellyite, crossite, braunite, hematite, rhodonite, Na–pyroxene, Na–amphibole, magnetite, viridine, rhodochrosite, rutile, titanite, calderite, deerite and celsian [Reinecke, 1982, Reinecke et al., 1985, Reinecke, 1986, Reinecke, 1987]. On Andros the ferromanganese metasediments occur in a widespread lateral distribution. They form concordant layers and lenses within a uniform sequence of quartz–rich metapelitic schists which can be derived from pelagic siliceous mudstones [Reinecke et al., 1985]. Three main types of ferromanganese metasediments were geochemically investigated. Firstly, a piemontite–spessartine and piemontite quartzites, which contain braunite–rich lenses; secondly, spessartine quartzites; and thirdly, Na–pyroxene quartzites [Reinecke et al., 1985, Reinecke, 1986].

Chapter 2

Materials and Methods

2.1 Sampling

Sampling was conducted in the area of Varnavas, as shown in the map of Figure 1.4.

The majority of the samples were collected by digging circa 40–50cm into the ground in order to obtain non-weathered ones. A photo of the place that Vrn1 was taken is in Figure 2.1. Each sample's mass was around 0.75–3kg. Approximately 5–6kg of material was sampled in each of the five positions.



FIGURE 2.1: A section of the quartz–piromontite bearing schist, on the ground.

Indicative photographs are provided in Figure 2.2, showing

- the dominant quartzitic and piromontitic mineralogy of the silicate minerals in the schists with manganese ore and
- hematitic layers in the quartzite.

More details will follow in Sec. 3.1.

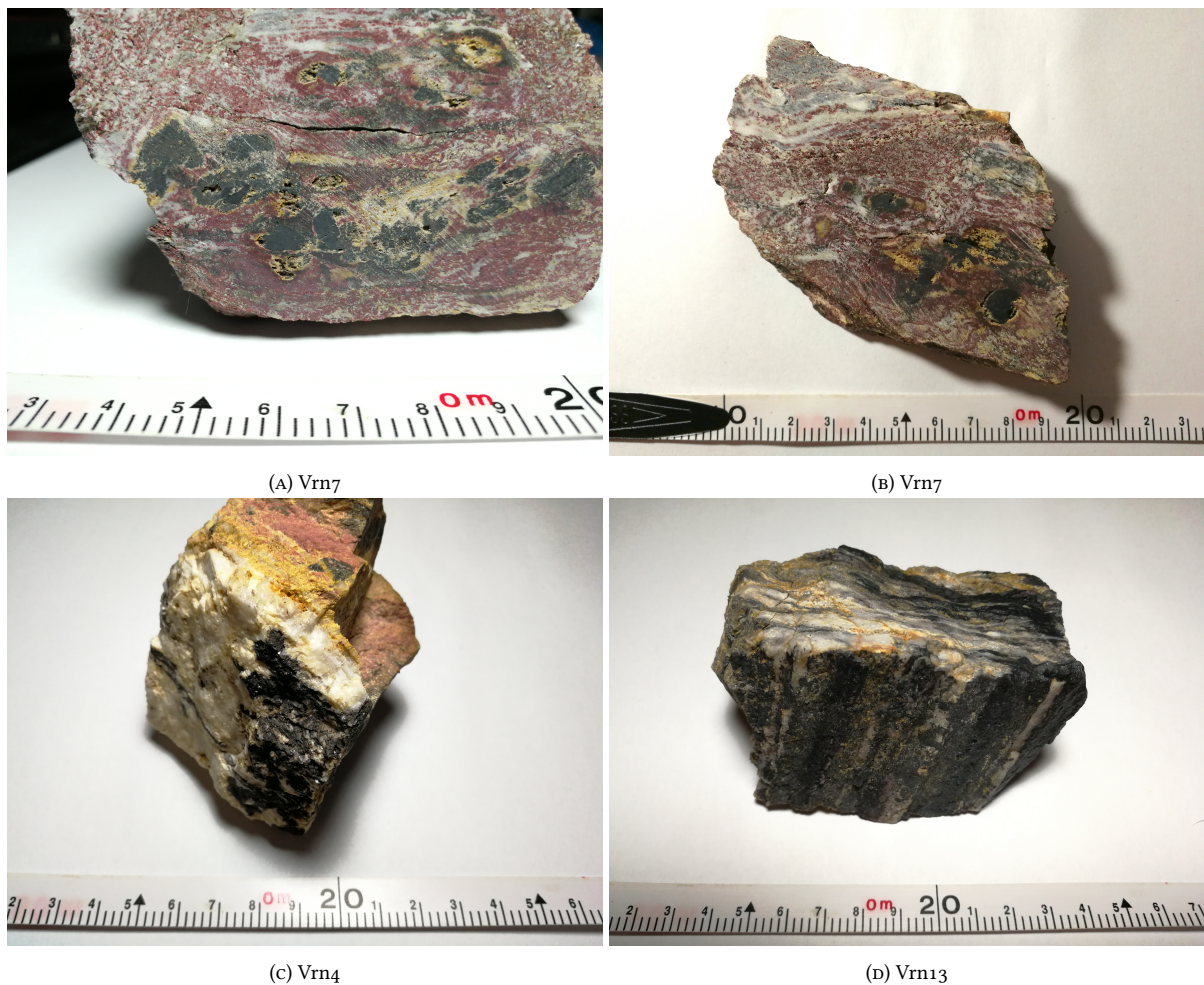


FIGURE 2.2: Sample photographs.

The samples were taken transversely to main schistosity in a SW–NE direction. We initiated from sample Vrn1 to Vrn 4 and Vrn6 to Vrn12 which is the Mn–rich part, and continued to Vrn15, Vrn13 to Vrn14, which is the Fe–rich part. The sample Vrn5 is a quartzitic vein which is cross–cutting stratigraphy. Between Vrn4 and Vrn6 there exists a quartzitic lens which contains Fe–rich ore. Table 2.1 provides a brief description of the samples. The Fe–rich part seems to be stratigraphically lower than the Mn–part.

2.2 Optical Microscopy

The petrographic analysis and the first stage of the mineral characterization was conducted using thin and polished sections. These were conducted at the Hellenic Survey of Geology and Mineral Exploration in the Mineralogy – Petrography Lab, from the samples briefly described in Tab. 2.1. There were utilized two research optical (light) microscopes, one in the Department of Economic Geology and Geochemistry, Faculty of Geology and Geoenvironment, National and Kapodistrian University of Athens (Leica®) and the other in the Mineralogy – Petrography Lab, Hellenic Survey of Geology and Mineral Exploration (Carl Zeiss®).

2.3 Analytical Techniques

Some of the methods mentioned in the following subsections require pulverized material. The sample preparation and pulverization were conducted in the Faculty of Geology and Geoenvironment, National and Kapodistrian University of Athens. Most of the samples were massive and were broken into small chips with a jaw breaker. The chip samples were grounded to less than 200 mesh fine powder by using an agate mill. Each ore–poor sample approximately weighted 300g,

TABLE 2.1: A brief description of the analyzed samples.

Samples	Description	Comments
Vrn1	Quartz–piemontite–rich schist with Mn–mineralization	host rock
Vrn2	Quartz–piemontite–rich schist with Mn–mineralization	host rock
Vrn3	Vrn3–1 Quartz–piemontite–rich schist with Mn–mineralization	host rock
	Vrn3–2 Quartz–piemontite–rich schist with Mn–mineralization	piemontite–rich separate
Vrn4	Quartz–piemontite–rich schist with Mn–mineralization	host rock
Vrn5	Quartzitic vein	-
Vrn6	Vrn6–1 Quartz–piemontite–rich schist with Mn–mineralization	Mn–ore rich
	Vrn6–2 Mn–ore enrichment	
Vrn7	Vrn7–1 Quartz–piemontite–rich schist	Mn–ore rich
	Vrn7–2 Mn–ore enrichment	-
	Vrn7–3 Mn–ore enrichment	-
Vrn8	Quartz–piemontite–rich schist	Mn–ore rich
Vrn9	Quartz–piemontite–rich schist	Mn–ore rich
Vrn10	Quartz–piemontite–rich schist	Mn–ore rich
Vrn11	Quartz–piemontite–rich schist	Mn–ore rich
Vrn12	Quartz–piemontite–rich schist with Mn–mineralization	host rock
Vrn13	Albite–quartzite	Fe–ore rich
Vrn14	Fe–ore enrichment	-
Vrn15	Albite–quartzite with Fe–mineralization	host rock

where a portion of one fifth (30–75g) was kept for the XRD analysis and the rest for the geochemical analyses. For the ore–rich samples, prior to this preparation, we made separates of ore material and then we followed the same root as above.

2.3.1 Mineral Characterization Methods and Mineral Chemistry

X–Ray Diffractometry

The XRD analysis was conducted in the Faculty of Geology and Geoenvironment, National and Kapodistrian University of Athens utilizing a Siemens®D–5005 diffractometer. The selected X–Ray line used was 1.54056 CuK α 1. The first encounter with the XRD graphs was by using the Bruker®Eva software.

Raman Spectroscopy

The Raman Vibrational Spectroscopy analysis was conducted in the Theoretical & Physical Chemistry Institute, National Hellenic Research Foundation. We utilized a 488nm laser beam for excitation in a Renishaw®inVia Reflex and a dispersive confocal reflection microscopy system for targeting on thin and polished petrographic sections.

Scanning Electron Microscopy – Energy Dispersive Spectrometry

The XRD analysis was conducted in the Faculty of Geology and Geoenvironment, National and Kapodistrian University of Athens utilizing a Jeol®JSM–5600, coupled with an EDS Oxford®Link Isis 300. There were mostly used back–scattered images and the analyses were calibrated using cobalt.

2.3.2 Geochemical Analysis

X–Ray Fluorescence

The X–Ray Fluorescence analysis was conducted in the Laboratory of Metallurgy, School of Mining and Metallurgy Engineering, National Technical University of Athens, providing impulses for each tested element and a 1 σ confidence interval. As a result the concentration values provided are depending on sampling and not on a pre–defined lower– and upper–limit list. The preparation required 32mm–pressed pellets and appropriate digestion with HWC binder.

The elements that were analyzed are the following: Na, Mg, Al, Si, P, S, Cl, K, Ca, Ti, V, Cr, Mn, Fe, Co, Ni, Cu, Zn, Ga, Ge, As, Se, Br, Rb, Sr, Y, Mo, Ag, Cd, Sn, Sb, Te, I, Ba, W, Hg, Tl, Pb, Bi, Th and U.

Inductively Coupled Plasma – Mass Spectrometry

The ICP–MS analysis of ore and host rock was conducted in the Acme Labs, Bureau Veritas in Vancouver. The preparation required lithium borate fusion digestion and for the PGEs and Au fire assay.

The elements that were analyzed are the following: Ba, Be, Co, Cs, Ga, Hf, Nb, Rb, Sn, Sr, Ta, Th, U, V, W, Zr, Y, La, Ce, Pr, Nd, Sm, Eu, Gd, Tb, Dy, Ho, Er, Tm, Yb, Lu, Mo, Cu, Pb, Zn, Ni, As, Cd, Sb, Bi, Ag, Au, Hg, Tl, Se, Pt and Pd. Table 2.2 contains the detection and upper limits, provided from Bureau Veritas.

Computational Processing and Statistics

The data processing, either computational (numerical, graphic) or statistical (graphic, correlation, dendrogram techniques), was conducted using Microsoft®Office Excel 2019, Matlab®17a, Minitab®16 and GeoChemical Data ToolKIT [Janoušek et al., 2006]. The thesis' manuscript was written using L^AT_EX(2 ϵ)® and T_EXversion 2019.

TABLE 2.2: Lower and upper detection limits for the ICP-MS analysis.

Element	Detection Limit	Upper Limit
lithium borate fusion		
Ag (ppm)	0.1	100
As	0.5	10000
Ba	1	50000
Be	1	10000
Bi	0.1	2000
Ce	0.1	10000
Cd	0.1	2000
Co	0.2	10000
Cs	0.1	1000
Cu	0.1	10000
Dy	0.05	10000
Er	0.03	10000
Eu	0.02	10000
Ga	0.5	10000
Gd	0.05	10000
Hf	0.1	10000
Hg	0.01	50
Ho	0.02	10000
La	0.1	50000
Lu	0.01	10000
Mo	0.1	2000
Nb	0.1	1000
Nd	0.3	10000
Ni	0.1	10000
Pb	0.1	10000
Pr	0.02	10000
Rb	0.1	1000
Sb	0.1	2000
Se	0.5	100
Sm	0.05	10000
Sn	1	10000
Sr	0.5	50000
Ta	0.1	1000
Tb	0.01	10000
Th	0.2	10000
Tl	0.1	1000
Tm	0.01	10000
U	0.1	10000
V	8	10000
W	0.5	10000
Y	0.1	50000
Yb	0.05	10000
Zn	1	10000
Zr	0.1	50000
Au (ppb)	0.5	100000
fire assay		
Au (ppb)	1	1000
Pt	0.1	1000
Pd	0.5	1000

Chapter 3

Results

3.1 Petrography

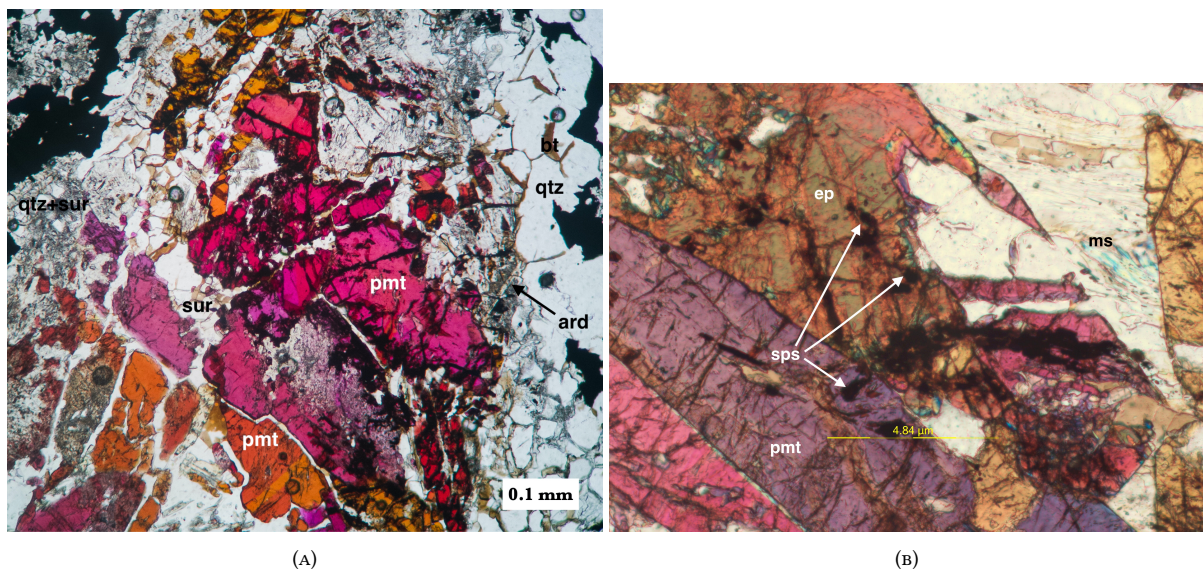
3.1.1 Quartz–piemontite schists

The quartzitic–piemontitic schists of the Varnavas area show a white–pink/dark pink millimeter–scale well–defined compositional banding as mineralogical zonation (Fig. 2.2a, 2.2b). Macroscopically the Mn±Fe–ore has a dark grey / black color and is interlayered between a quartzitic–sursassitic–ardennitic layers, showing a pink–to–yellowish hue.

The main silicate mineral phases are quartz and piemontite, which are generally grown as coarse crystals (Fig. 3.1a) and in many cases of millimeter–scale porphyroblasts. These two minerals are responsible for the granoblastic texture.

Quartz is usually shown as euhedral or subhedral crystals and may also show 120°–triple–junctions. Quartz also exhibits its usual undulose extinction. When subhedral the grain boundaries of quartz are irregular due to grain boundary migration. Quartz has also undergone bulging recrystallisation. In contrast to the isogonal triple junctions, quartz may show extensive subhedral crystals that participate in a polygonal fabric, a static recrystallization form, which is mostly usual when muscovite / paragonite, biotite or chlorite exist between the quartzitic crystal boundaries.

Piemontite is the second dominant mineral and generally participates with quartz in the granoblastic texture. Piemontite also can have rarely euhedral crystals and most often subhedral to anhedral ones. Piemontite shows striking red–yellow–violet pleochroism. It also shows either zonation, having an epidotic center (possibly Fe³⁺–richer) to a more piemontitic (Mn³⁺–rich) crystal boundary, or parallel blades with not such zonation (Fig. 3.1b). Some piemontite crystals are disseminated as in the left lower quarter of (Figure 3.1a), or may exhibit a skeletal structure. Piemontite may exhibit fracturing or micro–boudinage forms. Piemontite crystals also show bulging recrystallization. Spessartine can be found enclosed in piemontite (Fig. 3.1b) [Bonazzi and Menchetti, 2004].



There also exist more fine–grained rock–forming minerals. Sursassite has mostly a blade form and shows pale yellow – pale orange/brown pleochroism. Sursassite is also surrounding the Mn–oxide nodular forms in a quartzitic–sursassitic–ardennitic(–As) fine–grained matrix. Ardennite(–As) is spatially related to piemontite, as it has been observed to grow alongside piemontitic rims. In a few cases piemontite and ardennite(–As) can also be intergrown. Both sursassite and ardennite(–As) show pinning structures on piemontite (Fig. A.4b, A.6).

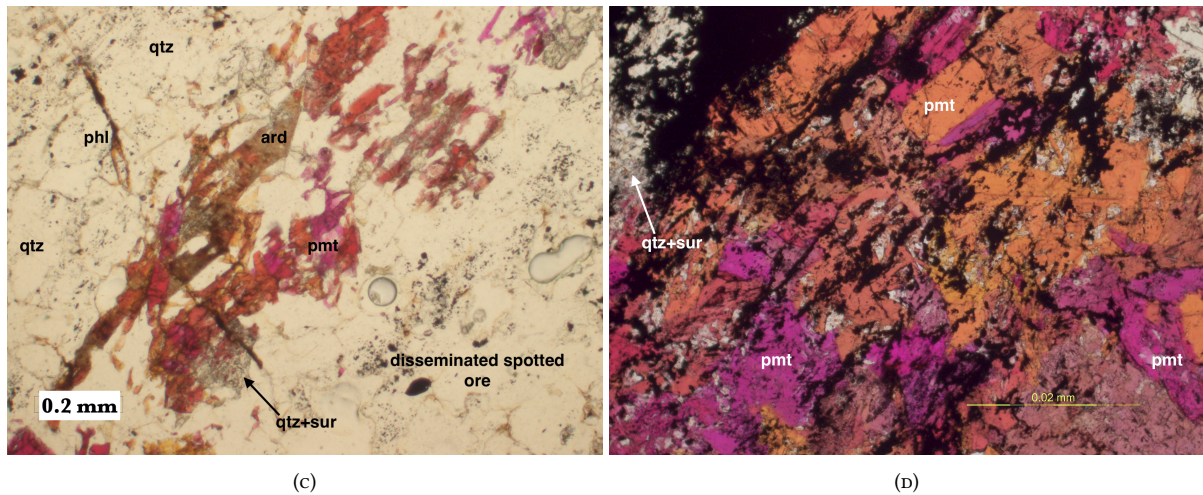


FIGURE 3.1: Microphotographs of piemontite schists thin sections. (A) Coarse crystals of quartz, subeuhedral and disseminated piemontite, intergranular flakes of biotite, small blades of sursassite and opaque minerals (transmitted light, plane-polarized, Vrn6). (B) Euhedral blades of piemontite, some with an epidotic center, enclosed spessartine, quartz and sparse muscovite (transmitted light, cross-polarized, Vrn12). (C) . (D) . Abbreviations: **qtz** quartz, **pmt** piemontite, **sur** sursassite, **ep** epidote, **ard** ardennite(-As), **bt** biotite, **ms** muscovite, **phl** phlogopite.

Spessartine cannot be easily distinguished in the majority of samples, but there can be found in disseminated form along with quartz and ardennite(-As) (Fig. 3.1a). It can be distinguished by high relief and optical isotropic characteristic (Fig. A.3, A.6a), even when disseminated.

Micas are contributing less in the whole-rock mineralogy relatively to the Mn-poor schists in the surrounding area of Varnavas. Biotite is mostly intragranular and phlogopite has the form of continuous curved flakes and may be Mn-rich due to the fact that it is almost weakly pleochroic and yellowish brown to dark brown in color [Smith et al., 1983]. Chlorite is present in almost every sample either as lamellar crystals, small flakes or has the same form as phlogopite, with which it is intergrown and may share the same Mn^{3+} -enrichment (Fig. A.1). The samples also contain paragonite which has the usual sheeted or lepidoblastic form and with strong anomalous interference colours of the 2nd order. Folds and kinks are particularly common in micas and chlorite. In (Fig. A.1) spool-shaped micas porphyroblast with symmetric distribution of deflection folds on both sides from phlogopite and Mn-chlorite.

3.1.2 Mn-Fe-ore

The Mn-Fe-ore in the quartzitic-piemontitic schists is stratabound and it occurs in four main forms. More than one type can be at the same sample, but each sample has a dominant form. The Mn-ore can have (i) a disseminated, a (ii) veinlet (either cross-cutting other crystals or intergranular / skeletal), (iii) a (thin) laminated or (iv) a massive form (see Type I).

An example of disseminated ore minerals is shown in Figure A.2. The rock-forming minerals are quartz and piemontite, which host the opaque minerals. Piemontite is cross-cut by spotted-formed Mn-oxides or in the form of small veinlets. The larger spots are nodular-like but with no internal structure and are mainly composed of todorokite, pyrolusite, cryptomelane and secondarily hollandite. Both the pairs of todorokite-pyrolusite and cryptomelane-pyrolusite seem to be intimately intergrown in most cases, but we can also rarely distinguish separate todorokite and pyrolusite crystals. Similarly, the ferromanganese ore can have a crustal form, in terms of thin laminations, either massive or disseminated.

More massive forms of the ore is shown in in Fig. A.2 and Fig. A.3a, where there is as part of a disseminated set of smaller spots and as large portion of a skeletal intergranular ore accumulation. The Mn-ore can also be found in cross-cutting veinlets (Fig. A.3) or intergranular veinlets (Fig. A.4).

The albitic quartzite shows no banding in the quartzitic part, whereas shows a white-grey / black millimeter- to centimeter-scale banding in the hematitic portions (see Type II).

Hematite shows high reflectivity in reflected light plane-polarized microscopy and red internal reflections in cross-polarized.

Several textbooks were utilized for the completion of Sec. 3.1. These were [Barker, 2014, MacKenzie et al., 2017, Passchier and Trouw, 2005, Pichler et al., 1997, Pracejus, 2015].

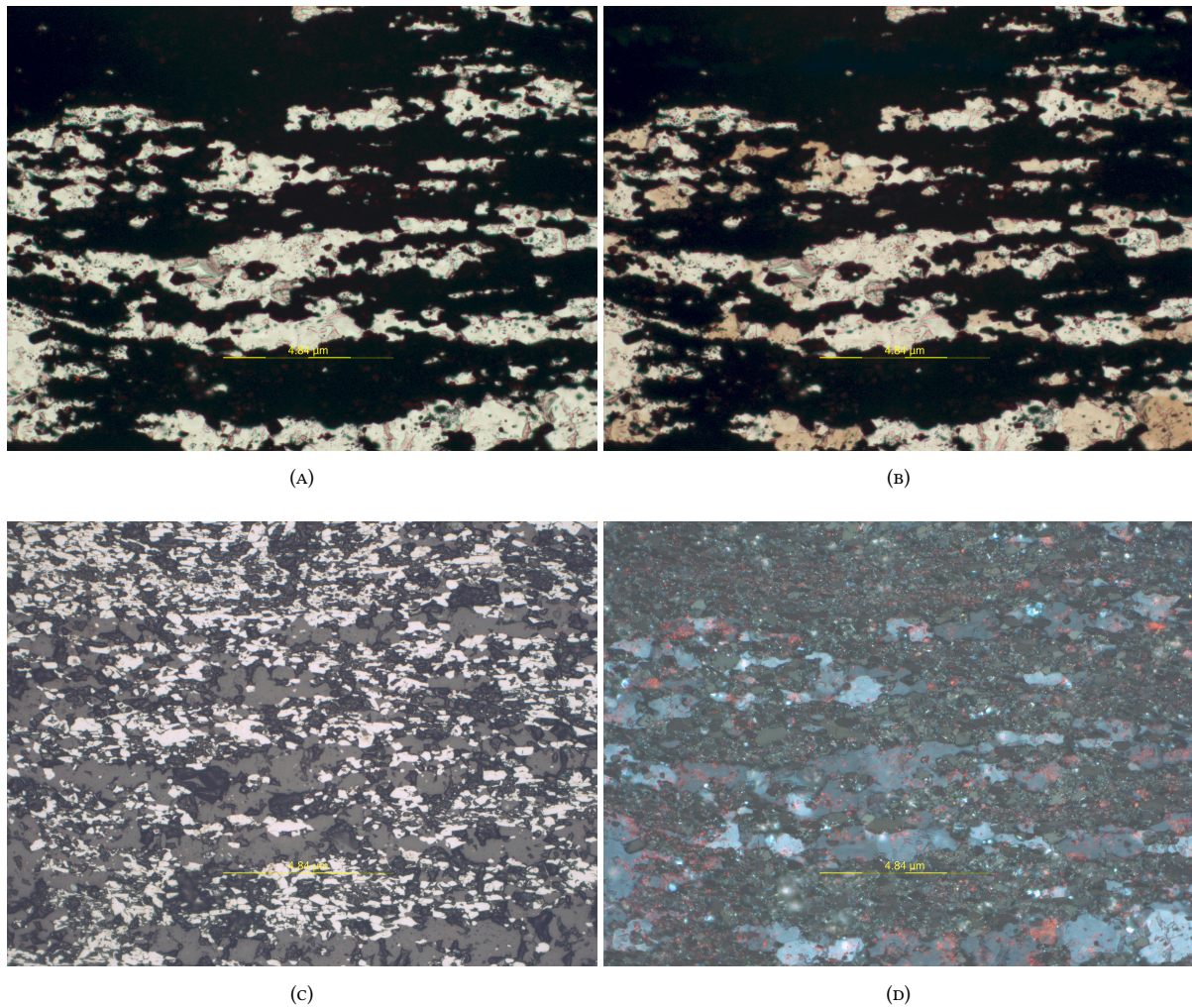


FIGURE 3.2: Microphotographs of quartzites thin sections. Laminated Fe-mineralization (Vrn14). (A) (transmitted light, plane-polarized, Vrn14). (B) Same sample (transmitted light, cross-polarized, Vrn14). (C) Same sample, depicting variations in the reflectivity of the ore mineral phases (reflected light, plane-polarized, Vrn14). (D) Same sample, with red internal reflections for hematite (reflected light, cross-polarized, Vrn14).

3.2 Mineralogy and Mineral Chemistry

The detailed combined petrographic analysis through transmitted and reflected light microscopy, the XRD analysis, the Raman Spectrometry analysis and the SEM analysis have been crucial in the identification of the mineral assemblage shown for the mineral phases in Tab. 3.1.

The mineral assemblages existing in the manganeseiferous metasediments can be distinguished in groups in respect to certain petrographic types:

- **Type I:** Quartz-piemontite-albite-rich schists with quartz - piemontite mineralogical zonation, greenschist facies paragenesis and Mn-Fe-mineralization.
 - **Type Ia:** The Type I paragenesis with random Mn-ore. It is assumed to be almost pure host rock, as it is the most Mn-poor part of the formation in terms of metallic minerals, at least among those to be piemontite-bearing.
 - **Type Ib:** The Type I paragenesis with crustal-like disseminated pyrolusite - todorokite - hollandite - cryptomelane - psilomelane - hematite (Mn-Fe-ore) and random hausmannite crystals. Thin lamellae of ore cross-cut piemontite crystals, whereas cross-cut other ore lamellae as next ore generation.
 - **Type Ic:** Quartz-piemontite-epidote-albite-rich schists with quartz - piemontite mineralogical zonation, greenschist facies paragenesis and nodular-like pyrolusite - todorokite - hollandite - cryptomelane - psilomelane - hematite (Mn-Fe-ore) and random hausmannite - manganite, as well as magnetite crystals. The nodular forms have neither concentric nor repetitive internal structure, the Fe-ore is disseminated and the Mn-ore is massively distributed. The least altered nodule observed has a rather radial symmetry, with a rutile-rich layer.

TABLE 3.1: A synopsis of the mineral paragenesis of the analyzed samples.

Mineral	Samples														
	Vrn1	Vrn2	Vrn3	Vrn5	Vrn6	Vrn7	Vrn8	Vrn9	Vrn10	Vrn11	Vrn12	Vrn13	Vrn14	Vrn15	
quartz	+														
albite	+	+													
muscovite/paragonite															
biotite/phlogopite/tamaitite	+	+													
chlorite/pennantite	+	+													
chloritoid	+														
calcite				+											
piemontite	+	+													
epidote	+	+													
clinozoisite															
allanite															
sursassite															
spessartine	+	+													
pyroxmangite															
ardennite-(As)	+	+													
rutile															
hematite		+													
maghemite															
magnetite															
magnesioferrite															
pyrolusite															
todorokite/romanèchite	+	+													
cryptomelane															
psilomelane															
hollandite															
coronadite															
hausmannite															
jacobsite															
bixbyite															
manganite															
manganosite															
pyrochroite															
braunite															
apatite															
zircon															
monazite/xenotime/gasparite															
arsenolite															

- **Type II:** Albite-rich quartzite with random epidote and almandine crystals and thin Co-Mn(\pm Ti)-hematite laminations (Fe-ore).

- **Type III:** A quartz-rich vein (10–15cm width) with sparse calcite cross-cutting the greenschists' stratigraphy. It is not ore-bearing.

A brief grouping of mineral assemblages is shown in Table 3.2.

TABLE 3.2: Groups of the main mineral^a assemblages in respect to lithotype.

Type	Host Rock Minerals	Ore Minerals
I	qtz + pmt + ep + sur + ard + chl + sps + ms ± bt ± all ± mon	pri + tdk + psl + crp + hol + hem + rt ± hnt ± mgn ± mgs ± mt ± crn
II	qtz + ab ± ap	hem ± mgf ± mhm
III	qtz + cal	–

^a Mineral abbreviations: **qtz** quartz, **ab** albite, **ms** muscovite, **bt** biotite, **chl** chlorite, **cld** chloritoid, **pmt** piemontite, **ep** epidote, **clz** clinozoisite, **all** allanite, **sur** sursassite, **ard** ardenneite(-As), **sps** spessartine, **cal** calcite, **hem** hematite, **mt** magnetite, **rt** rutile, **pri** pyrolusite, **tdk** todorokite, **psl** psilomelane, **crp** cryptomelane, **hol** hollandite, **crn** coronadite, **hnt** hausmannite, **mgn** manganite, **mgs** manganosite, **mhm** maghemite, **mgf** magnesioferrite, **ap** apatite, **mon** monazite.

The minerals that are well- to relatively well-crystallized and above a certain percentage over the whole rock were identified through XRD analysis, as shown in Fig. B.1 and C.1. In-depth analysis and data-base comparative methods have provided a more detailed view even of some minor mineral phases, which is shown in Fig. 3.5. The nano- to crypto-crystalline nature of the ore minerals requires the utilization of other methods, as it was already mentioned. The Raman Spectrometry analysis results are shown in Figure E.1. The prototype mineral data (XRD and Raman shift graph data) were taken from the RRUFF™Project¹.

3.2.1 Ore minerals

We primarily aim at the analysis of the ore Mn(±Fe-)minerals². These are manganese oxides and hydroxides and hematite. We shall divide this general assemblage into two groups, the first for the main ore minerals and the second for the subordinate ones.

Main ore minerals

The main ore minerals are pyrolusite, cryptomelane, psilomelane, todorokite and hollandite for the Type I lithotype and hematite for the Type II. We provide their X-Ray Diffraction, Raman shift patterns and EDS analyses, where applicable.

We should note here that:

- Pyrolusite (MnO₂) is poorly crystallized and intimately intergrown with either cryptomelane or todorokite and hollandite group minerals, so it is quite challenging to distinguish the mineral phases, even in SEM (Fig. 3.6c, 3.6d, 3.6h). We also note that in the XRD there was difficulty to compare with other pyrolusites from the RRUFF™database, due to the main peak of some prototype ones³ (Fig. 3.3a). Nevertheless, the EVA™database provides prototypes without this issue (Fig. B.1a, B.1e, B.1g, B.1h, B.1i, B.1k, B.1l, B.1n). The Raman shift patterns provide a more clear view for pyrolusite (Fig. E.1d, E.1h).
- XRD analysis for cryptomelane (K(Mn⁴⁺, Mn²⁺)₈O₁₆) and psilomelane ((Ba,H₂O)₂Mn₅³⁺O₁₀) was partially unsuccessful, as only cryptomelane was found in one sample (Fig. B.1n). We have established psilomelane by Raman Spectrometry (Fig. E.1d). A SEM-EDS analysis is shown in Tab. 3.3. Cryptomelane is shown in SEM images in Figures 3.6e and 3.6j.
- Todorokite group minerals⁴ ((Na,Ca,K,Mg,Ba)₂(Mn⁴⁺, Mn³⁺)₆O₁₂ · 3 – 4.5H₂O) are well-established in the XRD (Fig. 3.3b and B.1a, B.1c, B.1e, B.1f, B.1g, B.1h, B.1i, B.1j, B.1o, B.1p) and the Raman shift patterns (Fig. E.1). The first Raman shift photograph and graph (Fig. E.1a, E.1b) shows almost pure todorokite, whereas todorokite can occur within a more complex assemblage (Fig. E.1d, E.1h). Pyrolusite and todorokite are the most common minerals in the Mn-rich samples. Analyses of todorokite group minerals are provided in Tab. 3.3. These minerals, as shown in the SEM images (Fig. 3.6a, 3.6c, 3.6d, 3.6f, 3.6h, 3.6j, 3.6n), are responsible for the extensive tubular Mn-oxohydroxide network in nodular and in thin-laminated forms.

¹<https://rruff-2.geo.arizona.edu>

²The chemical formulas provided for the minerals are the ideal ones.

³This problem can also be found in other manganese ore minerals.

⁴Todorokite and romanèchite.

- Hollandite ($\text{Ba}(\text{Mn}^{4+}, \text{Mn}^{2+})_8\text{O}_{16}$) is poorly established in the XRD (Fig. 3.3c and B.1a, B.1i), but as it is shown in the Raman shift patterns, hollandite is the mineral with the most strong intensity peak (Fig. E.1d). Hollandite group mineral's chemistry is provided in Tab. 3.3. Pure hollandite crystals are shown in Fig. 3.6a and 3.6h.
- Hematite (Fe_2O_3) is present microscopically in the manganeseiferous schists as small grains, while it is a major constituent in the quartzites. Hematite is established in the quartzitic – piemontitic schists and the quartzites through XRD (Fig. 3.3d and B.1h, B.1q, B.1r, B.1s). The SEM–EDS analyses of hematite are divided into two groups, one for the Mn(\pm Fe)–schists (Tab. 3.3) and the other for the Fe–quartzites (Tab. 3.4). Hematite shows two quite different forms of crystal growth and spatial relationships with other minerals, as shown in the SEM images for the schists (Fig. 3.6c, 3.6d, 3.6e) and the quartzites (Fig. 3.6o, 3.6p).

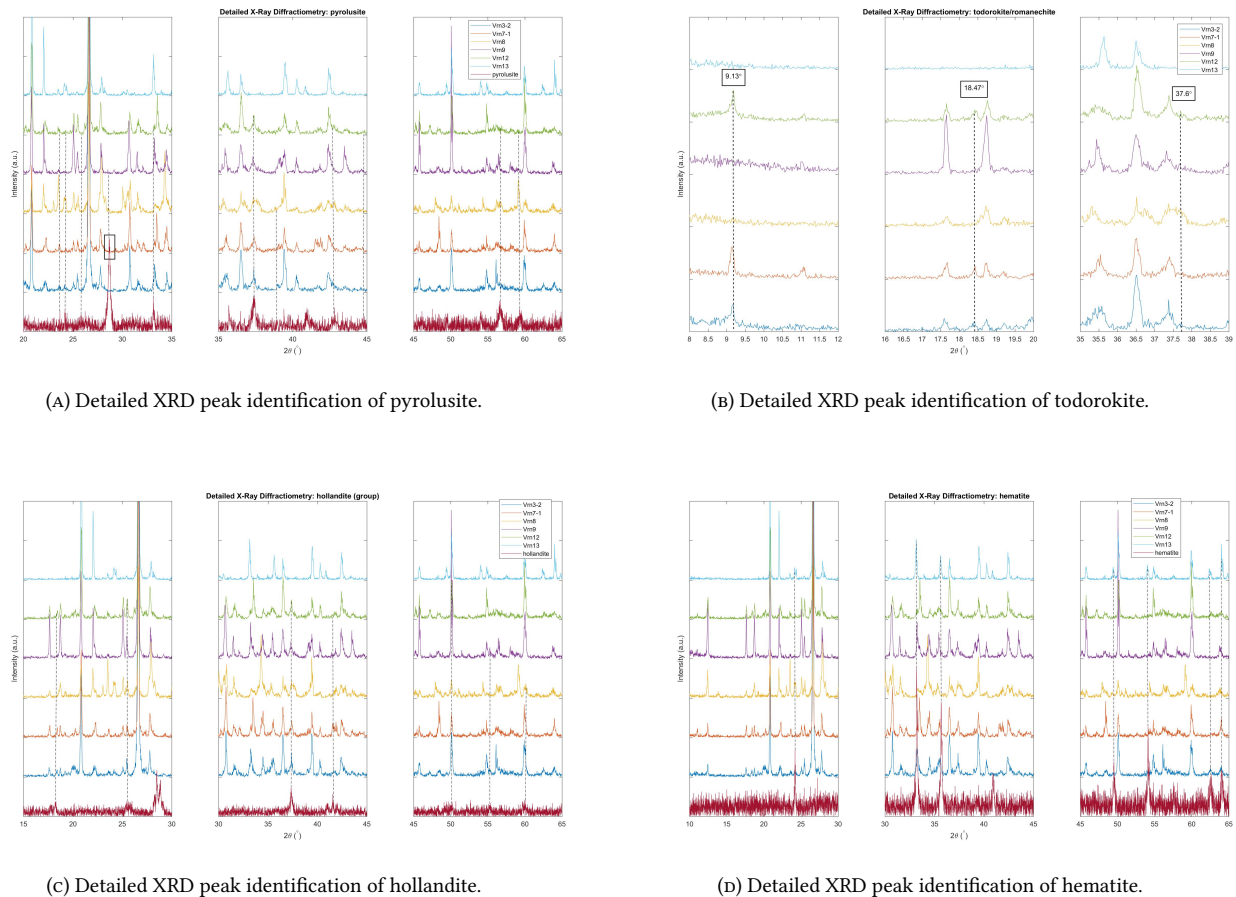


FIGURE 3.3: Detailed XRD peak identification of selected main ore minerals

Subordinate ore minerals

The subordinate ore minerals in the quartz–piemontite schists are manganite, manganosite, hausmannite, coronadite, bixbyite, pyrochroite, jacobsonite and braunite, for the Mn–ore minerals and magnetite, maghemite, rutile and tistarite for the non–manganese–bearing.

We note here that:

- Manganite ($\text{MnO}(\text{OH})$) is mostly found through the optical microscope and its internal reflection colors, included in the pyrolusite – todorokite tubular network. Nevertheless, we have samples that show XRD peaks for manganite (Fig. 3.4a and B.1f, B.1k, B.1n).
- Manganosite (MnO) can be found through the use of scanning electron microscope, spatially related to and intergrown with todorokite (Fig. 3.6d, 3.6n). We provide its EDS analysis in Tab. 3.5.
- Hausmannite (Mn_3O_4) is found through reflection microscopy (blood–red internal reflections), XRD analysis (Fig. 3.4b, B.1g, B.1k, B.1m, B.1n) and SEM, where is closely related to the todorokite–group–minerals tubular network. We provide its mineral chemistry in Tab. 3.5

TABLE 3.3: Mineral Chemistry table for the major ore-minerals (I).

Element (wt. %)	quartz-piemontite schists															
	rmn	rmn	rmn	tdk	psl	hol	hol	hol	hol	hol	hol	hem	hem	hem	hem	
Si		0.26	5.87	2.12	0.54	0.33	6.49	0.75				0.29				
Ti												0.41			1.80	0.82
Al	0.50		3.09		1.17		2.50	0.37								
Fe	1.73		4.68	3.22	4.20		3.56	3.69				66.42	65.43	65.49	62.39	63.61
Mn	57.53	60.15	37.40	48.62	51.27	50.16	44.79	48.80	60.21			3.02	1.18	1.28	2.45	2.11
Mg	0.84							1.61								
Ca	1.38	1.58	3.85		1.85		0.99	1.15	2.02				0.32			
Na			1.38	1.65				3.95								
K	2.18	2.18	0.47	0.43	1.99		0.50	0.38								
Sr	1.61	1.50						0.61	1.70							
Ba	3.36	3.68	8.89	14.28	1.31	24.78	8.96	10.31	4.69							
P					0.58											
Co													3.08	3.56	3.36	3.66
O	28.56	28.35	31.43	27.37	34.77	20.65	32.25	28.37	29.02	30.14	30.36	30.36	29.77	29.67	29.99	29.80
Total	97.69	97.70	97.06	97.69	97.68	95.92	100.04	99.99	97.64	99.99	99.99	99.99	100.02	100.00	99.99	100.00

^a Mineral abbreviations: **rmn** romanèchite and **tdk** todorokite (todorokite supergroup), **psl** psilomelane, **hol** hollandite, **hem** hematite.

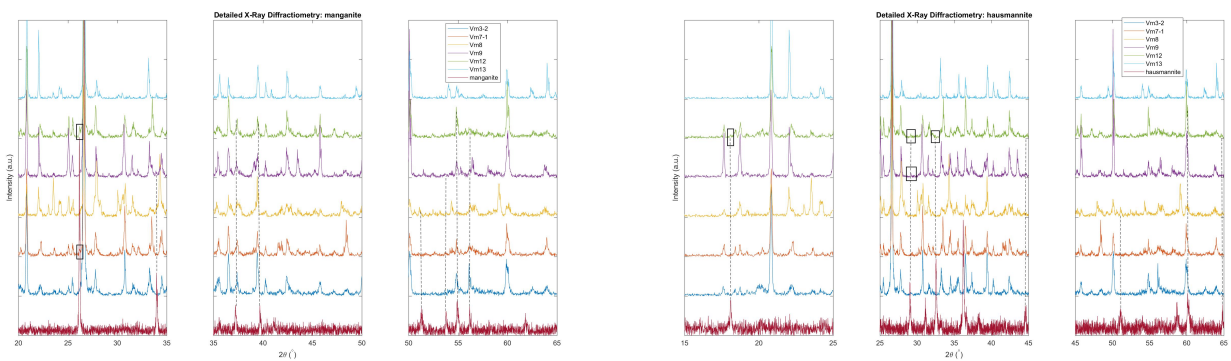
- Coronadite ($\text{Pb}(\text{Mn}^{4+}, \text{Mn}^{2+})_8\text{O}_{16}$), mineral of the hollandite supergroup, has only been established by Raman Spectroscopy (Fig. E.1d).
- Bixbyite (Mn_2O_3) is found through reflection microscopy (grey-greenish reflection), XRD analysis (Fig. 3.4c) and Raman Spectroscopy (Fig. E.1j).
- Jacobsite (MnFe_2O_4) is found only through XRD analysis (Fig. 3.4d).
- Braunitz ($\text{Mn}_7\text{SiO}_{12}$) is found through XRD analysis (Fig. 3.4e and B.1n) and SEM (Fig.). The EDS analysis of braunitz is in Tab. 3.5.

TABLE 3.4: Mineral Chemistry table for the major ore-minerals (II).

Element (wt. %)	albite quartzites					
	hem	hem	hem	hem	hem	hem
Si	0.3			0.96		
Ti						0.86
Fe	66.02	67.07	66.87	65.26	67.00	65.50
Co	3.88	3.24	3.46	3.64	3.32	3.86
O	29.78	29.70	29.67	30.13	29.69	29.78
Total	99.98	100.01	100.00	99.99	100.01	100.00

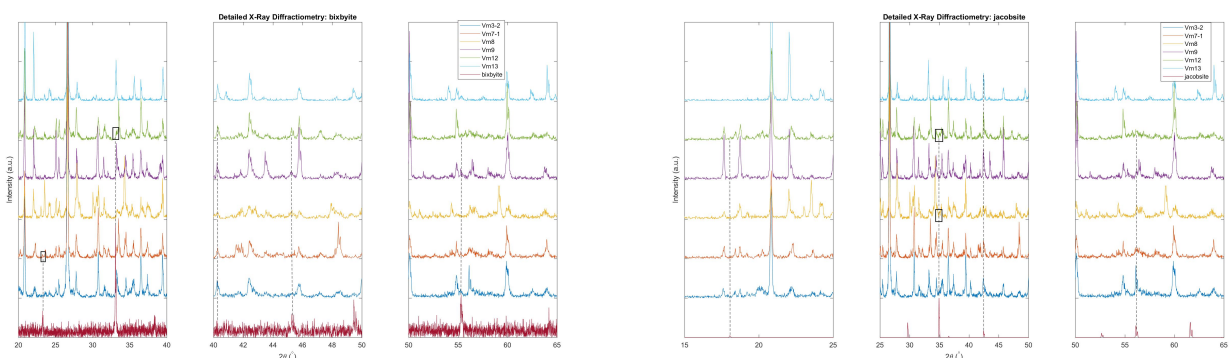
^a Mineral abbreviations: **hem** hematite.

- Magnetite (Fe_3O_4) is the second iron-oxide present in the samples and is found only in the manganiferous schists and determined by microscopy, XRD analysis (Fig. 3.4f and B.1n) and SEM (Fig. 3.6n). Table 3.5 contains its mineral chemistry.
- Rutile (TiO_2) is established through XRD analysis (Fig. 3.4g and B.1n), Raman Spectroscopy (Fig. E.1h) and SEM analysis (Fig. 3.6m). Rutile's mineral chemistry is in Table 3.5.
- Maghemite ($\gamma\text{-Fe}_2\text{O}_3$) is found only through XRD analysis (Fig. B.1r).
- Magnesioferrite (MgFe_2O_4) is found only in the polarizing microscope (orange/red triangle-sectioned prisms).



(A) Detailed XRD peak identification of manganite.

(B) Detailed XRD peak identification of hausmannite.

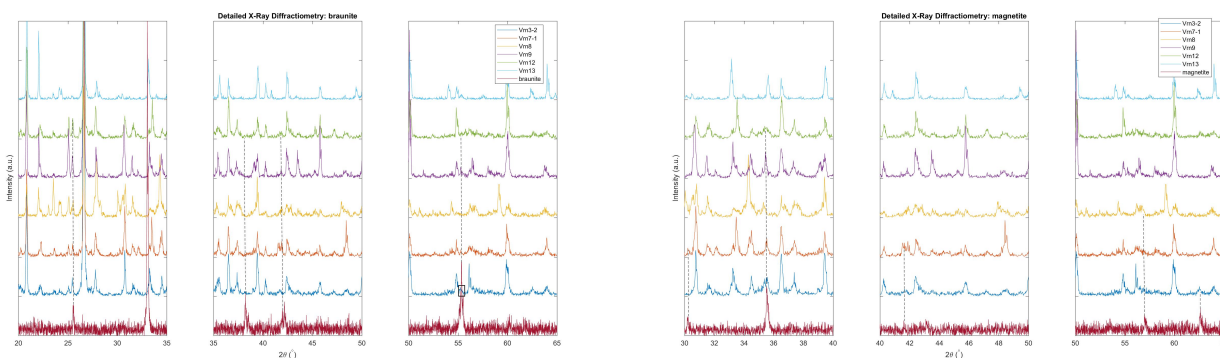


(C) Detailed XRD peak identification of bixbyite.

(D) Detailed XRD peak identification of jacobite.

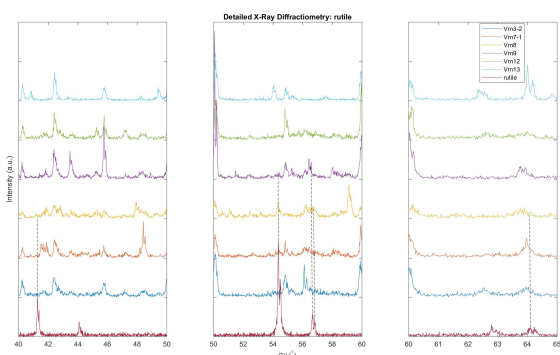
3.2.2 Mn-Silicate minerals

The manganese-bearing silicate minerals are piemontite, sursassite, ardennite(-As), spessartine (Mn-rich garnet), pennantite (Mn-rich chlorite), pyroxmangite and pumpellyite(-Mn).



(E) Detailed XRD peak identification of braunite.

(F) Detailed XRD peak identification of magnetite.



(G) Detailed XRD peak identification of rutile.

FIGURE 3.4: Detailed XRD peak identification of selected subordinate ore minerals.

TABLE 3.5: Mineral Chemistry table for the subordinate ore-minerals.

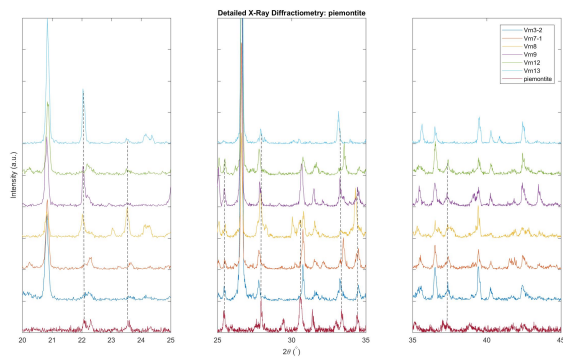
Element (wt. %)	quartz-piemontite schists											
	hnt	mgs	mgs	brn	mt	mt	mt	mt	mt	mt	rt	rt
Si				5.19				0.88	0.30		2.06	0.83
Ti						0.32		0.42		0.40	50.53	56.06
Al									0.43		1.12	0.33
Fe				2.04	77.78	74.23	74.74	72.83	69.88	72.82	1.61	0.84
Mn	72.06	73.95	72.52	64.99		3.07	2.97	2.88	1.03	5.14	4.36	1.69
Mg												
Ca											0.44	0.33
Co									3.89	3.24		
Pt									1.47			
O	27.94	26.05	27.27	27.78	22.26	22.37	22.28	22.97	22.43	22.40	39.87	39.94
Total	100.00	100.00	99.79	100.00	100.04	99.99	99.99	99.98	99.43	104.00	99.99	100.02

^a Mineral abbreviations: **hnt** hausmannite, **mgs** manganosite, **brn** braunite, **mt** magnetite, **rt** rutile.

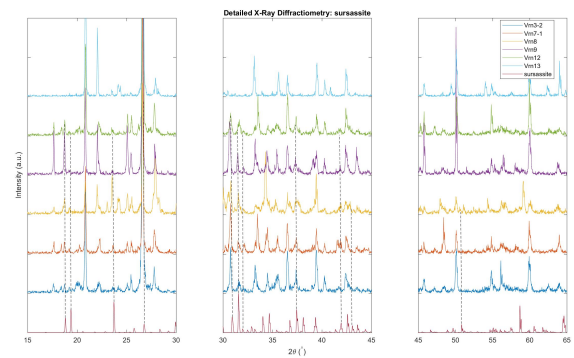
We note for the manganese-rich silicate minerals that:

- Piemontite ($\text{Ca}_2(\text{Al}, \text{Mn}^{3+}, \text{Fe}^{3+})_3(\text{SiO}_4)_3(\text{OH})$) is the main manganese-rich silicate mineral, which is profoundly shown in the polarizing microscope. Nonetheless, it is also confirmed by XRD analysis (Fig. 3.5a and B.1a, B.1b, B.1c, B.1e, B.1f, B.1g, B.1h, B.1i, B.1j, B.1k, B.1l, B.1m, B.1n, B.1o, B.1p), Raman Spectroscopy (Fig. E.1f) and SEM analysis (Fig. 3.6b, 3.6c, 3.6e, 3.6g, 3.6h, 3.6i, 3.6l). The mineral chemistry of piemontite is provided in Tab. 3.6.
- Sursassite ($\text{Mn}_2^+ \text{Al}_3(\text{SiO}_4)(\text{Si}_2\text{O}_7)(\text{OH})_3$), is shown through XRD analysis (Fig. 3.5b and B.1c, B.1e, B.1f, B.1g, B.1i, B.1j, B.1k, B.1m, B.1n, B.1o) and SEM. The EDS analysis of sursassite is in Tab. 3.6.

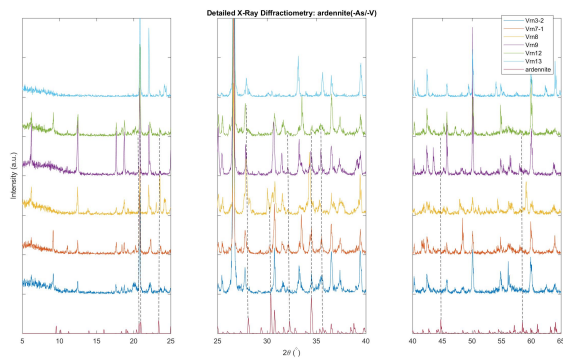
- Ardennite(-As) ($\text{Mn}^{2+}, \text{Ca}, \text{Mg}_4(\text{Al}, \text{Mg}, \text{Fe})_6(\text{SiO}_4)_2(\text{Si}_3\text{O}_{10})(\text{AsO}_4)(\text{OH})_6$), like piemontite and sursassite, is easily established through the microscope. Ardennite is also established by XRD analysis (Fig. 3.5c and B.1a, B.1b, B.1e, B.1f, B.1g, B.1h, B.1i, B.1j, B.1k, B.1l, B.1m, B.1n) and SEM analysis (Fig. 3.6g, 3.6k), with its EDS analysis in Tab. 3.6.
- Spessartine ($\text{Mn}_3^{2+}\text{Al}_2(\text{SiO}_4)_3$) is more difficult to be confirmed in the polarizing microscope, but it is shown through XRD (Fig. 3.5d and B.1g, B.1j, B.1o) and SEM analysis (Fig. 3.6b, 3.6h, 3.6l, 3.6m). Table 3.6 contains details about its mineral chemistry.
- Mn-Pumpellyite ($\text{Ca}_2(\text{Mn}^{2+}, \text{Mg})(\text{Al}, \text{Mn}^{3+}, \text{Fe})_2(\text{SiO}_4)(\text{Si}_2\text{O}_7)(\text{OH})_2 \cdot (\text{H}_2\text{O})$) is only found through SEM analysis (Fig. 3.6a), with respective EDS analysis in Tab. 3.6.
- Mn-Chlorite or pennantite ($\text{Mn}_5\text{Al}(\text{Si}_3\text{Al})\text{O}_{10}(\text{OH})_8$) was conjectured through the optical microscope and is established through XRD analysis (Fig. 3.5e and B.1i).



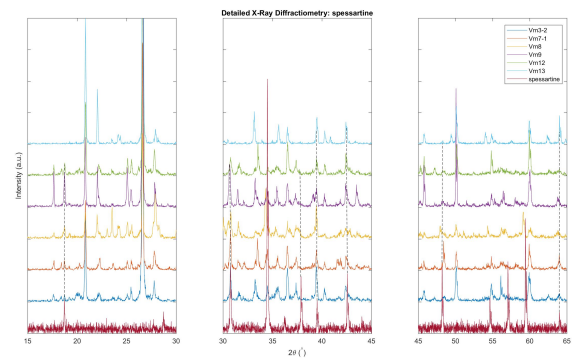
(A) Detailed XRD peak identification of piemontite.



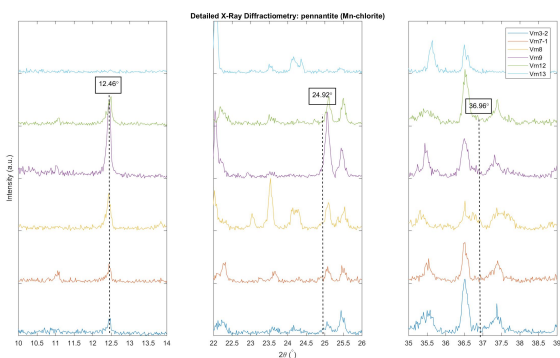
(B) Detailed XRD peak identification of sursassite.



(c) Detailed XRD peak identification of ardennite.



(d) Detailed XRD peak identification of spessartine.



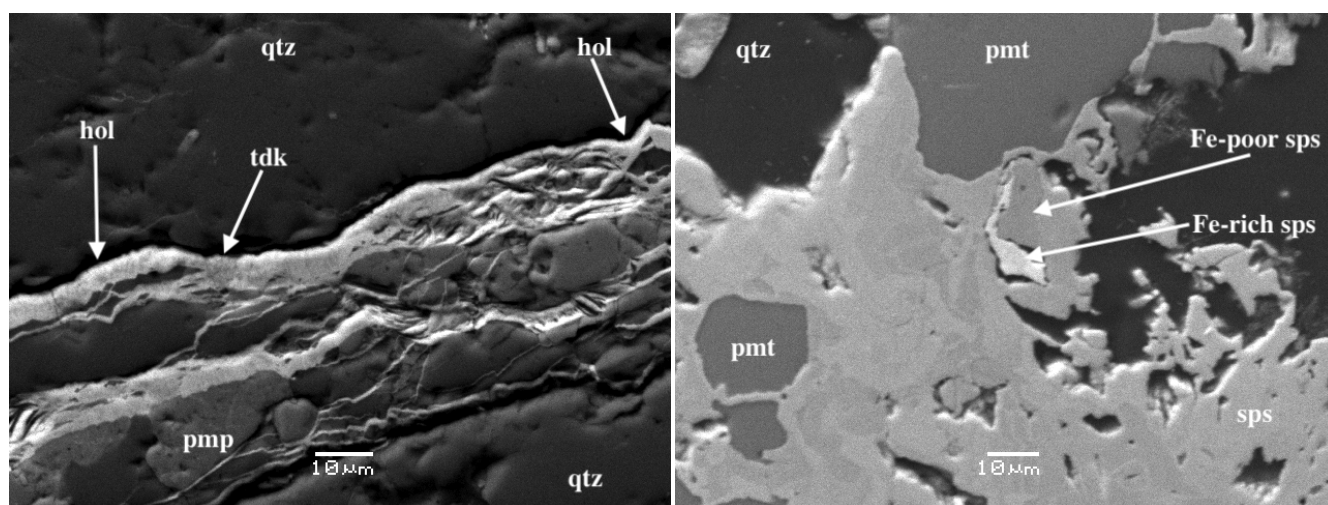
(E) Detailed XRD peak identification of pennantite (Mn-chlorite).

FIGURE 3.5: Detailed XRD peak identification of the Mn-silicate minerals

TABLE 3.6: Mineral Chemistry table for the manganeseiferous rock-forming minerals.

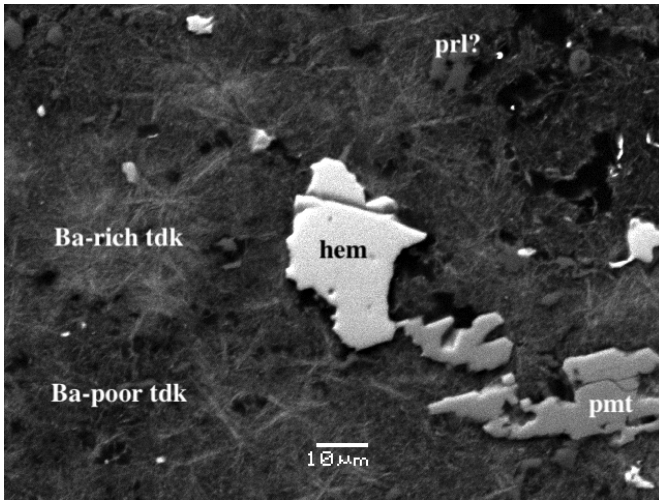
Element	quartz-piemontite schists												
	pmt	pmt	pmt	pmt	sur	ard	ard	ard	sps	sps	sps	sps	pmp
Si	18.89	18.62	19.51	18.00	12.92	14.40	15.64	13.97	18.80	17.05	16.14	16.99	17.50
Ti											0.29	0.76	
Al	11.17	10.95	11.26	12.02	14.12	12.98	13.06	13.73	10.22	7.99	9.13	10.07	8.67
Fe	4.42	3.55	4.00	7.57	13.16	1.20	0.42	1.22	3.37	6.24	2.59		3.74
Mn	7.21	7.37	6.37	3.62	19.02	14.75	15.48	16.31	25.56	11.34	28.49	27.20	17.40
Mg									3.05				
Ca	15.17	15.35	14.47	14.02		3.15	3.19	3.02	2.23	6.86	2.55	3.78	10.90
Na													
K	0.24	0.23											
P		0.73											
As						11.59	9.62	6.48					
Ce										10.36			
Nd										1.89			
O	40.93	41.23	41.77	41.96	40.37	39.88	40.72	41.11	39.82	38.24	41.29	42.21	41.21
Total	98.03	98.03	96.84	97.19	99.59	97.95	98.13	98.89	100.00	99.97	100.48	101.01	99.42

^a Mineral abbreviations: **pmt** piemontite, **sur** sursassite, **ard** ardennite(-As), **sps** spessartine, **pmp** pumpellyite(-Mn).

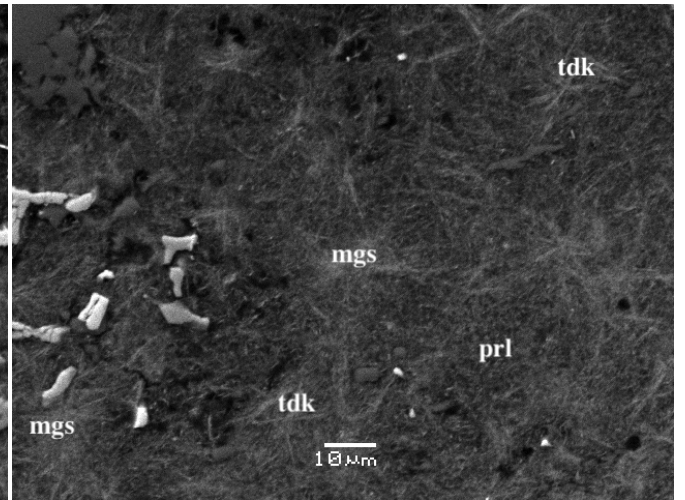


(A)

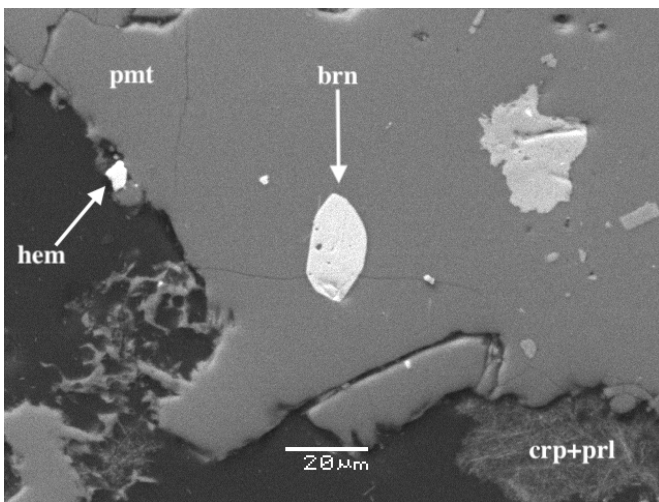
(B)



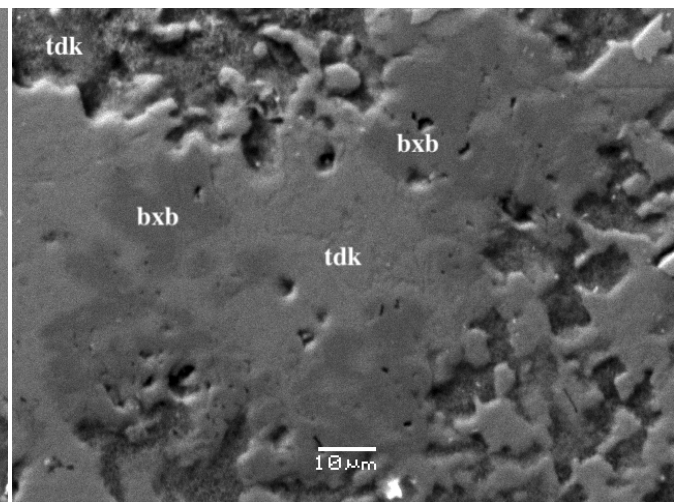
(c)



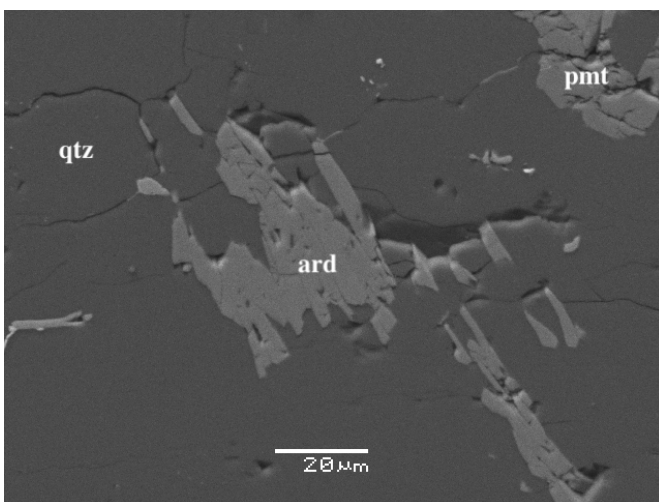
(d)



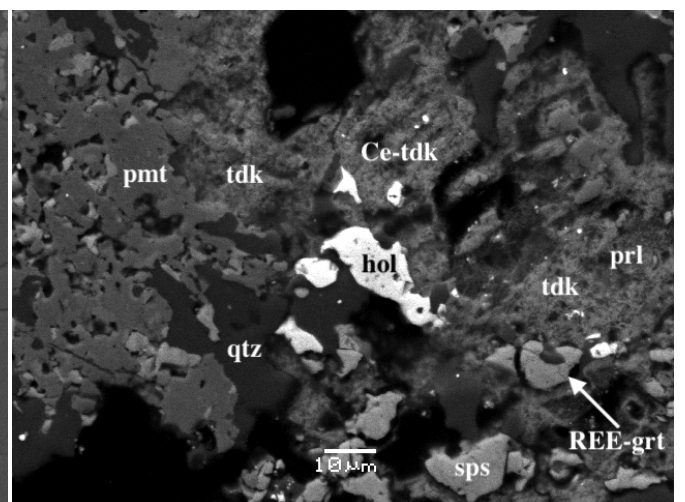
(e)



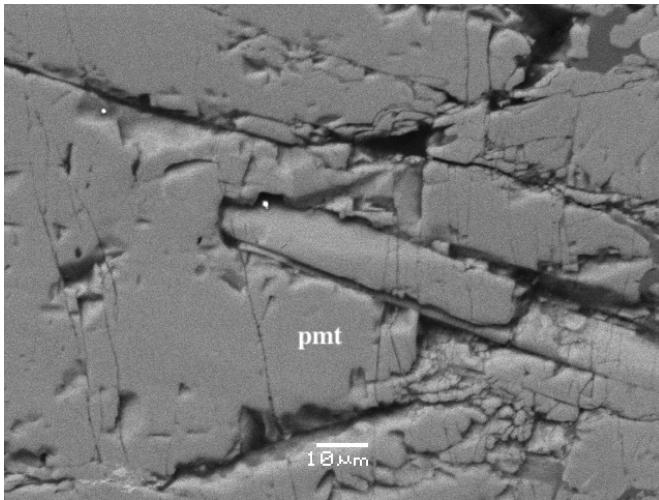
(f)



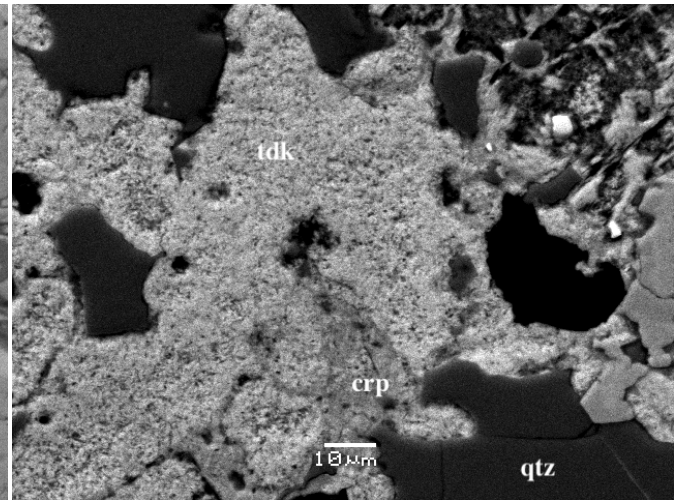
(g)



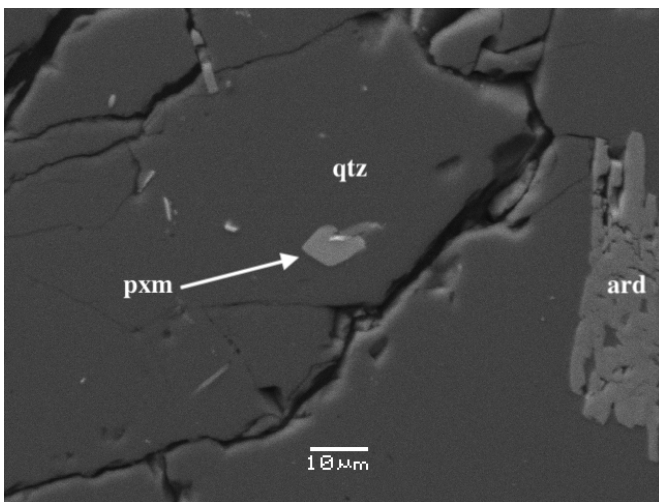
(h)



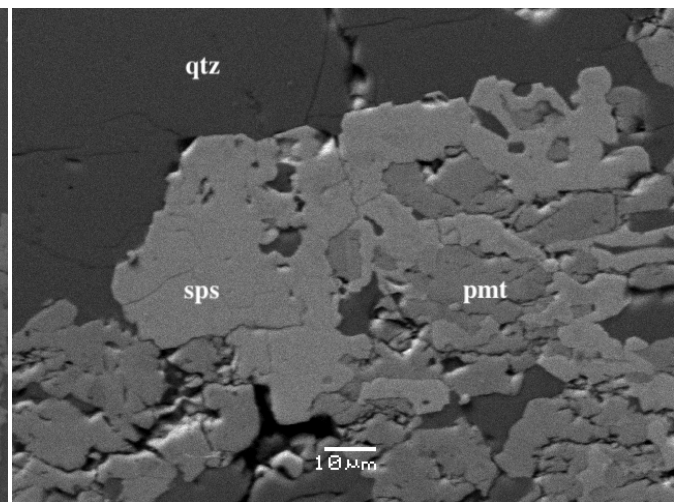
(i)



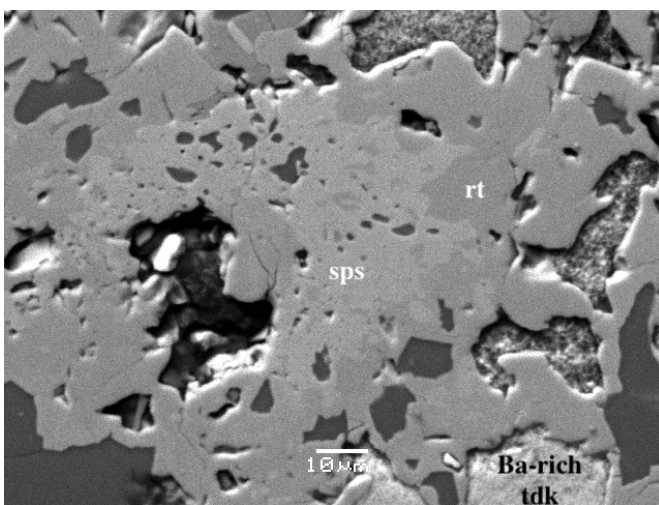
(j)



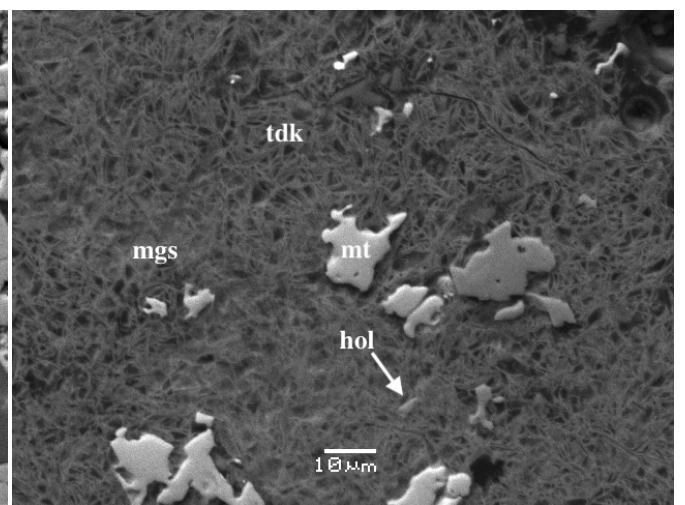
(k)



(l)



(m)



(n)

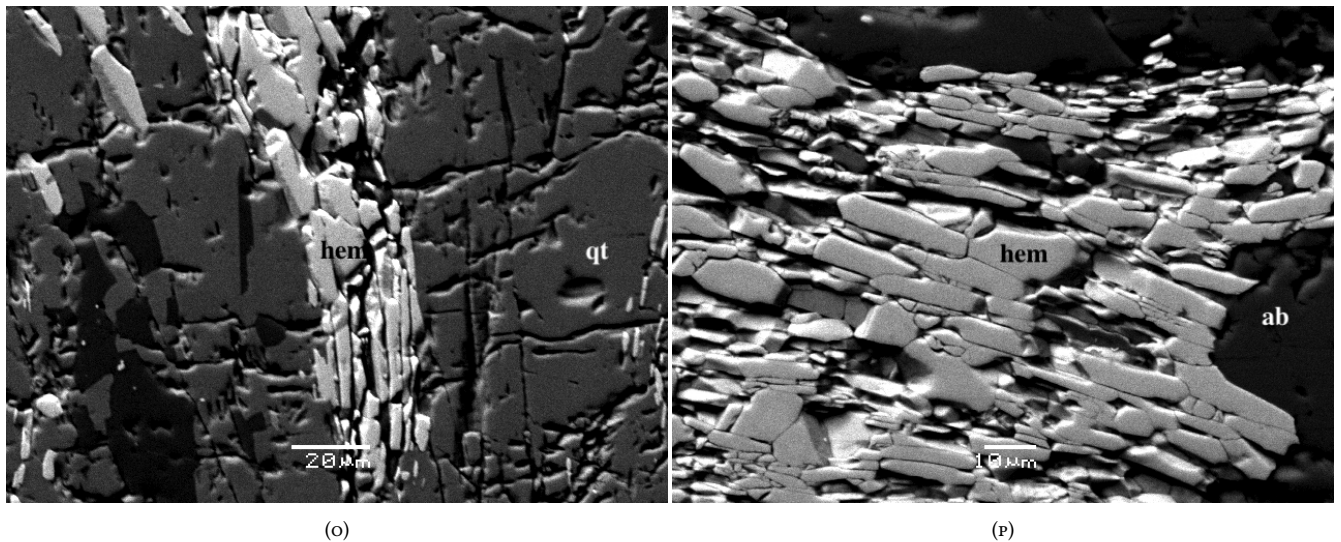


FIGURE 3.6: Back-scatter microphotographs (SEM).

In Ap. F we provide a SEM-EDS mapping, which shall be discussed in Ch. 4.

3.3 Bulk and Local-Bulk Geochemistry

3.3.1 Geochemical Analysis

Here we present the bulk geochemical analysis of the manganiferous metasediments. Moreover the local-bulk geochemistry of ore samples is also presented. The latter ones are characterized as ore-rich samples. We have divided the bulk geochemical results in three tables. The first table (Tab. 3.7) provides information regarding the major elements and the Mn/Fe-ratio index. The second table (Tab. 3.8) contains the rock-concentrations of the trace elements, except for the rare-earth and the platinum group elements. The third table (Tab. 3.9) contains the concentrations of the REEs, the precious metals and the PGEs.

We will treat separately the two geochemical groups we discussed in the previous paragraph.

Metasediments

The major element geochemistry was conducted using X-Ray Fluorescence. We note regarding the major elements in the metasediments that:

- Manganese (Mn) has a maximum and a mean concentration value of 5.35% w/w and 2.15% w/w, respectively, regarding the quartz-piemontite schists. The concentration of Mn in the quartzites is very low with a maximum value of 0.06% w/w in the most Fe-poor portion. Statistical correlation between Mn, Fe and other elements will be provided in Subs. 3.3.4.
- Iron (Fe) has a mean value of 3.05% w/w.
- The Mn/Fe ratio has a 0.244–3.031 and 0.001–0.013 range for the quartz-piemontite schists and the quartzites, respectively, while it is an excellent index when plotted in binary diagrams (Subs. 3.3.3).
- Silica (Si) and aluminum (Al) have a 25.85–29.23% w/w and 6.28–9.61% range, respectively, for the piemontitic schists, whereas the host rock of the hematite ore has 36.48% w/w and 2.74% w/w.
- The Si/Al ratio has a range of 2.69–4.65 in the Mn-rich metasediments and 13.31 in the quartzites. This ratio is one of those utilized to discrimination binary diagrams.
- Titanium (Ti) has a range of 0.14–0.22% w/w, in the manganiferous metasediments, which shows little diversification between the samples, regardless the lithotype. The ore-poor portion of the quartzites has 0.07% w/w. The least value is that of the Vrn5 sample (Type III lithotype).
- Magnesium (Mg) and calcium (Ca) show similar behavior between the Type I and II lithotypes, by being enriched in the first. To be more specific, in the ore-poor Mn-schists we have mean values of 2.42% and 3.74% w/w for Mg and Ca, respectively. The quartz-rich metasediments have 0.22% and 0.32% w/w, respectively.

TABLE 3.7: Major oxide geochemical analysis and Mn/Fe ratio (XRF analysis).

Major Oxide (wt. %) ^a	Samples														
	Vrn2	Vrn3-1	Vrn3-2	Vrn5	Vrn6-1	Vrn6-2	Vrn7-3	Vrn8	Vrn9	Vrn10	Vrn12	Vrn13	Vrn14	Vrn15	
SiO ₂	58.40	61.10	62.53	80.03	43.21	49.16	52.56	51.17	55.34	49.65	55.30	59.11	43.23	78.04	
TiO ₂	0.24	0.30	0.31	0.01	0.15	0.15	0.34	0.31	0.19	0.20	0.37	0.11	0.11	0.12	
Al ₂ O ₃	11.87	16.06	15.90	0.01	6.15	7.22	19.88	14.60	8.54	11.46	18.15	4.49	1.58	5.18	
Fe ₂ O ₃	2.52	5.23	5.19	0.58	3.69	4.70	3.77	2.96	3.42	2.31	4.49	22.23	46.77	6.00	
Mn ₂ O ₃	7.68	1.28	1.29	0.02	10.95	12.72	5.04	8.80	9.68	12.01	2.08	0.06	0.05	0.08	
MgO	5.42	2.96	2.97	0.03	2.11	2.55	3.10	8.49	4.15	2.51	4.69	0.16	0.03	0.37	
CaO	5.60	4.70	4.88	3.05	5.33	6.06	5.92	6.28	6.78	5.92	5.78	0.18	0.05	0.45	
Na ₂ O	3.48	3.33	3.11	0.18	0.64	0.74	4.07	3.53	1.20	1.82	3.21	2.69	0.13	3.64	
K ₂ O	bdl ^c	0.32	0.32	bdl	0.04	0.05	0.43	bdl	0.07	bdl	0.30	bdl	bdl	bdl	
P ₂ O ₅	0.03	0.03	0.04	bdl	0.04	0.04	0.03	0.05	0.04	0.05	0.03	0.05	0.02	0.03	
Sum	95.24	95.31	96.54	83.91	72.31	83.39	95.14	96.19	89.41	85.93	94.40	89.08	91.97	93.91	
Mn/Fe ^b	3.031	0.244	0.247	0.035	2.954	2.692	1.330	2.963	2.813	5.182	0.461	0.003	0.001	0.013	

^a Rounded up to 2 decimal digits.^b Rounded up to 3 decimal digits.^c Abbreviation: **bdl** below detection limit.

- Potassium (K) and phosphorus (P) have very low concentration values, in both the manganiferous schists and the hematite quartzites. Potassium is non-traceable in some samples. Sodium (Na) on the other hand does not show radical diversification between the three lithotypes.

- The sum of the major element oxides is generally around 90%, due to the fact that most metamorphic silicates and some of the oxides are hydrated.

TABLE 3.8: Trace element geochemical analysis (XRF and ICP-MS analysis).

Element (ppm) ^a	Samples														
	Vrn2 ^b	Vrn3-1	Vrn3-2 ^b	Vrn5 ^b	Vrn6-1	Vrn6-2 ^b	Vrn7-3	Vrn8	Vrn9	Vrn10	Vrn12	Vrn13	Vrn14	Vrn15 ^b	
Rb	1.1	8.5	9.1	3.0	1.0	2.4	9.2	1.1	0.9	0.3	6.8	3.0	2.5	6.1	
Cs	N/A ^c	0.4	N/A	N/A	0.1	N/A	0.4	bdl	bdl	bdl	0.3	0.2	bdl	N/A	
Be	N/A	bdl	N/A	N/A	bdl	N/A	bdl	bdl	bdl	bdl	3.0	bdl	bdl	N/A	
Sr	566.8	437.5	424.1	21.8	1271.6	1022.0	856.3	685.6	939.2	437.7	660.4	8.8	2.5	10.8	
Ba	242.0	241.0	312.0	24.0	2767.0	2617.0	1220.0	244.0	1434.0	407.0	289.0	97.0	101.0	63.0	
Zr	N/A	144.6	N/A	N/A	135.8	N/A	213.1	219.7	123.4	152.5	191.2	37.5	15.0	N/A	
Hf	N/A	4.5	N/A	N/A	3.7	N/A	6.7	6.8	3.5	4.6	5.8	0.9	0.3	N/A	
V	18.7	bdl	15	bdl	9.0	bdl	12.0	34.0	bdl	67.0	bdl	23.0	24	bdl	
Nb	N/A	3.7	N/A	N/A	1.0	N/A	6.6	5.0	1.3	3.9	4.0	1.5	2.9	N/A	
Ta	N/A	0.5	N/A	N/A	0.3	N/A	0.5	0.6	0.4	0.4	0.7	bdl	bdl	N/A	
Cr ^b	110.0	68.6	63.7	135.7	98.0	209.0	15.0	108.0	159.0	81.0	71.7	15.0	18.0	55.2	
Mo	bdl ^d	0.3	bdl	bdl	3.9	bdl	3.2	2.7	2.7	0.8	0.9	bdl	4.4	bdl	
W	237.4	213.4	267.4	828.9	149.4	240.0	94.6	113.2	218.2	114.3	197.1	1.1	3.2	516.6	
Co	172.0	26.6	96.0	177.1	78.1	75.0	55.7	116.0	74.9	83.3	40.4	279.0	723.0	146.0	
Ni ^b	19.7	11.1	16.1	7.4	16.4	22.6	20.8	22.3	21.8	13.9	18.7	0.9	3.6	8.3	
Cu	4.8	1.8	5.0	4.5	40.0	116.2	1.7	21.7	44.3	4.3	36.1	8.6	11.2	8.1	
Zn	58.5	14.0	30.1	19.9	23.0	17.7	9.0	45.0	36.0	17.0	16.0	10.0	71.0	27.7	
Cd	bdl	bdl	bdl	bdl	0.1	bdl	3.6	bdl	0.2	bdl	bdl	bdl	0.1	bdl	
Hg	4.1	bdl	2.9	bdl	0.1	7.9	4.9	2.7	6.4	bdl	bdl	bdl	bdl	bdl	
Ga	14.3	16.7	15.4	bdl	13.1	6.9	22.7	20.8	13.7	17.5	19.5	5.3	3.3	6.8	
Tl	bdl	0.4	1.8	1.3	bdl	4.3	0.2	bdl	0.1	14.0	0.2	1.9	0.2	bdl	
Ge ^b	5.7	8.3	8.6	3.5	2.9	4.2	4.4	6.8	3.9	7.5	6.5	6.5	bdl	bdl	
Sn	4.8	3.0	5.0	4.1	1.0	5.3	3.0	2.0	1.0	2.0	2.0	bdl	bdl	bdl	
Pb ^b	103.3	134.3	131.1	2.5	330.4	383.3	135.2	104.9	433.8	87.3	196.7	4.9	9.6	13.1	
As ^b	449.7	21.6	23.6	0.7	741.4	872.1	1192.0	288.4	607.5	13330.0	42.6	29.2	19.3	20.2	
Sb ^b	23.3	3.9	4.0	3.6	1.2	4.5	16.9	31.7	1.1	63.1	0.3	2.6	2.5	3.7	
Bi	3.0	bdl	1.8	bdl	bdl	4.7	bdl	bdl	bdl	14.0	2.1	bdl	bdl	bdl	
S ^b	0.6	2.0	0.7	0.7	2.0	2.0	0.6	0.3	2.0	1.1	2.0	1.3	1.6	2.0	
Se	bdl	bdl	bdl	bdl	bdl	bdl	bdl	bdl	bdl	bdl	bdl	bdl	bdl	bdl	
Te ^b	5.8	6.2	6.5	15.0	6.7	6.9	6.8	6.8	7.3	6.9	6.4	6.5	7.2	6.2	
Th	6.2	9.0	7.8	2.0	9.4	2.3	13.2	11.2	9.4	7.9	12.8	1.6	1.0	3.5	
U	2.7	0.4	3.7	1.1	11.2	18.7	0.9	0.3	5.8	0.4	0.4	0.2	bdl	bdl	

^a Rounded up to 1 decimal digit.

^b XRF analysis only.

^c Abbreviation: N/A not applicable.

^d Abbreviation: **bdl** below detection limit.

The trace elements for which we provide concentration data were measured utilizing XRF and ICP–MS instrumentation. Regarding the trace element geochemistry in the metasediments we can note that:

- The IA alkali metals rubidium (Rb) and cesium (Cs) have low or non–detectable concentration values, as the alkali metals of the major elements (Na, K). Lithium (Li) is not measured. There is no difference between the Mn– or the Fe–rich portions or the metasediments.
- The IIA alkali earth metals strontium (Sr) and barium (Ba) show high concentration values in the Mn–schists, with maximum values of 660ppm and 312ppm respectively. Beryllium (Be) does not share this feature. The Fe–poor quartzite has 11ppm and 63ppm, respectively.
- Both alkali and alkali earth metals have very low values in the Fe–quartzites and in the hematitic samples.
- The metals of the IVB group of the periodic table, zirconium (Zr) and hafnium (Hf), show a similar behavior with greater values in the Mn–schists and lesser in the Fe–quartzites, by one order of magnitude. There is no difference between ore–poor and ore–rich samples. The maximum values in manganese–rich metasediments are 191ppm and 5.8ppm for Zr and Hf, respectively.
- The metals of the VB–IIB groups, except for VIII B composite group, of the periodic table show the same feature as the IVB group, but with more diverse range between the lighter and the heavier elements in each group.
- Tungsten is an exception in the above general observation, with a mean concentration of 229ppm.
- The d–block metal of the IIIB group, yttrium (Y), behaves like the lanthanides so we include it in the next table (Tab. 3.9) with the rare–earth elements. Scandium (Sc) is not measured.
- The four metals of the VIII B–IIB groups, cobalt (Co), nickel (Ni), copper (Cu) and zinc (Zn) show concentration ranges of 27–172ppm, 11–20ppm, 2–36ppm and 14–59ppm, respectively. Cobalt shows higher values in the iron–rich albitic quartzites and nickel and copper are more enriched in the manganese–rich quartzitic–piemontitic schists.
- The measured actinides, thorium (Th) and uranium (U), have a concentration range of 6.20–12.80ppm and 0.4–3.7ppm, respectively, in the Mn–schists. The quartzites have low actinide values.
- Lead (Pb) has a maximum and mean value of 198ppm and 186ppm, respectively, in the manganese–rich schists. Significantly lower concentration values are noted for the quartzites.
- Arsenic (As) has a range of 22–45ppm.
- Antimony (Sb) and tellurium (Te) have maximum values of approximately 23ppm and 6.5ppm, respectively. The samples are quite poor at sulfur (S) and selenium (Se) is non–traceable.

The concentrations of the rare–earth elements and the precious metals (here Ag, Au) in the manganese–rich metasediments were measured utilizing XRF (for Y and Ag) and ICP–MS (the previous ones and all the rest). We note that:

- A general observation regarding the rare–earth elements is that the Fe–quartzites are depleted, in contrast to the Mn–schists.
- Yttrium (Y) has mean value of 41.8ppm, respectively.
- The RRE with the greatest concentration values is cerium (Ce), with maximum and mean value of 88.3ppm and 85.6, respectively.
- Neodymium (Nd) has maximum value of 15.3ppm.
- Two HREEs, erbium (Er) and ytterbium (Yb) have maximum values of 6.5ppm and 7.7ppm, respectively.
- The mean sum of all REEs is 195ppm and the mean ratio of light over heavy REEs is 1.84 in the quartz–piemontite schists.
- The maximum and the mean concentration value of silver (Ag) is 4.70ppm and 2.18ppm, respectively.
- The concentration value of gold (Au) is 1.7ppb.
- We do not have PGEs measured for the metasediments.

TABLE 3.9: Rare earth element, precious and platinum group metals geochemical analysis and REE indices (XRF, ICP-MS analysis and fire assay fusion).

Element ^a	Samples														
	Vrn2 ^f	Vrn3-1	Vrn3-2 ^f	Vrn5 ^f	Vrn6-1	Vrn6-2 ^f	Vrn7-3	Vrn8	Vrn9	Vrn10	Vrn12	Vrn13	Vrn14	Vrn15 ^f	
La (ppm)	N/A ^g	16.0	N/A	N/A	45.0	N/A	29.2	22.2	32.9	29.0	17.8	3.2	0.8	N/A	
Ce	N/A	88.3	N/A	N/A	108.5	N/A	119.5	47.5	96.2	53.5	82.9	6.9	1.6	N/A	
Pr	N/A	3.9	N/A	N/A	8.2	N/A	7.2	4.7	6.4	6.9	4.0	0.7	0.1	N/A	
Nd	N/A	14.0	N/A	N/A	29.7	N/A	26.6	19.1	24.4	26.2	15.3	2.8	0.3	N/A	
Pm	N/A	N/A	N/A	N/A	N/A	N/A	N/A	N/A	N/A	N/A	N/A	N/A	N/A	N/A	
Sm	N/A	3.6	N/A	N/A	6.7	N/A	6.0	4.7	5.5	5.3	3.5	0.6	bdl	N/A	
Eu	N/A	0.7	N/A	N/A	1.3	N/A	1.2	1.0	1.0	1.1	0.8	0.1	bdl	N/A	
Gd	N/A	3.5	N/A	N/A	7.7	N/A	6.9	6.3	6.4	6.8	4.5	0.6	0.1	N/A	
Tb	N/A	0.7	N/A	N/A	1.4	N/A	1.3	1.1	1.2	1.3	0.9	0.1	0.0	N/A	
Dy	N/A	4.9	N/A	N/A	9.8	N/A	9.1	7.5	7.6	8.6	7.0	0.7	0.3	N/A	
Ho	N/A	1.4	N/A	N/A	2.2	N/A	2.2	1.8	1.7	2.1	1.8	0.2	0.1	N/A	
Er	N/A	5.0	N/A	N/A	7.1	N/A	7.4	5.4	5.6	6.7	6.5	0.6	0.3	N/A	
Tm	N/A	1.0	N/A	N/A	1.1	N/A	1.2	0.8	0.9	1.0	1.1	0.1	0.1	N/A	
Yb	N/A	7.1	N/A	N/A	7.4	N/A	7.7	5.6	6.0	7.1	7.7	0.9	0.6	N/A	
Lu	N/A	1.1	N/A	N/A	1.2	N/A	1.2	0.9	1.0	1.1	1.1	0.2	0.1	N/A	
Y	N/A	36.3	N/A	N/A	55.0	N/A	55.5	41.4	42.8	50.8	47.2	3.9	1.8	N/A	
Ce/Ce ^b (dl ^c)	N/A	2.6	N/A	N/A	1.3	N/A	1.9	1.1	1.6	0.9	2.3	1.1	1.3	N/A	
Eu/Eu [*]	N/A	0.9	N/A	N/A	0.8	N/A	0.9	0.8	0.8	0.8	0.9	0.8	N/A	N/A	
∑LREE (ppm)	N/A	126.5	N/A	N/A	199.4	N/A	189.7	99.2	166.4	122.0	124.3	14.3	2.8	N/A	
∑HREE	N/A	61.0	N/A	N/A	92.9	N/A	92.5	70.8	73.2	85.5	77.8	7.3	3.4	N/A	
∑REE	N/A	187.5	N/A	N/A	292.3	N/A	282.2	170.0	239.6	207.5	202.1	21.6	6.2	N/A	
Ag	4.7	bdl ^h	4.0	3.7	bdl	bdl	bdl	3.1	bdl	bdl	bdl	bdl	bdl	3.1	
Au ^d (ppb)	N/A	1.7	N/A	N/A	bdl	N/A	bdl	1.1	0.7	bdl	bdl	bdl	0.6	N/A	
Au ^e	N/A	N/A	N/A	N/A	3.0	N/A	3.0	N/A	3.0	N/A	N/A	bdl	bdl	N/A	
Pt	N/A	N/A	N/A	N/A	0.8	N/A	0.7	N/A	0.9	N/A	N/A	bdl	bdl	N/A	
Pd	N/A	N/A	N/A	N/A	0.5	N/A	bdl	N/A	bdl	N/A	N/A	bdl	bdl	N/A	

^a Rounded up to 1 decimal digit.

^b We utilize the formulas $Ce^* = \sqrt{La_{sample}/NASC} \cdot Pr_{sample}/NASC$ and $Eu^* = \sqrt{Sm_{sample}/NASC} \cdot Gd_{sample}/NASC$.

^c Abbreviation: **dl** dimensionless.

^d Lithium borate fusion and ICP-MS analysis.

^e Fire assay fusion coupled with ICP-MS analysis.

^f XRF analysis only.

^g Abbreviation: **N/A** not applicable.

^h Abbreviation: **bdl** below detection limit.

Ore-rich Samples

We note regarding the major elements in the ore-rich samples that:

- Mn has a maximum and a mean concentration value of 8.85% w/w and 6.87% w/w, respectively, regarding the manganiferous ore-rich samples.
- Fe has a mean value of 2.59% w/w in the manganese ore-rich samples and 24% w/w in the hematitic bands.
- The Mn/Fe ratio has a 1.330–5.182 and 0.001–0.003 range for the Mn-ore and the Fe-ore, respectively.
- Si and Al have a 20.20–25.87% w/w and 3.25–10.52% range, respectively, for the manganiferous ore-rich samples, whereas the hematite ore has 20.21–27.63% w/w and 0.84–2.38% w/w.
- The Si/Al ratio has a range of 2.34–6.21 in the Mn-rich ore samples and 11.63–24.17 in the Fe-ore.
- Ti has a range of 0.09–0.20% w/w, in the Mn-rich ore samples and the Mn-separates.

Regarding the trace element geochemistry in the ore-rich samples we can note that:

- Sr and Ba show high concentration values in the manganiferous ore-rich samples, too, with maximum values of 1271ppm and 2767ppm respectively.
- Mo and W range between 0.8–3.9ppm and 95–218ppm, respectively, in the manganese-rich ore-samples. Analogously in the hematitic portion of the quartzites we have maximum values of these elements of 4.4ppm and 3.2ppm.
- Co, Ni, Cu and Zn show concentration ranges of 75–116ppm, 14–23ppm, 2–116ppm and 9–45ppm, respectively, for the Mn-rich ore. The same trace elements have maximum values of 723ppm, 4ppm, 11ppm and 71ppm, respectively, in the Fe-rich ore.
- Th and U have a concentration range of 2.3–13.2ppm and 0.3–18.7ppm, respectively.
- Pb has a maximum and mean value of 434ppm and 246ppm, respectively.
- There is a remarkable enrichment in arsenic (As), i.e. up to 1.33% w/w, with a mean value of 2840ppm.
- Sb and Te have maximum values of approximately 32ppm and 7ppm, respectively.

We note regarding the REE and precious metals in the ore-rich samples that:

- Y has mean values of 49ppm.
- La, Ce, Nd, Eu, Gd and Dy have maximum values of 45ppm, 120ppm, 30ppm, 1.3ppm, 7.7ppm and 9.8ppm, respectively.
- The maximum sum of all REEs is 199ppm and the mean ratio of light over heavy REEs is 1.86, for the manganiferous ore-rich samples.
- The maximum concentration value of Ag is 6.8ppm, in the hematitic portion.
- The maximum concentration values of Au, Pt and Pd are 3.0ppb, 0.9ppb and 0.5ppb, respectively.

3.3.2 Normalization Diagrams

Our geochemical data are normalized using the Upper Continental Crust (UCC) and the North Atlantic Shale Composite (NASC) concentration values. The data sets of the normalizers can be found in [Rudnick and Gao, 2014], [Taylor and McLennan, 1985], [Taylor and McLennan, 2008] and [Gromet et al., 1984], respectively. The UCC normalization was chosen in order to present a general trend for enrichments or depletions of the elements (Fig. 3.7). The NASC normalization is more related to the petrogenesis of the volcanosedimentary protolith of the sequence in Varnavas, assuming isochemical, or almost isochemical, metamorphic events⁵ (Fig. 3.8). An alternative to NASC would be a normalization based on the Post-Archean Australian Shale (PAAS).

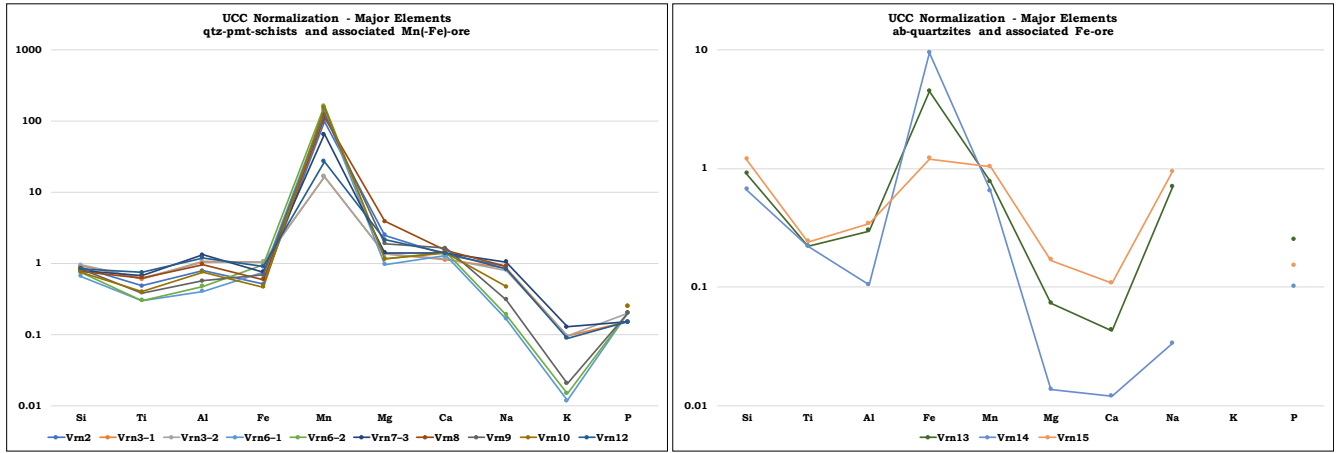
A general observation on the UCC and NASC normalized geochemical data would be the expected enrichment in Mn. In the UCC case we have a Mn-enrichment of 16–163 times (Fig. 3.7a), while in the NASC case 19–191 times (Fig. 3.8a) in the Vrn1–12 samples, which refer to manganiferous schists. The iron-rich quartzites have a depletion at a minimum of 0.64 and 0.75 times (Fig. 3.7b and 3.8b) in the UCC and NASC normalization, respectively.

Iron is moderately depleted in the Mn-schists with a minimum of 0.46 and 0.41 times (Fig. 3.7a and 3.8a) in the UCC and the NASC normalization, respectively, whereas in the Fe-quartzites iron is enriched by a factor of 1.2–9.4 and 1.1–8.3 (Fig. 3.7b and 3.8b).

⁵This assumption shall be of use in the following subsection and chapter, too.

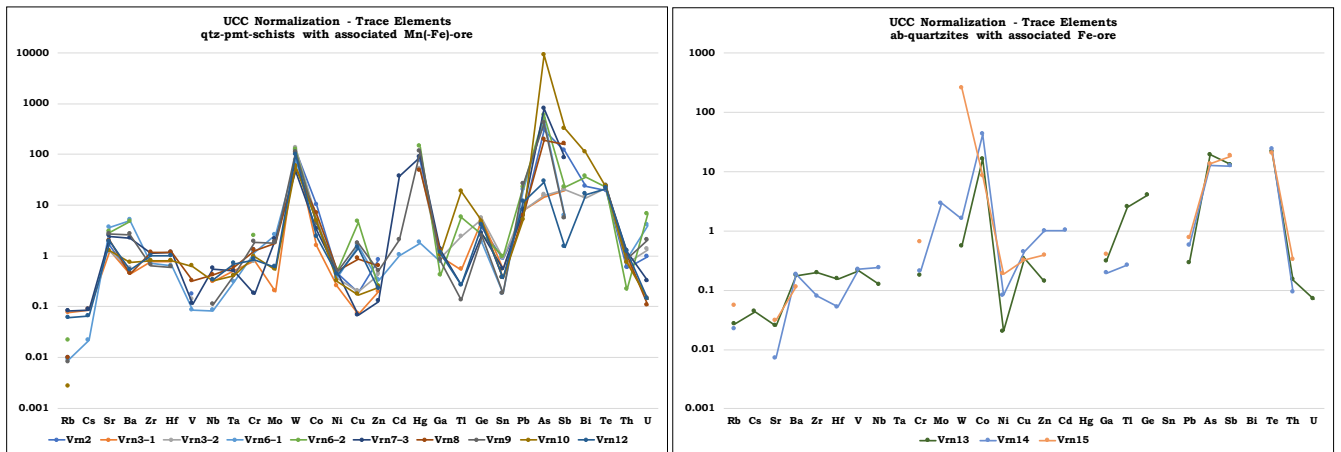
Magnesium is moderately enriched in the Mn-schists with a maximum factor of 3.9 and 3, although in the Fe-quartzites it is depleted by 100 times, in the UCC and NASC normalization, respectively. Calcium is also moderately enriched in the Mn-schists, but by a less factor. Alkali metals are strongly depleted in both normalization schemes or even non-traceable, as noticed in the previous subsection (Subs. 3.3.1).

Silica, aluminum and titanium are all three mildly depleted, in both the quartz-piemontite schists and the albite quartzites, with an exception of Al in some samples of the first lithotype and Si in one sample of the second lithotype.



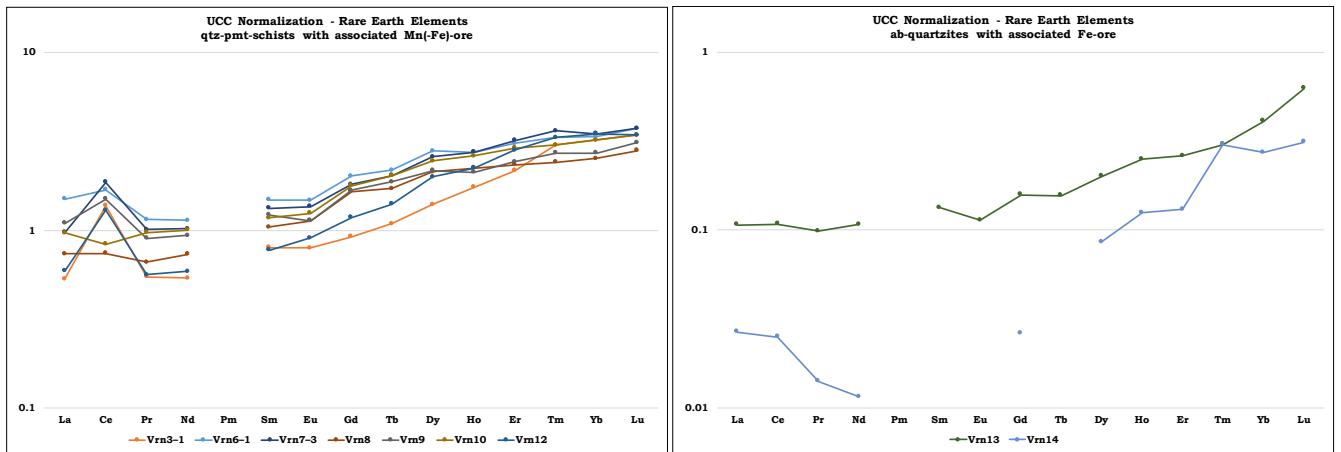
(A)

(B)



(C)

(D)



(E)

(F)

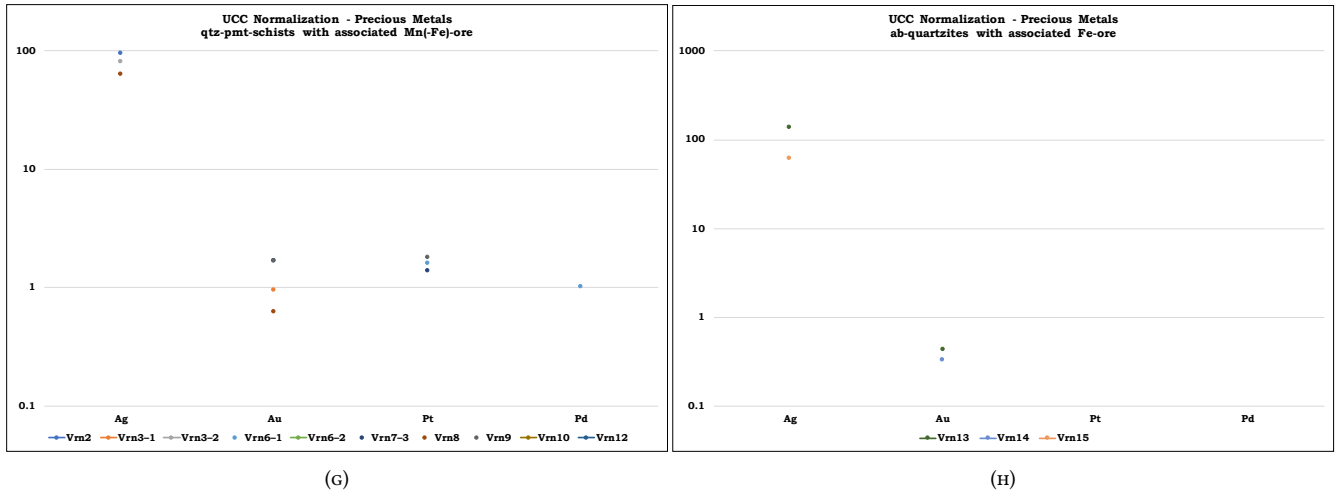
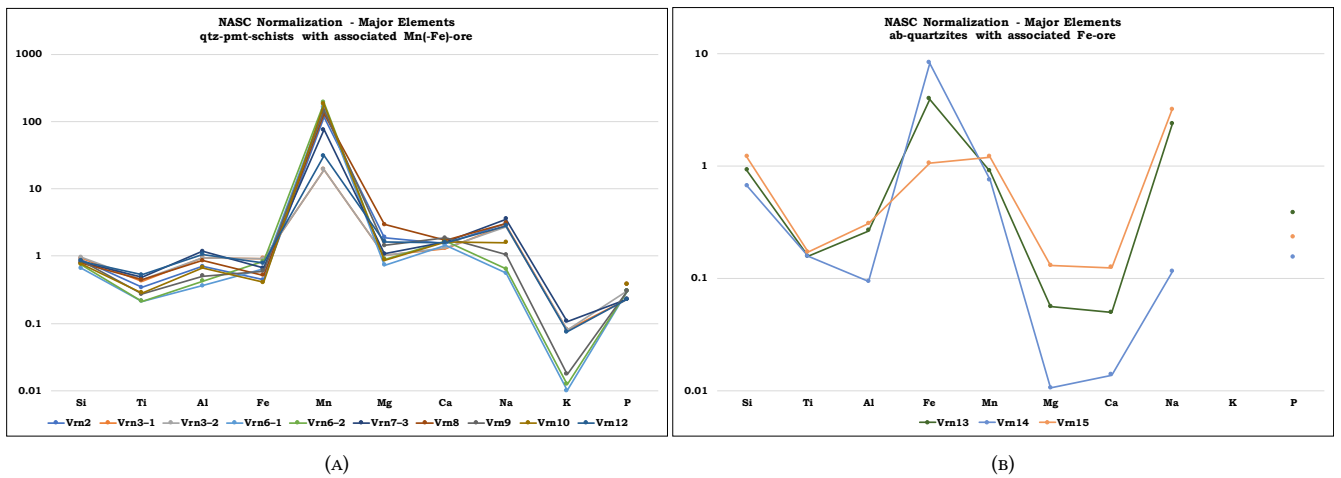


FIGURE 3.7: Normalization diagrams of the Varnavas Mn- and Fe-ore samples against Upper Continental Crust.

We can generally note, regarding the trace elements in the Mn-ore that As is enriched >10000 times enriched in one sample, W, Hg, Sb, Bi, are enriched >100 times in some samples, Co, Cd, Tl, Pb, Te are also enriched >10 times in some samples and Sr, Ba, Zr, Hf, Cr, Mo, Cu, Ge, U are enriched >1 times in some samples, when normalizing in respect to the Upper Continental Crust (Fig. 3.7c). The normalization in respect to the North Atlantic Shale Composite shows As, W enrichment >100 times in some samples, Sb >10 times in one sample and Sr, Ba, U enrichment >1 times, in some samples (Fig. 3.8c).

Serious depletion in both normalization schemes refers to Rb and Cs. All samples show mild depletion in V, Nb, Ta, Ni, Zn, Sn (Fig. 3.7c, 3.7d, 3.8c, 3.8d).



The REE pattern of the Mn-rich rocks in both normalization schemes shows an enrichment of the HREEs relatively to the LREEs⁶, a positive Ce- and a negative Eu-anomaly (Fig. 3.7e and 3.8e). The Fe-rich quartzites show similar patterns, but with a serious depletion in Nd (Fig. 3.7f and 3.8f). Regarding the Ce- and Eu-anomaly formulas we utilized the formulas:

$$Ce/Ce^* = \frac{Ce_{sample}}{Ce_{NASC}} \cdot \frac{\sqrt{\frac{La_{sample}}{La_{NASC}} \cdot \frac{Pr_{sample}}{Pr_{NASC}}}}{1} \quad \text{and} \quad Eu/Eu^* = \frac{Eu_{sample}}{Eu_{NASC}} \cdot \frac{\sqrt{\frac{Sm_{sample}}{Sm_{NASC}} \cdot \frac{Gd_{sample}}{Gd_{NASC}}}}{1}$$

There are several formulas to present these REE-anomalies. These presented are based on the geometric mean in the denominator and have a more graphic and intuitional approach, referring to the normalization spider diagrams (Subs. 3.3.2). Two other formulas are based on the common arithmetic/linear mean or the harmonic mean.

⁶Increasing normalized values as a function of atomic number.

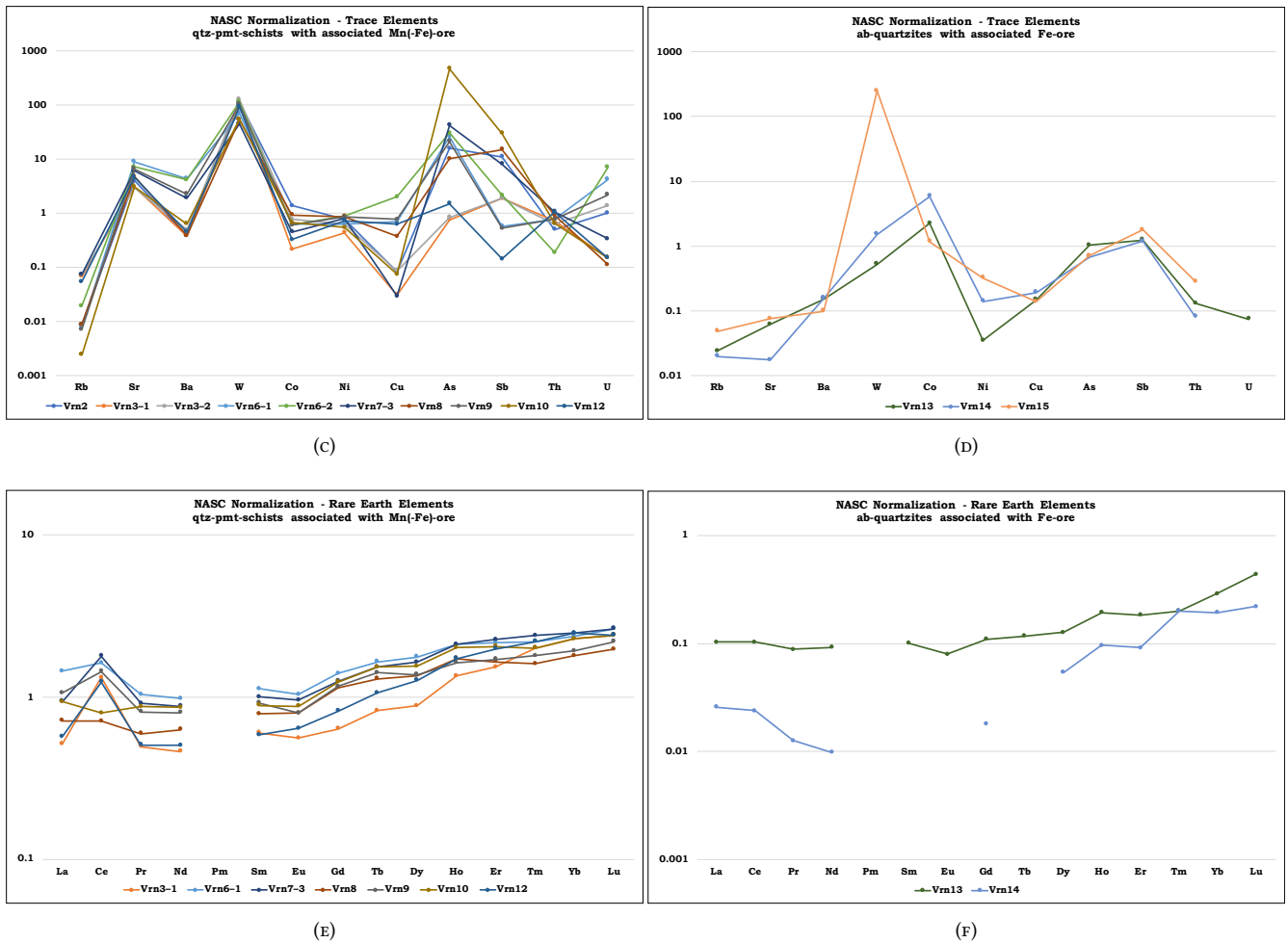


FIGURE 3.8: Normalization diagrams of the Varnavas Mn- and Fe-ore samples against the North Atlantic Shale Composite.

Cerium anomaly (Ce^*) in the sedimentary rocks depicted in the NASC-normalized diagrams plays an important role as an indicator of tectonic environment of deposition. The shale normalized Ce -anomaly and total REE abundance ($\sum REE$) variations generally preserved in deep sea sediments due to stable characteristics of REE in different geologic processes. [Murray et al., 1990, Murray et al., 1991] showed that the sedimentary rocks near the spreading ridge under the influence of metalliferous activity are characterized by extremely low Ce anomalies ($Ce^*=0.29$). The same rocks from an ocean-basin floor and from continental margin region have less extreme Ce -anomalies, with Ce^* values of about 0.55 and slight Ce^* anomalies ranging from 0.90 to 1.30, respectively. The Varnavas manganeseiferous sediments display either slight or positive anomaly, i.e Ce^* values ranging from 0.9 to 1.9. These results indicate a continental margin region (Fig. 3.8e).

Regarding the precious metals, we note that Ag is enriched by a factor of 100 in both lithotypes. Au is neither enriched nor depleted and mildly depleted in the Mn-schists and Fe-quartzites, respectively. Pt is moderately enriched in the first lithotype and Pd is neither enriched nor depleted (Fig. 3.7g and 3.7h).

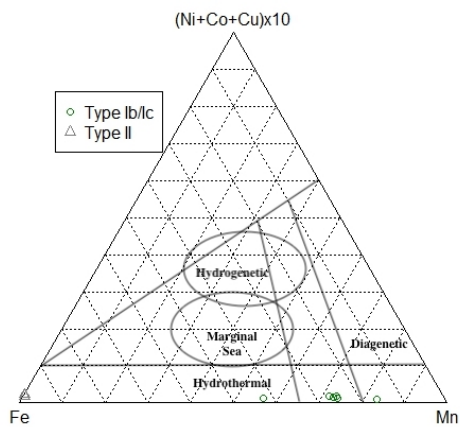
3.3.3 Binary and Ternary Classification Diagrams

This subsection is devoted in clarifying the geochemical classification of the Mn(\pm Fe)-ore in Varnavas area. We utilize both binary and ternary graphs. The ternary graphs are the:

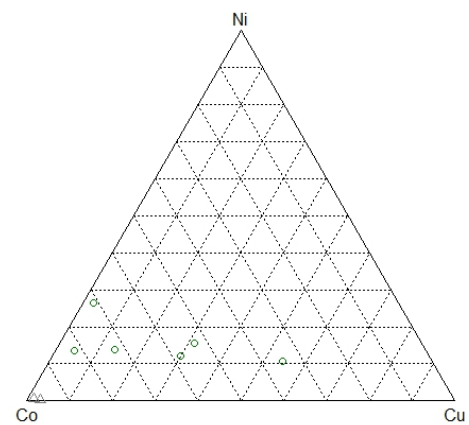
- Fe–Mn–(Co+Ni+Cu) $\times 10$, which is used to discriminate hydrothermal, diagenetic and hydrogenetic ferromanganese deposits [Bonatti and Rydell, 1972] and also utilized in [Berezhnaya et al., 2018, Crerar et al., 1982, Guan et al., 2017, Hein and Mizell, 2013, Liao et al., 2019, Marino et al., 2017, Pelletier et al., 2017, Sinisi et al., 2018],
- Co–Ni–Cu, which is used to determine the selectiveness in Co, Ni, or Cu – if any – in the ferromanganese deposits [Pelletier et al., 2017],

- Fe–Mn–Si $\times 2$, which is used to relate the mean volcanic arc end–member to pure Mn–oxide end–member and the samples' projections [Hein and Mizell, 2013, Sinisi et al., 2018],
- (Cu+Zn)–(Ni+Cr)–Mo, which is used to determine the possible source rocks that were leached of metals which in turn were supplied to ferromanganese deposits [Hein and Mizell, 2013],
- (Cu+Ni) $\times 15$ –(Zr+Y+Ce) $\times 100$ –Mn/4, which is a discrimination scheme for oceanic ferromanganese deposits using high field strength and rare earth elements [Liao et al., 2019].

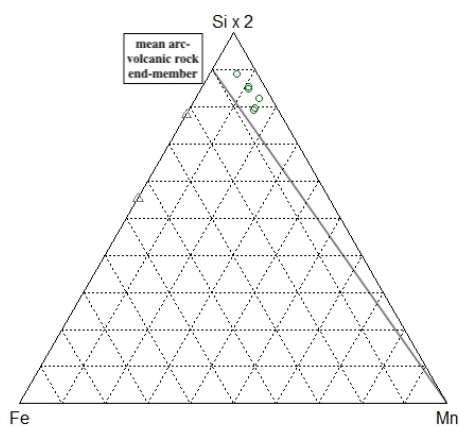
We explicitly note that the ternary graphs are plotted using only the ore samples.



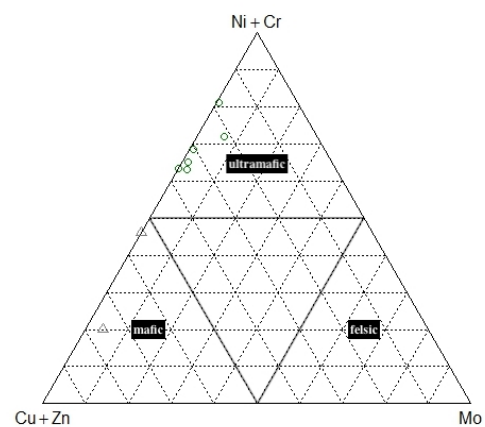
(A) Fe–Mn–(Co+Ni+Cu) $\times 10$



(B) Co–Ni–Cu

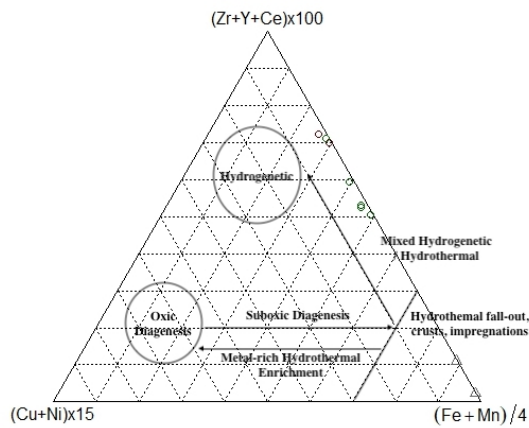


(C) Fe–Mn–Si $\times 2$



(D) (Cu+Zn)–(Ni+Cr)–Mo

The binary graphs utilized are:

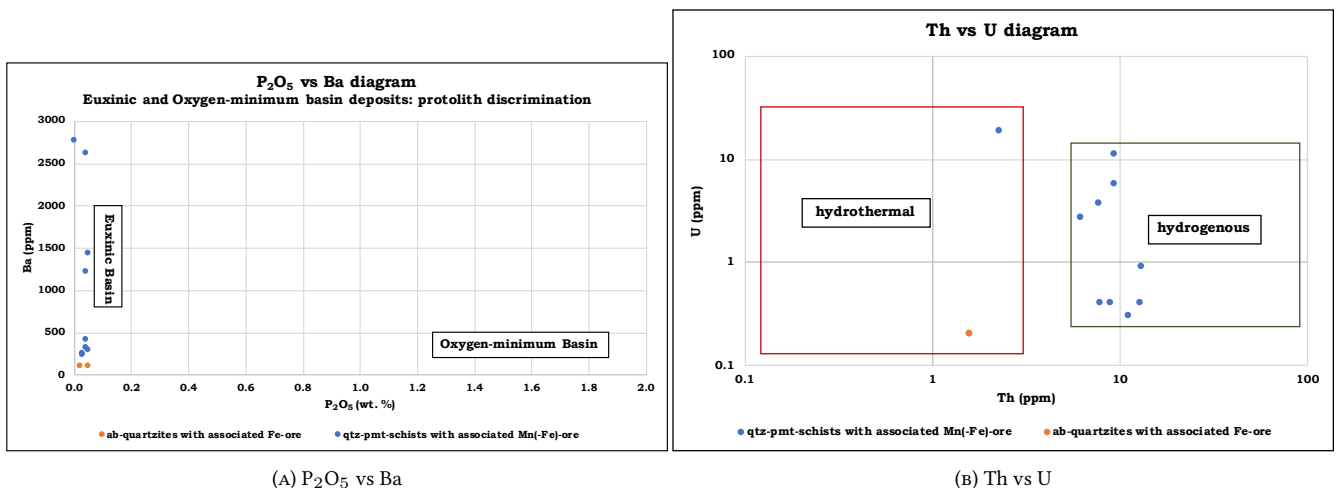


$$(E) (Cu+Ni) \times 15 - (Zr+Y+Ce) \times 100 - (Fe+Mn)/4$$

FIGURE 3.9: Ternary discrimination diagrams for the ore-samples.

- the P_2O_5 vs Ba diagram, which is used in order to discriminate the palaeodepositional environment [Maynard, 2014],
- the Th vs U diagram, which is used to distinguish the hydrothermal from the hydrogenous manganeseiferous accumulates [Flohr, 1992],
- the Co+Ni vs As+Cu+Mo+Pb+V+Zn diagram, which is used to determine whether the deposit is of hydrothermal or hydrogenetic / diagenetic origin [Nicholson, 1992],
- the Al vs Si diagram, which is used to determine if the initial sediment was hydrothermal or hydrogenetic in nature [Nath et al., 1997],
- the Mg vs Na diagram, which is used to distinguish the basin-type where these manganeseiferous rocks formed, in terms of fresh-water input or in a shallow or not marine environment [Nicholson, 1992] and
- the Mn/Fe vs Co/(Ni+Cu) diagram, which provides the relationship of hydrogenetic and diagenetic inputs to the composition of polymetallic nodules [Josso et al., 2017].

The binary diagrams are plotted using all data, except the Type III lithotype.



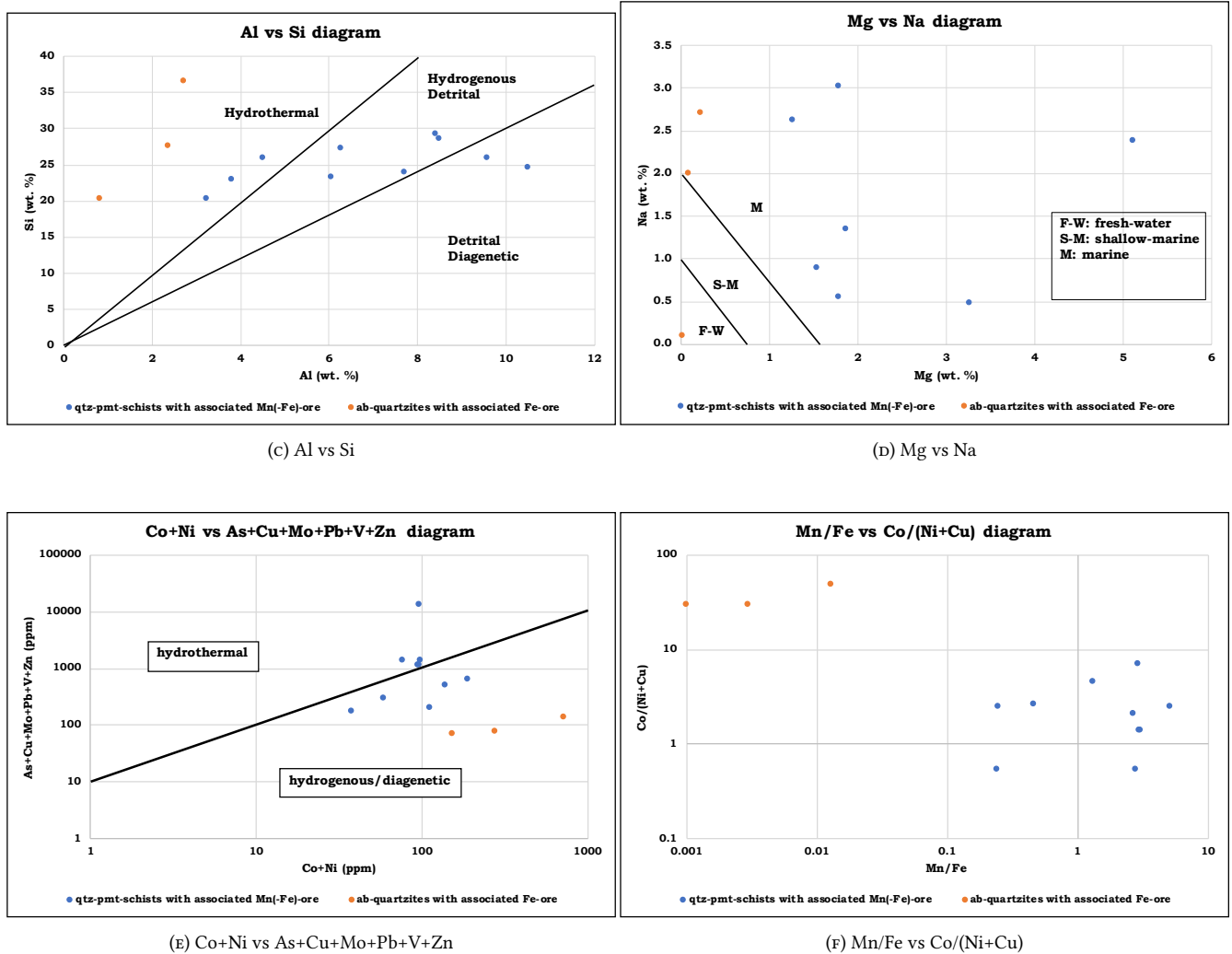


FIGURE 3.10: Binary discrimination diagrams.

We also utilize geotectonic classification diagrams, which are provided in Appendix G.

3.3.4 Correlation Analysis

The correlation analysis between the major and trace elements of our samples is divided into two presentation methodologies. We provide the Pearson correlation matrix of the Mn-schists in Appendix H and the similarity dendrograms for both Type I and II lithotypes in the present subsection.

Statistical correlation may provide insight into the genetic geochemical relations between major and trace elements which comprise the sample rocks. We accept the Pearson correlation coefficients that are characterized by p -value < 0.05 , as stated in Ap. H, and the groupings in the following dendrograms with high similarity percentages.

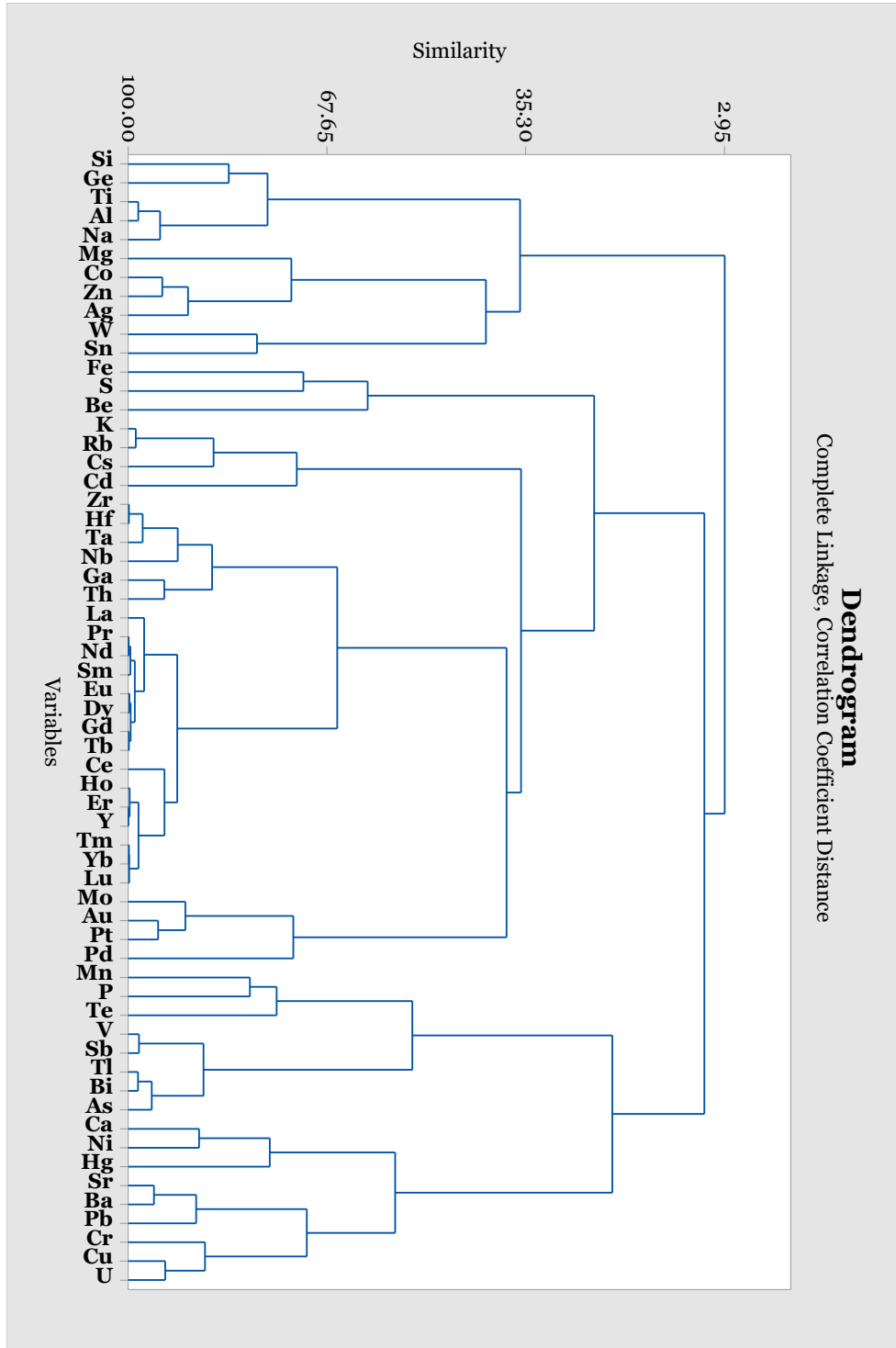


FIGURE 3.11: Similarity dendrogram for the qtz-pmt-schists.

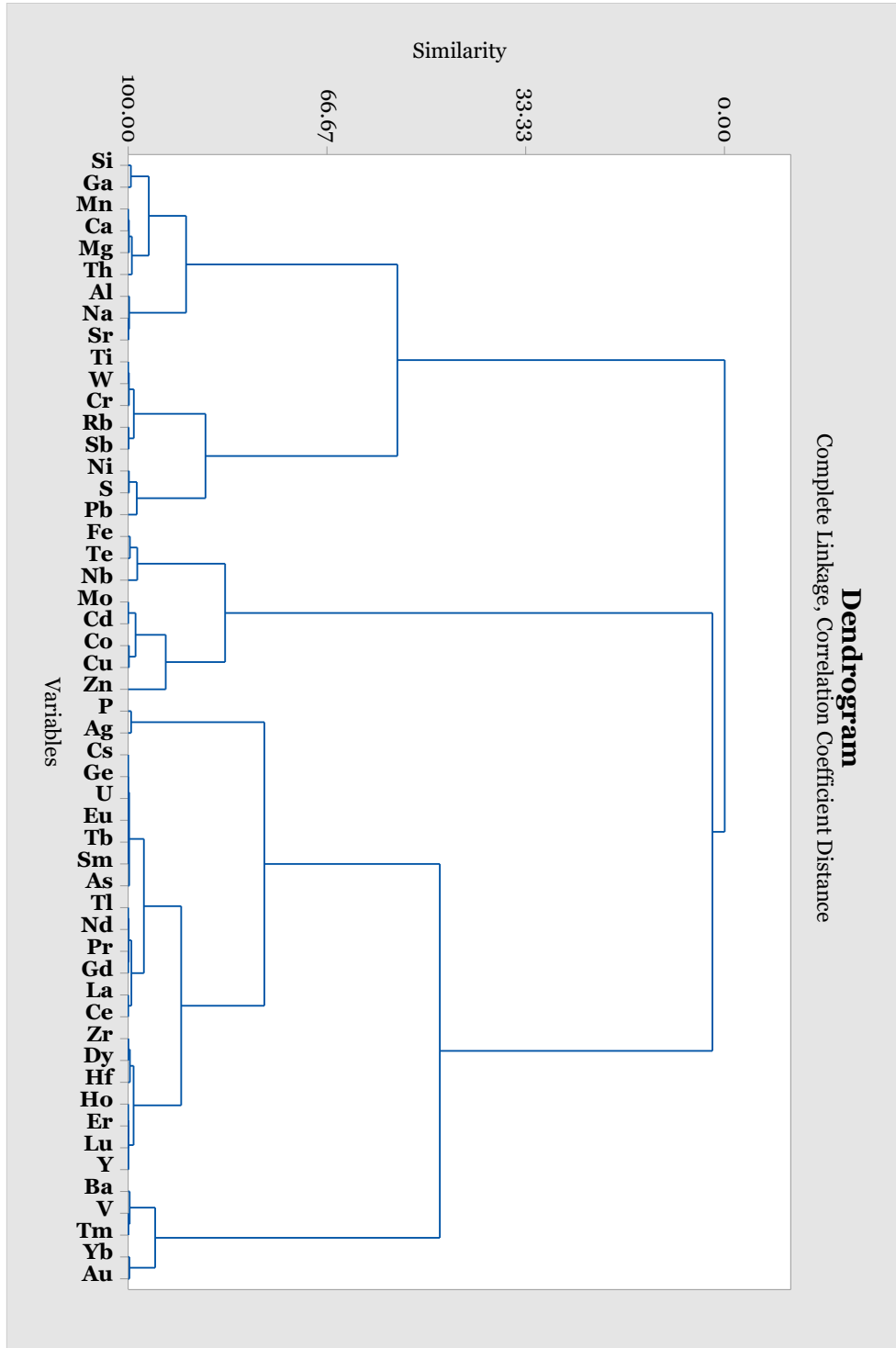


FIGURE 3.12: Similarity dendrogram for the ab-quartzites.

Chapter 4

Conclusions and Discussion

Detailed mineralogical analysis utilizing polarizing optical microscopy, X-Ray diffractometry, Raman spectrometry and scanning electron microscope coupled with energy-dispersive analyzer, in combination, have contributed in the identification of the very fine-grained and spatially complex mineral assemblage of the Mn-Fe ore in the studied samples. According to microscopic observations and textural relationships of the Mn±Fe ore-bearing metasediments two main lithotypes are identified:

1. the manganian quartzitic schists (**Lithotype I**^{1,2}) and
2. the ferric albitic quartzites (**Lithotype II and III**) in the area of Varnavas.

The assemblages are:

Lithotype I

quartz + albite + piemontite + sursassite + ardennite(-As) + spessartine + biotite/phlogopite + muscovite/paragonite + epidote + chlorite ± pumpellyite(-Mn) + monazite/gasparite ± allanite ± chlotitoid ± clinozoisite ± zircon

with ore-minerals

todorokite/romanèchite + pyrolusite + hollandite + cryptomelane + psilomelane + hematite ± manganite ± hausmannite ± magnetite ± rutile ± manganosite ± bixbyite ± coronadite ± braunite ± jacobsite

and

Lithotypes II, III

quartz + albite + calcite ± apatite ± zircon

with their respective ore-minerals

hematite ± magnesioferrite ± maghemite.

The mineral assemblage that is provided above (and in Tab. 3.1) can characterize our rocks as Type IIA or IIB, according to [Dasgupta et al., 1990], i.e. as being dominated by Mn-silicates with minor Mn-oxohydroxides or with bands with the inverse case. This paragenesis can be related to the mineralogy-based discrimination scheme by [Roy, 1968], where we have a **greenschist-facies metamorphosed formation which has been altered by supergene processes**, with the most affected being the ore minerals. The metamorphic fabric has not been altered by any supergene activity.

Some of the above minerals are important scavengers of critical base or technological metals or, even, precious ones. Spessartine is shown to be REE-bearing (Fig. 3.6h, Tab. 3.6 and Fig. F.1h, F.1i, F.1j). The todorokite/romanèchite tubular network seems to be Ce-adsorptive and possibly Ga- and Tl-adsorptive (Fig. 3.6h and F.1h). Trivalent cations like REEs, Ga and Tl and some tetravalent ones like Ce⁴⁺ are promising to be sorpted into this network, possibly by being immobilized between phyllo-manganate structures or by substituting Mn³⁺ or Mn⁴⁺. Hollandite supergroup mineral inclusions in the todorokite network or Sr-Ba-adsorption and/or K-Na-Ca-Mg-substitution by Sr and Ba in todorokite is related to high Sr, Ba values in todorokite/romanèchite (Tab. 3.3 and Fig. F.1g). Sparse Pb in the Mn-network is most probably attributed to coronadite inclusions in todorokite (Fig. F.1i and E.1d). Both hematite and magnetite are Co(±Mn±Ti)-bearing, with magnetite also being Pt-bearing (Tab. 3.4 and 3.5) and hematite Gd-bearing (Fig. F.1e compared to F.1j).

The samples studied were enriched in the following elements:

Lithotypes I:

Mn-As-Sb-W-Hg-Ag-Bi-Pb-Cd-Te-Tl-Co-U-Ba-Cu-Sr-Cr-Mo-HREE-Pt

¹Lithotypes Ia (host rock), Ib, Ic (ore).

²Tab. 3.2.

and

**Lithotype II:
Fe–W–Co–Ag–As–Th–Ge–Tl,**

(Fig. 3.7). We assume in what follows that regionally the metamorphic events and the subsequent supergene processes were almost isochemical. The relatively low Co- and Cu-enrichments and the depletion in Ni suggest a hydrothermal origin of the volcanosedimentary precursor (Fig. 3.7 and 3.9a). This assumption is also defended by the fact that the mean Si/Al ratio is above 6 and the maximum ratio is 24, so the un-metamorphosed protolith might have been formed with a **hydrothermal origin, but with a minor hydrogenous-detrital input** [Nicholson, 1992]. This is also suggested by the rest of the discrimination diagrams provided in Ch. 3 (Fig. 3.9e and 3.10f [Josso et al., 2017], 3.10e [Nicholson, 1992], 3.10b [Flohr, 1992], 3.10c [Nath et al., 1997]). This means that the protolith sediment was distal from the volcanic source. The leached rocks that provided our samples with metals were ultrabasic to basic as suggested by Fig. 3.9d [Hein and Mizell, 2013].

The possible basic to ultrabasic magmatic activity that provided the sediment with metals could possibly be **volcanism related to an ocean island or a continental island arc** (Ap. G, [Bhatia and Crook, 1986]).

A plot of P and Ba [Fig. 3.10b, Maynard, 2014] suggests that the (volcano)sedimentary protolith was formed in a euxinic depositional environment, which means that the required oceanic anoxia is caused by restricted circulation in a basin through isolation from open ocean. The depositional environment can also be characterized as marine / deep-sea (Fig. 3.10d, [Nicholson, 1992]), but the Ce* and \sum REE results also indicate a continental margin region [Murray et al., 1990, Murray et al., 1991].

Manganese is present in nodules and crusts, formed in these deep-sea environments as discussed in the previous paragraph. Nodules and crusts are distributed widely over the seafloor. Higher-grade modern sediment nodules or crusts of hydrothermal origin contain circa 44% w/w Mn along with significant amounts of cobalt (up to 2.24% w/w), copper (up to 0.18% w/w), nickel (up to 4.67% w/w), molybdenum (up to 0.18% w/w), but very low arsenic (up to 31ppm) and lead (up to 12ppm) [Pelleter et al., 2017]. The REEs in hydrothermal manganese deposits have lower concentration values in contrast to hydrogenetic deposits, in which are usually quite enriched. On the other hand, higher-grade nodules and crusts of slow-growth hydrogenetic and diagenetic origin show circa 28% w/w Mn and relatively lower values for cobalt (up to 0.15% w/w) and nickel (up to 1.24%) [Pattan et al., 2017]. The samples from the Varnavas area definitely show lower-grade manganese, low concentrations of base metals except for lead, relatively low REEs – which is also indicative for a hydrothermal origin, but HFSE-element concentrations that resemble hydrogenetic manganese sediments. This feature may refer to later adsorption during diagenesis through porous fluids or, less probable due to high immobility, during the metamorphic events.

The statistical correlation analysis (Fig. 3.11, Ap. H) for the quartzitic piemontitic schists between the chemical elements by forming Pearson correlation matrices and similarity dendrograms has provided us with a grouping of the trace elements:

- Group1: **Ba–Sr–Cu–Cr–Pb–S–U–Pt–W–Sn,**
- Group2: **As–V–Sb–Bi–Tl,**
- Group3: **HFSE–Mo–Pt–Au–Th–REE–Cs–Ga,**
- Group4: **Zn–Co–Ag** and
- Group5: **Ni–Hg.**

Manganese has only one statistically significant positive correlation to Cr, and has negative ones with Na, K and Rb (p – value < 0.05). Positive statistical correlations of Mn, but not statistically significant, are to Ca, P, Ba, Sr, Cu, Tl, Pb, Te, Th, U (p – value < 0.2). Iron is positively correlated to K and Rb, though negatively to V, Co and Sb. The Group1 and Group3 correlation patterns are determined by the (tubular-)network-forming manganese oxides todorokite, pyrolusite and, secondarily, manganosite along with enclosed crystals of magnetite and monazite / gasparite, with Ce and Pt serving as correlational bridges between the two groups³. The Group2 is defined by ardennite(–As) and is related to Ce, Y and HREEs in Group3 through monazite.

Finally, the presence of trivalent and tetravalent manganese and the positive Ce-anomaly suggest that the greenschist-facies metamorphic event – and, of course, the following supergene processes – was under high fO_2 (Fig. 3.8e), though not enough to oxidize manganosite and magnetite.

³Most probably as Ce⁴⁺.

Appendix A

Additional optical microscope photographs

This appendix provides some additional selected microphotographs obtained from the two optical microscopes utilized.

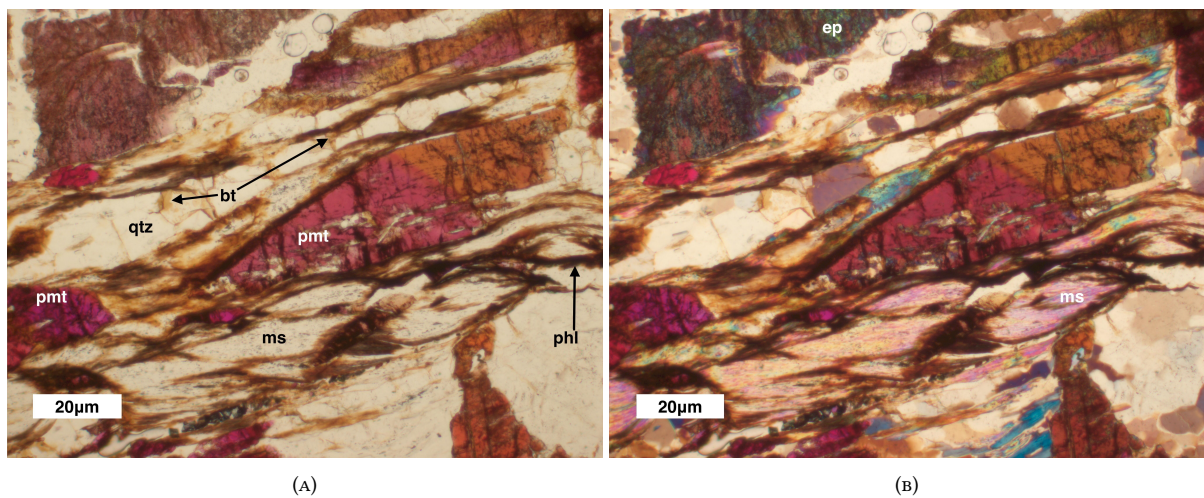


FIGURE A.1: Microphotographs. **(A)** Coarse crystals of quartz, euhedral and disseminated piemontite, intergranular flakes of biotite and continuous flakes of biotite and phlogopite and muscovite lamellar crystals and fishes (transmitted light, plane-polarized, Vr_{n2}). **(B)** Same thin section (transmitted light, cross-polarized, Vr_{n2}). Abbreviations: **qtz** quartz, **pmt** piemontite, **ep** epidote, **bt** biotite, **phl** phlogopite, **ms** muscovite.

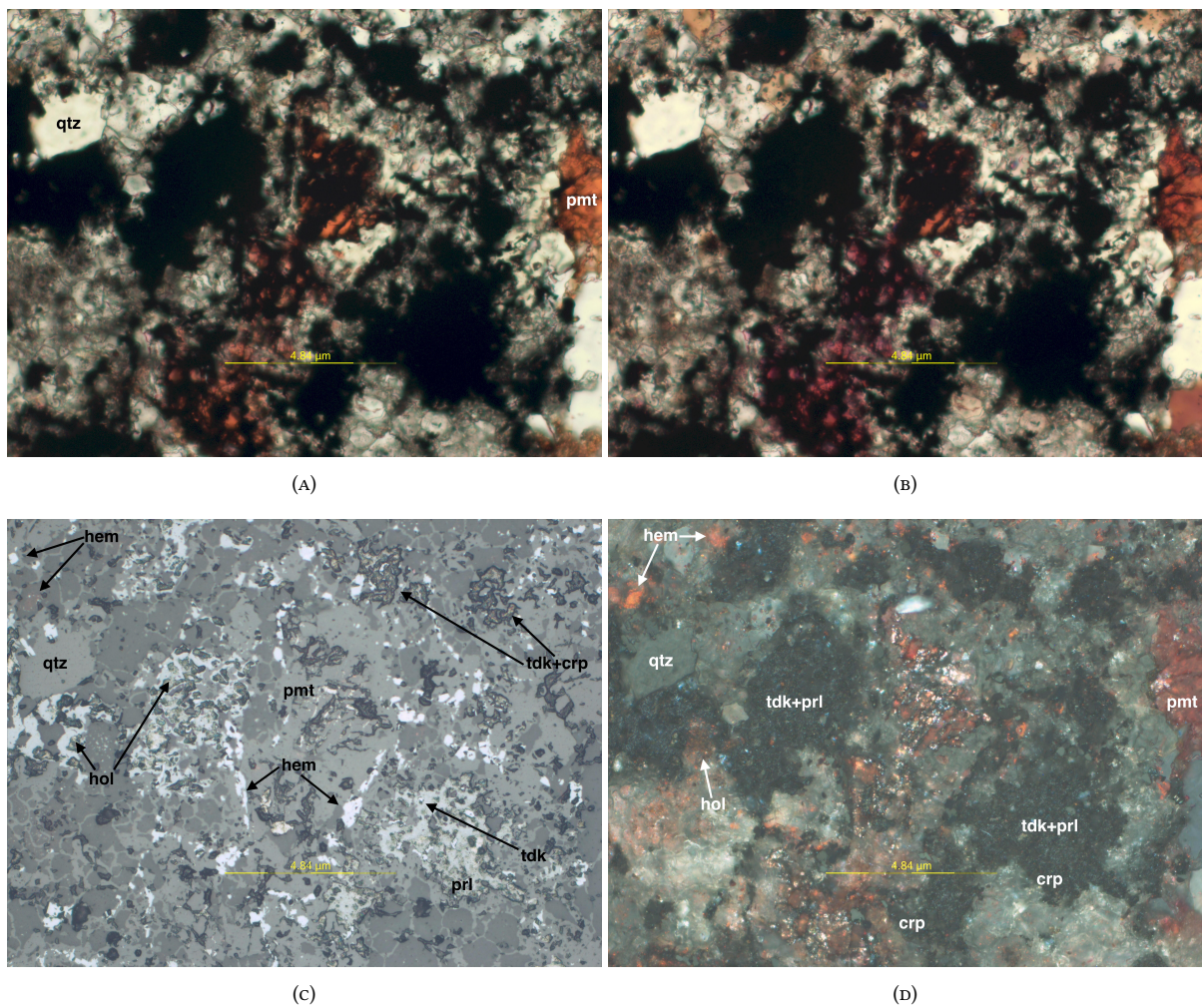


FIGURE A.2: Microphotographs. Mainly disseminated with larger massive portions Mn-Fe-mineralization (Vrn6). (A) Quartzitic-piemontitic groundmass with disseminated opaque minerals (transmitted light, plane-polarized, Vrn6). (B) Same sample (transmitted light, cross-polarized, Vrn6). (C) Same sample, depicting variations in the reflectivity of the ore mineral phases (reflected light, plane-polarized, Vrn6). (D) Same sample, with red internal reflections for hematite, brown birefringence for hollandite (reflected light, cross-polarized, Vrn6). Abbreviations: **qtz** quartz, **pmt** piemontite, **tdk** todorokite, **prl** pyrolusite, **crp** cryptomelane, **hol** hollandite, **hem** hematite.

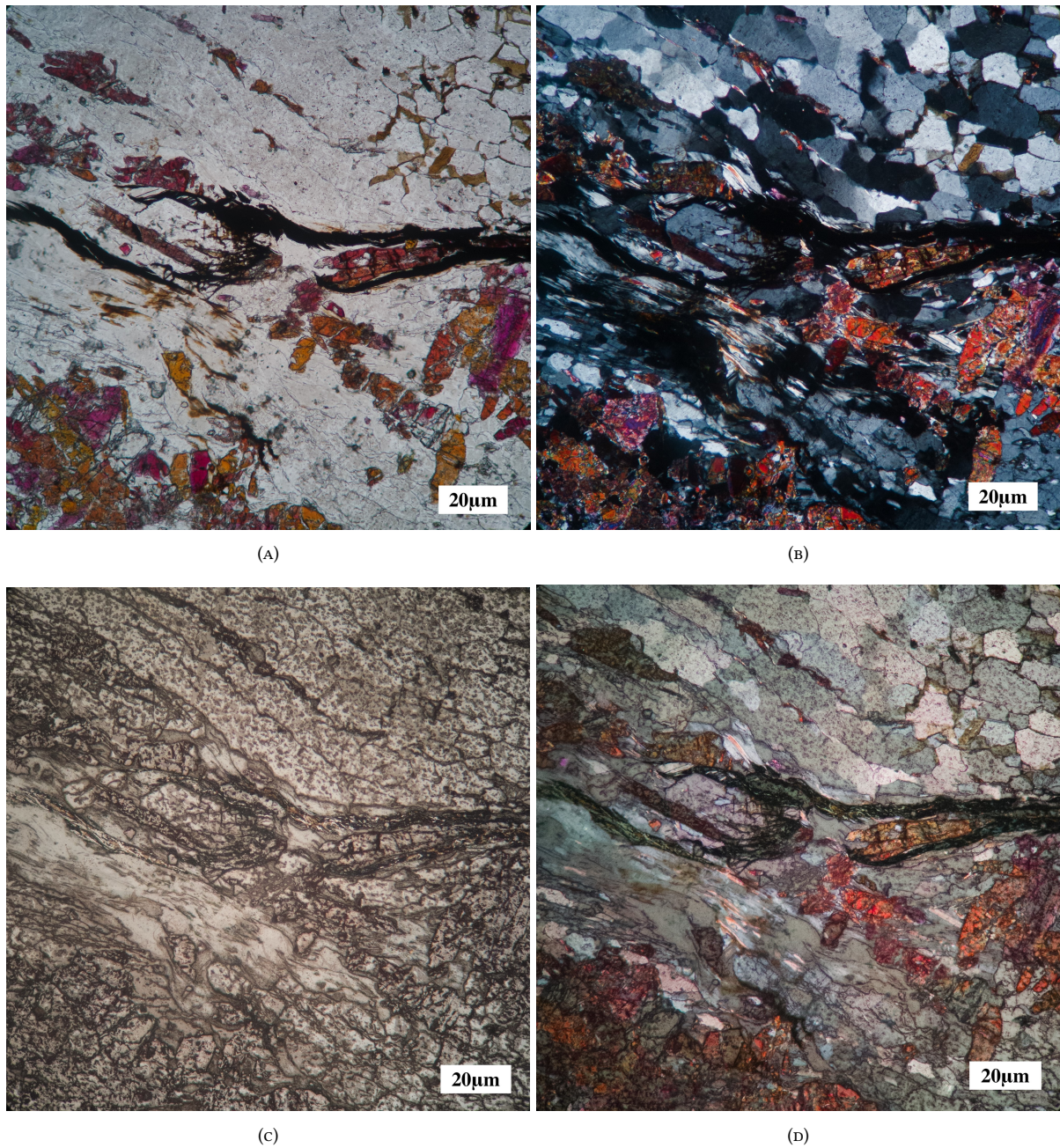


FIGURE A.3: Microphotographs. Veinlet (1) Mn-Fe-mineralization (Vrn9). **(A)** Quartz – piemontite – muscovite – phlogopite groundmass with veinlet-filling opaque minerals (transmitted light, plane-polarized, Vrn9). **(B)** Same sample (transmitted light, cross-polarized, Vrn9). **(C)** Same sample, depicting variations in the reflectivity of the ore mineral phases (reflected light, plane-polarized, Vrn9). **(D)** Same sample, with todorokite (dark grey to black), bixbyite (dark greenish grey) and manganite (light greenish grey), with no internal reflections (reflected light, cross-polarized, Vrn9).

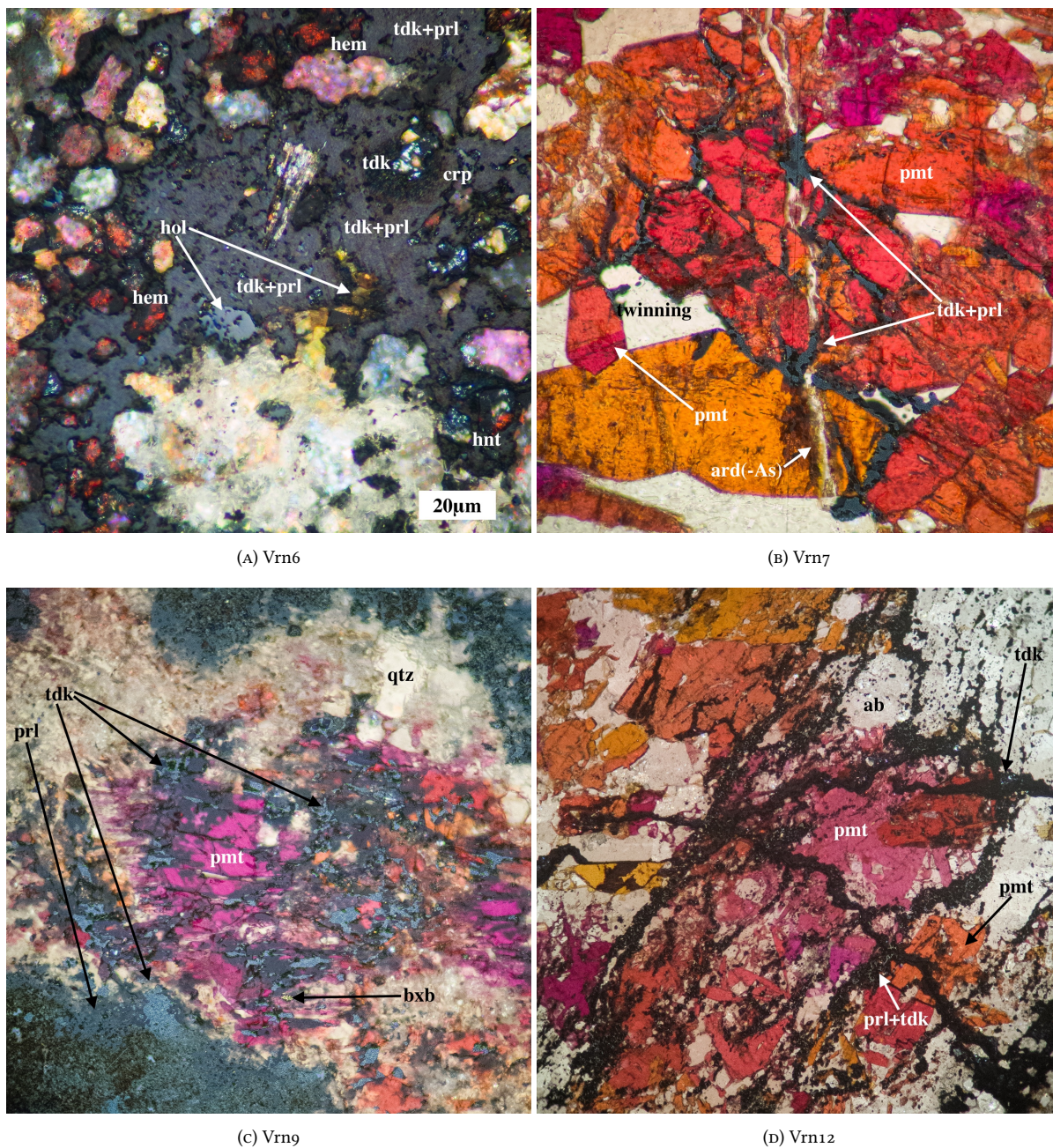


FIGURE A.4: Microphotographs. Veinlet (2) and intergranular Mn-Fe-mineralization (Vrn6, Vrn7, Vrn9, Vrn12). (A) (reflected light, cross-polarized, Vrn6). (B) (reflected light, cross-polarized, Vrn7). (C) (reflected light, cross-polarized, Vrn9). (D) (reflected light, cross-polarized, Vrn9). Abbreviations: **qtz** quartz, **pmt** piemontite, **sps** spessartine, **tdk** todorokite, **bx** bixbyite, **crp** cryptomelane, **mgs** manganosite, **hem** hematite.

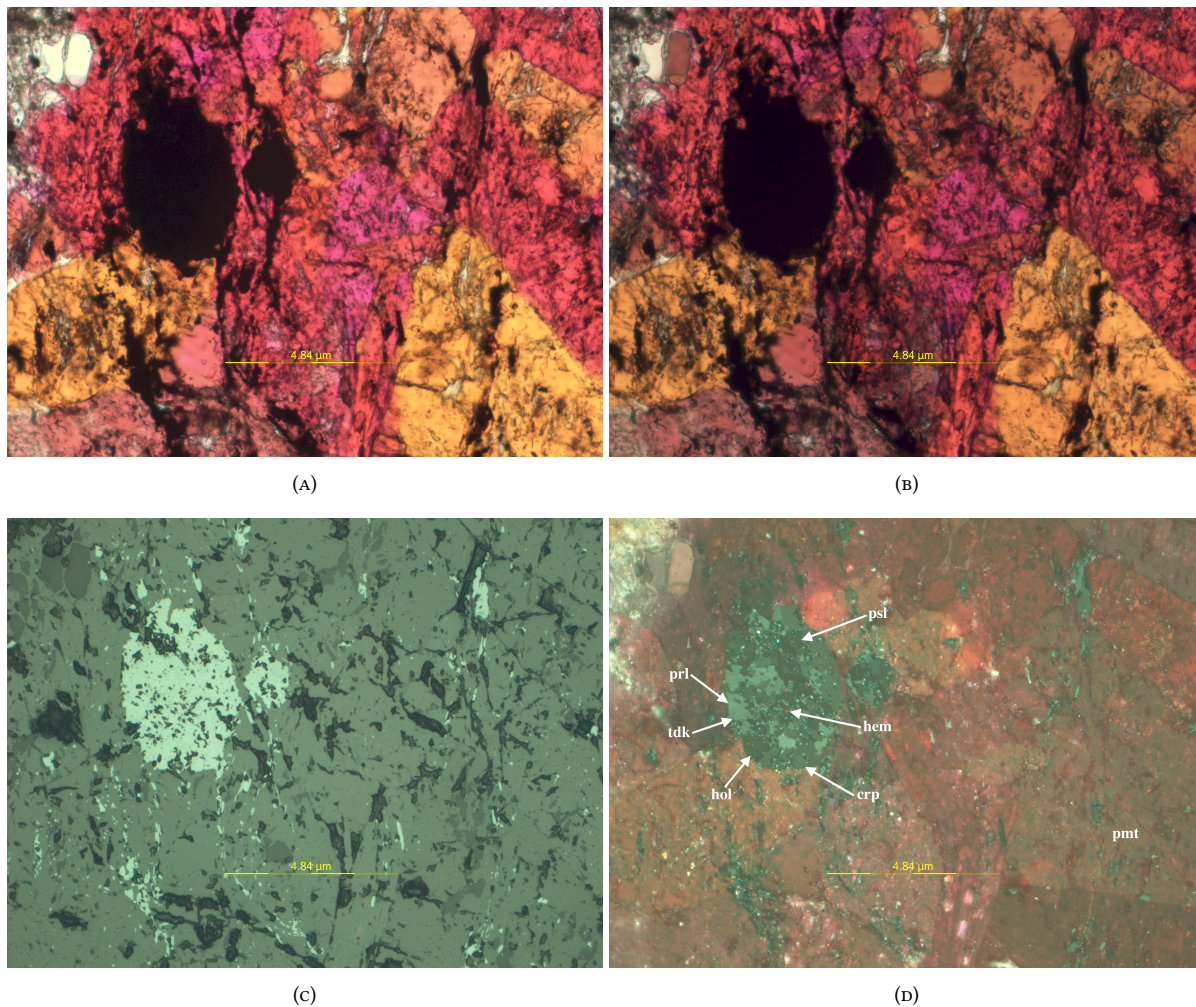


FIGURE A.5: Microphotographs. Micro-nodular massive and spotted Mn-Fe-mineralization (Vrn6). (A) Piemontite euhedral or subhedral crystals with micro-nodular massive Mn(\pm Fe)-ore (transmitted light, plane-polarized). (B) Same sample (transmitted light, cross-polarized). (C) Same sample, depicting in the current context slight variations in the reflectivity of the ore mineral phases (reflected light, plane-polarized). (D) Same sample, showing the variations in the ore mineralogy, grey for hematite and orange-red internal reflections, brownish grey for hollandite, light brownish grey for psilomelane, grey for pyrolusite and dark grey with light bluish grey anisotropies for todorokite (reflected light, cross-polarized). Abbreviations: **pmt** piemontite, **tdk** todorokite, **psl** psilomelane, **crp** cryptomelane, **prl** pyrolusite, **hol** hollandite, **hem** hematite.

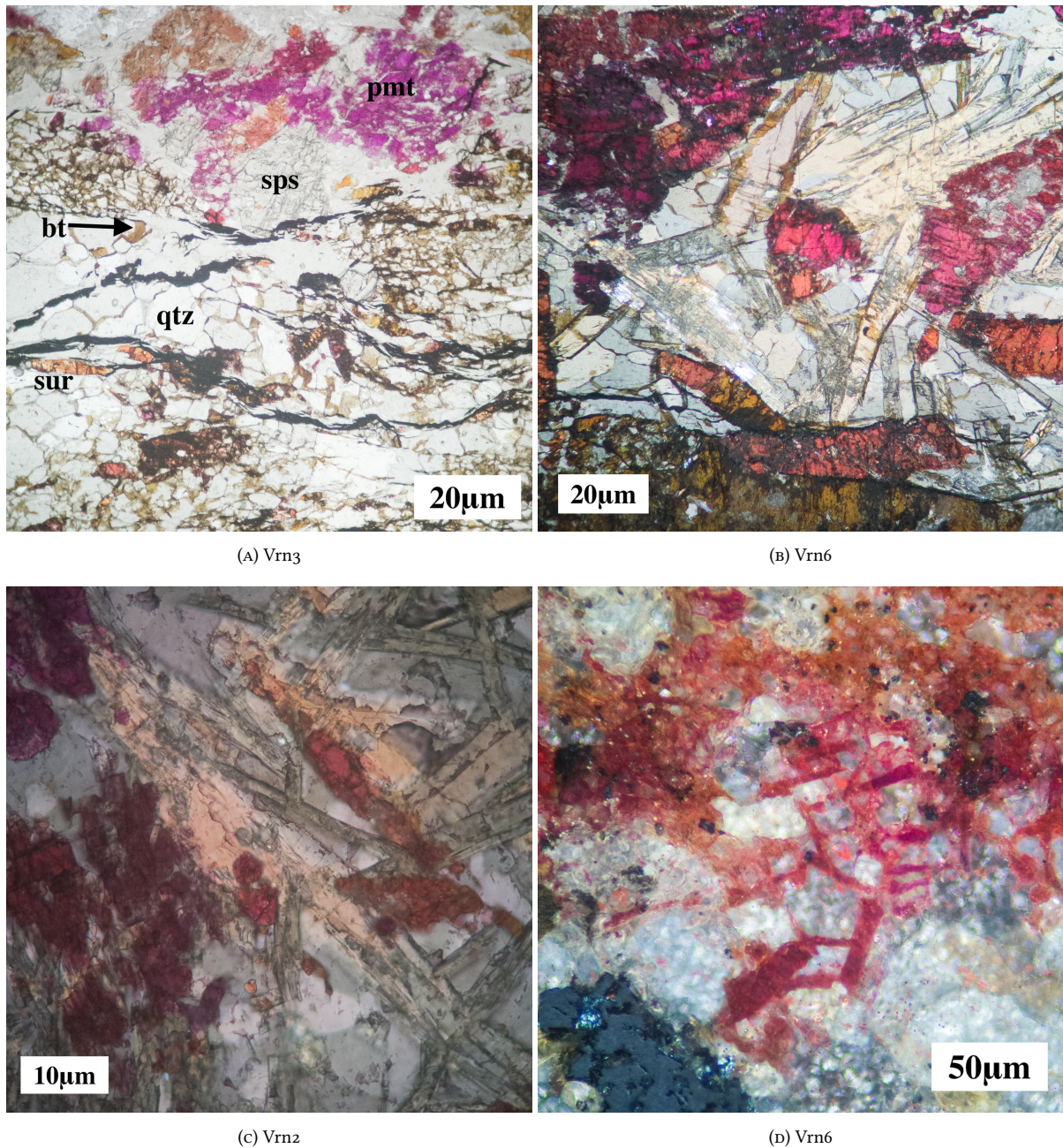
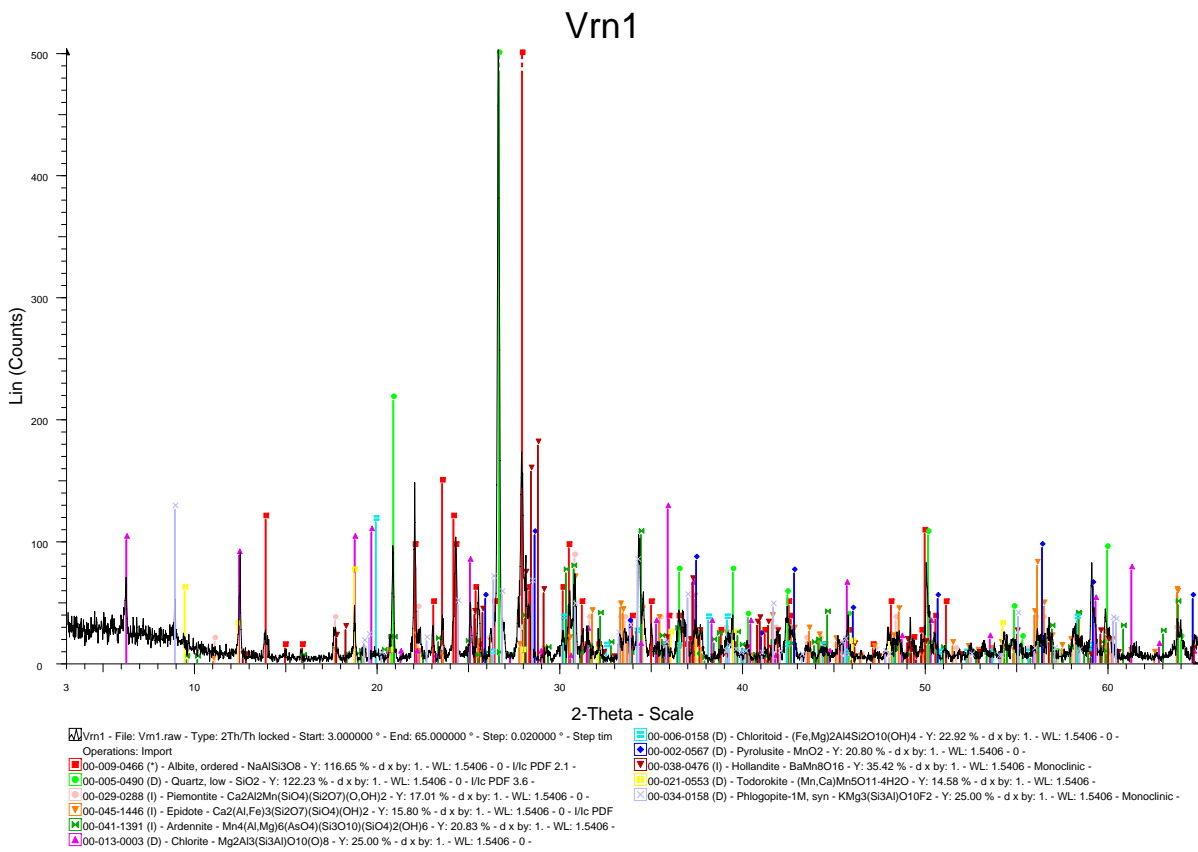


FIGURE A.6: Microphotographs. Micro-nodular massive or disseminated Mn-mineralization (Vrn2, Vrn3, Vrn6). (A) Piemontite disseminated porphyroblast in contact with a more disseminated spessartine porphyroblast in quartz-mica groundmass (transmitted light, plane-polarized). (B) Piemontite (or epidote) and sursassite elongated non-oriented crystals (reflected light, cross-polarized). (C) Sursassite, greenish grey translucent, and ardennite(-As), light yellow translucent, elongated crystals with spotted piemontite (reflected light, cross-polarized). (D) Euhedral non-oriented piemontite crystals with a mass of ardennite(-As) (reflected light, cross-polarized). Abbreviations: **pmt** piemontite, **qtz** quartz, **bt** biotite, **sur** sursassite, **sps** spessartine.

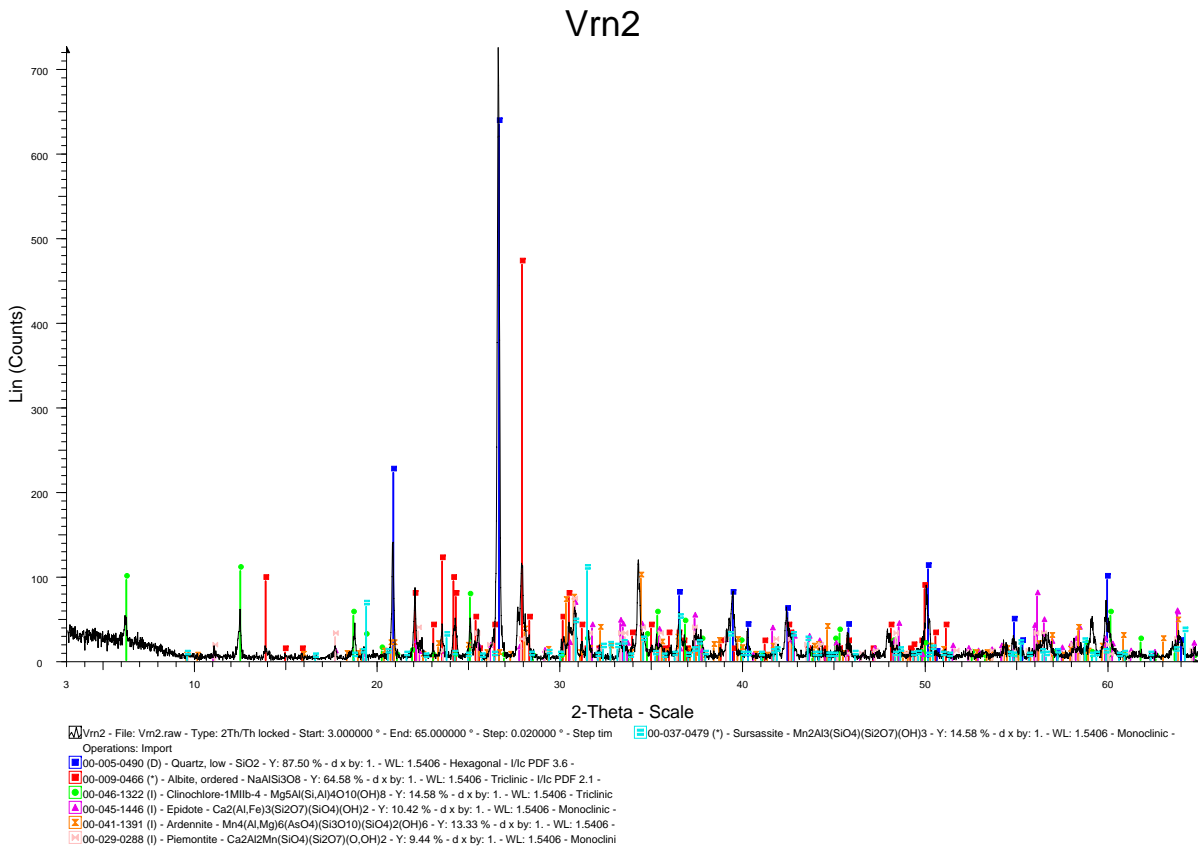
Appendix B

X-Ray Diffraction data

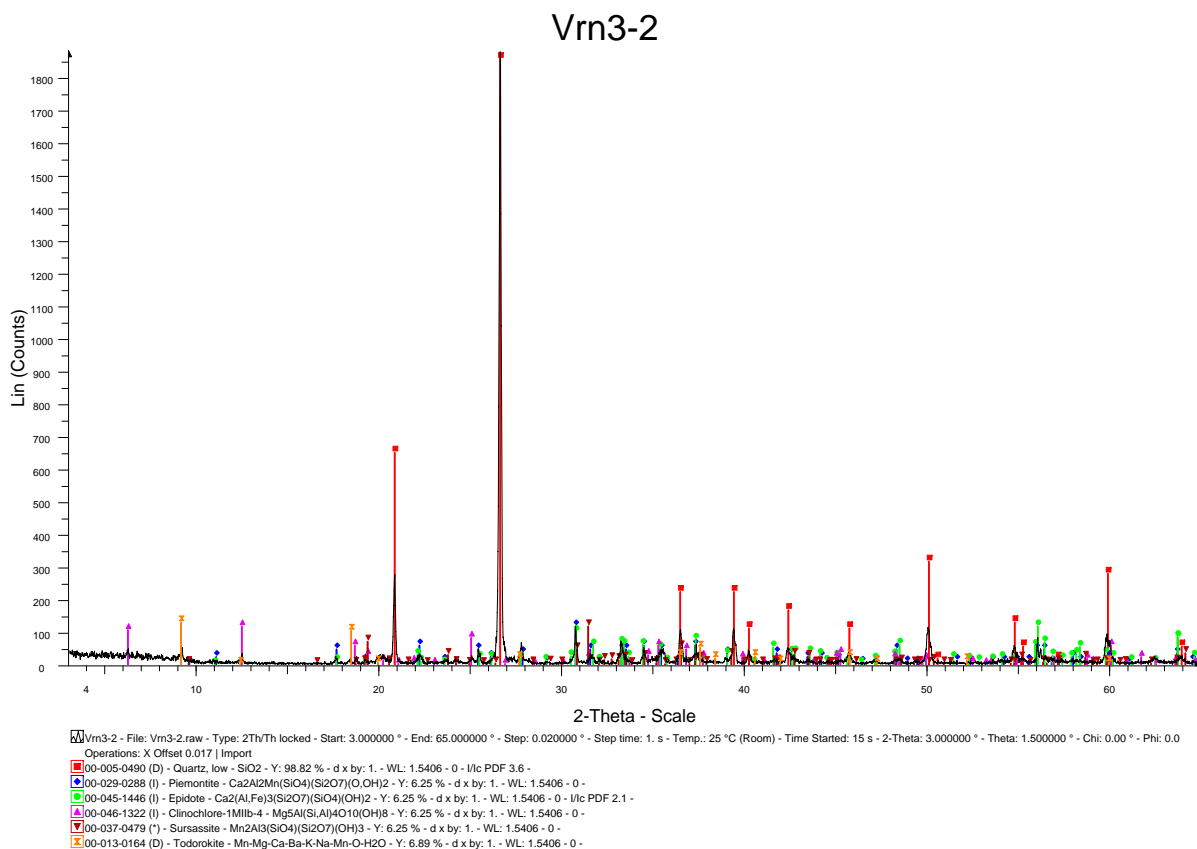
Appendix B contains the Bruker®EVA processed XRD patterns. More detailed versions are included in Ch. 3.



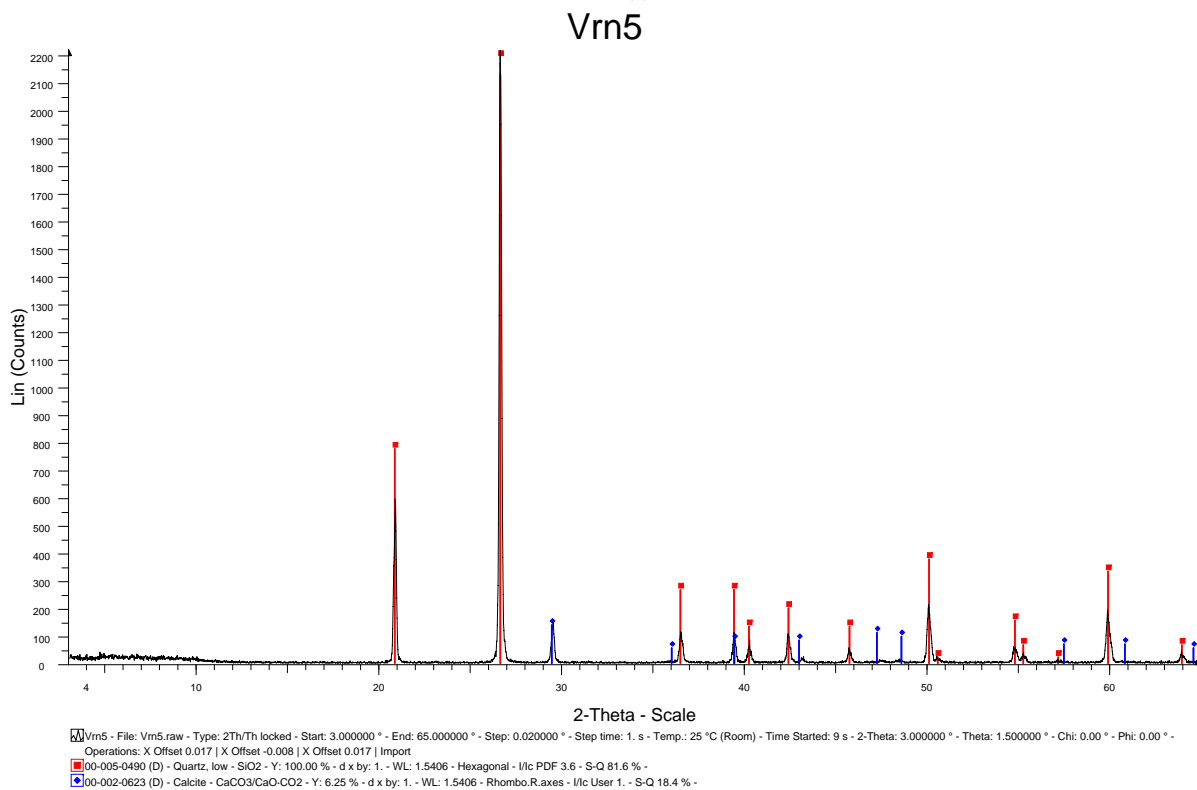
(A) Vrn1



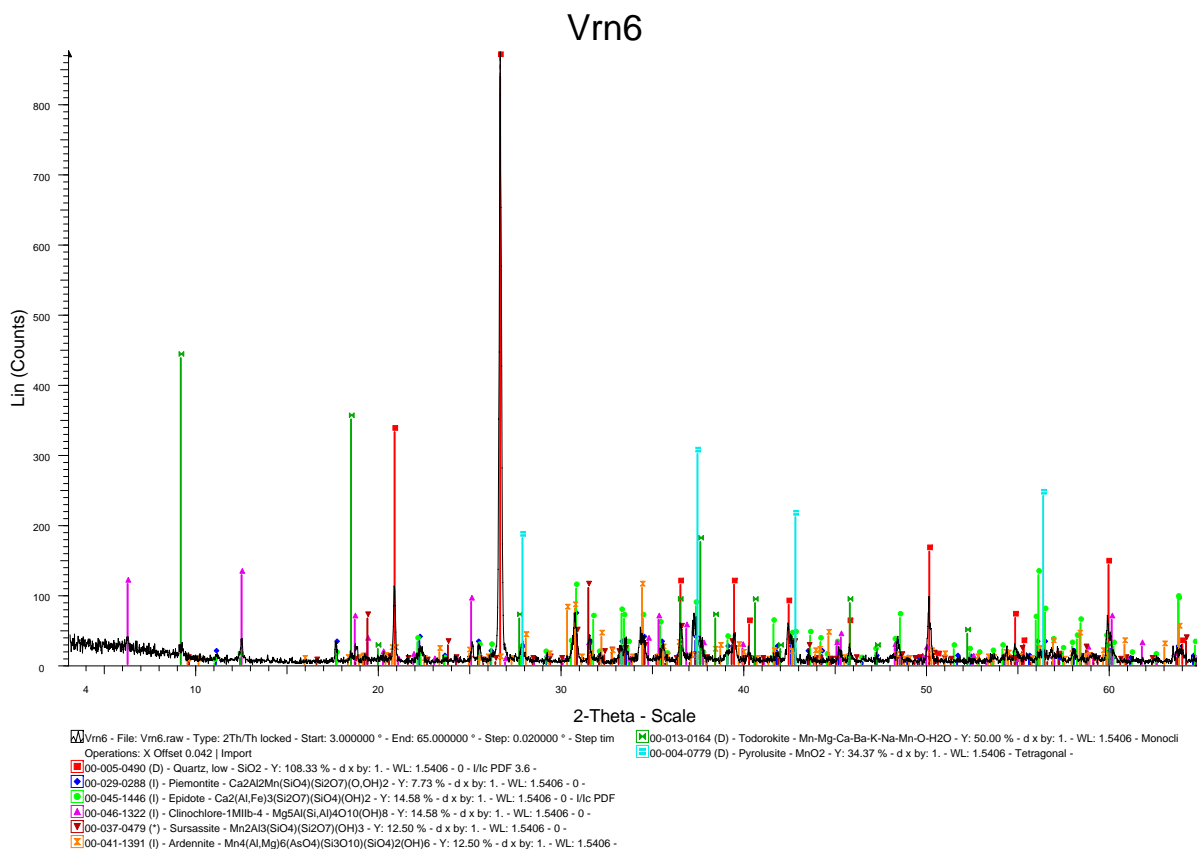
(B) Vrn2



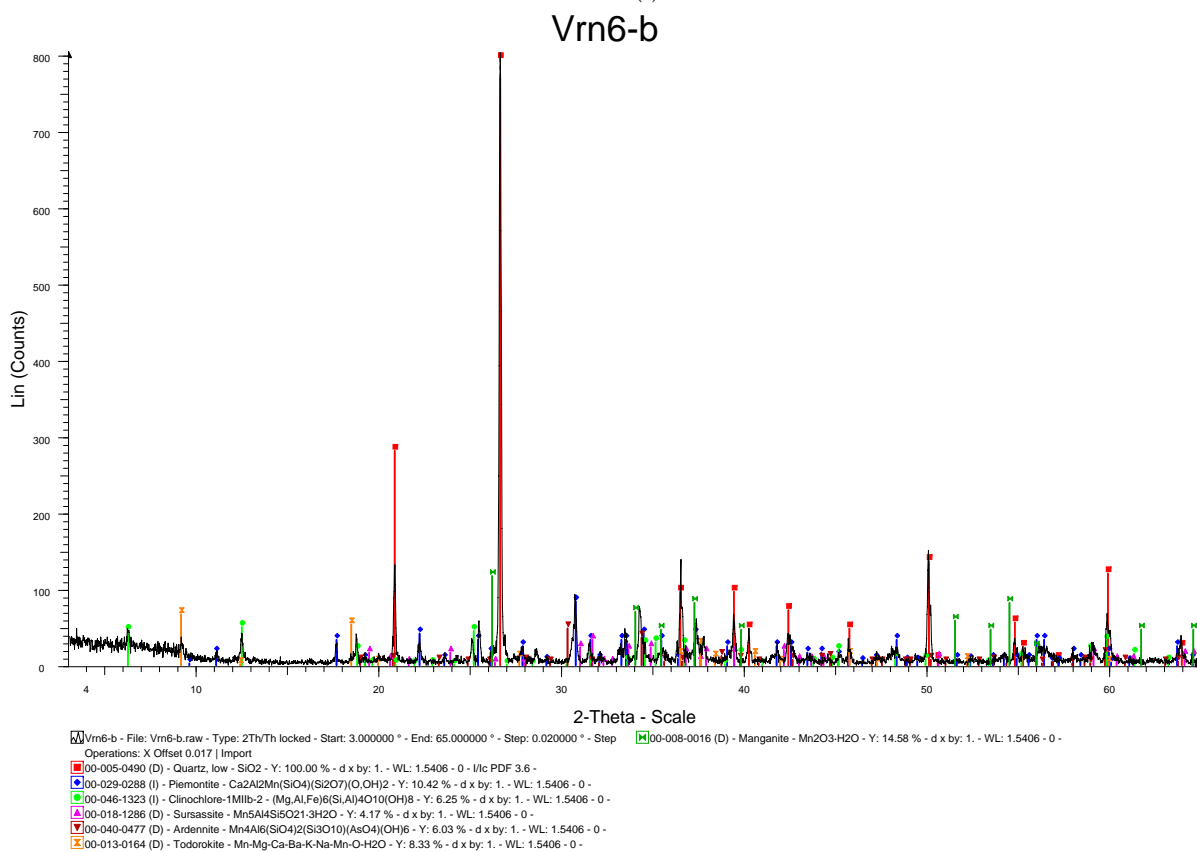
(c) Vrn3-2



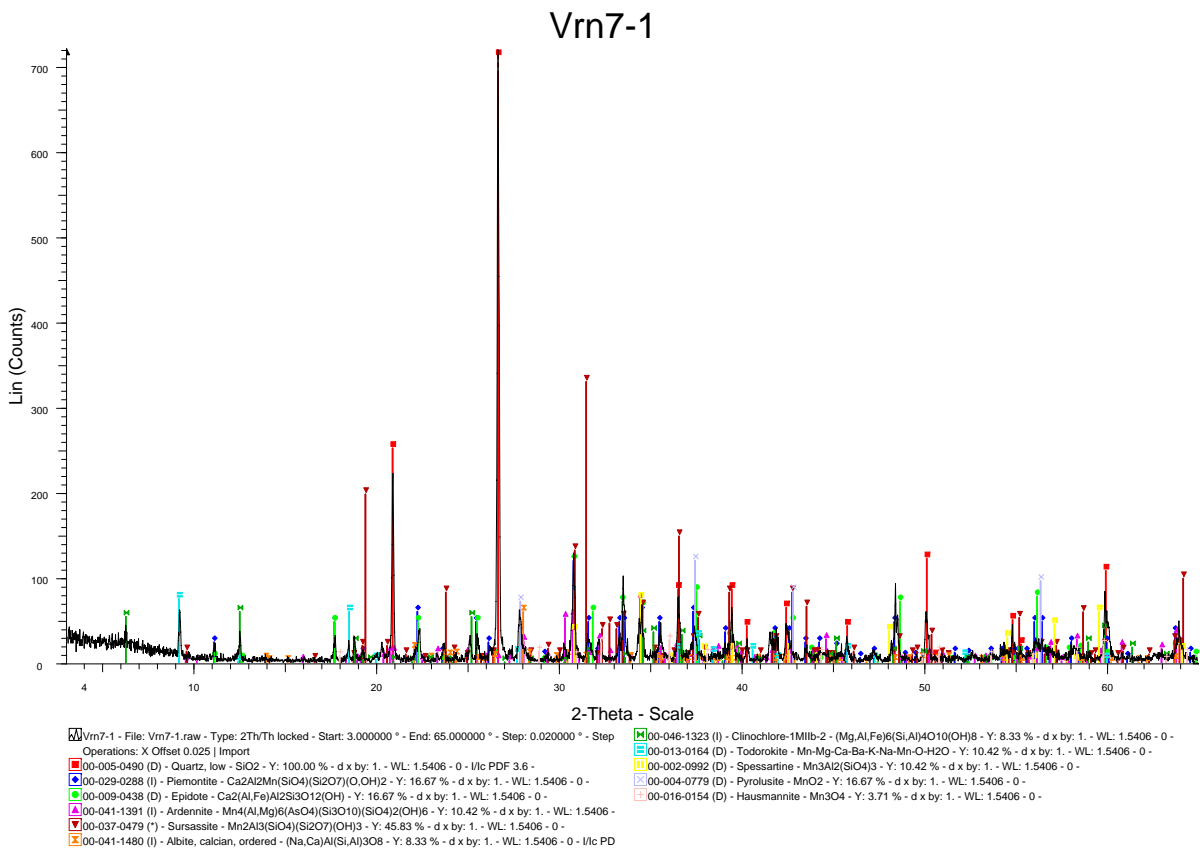
(d) Vrn5



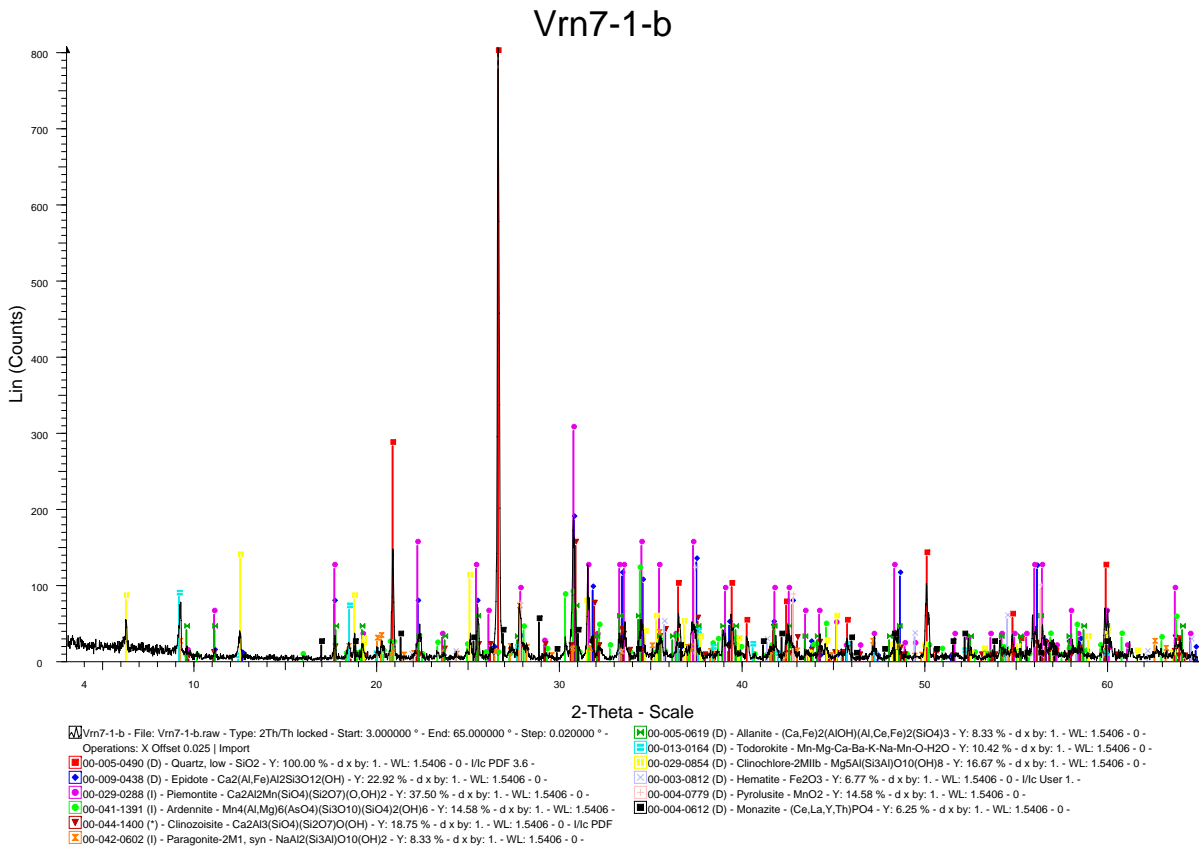
(E) Vrn6



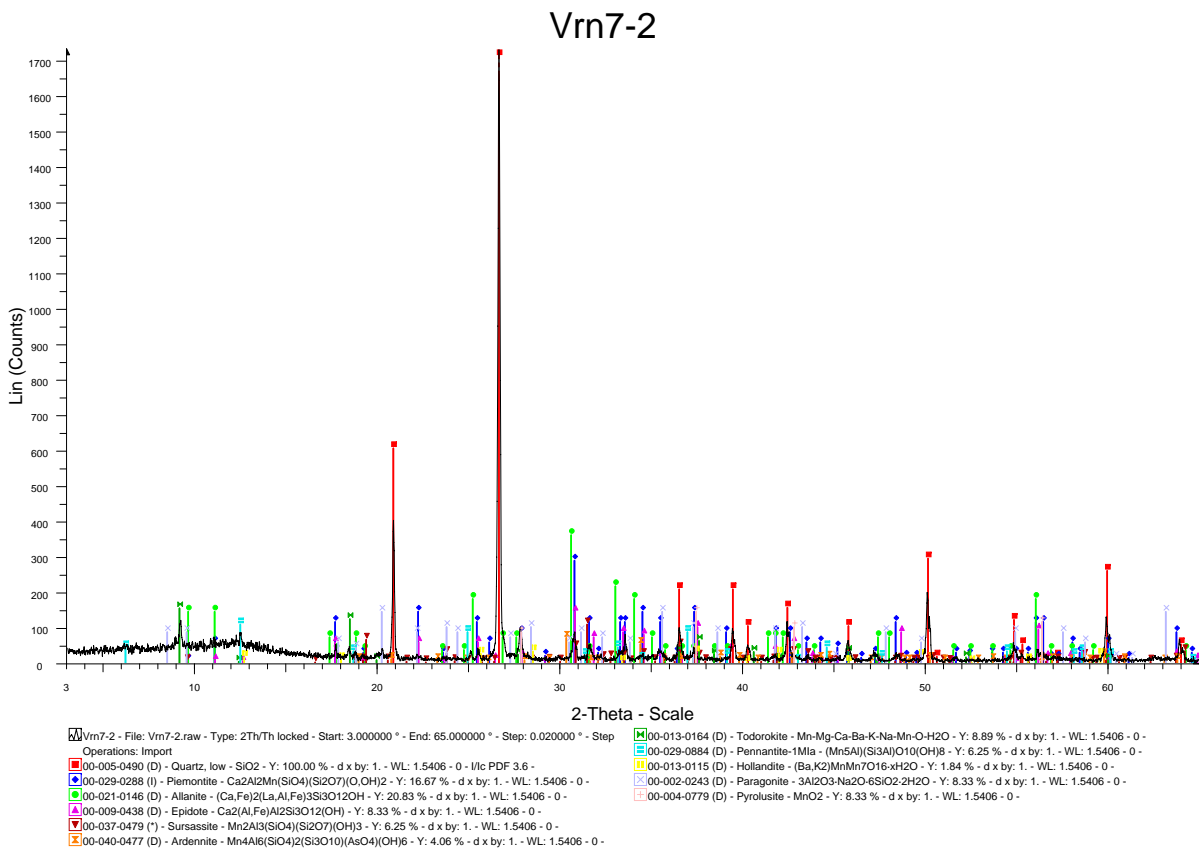
(F) Vrn6-b



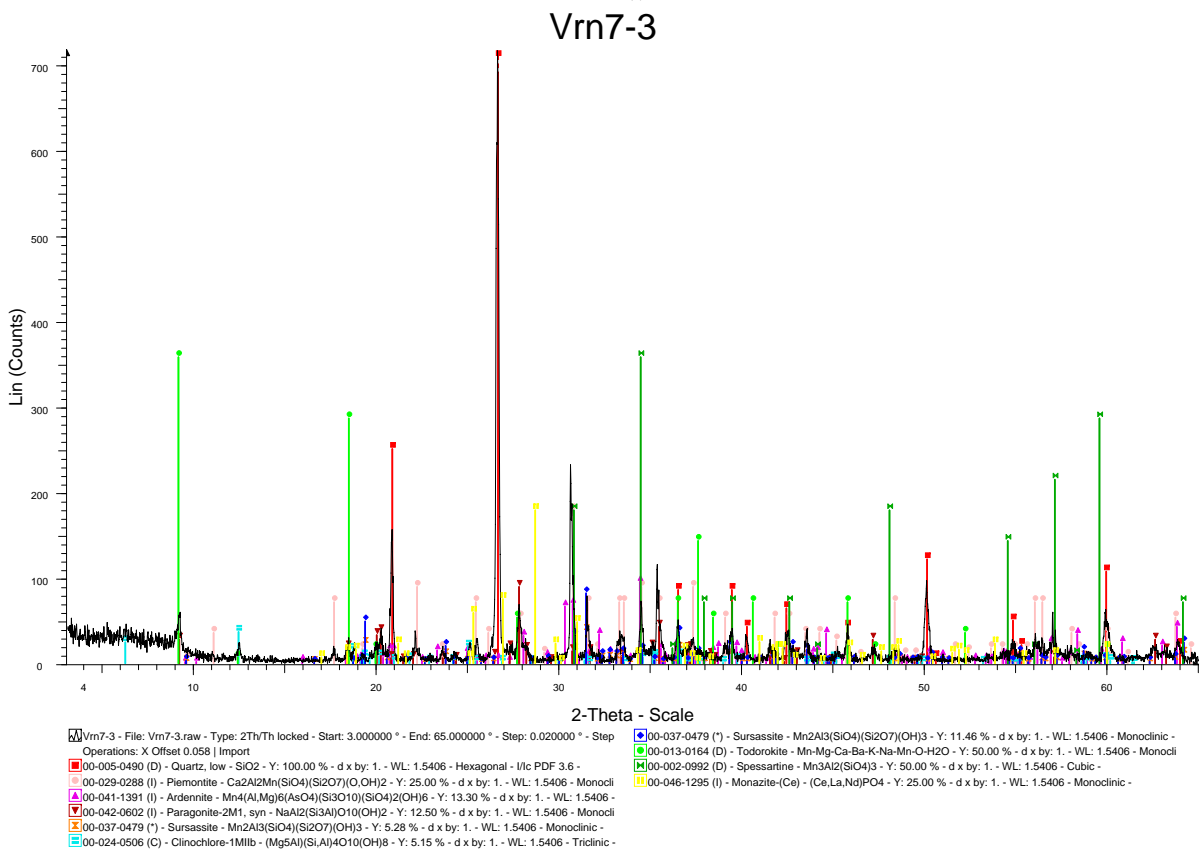
(g) Vrn7-1



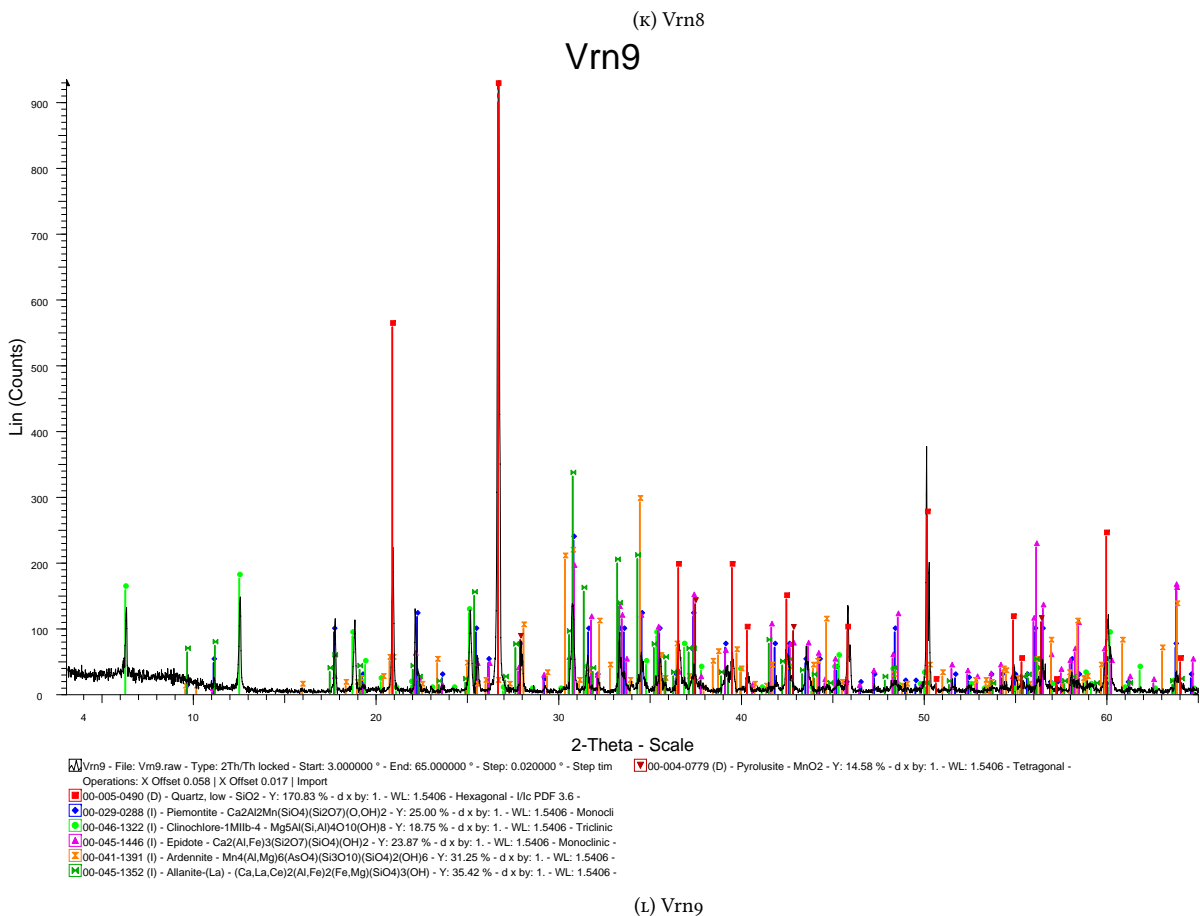
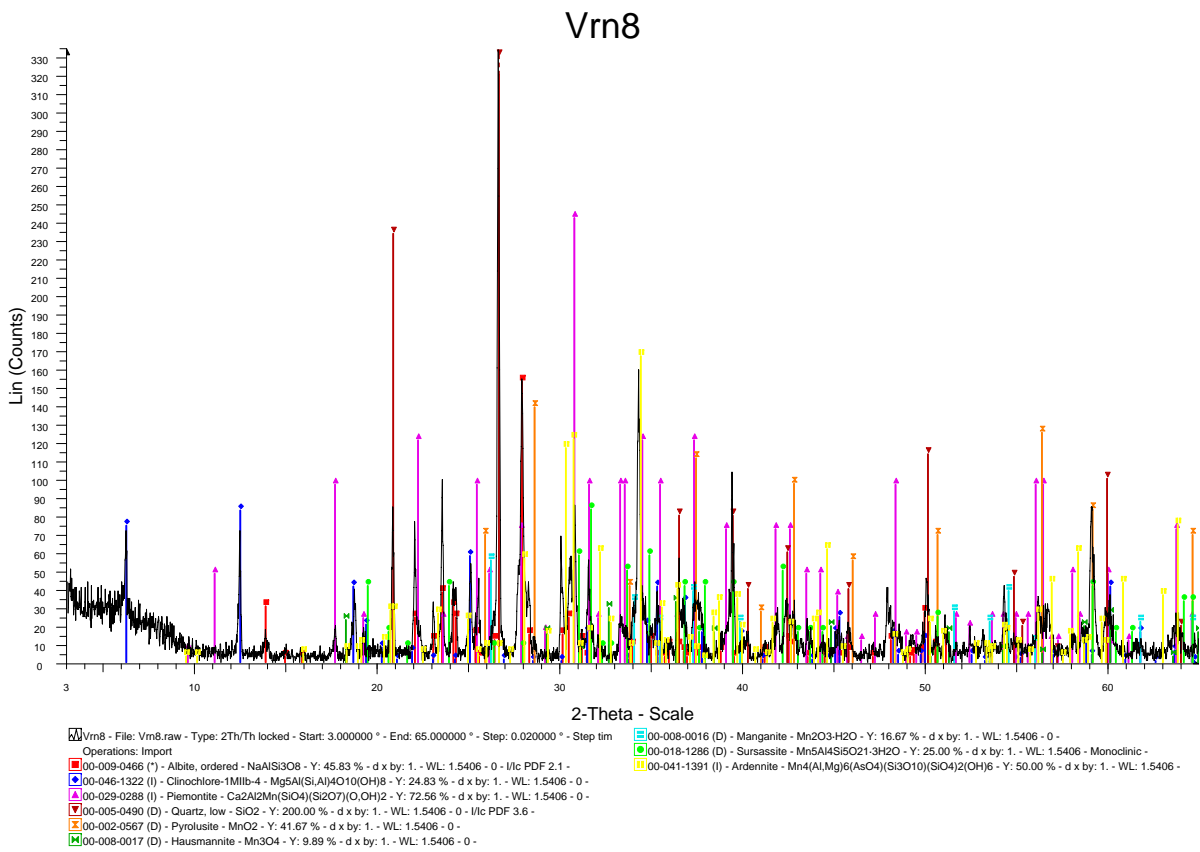
(h) Vrn7-1-b

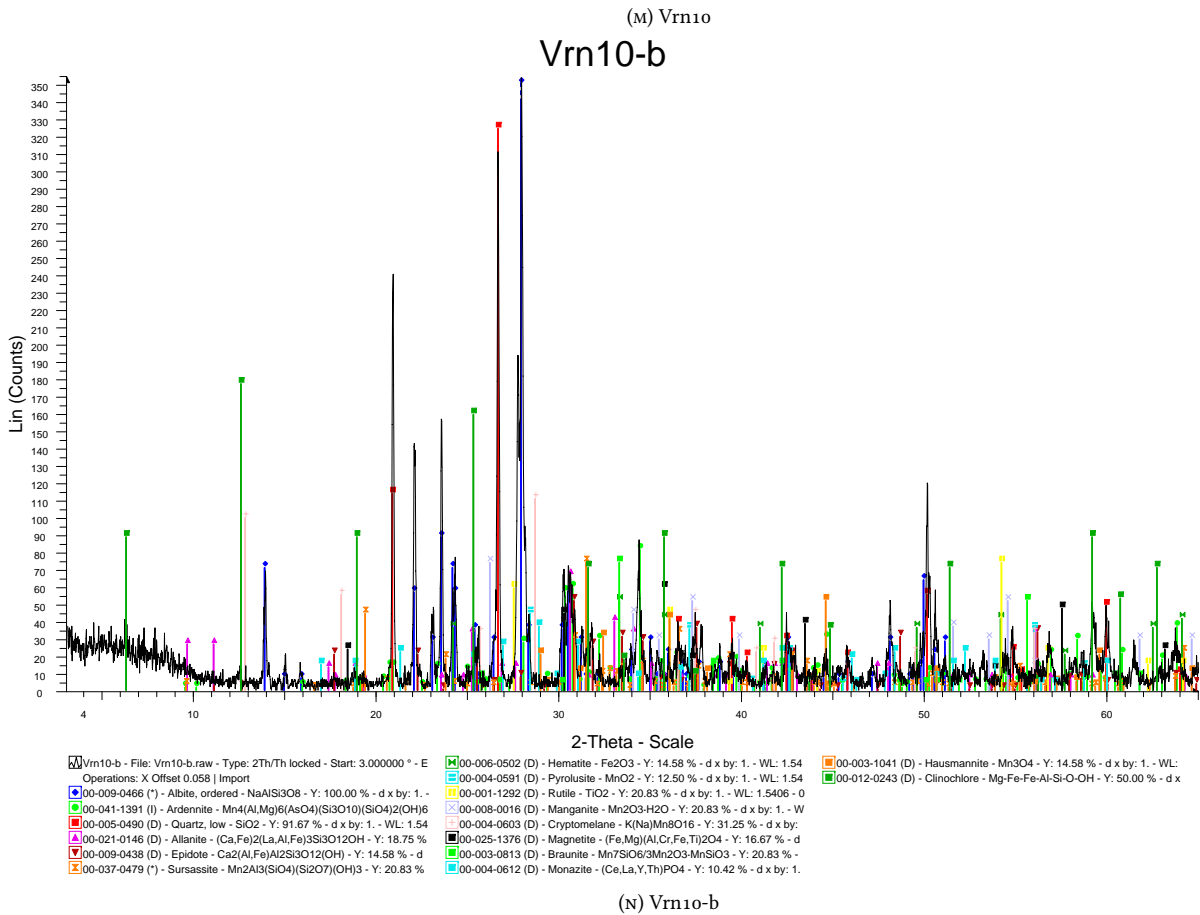
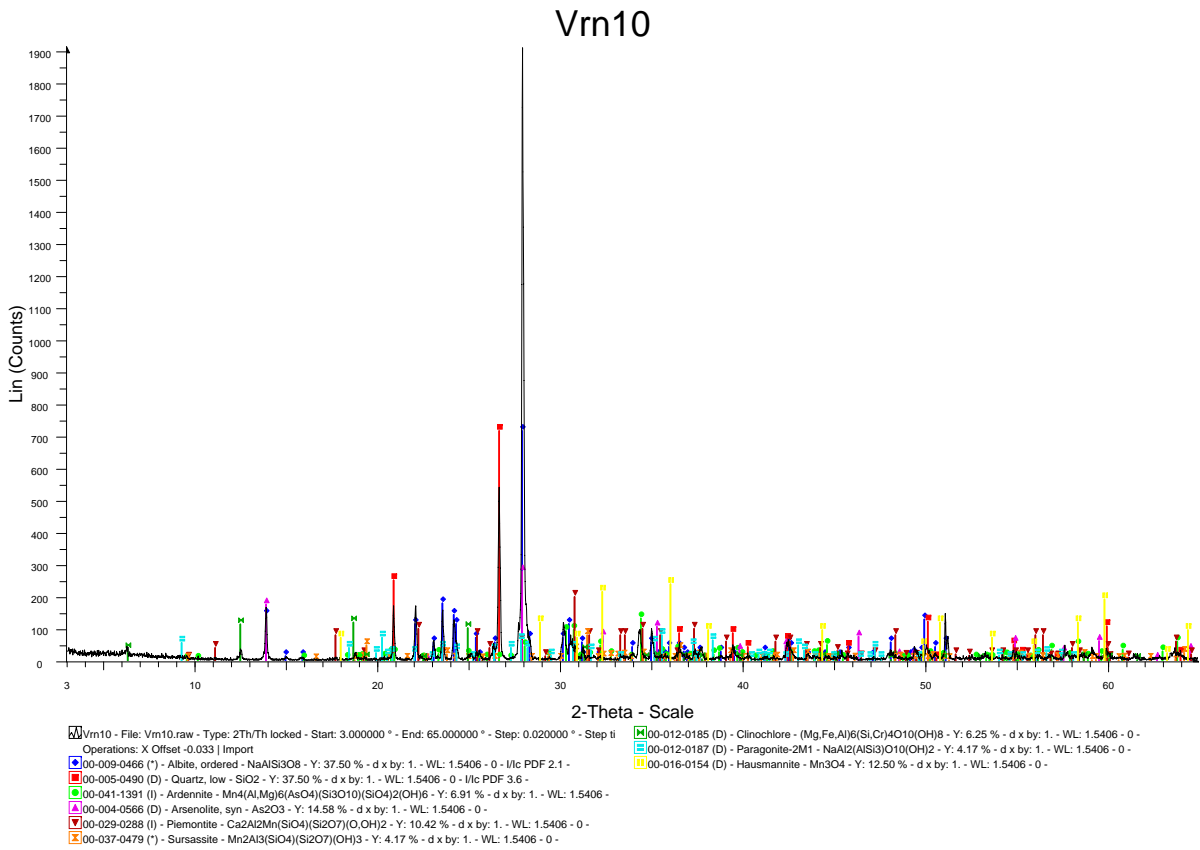


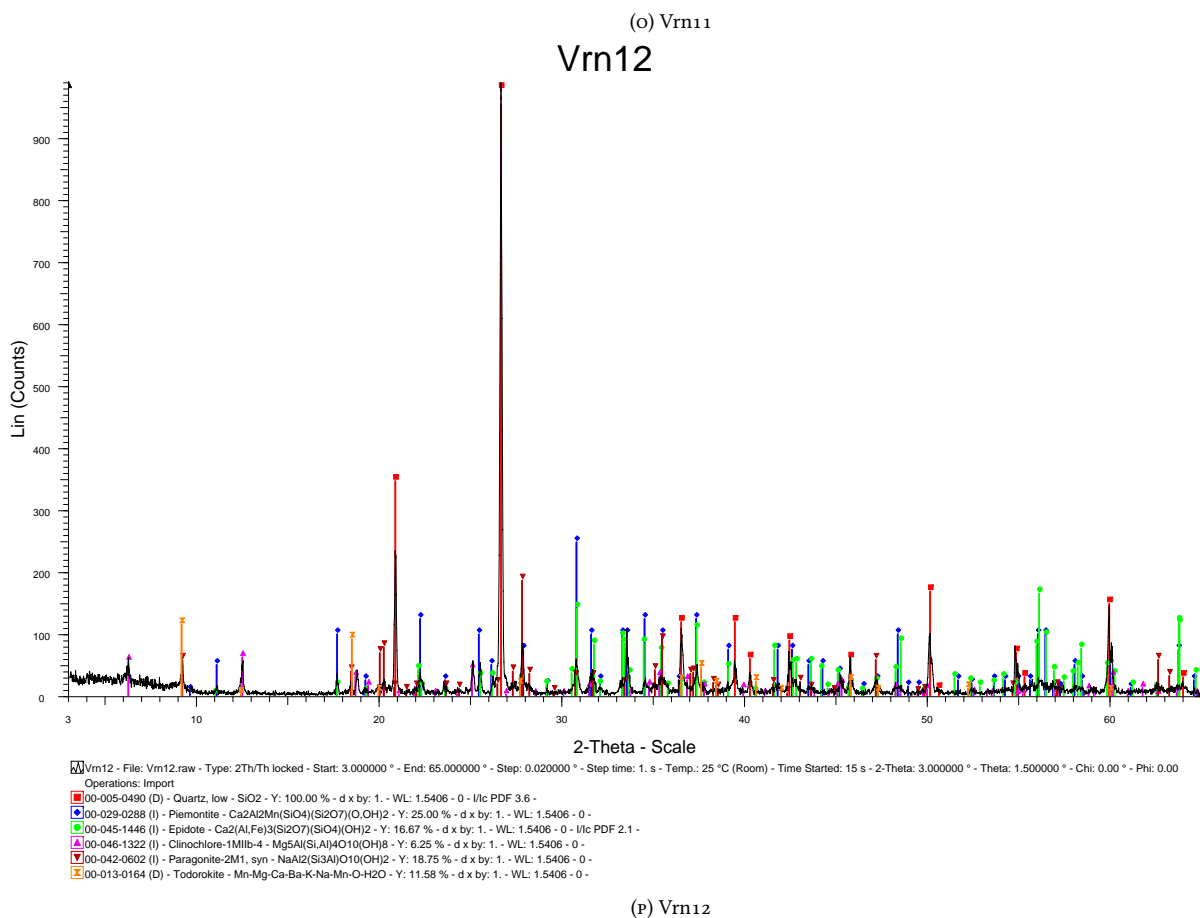
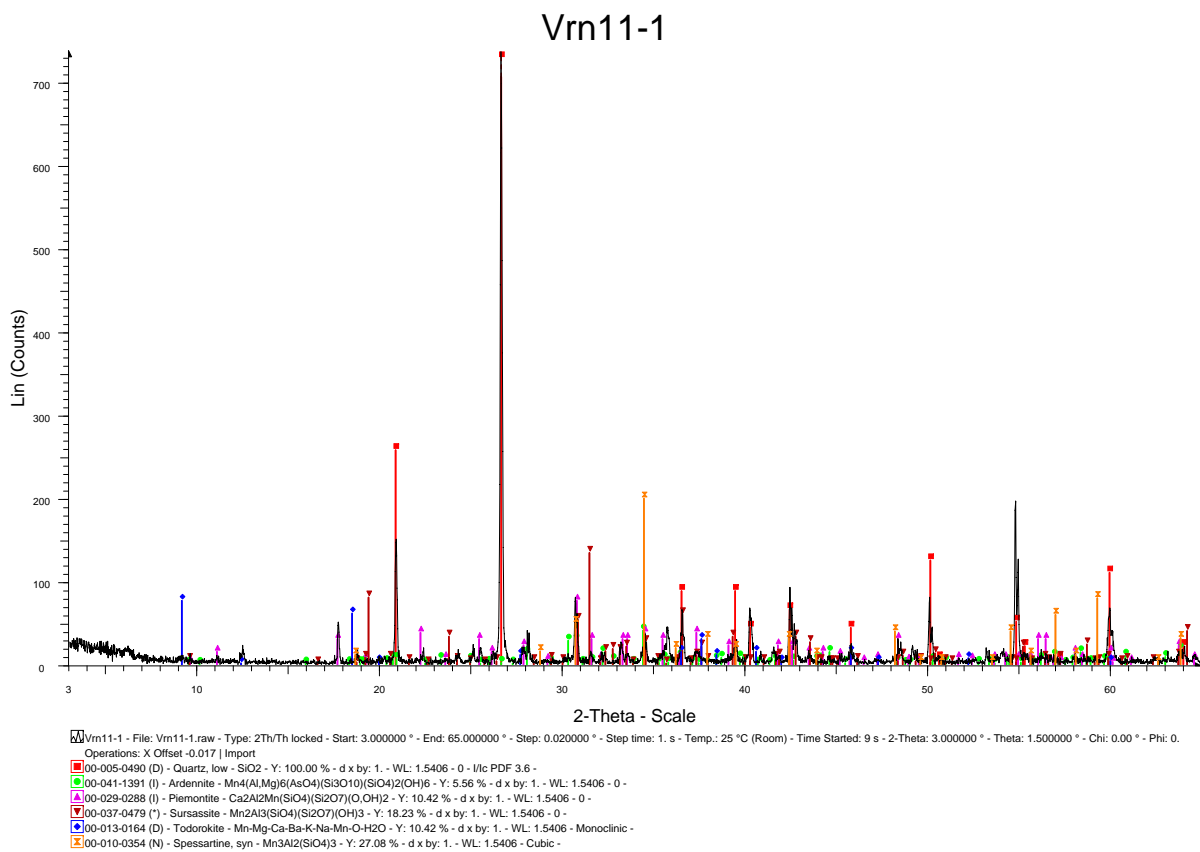
(i) Vrn7-2



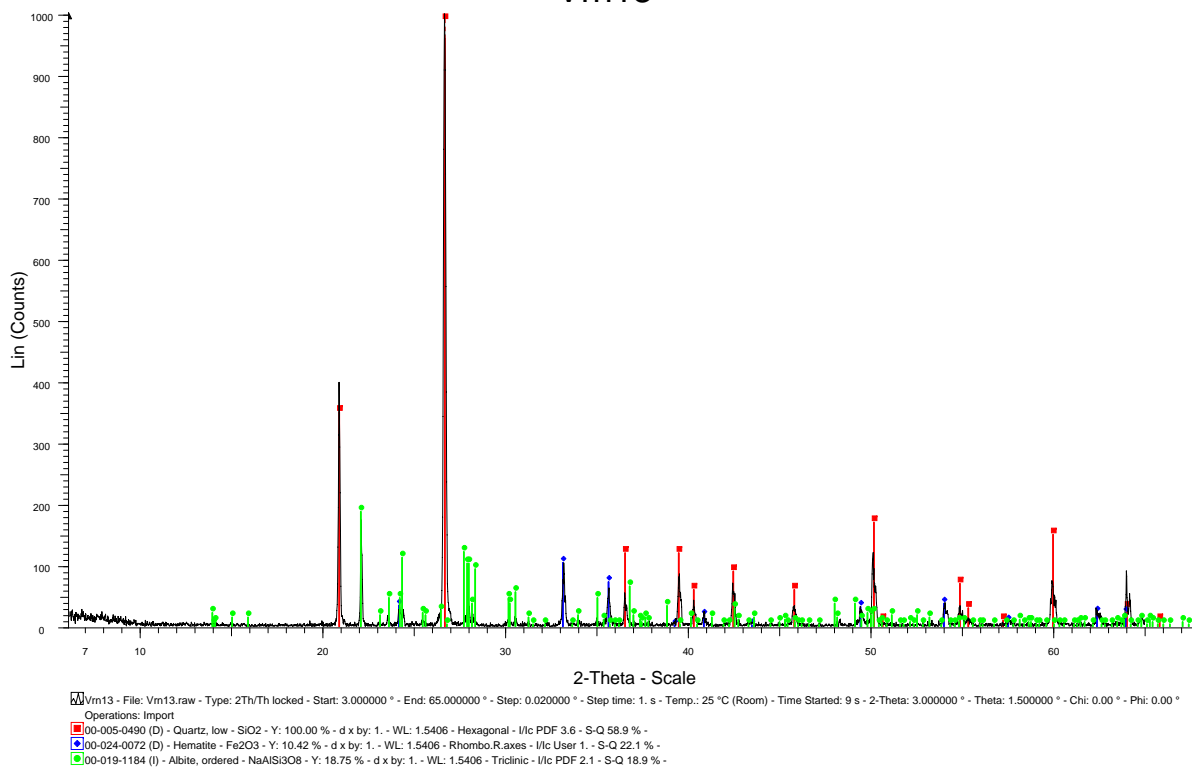
(j) Vrn7-3





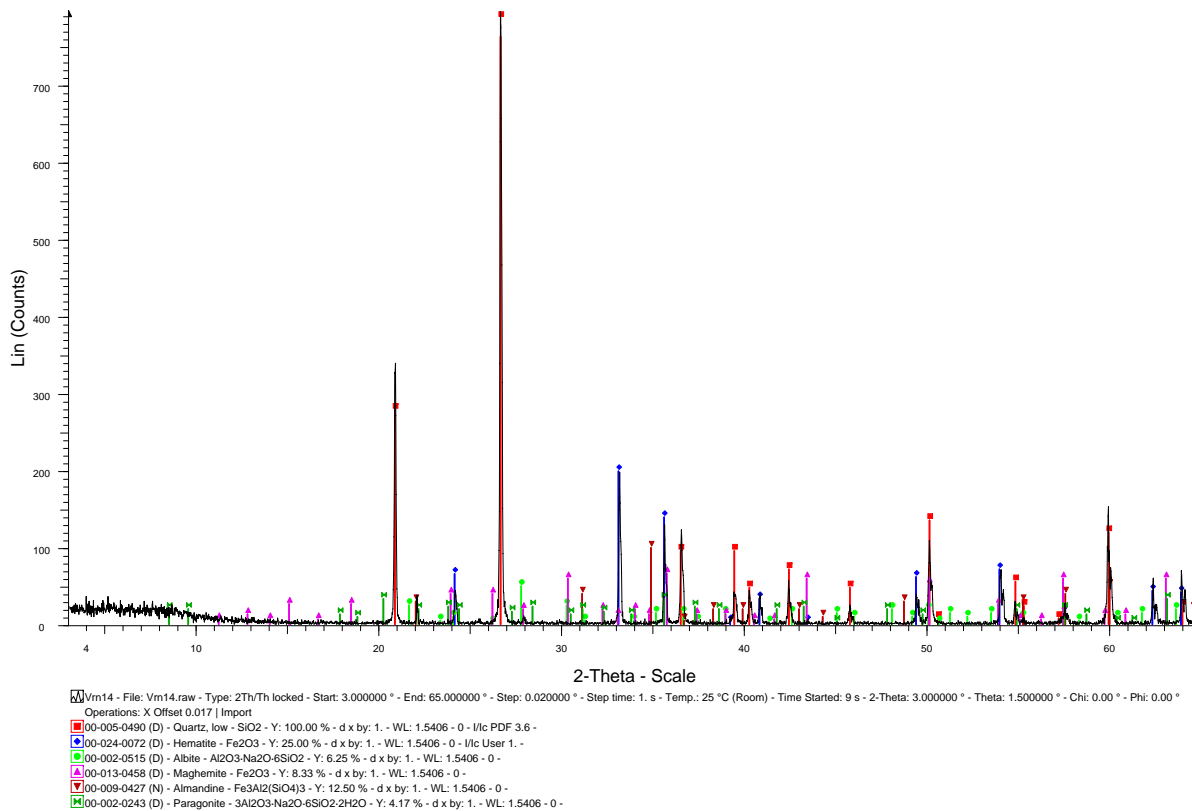


Vrn13

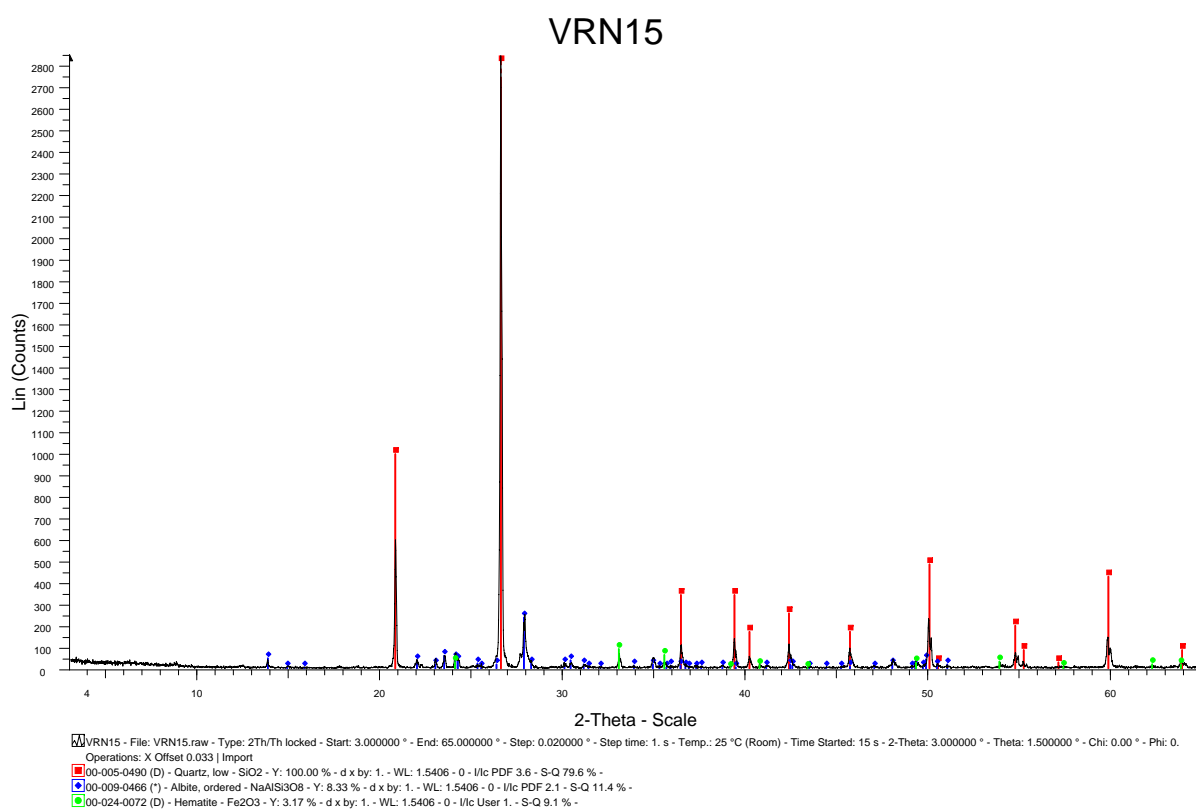


(Q) Vrn13

Vrn14



(R) Vrn14



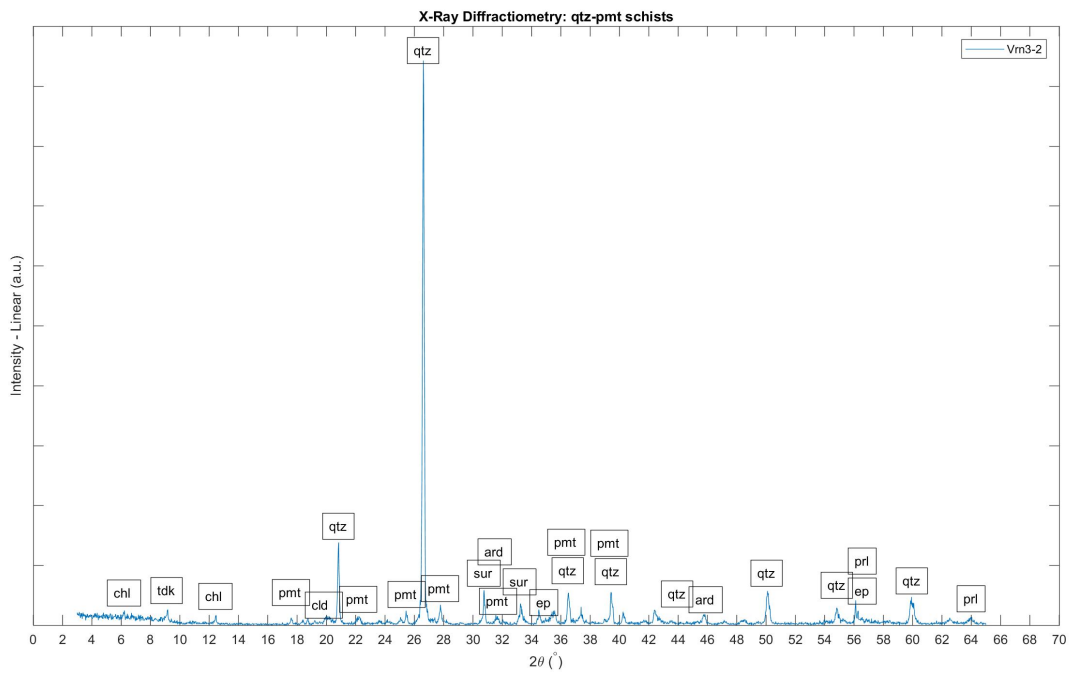
(s) Vrn15

FIGURE B.1: EVA processed XRD data.

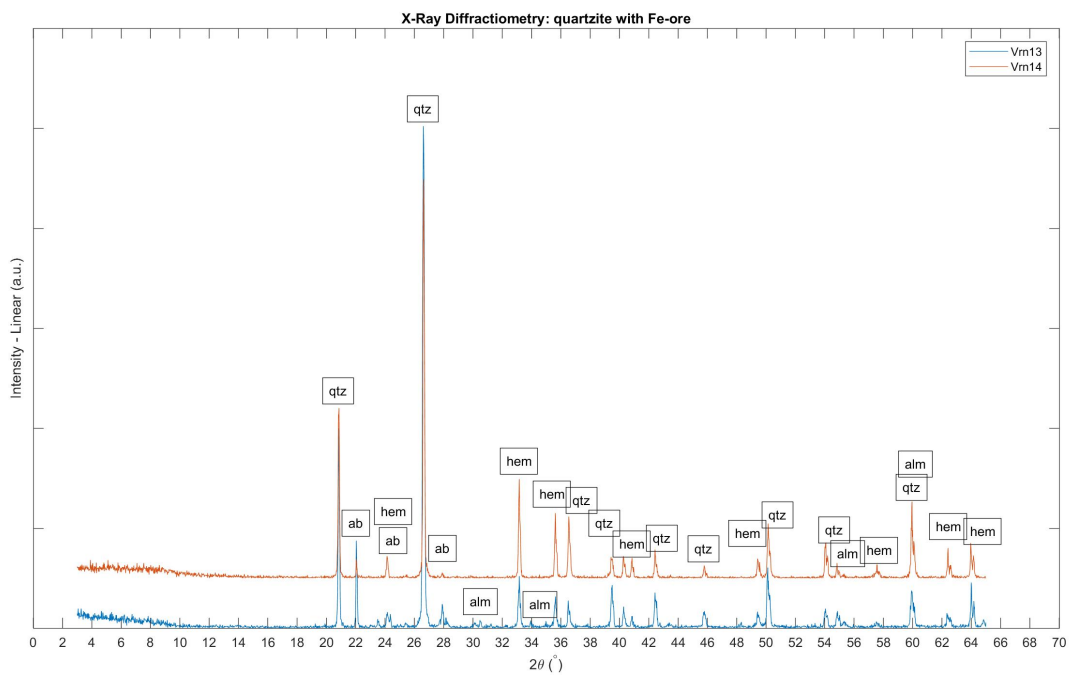
Appendix C

MATLAB processed grouped XRD Patterns

The XRD patterns of the four main lithological types are presented in this Appendix.



(A)



(B)

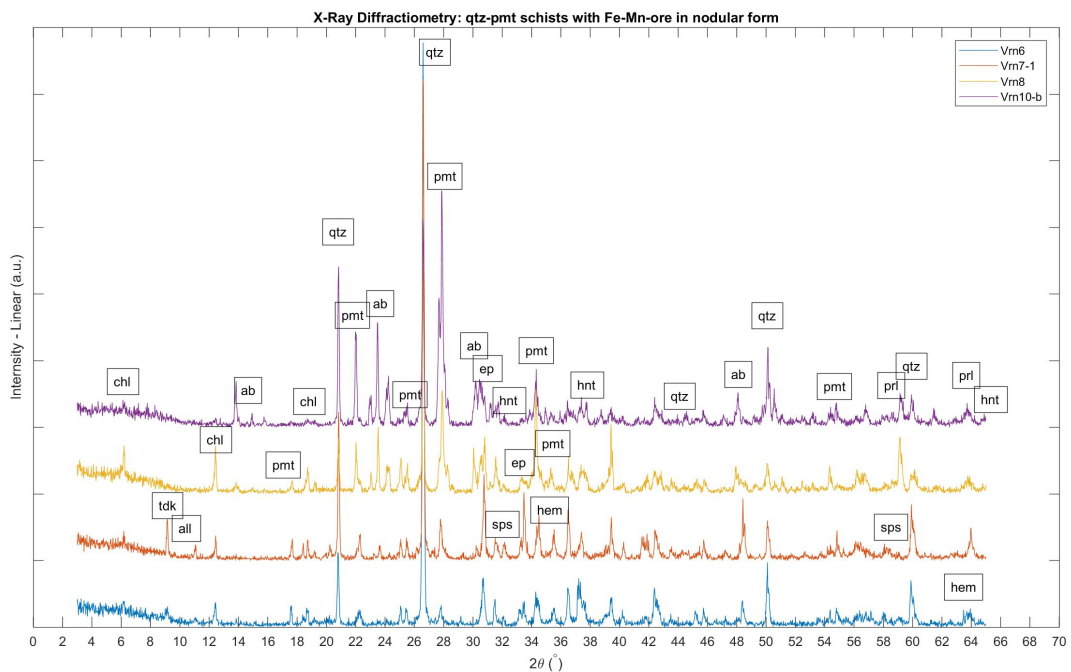
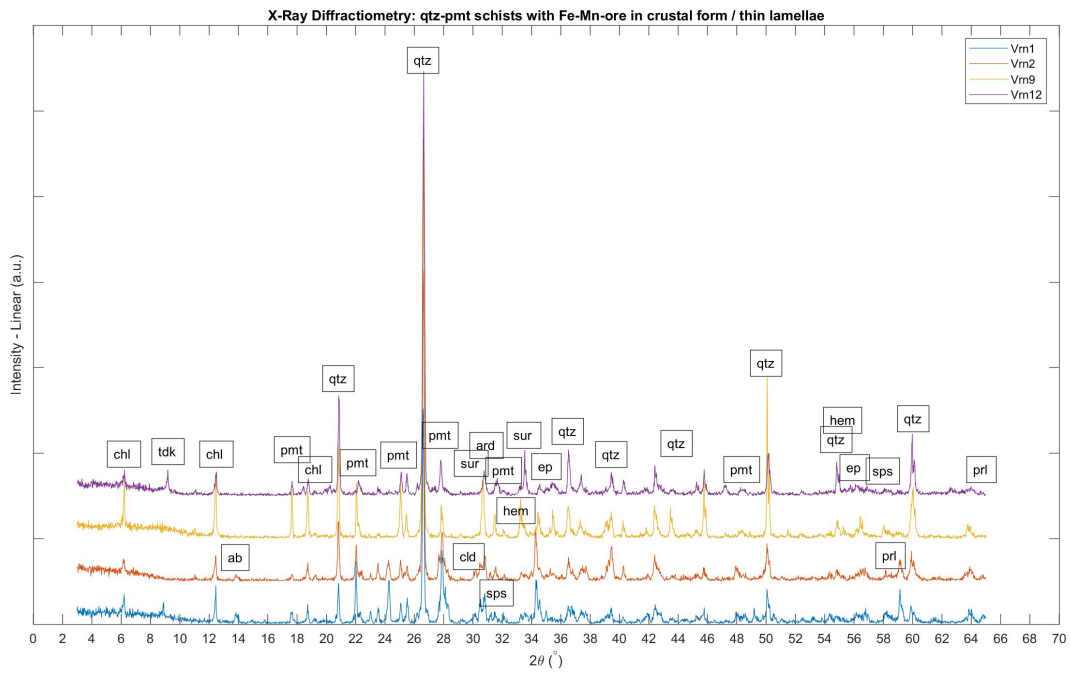
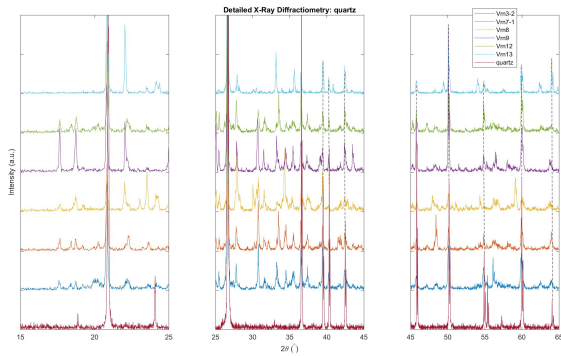


FIGURE C.1: Graphs of the XRD patterns. Grouped as: **(A)** XRD patterns of the Mn-rich host rock, **(B)** XRD patterns of the Fe-rich host rock and Fe-ore enrichment, **(C)** XRD patterns of Mn(\pm Fe)-ore in crustal form, **(D)** XRD patterns of Mn(\pm Fe)-ore in nodular form.

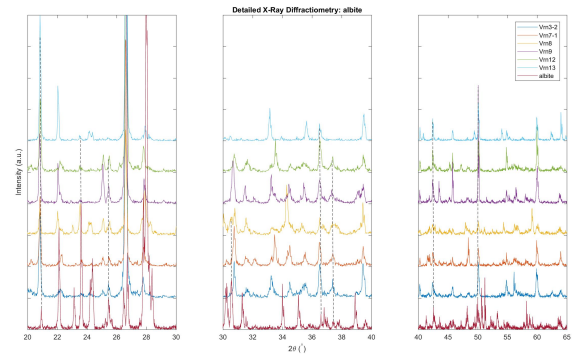
Appendix D

Additional XRD graphs

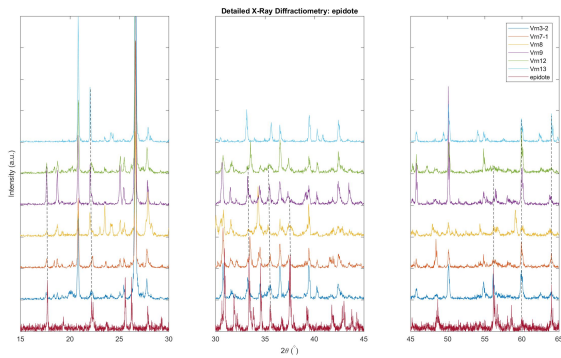
The main focus regarding Mineralogy and Mineral Chemistry in the present thesis, as mentioned in Sec. 3.2, is of the Mn(\pm Fe)-bearing ore minerals and some rock-forming ones. This Appendix contains data regarding the non-Mn-bearing silicate minerals and some other types of minerals.



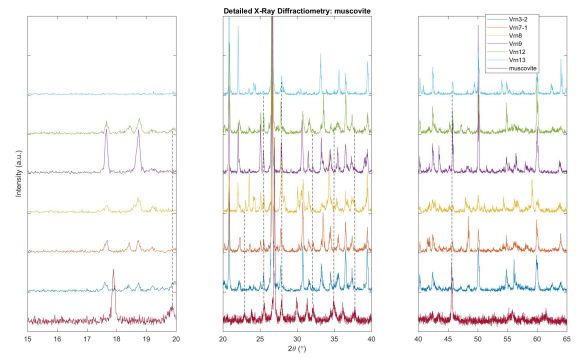
(A) Detailed XRD peak identification of quartz.



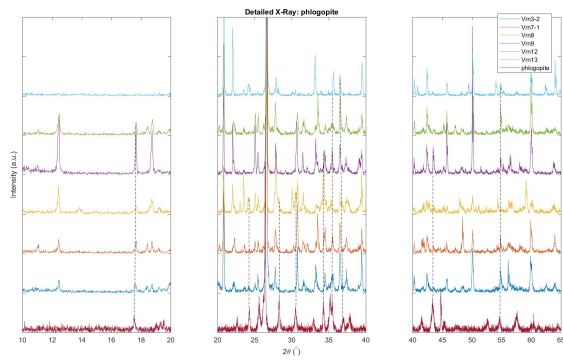
(B) Detailed XRD peak identification of albite.



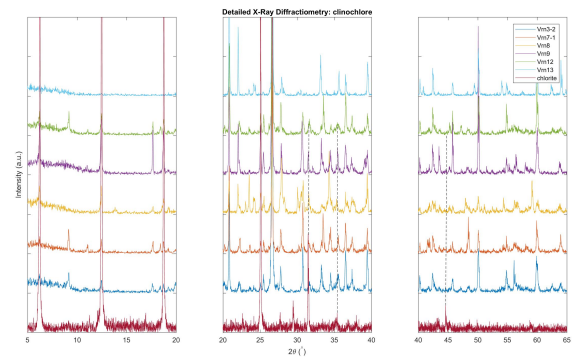
(c) Detailed XRD peak identification of epidote.



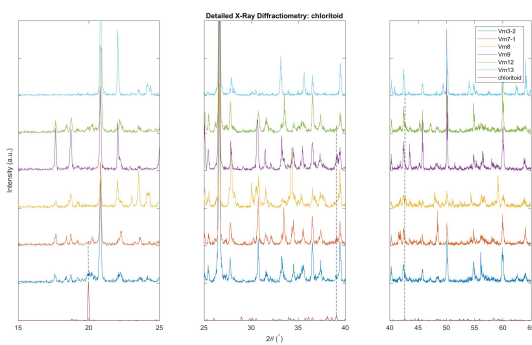
(b) Detailed XRD peak identification of muscovite/paragonite.



(E) Detailed XRD peak identification of phlogopite.



(F) Detailed XRD peak identification of clinochlore (chlorite).



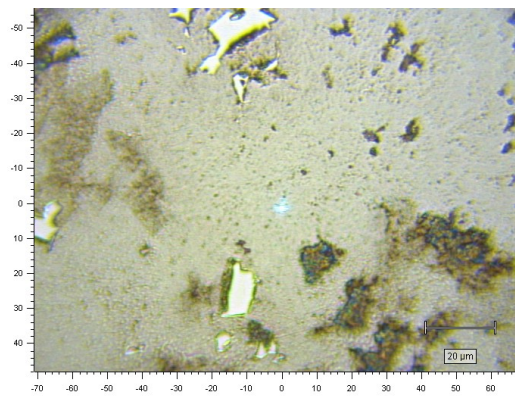
(G) Detailed XRD peak identification of chloritoid.

FIGURE D.1: Detailed XRD peak identification of non-Mn-bearing rock-forming minerals.

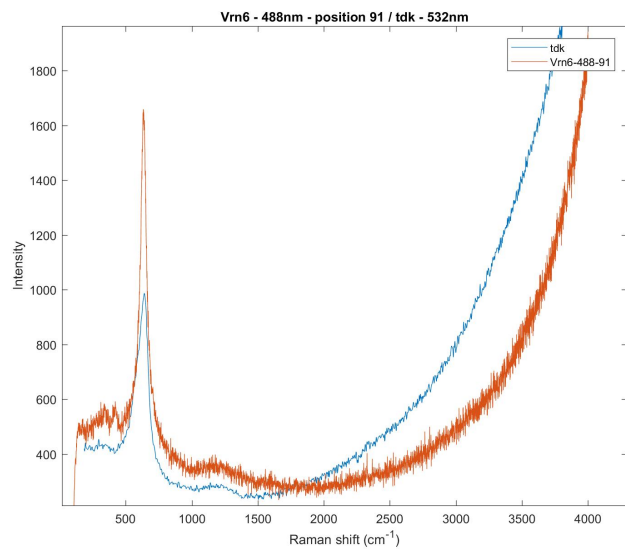
Appendix E

Raman Shift Graphs

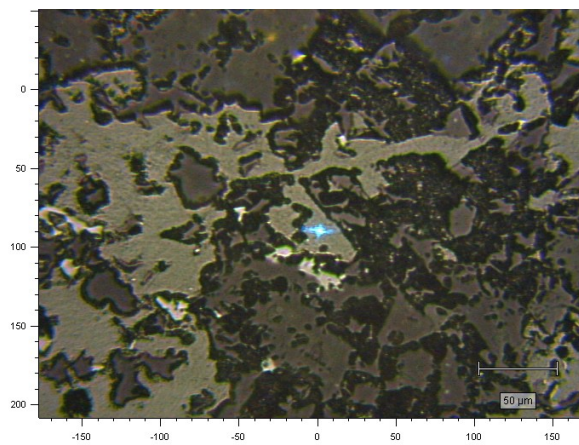
This appendix provides the confocal microphotographs and the Raman shift diagrams for the mineralogical research.



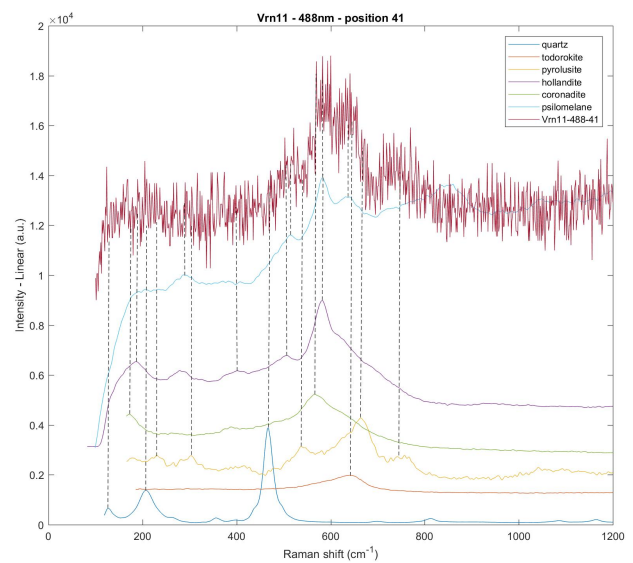
(A)



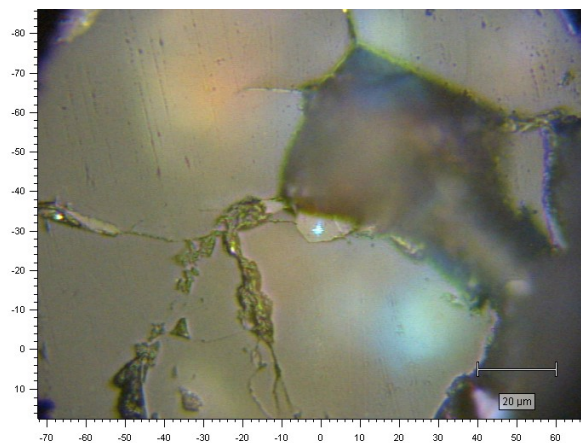
(B)



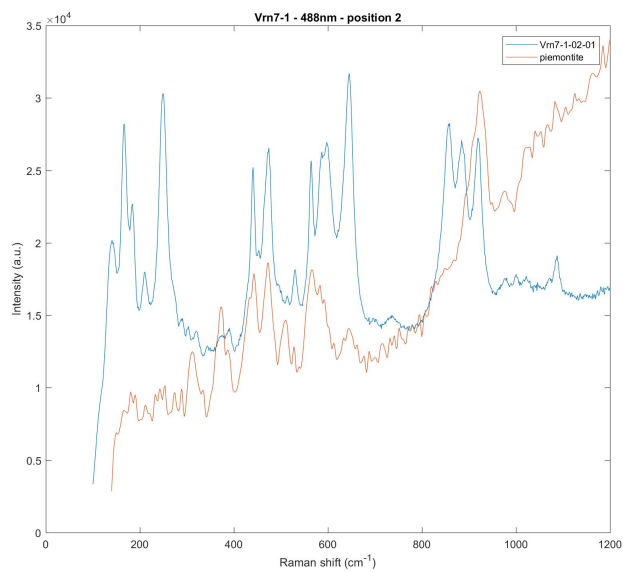
(C)



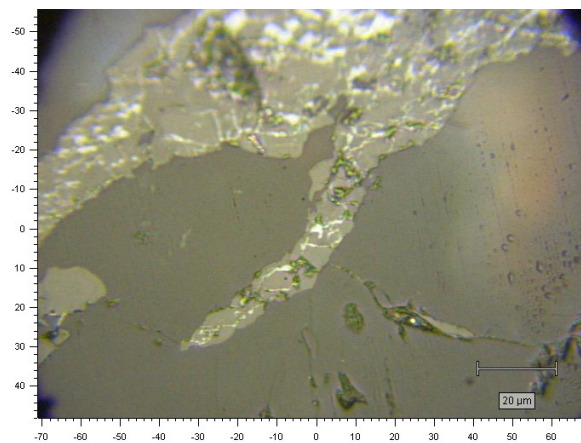
(D)



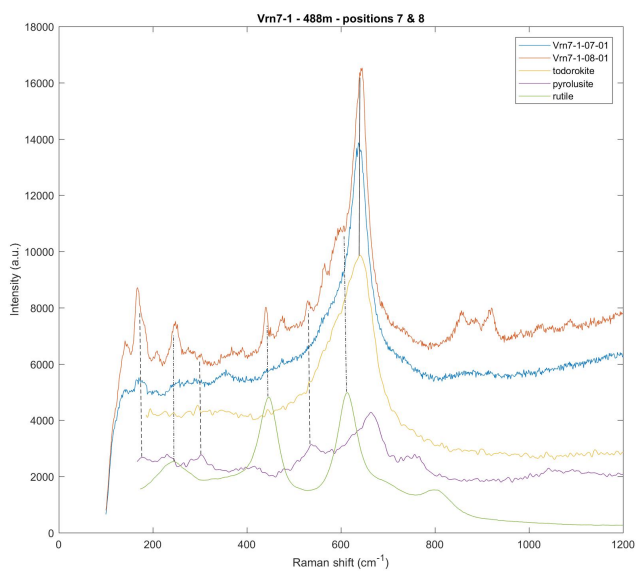
(E)



(F)



(G)



(H)

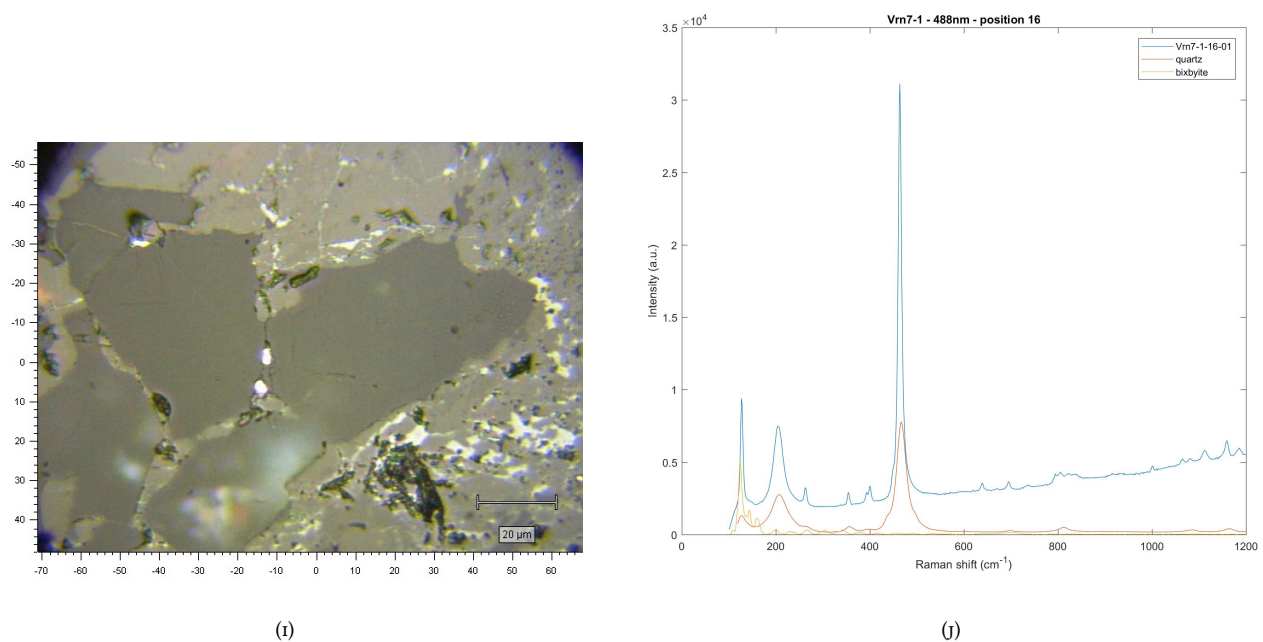
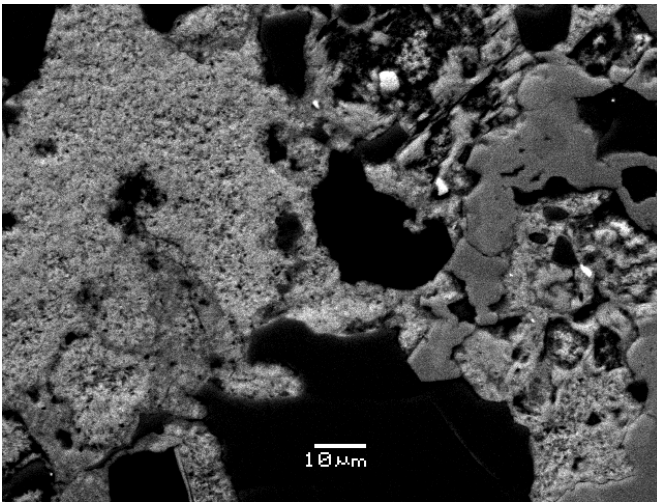


FIGURE E.1: Micro-photographs (confocal microscopy and reflected light) and Raman shift graphs. **(A)** Micro-photograph of a todorokite tubular net, **(B)** Perfect fit of raman vibrational spectrum of sample todorokite relatively to standard. The two minor peaks at the left of the todorokite peak may be of bixbyite due to the inversion of the peak-intensity and better fitting, **(C)** Microphotograph of a todorokite – pyrolusite – hollandite group net, **(D)** Multiple peak fit of quartz, todorokite, pyrolusite, hollandite, psilomelane, coronadite (hollandite group), **(E)** Microphotograph of piemontite and quartz, **(F)** Multiple peak fit of piemontite, **(G)** Microphotograph of a vein-form filled with Mn- and Ti-oxides, **(H)** Multiple peak fit of todorokite, pyrolusite and rutile, **(I)** Microphotograph of quartz surrounded by bixbyite, **(J)** Multiple peak fit of quartz and bixbyite (the higher peak inversion in contrast to quartz asserts the bixbyite presence).

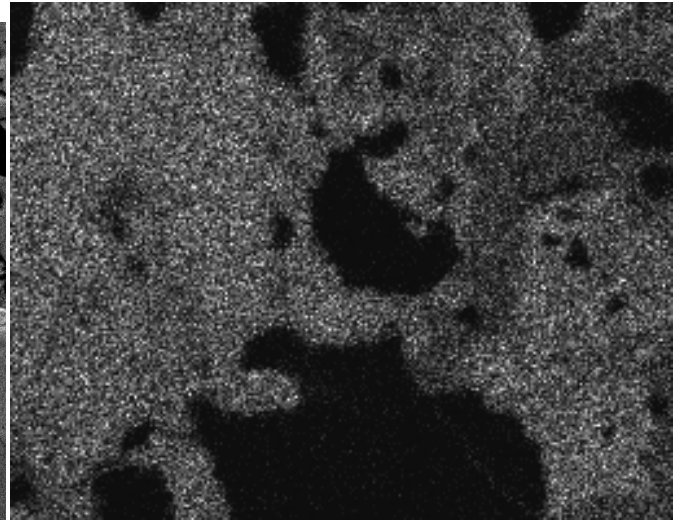
Appendix F

SEM-EDS mappings

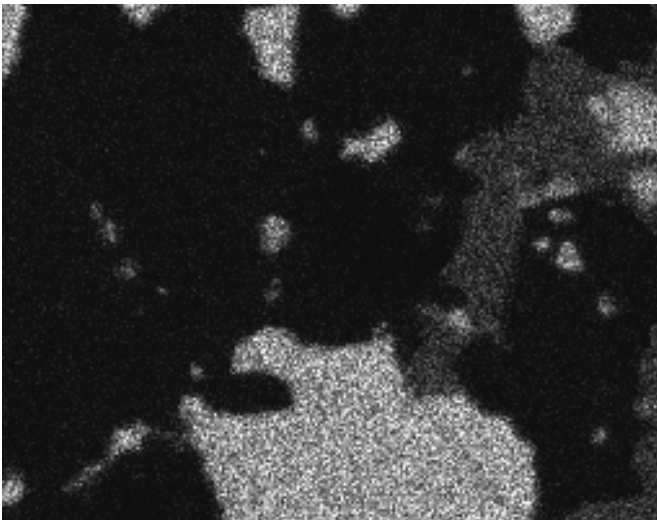
This appendix provides characteristic SEM-EDS mappings.



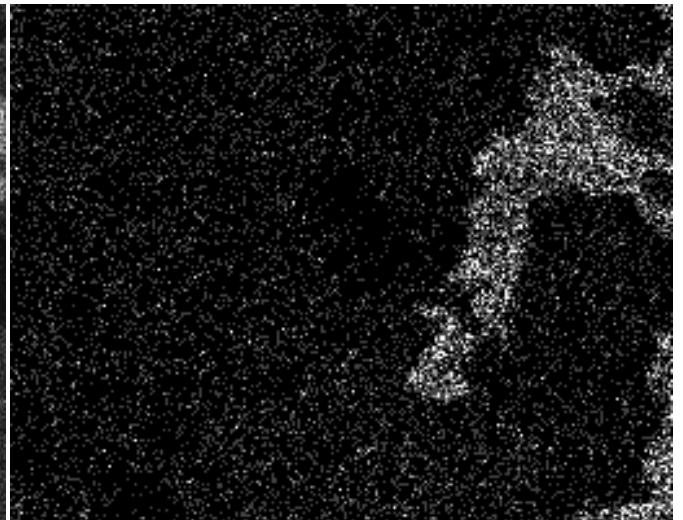
(A) BSE image



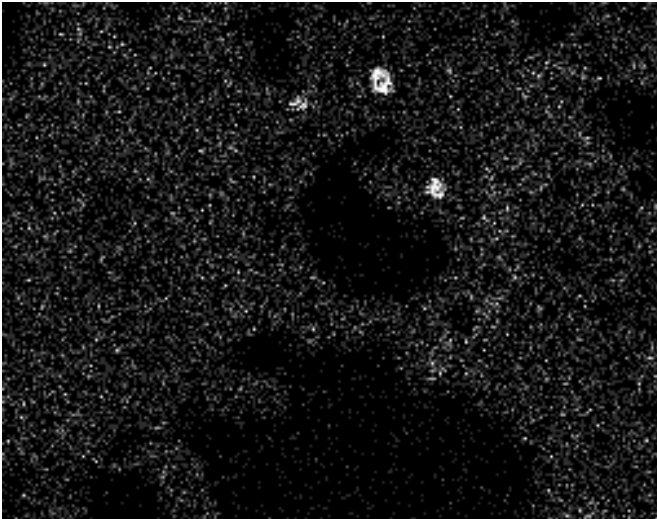
(B) Mn



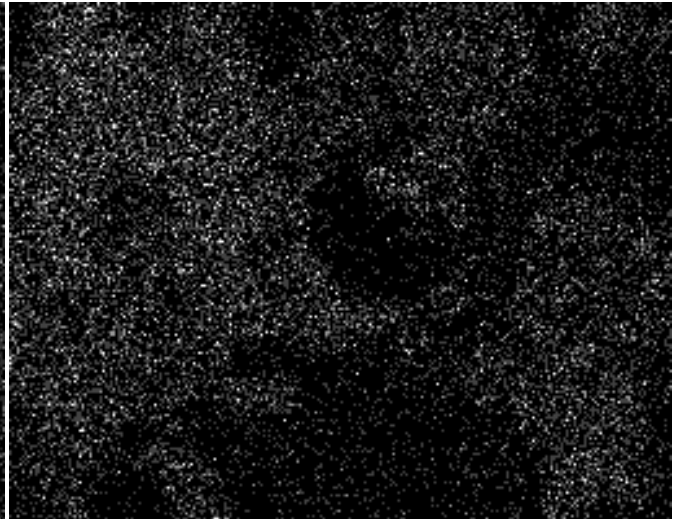
(C) Si



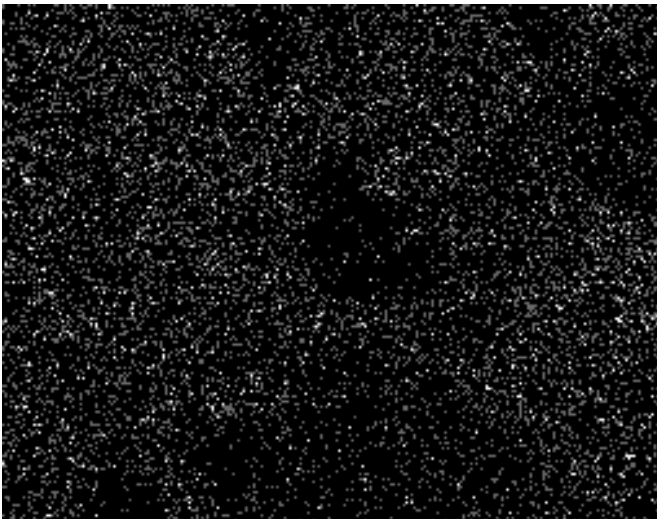
(D) Al



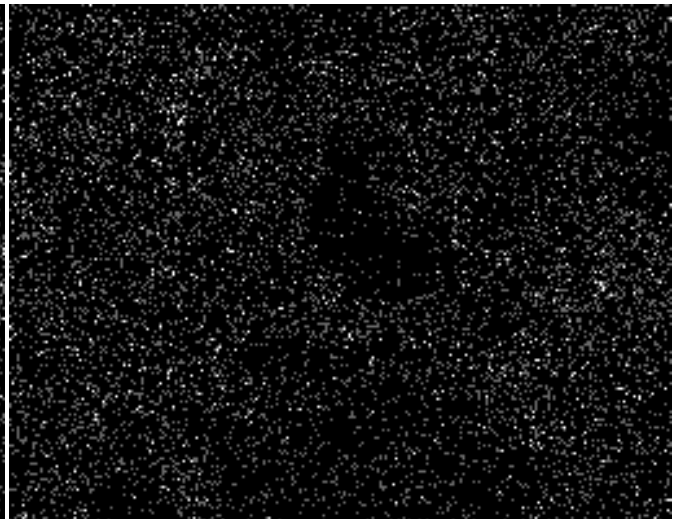
(E) Fe



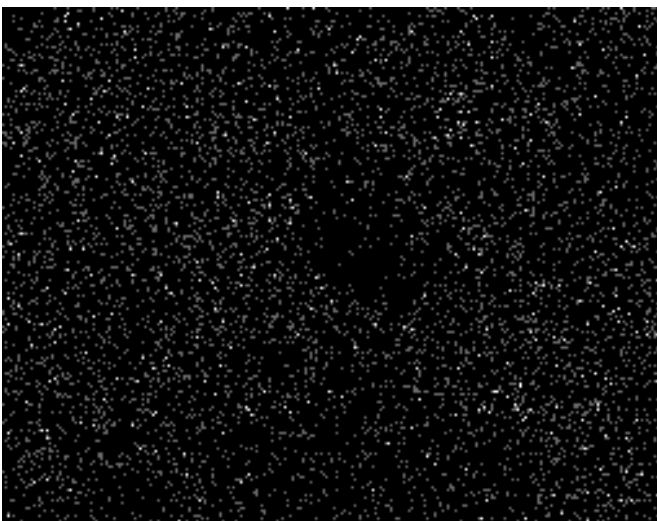
(F) K



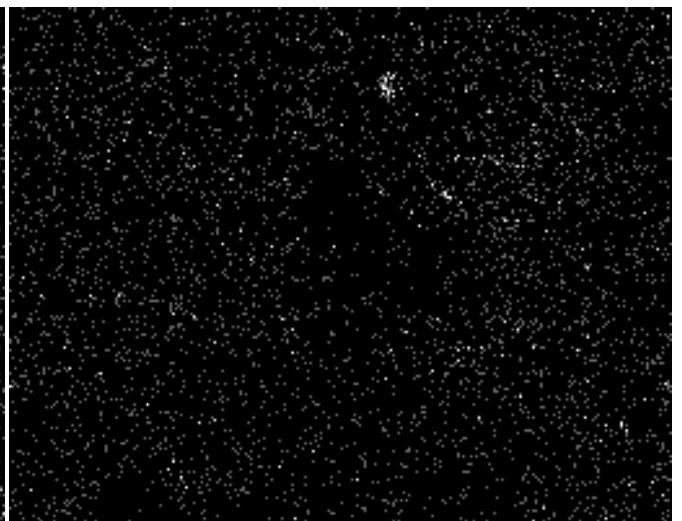
(G) Ba



(H) Ce



(I) La



(J) Gd

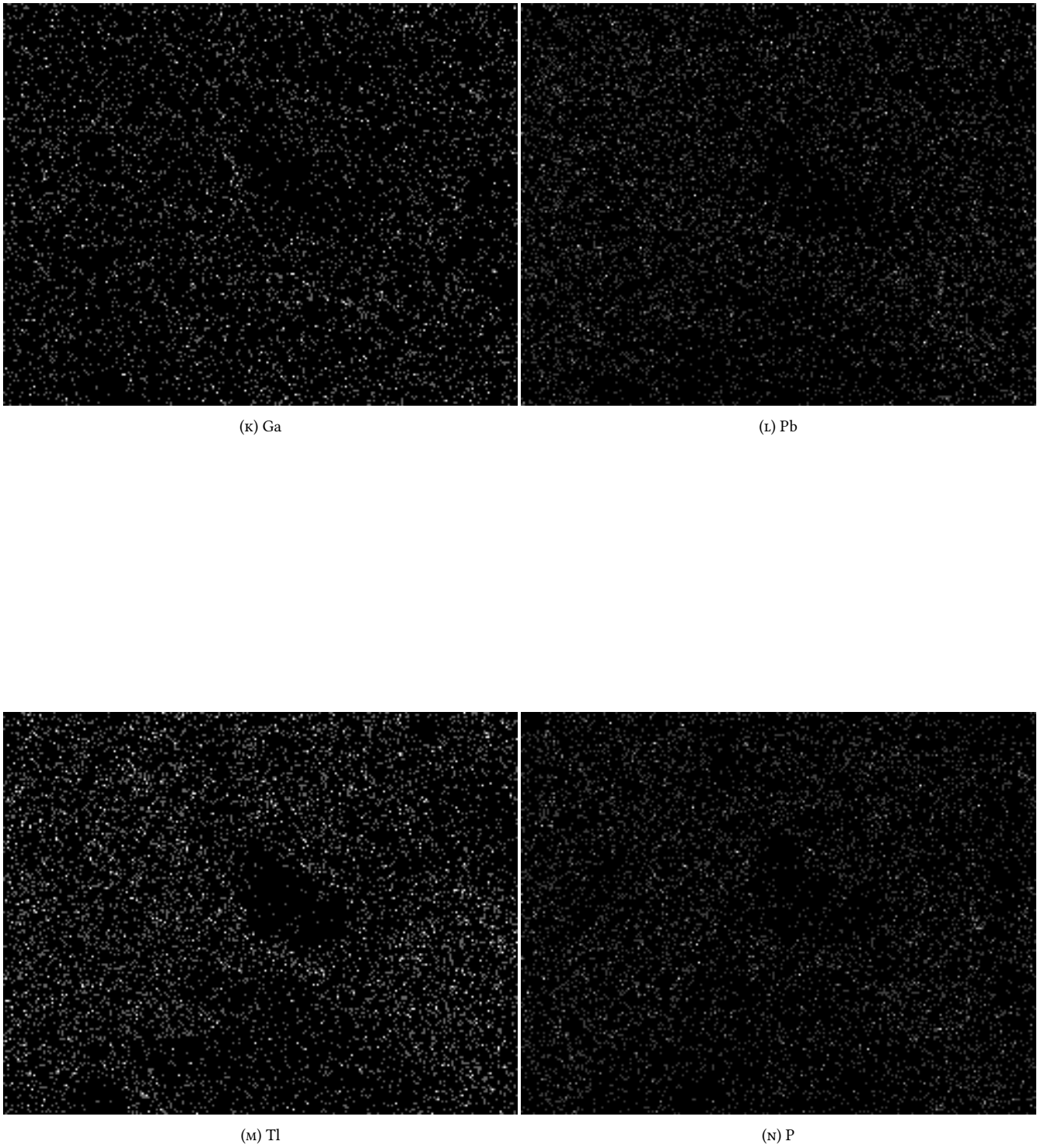
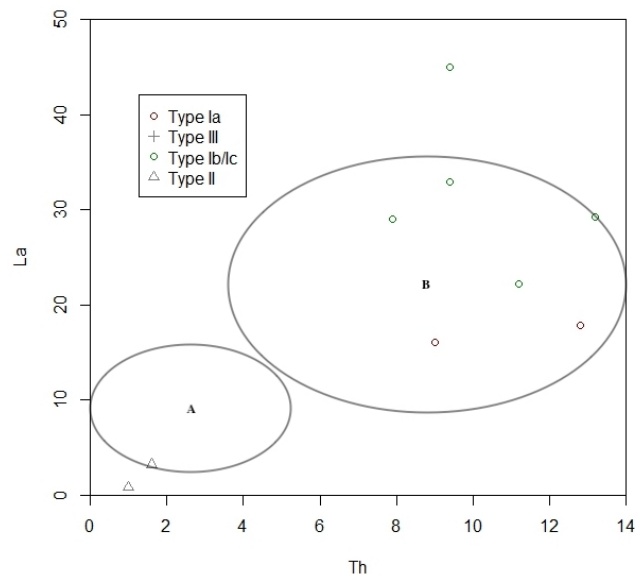


FIGURE F.1: SEM-EDS elemental mapping.

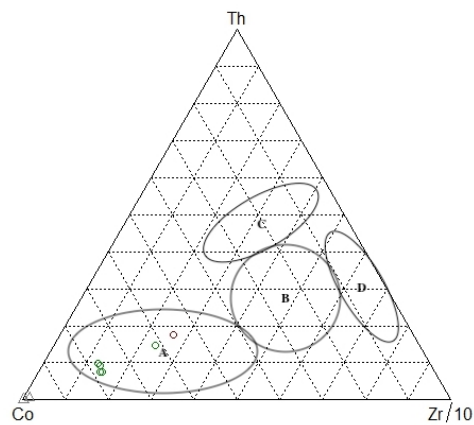
Appendix G

Geotectonic Classification Diagrams

In this appendix are contained some geotectonic binary and ternary classification diagrams. These are the following:



(A) Binary diagram Th vs La.



(B) Ternary diagram Co-Th-Zr.

FIGURE G.1: Binary and ternary geotectonic classification diagrams [Bhatia and Crook, 1986]. Abbreviations: **A** ocean island arc, **B** continental island arc, **C** active continental margin, **D** passive margin.

Appendix H

Correlation Matrix

This appendix provides the correlation matrix for the Type I lithotype and its associated ore mineralization. The correlation matrix for the Type II lithotype lacks statistical validity, due to the fact that there are not enough samples.

The matrix cells have the following form:

$$\frac{\textit{Pearson}(X_i, X_j)}{p - \textit{value}}$$

where $\textit{Pearson}(X_i, X_j)$ is the Pearson correlation coefficient between the chemical elements X_i and X_j . The statistically significant correlation coefficients are those with $p - \textit{value} < 0.05$. We have in bold font these coefficients.

Correlation Matrix (Pearson Coefficient): qtz-pmt-schists / Mn-ore

	Si	Ti	Al	Fe	Mn	Mg	Ca	Na	K	P	Rb
Ti	0.559 0.093										
Al	0.546 0.102	0.967 0.000									
Fe	0.402 0.249	0.281 0.431	0.257 0.474								
Mn	-0.776 0.008	-0.836 0.003	-0.803 0.005	-0.610 0.061							
Mg	0.132 0.717	0.394 0.260	0.242 0.500	-0.378 0.281	-0.044 0.903						
Ca	-0.407 0.243	-0.243 0.499	-0.270 0.450	-0.548 0.101	0.602 0.065	0.390 0.266					
Na	0.601 0.066	0.897 0.000	0.908 0.000	0.040 0.913	-0.715 0.020	0.473 0.168	-0.267 0.456				
K	0.495 0.145	0.720 0.019	0.783 0.007	0.670 0.034	-0.830 0.003	-0.281 0.432	-0.445 0.197	0.555 0.096			
P	-0.449 0.193	-0.400 0.252	-0.418 0.229	-0.413 0.236	0.604 0.064	0.192 0.596	0.370 0.292	-0.409 0.241	-0.623 0.054		
Rb	0.583 0.077	0.727 0.017	0.781 0.008	0.742 0.014	-0.872 0.001	-0.251 0.484	-0.569 0.086	0.590 0.073	0.975 0.000	-0.591 0.072	
Cs	0.189 0.600	0.591 0.072	0.657 0.039	0.435 0.209	-0.620 0.056	-0.208 0.564	-0.359 0.309	0.481 0.159	0.794 0.006	-0.692 0.027	0.722 0.018
Be	0.087 0.812	0.499 0.142	0.387 0.269	0.221 0.540	-0.401 0.250	0.145 0.689	0.031 0.933	0.191 0.597	0.307 0.388	-0.356 0.312	0.252 0.482
Sr	-0.740 0.015	-0.543 0.105	-0.583 0.077	-0.033 0.928	0.545 0.103	-0.192 0.595	0.385 0.272	-0.631 0.050	-0.248 0.490	0.031 0.933	-0.351 0.320
Ba	-0.703 0.023	-0.713 0.021	-0.693 0.026	0.111 0.760	0.598 0.068	-0.485 0.155	0.216 0.548	-0.782 0.008	-0.241 0.503	0.086 0.813	-0.301 0.398
Zr	-0.307 0.387	0.425 0.221	0.420 0.227	-0.210 0.559	-0.097 0.789	0.287 0.422	0.267 0.455	0.282 0.429	0.217 0.547	0.096 0.793	0.085 0.816
Hf	-0.272 0.447	0.466 0.174	0.467 0.173	-0.198 0.583	-0.126 0.729	0.305 0.392	0.257 0.473	0.333 0.347	0.247 0.492	0.079 0.827	0.120 0.740
V	-0.238 0.509	-0.088 0.808	-0.003 0.993	-0.685 0.029	0.370 0.293	0.143 0.693	0.132 0.717	0.070 0.848	-0.422 0.224	0.676 0.032	-0.404 0.247
Nb	-0.112 0.759	0.600 0.067	0.667 0.035	-0.154 0.671	-0.228 0.527	0.256 0.475	0.165 0.648	0.542 0.106	0.402 0.249	-0.018 0.961	0.306 0.390
Ta	-0.135 0.710	0.511 0.132	0.470 0.171	-0.080 0.825	-0.238 0.508	0.325 0.359	0.231 0.521	0.308 0.386	0.267 0.455	-0.011 0.976	0.147 0.686
Cr	-0.269 0.452	-0.708 0.022	-0.782 0.008	-0.053 0.884	0.647 0.043	0.062 0.864	0.472 0.169	-0.700 0.024	-0.670 0.034	0.315 0.376	-0.633 0.050
Mo	-0.605 0.064	-0.097 0.790	-0.123 0.735	-0.305 0.391	0.279 0.434	0.111 0.759	0.390 0.265	-0.161 0.657	-0.057 0.875	0.186 0.606	-0.209 0.562
W	0.595 0.069	-0.124 0.733	-0.200 0.579	0.523 0.121	-0.284 0.427	-0.164 0.651	-0.311 0.382	-0.152 0.676	0.050 0.892	-0.334 0.346	0.162 0.654
Co	0.032 0.930	-0.226 0.530	-0.275 0.442	-0.610 0.061	0.335 0.344	0.469 0.171	0.161 0.658	0.091 0.803	-0.609 0.061	0.235 0.514	-0.531 0.114

Ni	-0.265 0.459	-0.081 0.825	-0.153 0.673	-0.246 0.494	0.384 0.273	0.480 0.160	0.769 0.009	-0.072 0.843	-0.254 0.478	0.094 0.796	-0.306 0.390
Cu	-0.451 0.191	-0.547 0.101	-0.600 0.066	0.236 0.512	0.525 0.119	-0.153 0.672	0.391 0.263	-0.693 0.026	-0.335 0.344	0.146 0.687	-0.329 0.353
Zn	0.211 0.558	-0.117 0.748	-0.244 0.497	-0.491 0.149	0.168 0.643	0.666 0.036	0.210 0.560	0.129 0.722	-0.573 0.083	0.159 0.660	-0.505 0.136
Cd	-0.089 0.806	0.341 0.335	0.488 0.153	-0.028 0.938	-0.149 0.681	-0.153 0.674	0.137 0.706	0.396 0.257	0.567 0.088	-0.352 0.319	0.452 0.190
Hg	0.012 0.973	-0.297 0.405	-0.266 0.458	0.008 0.982	0.343 0.332	0.058 0.874	0.540 0.107	-0.195 0.589	-0.126 0.728	-0.024 0.947	-0.133 0.713
Ga	0.165 0.649	0.794 0.006	0.813 0.004	-0.204 0.571	-0.476 0.164	0.404 0.247	0.005 0.989	0.768 0.009	0.460 0.181	-0.087 0.811	0.389 0.267
Tl	-0.257 0.474	-0.344 0.331	-0.203 0.574	-0.346 0.327	0.443 0.200	-0.357 0.312	0.096 0.791	-0.308 0.387	-0.322 0.365	0.558 0.094	-0.311 0.382
Ge	0.672 0.033	0.552 0.098	0.558 0.094	0.232 0.520	-0.591 0.072	0.166 0.647	-0.508 0.134	0.552 0.098	0.286 0.423	0.083 0.820	0.417 0.230
Sn	0.448 0.194	0.058 0.874	0.115 0.751	0.339 0.337	-0.187 0.605	-0.112 0.757	-0.358 0.309	0.226 0.530	0.153 0.674	-0.260 0.468	0.311 0.382
Pb	-0.380 0.279	-0.627 0.052	-0.685 0.029	0.198 0.583	0.446 0.197	-0.302 0.397	0.421 0.226	-0.799 0.006	-0.243 0.499	0.034 0.927	-0.321 0.366
As	-0.307 0.388	-0.285 0.424	-0.142 0.695	-0.533 0.112	0.439 0.204	-0.279 0.435	0.153 0.673	-0.219 0.543	-0.329 0.354	0.532 0.114	-0.362 0.304
Sb	-0.219 0.544	-0.071 0.845	0.038 0.917	-0.739 0.015	0.399 0.253	0.188 0.603	0.222 0.538	0.136 0.708	-0.419 0.228	0.565 0.089	-0.413 0.235
Bi	-0.209 0.561	-0.317 0.372	-0.195 0.590	-0.419 0.227	0.430 0.215	-0.281 0.432	0.103 0.777	-0.252 0.482	-0.377 0.283	0.455 0.186	-0.360 0.307
S	-0.194 0.591	-0.391 0.264	-0.429 0.216	0.430 0.215	0.091 0.802	-0.503 0.138	-0.029 0.937	-0.642 0.045	0.006 0.986	-0.219 0.542	-0.052 0.886
Se	*	*	*	*	*	*	*	*	*	*	*
Te	-0.498 0.143	-0.363 0.302	-0.334 0.346	-0.115 0.751	0.517 0.126	-0.133 0.715	0.668 0.035	-0.541 0.106	-0.175 0.628	0.588 0.074	-0.285 0.424
Th	0.020 0.956	0.685 0.029	0.647 0.043	-0.066 0.857	-0.461 0.180	0.298 0.404	0.078 0.830	0.524 0.120	0.493 0.148	-0.187 0.605	0.365 0.300
U	-0.475 0.166	-0.742 0.014	-0.751 0.012	0.240 0.505	0.564 0.089	-0.407 0.243	0.132 0.717	-0.783 0.007	-0.348 0.325	0.120 0.740	-0.319 0.370
La	-0.611 0.061	-0.194 0.591	-0.182 0.615	-0.342 0.333	0.298 0.402	-0.127 0.728	0.287 0.422	-0.302 0.397	-0.097 0.791	0.241 0.502	-0.265 0.459
Ce	-0.303 0.394	0.151 0.677	0.178 0.622	-0.011 0.976	-0.107 0.769	-0.169 0.640	0.125 0.732	-0.004 0.991	0.345 0.329	-0.213 0.555	0.166 0.646
Pr	-0.558 0.093	-0.084 0.818	-0.038 0.918	-0.353 0.317	0.238 0.508	-0.130 0.720	0.284 0.426	-0.180 0.619	0.000 0.999	0.212 0.557	-0.174 0.631
Nd	-0.558 0.094	-0.070 0.847	-0.030 0.935	-0.377 0.283	0.248 0.489	-0.085 0.816	0.321 0.366	-0.168 0.642	-0.020 0.956	0.244 0.497	-0.194 0.592
Pm	*	*	*	*	*	*	*	*	*	*	*
Sm	-0.532 0.114	-0.029 0.937	-0.001 0.997	-0.333 0.347	0.203 0.574	-0.036 0.921	0.302 0.397	-0.130 0.720	0.009 0.981	0.213 0.555	-0.161 0.657
Eu	-0.539 0.108	0.030 0.934	0.054 0.883	-0.342 0.333	0.181 0.618	0.004 0.992	0.297 0.405	-0.083 0.820	0.020 0.956	0.222 0.537	-0.146 0.687

Gd	-0.565 0.089	-0.014 0.969	0.003 0.994	-0.402 0.250	0.245 0.494	0.041 0.910	0.368 0.296	-0.121 0.739	-0.052 0.886	0.296 0.406	-0.219 0.543
Tb	-0.541 0.107	0.004 0.992	0.027 0.940	-0.382 0.275	0.217 0.547	0.009 0.981	0.353 0.316	-0.113 0.756	-0.018 0.961	0.261 0.466	-0.189 0.601
Dy	-0.542 0.106	0.056 0.878	0.073 0.841	-0.346 0.328	0.170 0.639	0.011 0.976	0.316 0.373	-0.079 0.829	0.028 0.940	0.212 0.556	-0.143 0.693
Ho	-0.488 0.152	0.126 0.729	0.148 0.682	-0.305 0.392	0.101 0.781	0.015 0.968	0.268 0.455	-0.014 0.969	0.085 0.815	0.170 0.638	-0.080 0.826
Er	-0.444 0.199	0.168 0.643	0.192 0.596	-0.246 0.493	0.037 0.920	-0.020 0.955	0.233 0.518	0.009 0.980	0.154 0.672	0.088 0.809	-0.016 0.966
Tm	-0.350 0.321	0.224 0.533	0.250 0.487	-0.141 0.698	-0.068 0.852	-0.053 0.885	0.149 0.681	0.057 0.875	0.246 0.494	-0.022 0.951	0.082 0.822
Yb	-0.338 0.339	0.227 0.528	0.248 0.490	-0.139 0.702	-0.074 0.840	-0.041 0.911	0.132 0.717	0.056 0.879	0.227 0.529	-0.003 0.993	0.070 0.847
Lu	-0.361 0.305	0.178 0.623	0.200 0.580	-0.164 0.652	-0.031 0.931	-0.042 0.909	0.154 0.671	0.021 0.955	0.190 0.598	0.032 0.931	0.032 0.930
Y	-0.467 0.173	0.140 0.699	0.164 0.652	-0.266 0.457	0.066 0.856	-0.019 0.957	0.245 0.495	-0.012 0.973	0.127 0.727	0.114 0.754	-0.043 0.906
Ag	0.465 0.176	0.220 0.541	0.140 0.700	-0.185 0.609	-0.205 0.570	0.527 0.117	-0.205 0.569	0.452 0.190	-0.179 0.620	0.055 0.879	-0.040 0.912
Au	-0.297 0.404	-0.130 0.720	-0.105 0.773	-0.029 0.936	0.081 0.824	-0.147 0.686	0.184 0.612	-0.149 0.680	0.171 0.636	-0.126 0.728	0.027 0.941
Pt	-0.389 0.267	-0.304 0.394	-0.282 0.430	-0.140 0.699	0.246 0.493	-0.260 0.468	0.350 0.321	-0.354 0.315	0.049 0.893	-0.080 0.827	-0.122 0.736
Pd	-0.632 0.050	-0.464 0.177	-0.512 0.130	-0.046 0.899	0.300 0.399	-0.326 0.359	-0.221 0.539	-0.514 0.129	-0.236 0.511	0.089 0.807	-0.278 0.437
	Cs	Be	Sr	Ba	Zr	Hf	V	Nb	Ta	Cr	Mo
Be	0.361 0.305										
Sr	-0.074 0.839	-0.086 0.814									
Ba	-0.143 0.694	-0.242 0.501	0.916 0.000								
Zr	0.525 0.119	0.294 0.409	0.072 0.843	-0.171 0.636							
Hf	0.546 0.103	0.292 0.413	0.031 0.933	-0.209 0.563	0.998 0.000						
V	-0.390 0.266	-0.259 0.470	-0.411 0.238	-0.356 0.312	0.186 0.607	0.193 0.594					
Nb	0.628 0.052	0.214 0.553	-0.176 0.627	-0.344 0.331	0.899 0.000	0.925 0.000	0.270 0.450				
Ta	0.568 0.087	0.488 0.152	-0.044 0.903	-0.290 0.416	0.953 0.000	0.953 0.000	0.060 0.869	0.839 0.002			
Cr	-0.627 0.052	-0.174 0.631	0.419 0.228	0.506 0.136	-0.478 0.162	-0.498 0.143	-0.209 0.562	-0.613 0.060	-0.416 0.231		
Mo	0.134 0.711	-0.128 0.725	0.662 0.037	0.420 0.227	0.643 0.045	0.609 0.062	-0.024 0.948	0.398 0.255	0.466 0.175	-0.171 0.636	
W	-0.248 0.489	0.072 0.844	-0.169 0.642	-0.018 0.961	-0.815 0.004	-0.815 0.004	-0.536 0.110	-0.800 0.005	-0.623 0.054	0.427 0.219	-0.671 0.034

Co	-0.703	-0.356	-0.102	-0.162	-0.468	-0.465	0.362	-0.431	-0.549	0.232	-0.138
	0.023	0.313	0.780	0.654	0.172	0.175	0.304	0.214	0.100	0.518	0.703
Ni	-0.328	0.033	0.492	0.312	-0.032	-0.027	-0.216	-0.049	-0.082	0.474	0.284
	0.355	0.929	0.148	0.379	0.930	0.940	0.549	0.893	0.823	0.166	0.427
Cu	-0.302	0.084	0.630	0.725	-0.313	-0.329	-0.404	-0.419	-0.270	0.836	-0.050
	0.396	0.817	0.051	0.018	0.379	0.353	0.247	0.228	0.450	0.003	0.892
Zn	-0.632	-0.238	-0.115	-0.270	-0.355	-0.358	0.128	-0.424	-0.348	0.302	-0.078
	0.050	0.508	0.751	0.450	0.314	0.309	0.724	0.223	0.325	0.396	0.830
Cd	0.551	-0.121	0.189	0.112	0.388	0.413	-0.077	0.585	0.222	-0.525	0.442
	0.098	0.739	0.601	0.757	0.268	0.236	0.832	0.076	0.538	0.119	0.201
Hg	-0.330	-0.351	0.353	0.395	-0.430	-0.416	-0.326	-0.316	-0.473	0.586	-0.036
	0.352	0.320	0.317	0.259	0.215	0.232	0.358	0.373	0.167	0.075	0.922
Ga	0.514	0.268	-0.388	-0.620	0.771	0.796	0.313	0.861	0.727	-0.821	0.336
	0.129	0.454	0.268	0.056	0.009	0.006	0.379	0.001	0.017	0.004	0.343
Tl	-0.320	-0.152	-0.307	-0.062	-0.056	-0.054	0.766	0.051	-0.103	0.066	-0.302
	0.367	0.675	0.388	0.864	0.879	0.883	0.010	0.889	0.776	0.855	0.397
Ge	0.085	0.111	-0.941	-0.835	-0.030	0.007	0.354	0.166	0.091	-0.403	-0.621
	0.815	0.761	0.000	0.003	0.934	0.985	0.316	0.646	0.803	0.248	0.055
Sn	-0.154	-0.198	-0.320	-0.095	-0.768	-0.725	-0.135	-0.439	-0.742	0.153	-0.742
	0.671	0.583	0.368	0.794	0.009	0.018	0.711	0.204	0.014	0.673	0.014
Pb	-0.221	-0.020	0.779	0.798	-0.199	-0.242	-0.565	-0.458	-0.169	0.706	0.288
	0.539	0.956	0.008	0.006	0.581	0.500	0.089	0.183	0.641	0.023	0.420
As	-0.239	-0.147	-0.292	-0.133	0.144	0.141	0.848	0.209	0.067	-0.097	-0.102
	0.507	0.684	0.414	0.715	0.691	0.698	0.002	0.563	0.855	0.789	0.780
Sb	-0.300	-0.258	-0.421	-0.376	0.216	0.232	0.965	0.353	0.100	-0.168	-0.067
	0.400	0.472	0.226	0.284	0.549	0.520	0.000	0.317	0.784	0.643	0.854
Bi	-0.357	-0.037	-0.350	-0.131	-0.142	-0.138	0.755	-0.025	-0.162	0.091	-0.408
	0.311	0.919	0.321	0.718	0.695	0.703	0.012	0.946	0.656	0.802	0.242
S	0.212	0.322	0.419	0.503	-0.032	-0.069	-0.548	-0.265	0.116	0.408	-0.008
	0.557	0.365	0.229	0.139	0.931	0.849	0.101	0.459	0.750	0.242	0.984
Se	*	*	*	*	*	*	*	*	*	*	*
	*	*	*	*	*	*	*	*	*	*	*
Te	-0.250	-0.192	0.469	0.476	0.304	0.281	0.113	0.161	0.212	0.327	0.517
	0.487	0.596	0.172	0.165	0.394	0.432	0.756	0.657	0.557	0.356	0.126
Th	0.585	0.425	-0.041	-0.340	0.846	0.846	-0.005	0.765	0.828	-0.719	0.590
	0.076	0.221	0.910	0.337	0.002	0.002	0.990	0.010	0.003	0.019	0.073
U	-0.373	-0.234	0.702	0.878	-0.535	-0.560	-0.379	-0.633	-0.577	0.750	-0.008
	0.288	0.515	0.024	0.001	0.111	0.092	0.280	0.049	0.081	0.012	0.982
La	0.199	-0.032	0.488	0.327	0.714	0.671	0.156	0.435	0.588	-0.226	0.866
	0.582	0.930	0.152	0.357	0.020	0.034	0.666	0.209	0.074	0.531	0.001
Ce	0.644	0.175	0.372	0.190	0.788	0.764	-0.189	0.606	0.737	-0.420	0.746
	0.045	0.628	0.290	0.599	0.007	0.010	0.601	0.063	0.015	0.227	0.013
Pr	0.301	-0.014	0.373	0.222	0.793	0.760	0.231	0.582	0.664	-0.334	0.821
	0.398	0.968	0.289	0.538	0.006	0.011	0.521	0.078	0.036	0.346	0.004
Nd	0.278	-0.007	0.357	0.197	0.810	0.778	0.255	0.599	0.684	-0.323	0.823
	0.438	0.985	0.311	0.585	0.004	0.008	0.477	0.067	0.029	0.363	0.003
Pm	*	*	*	*	*	*	*	*	*	*	*
	*	*	*	*	*	*	*	*	*	*	*
Sm	0.320	-0.004	0.367	0.187	0.839	0.808	0.196	0.621	0.719	-0.328	0.845
	0.367	0.991	0.297	0.604	0.002	0.005	0.588	0.055	0.019	0.355	0.002

Eu	0.340 0.337	0.061 0.867	0.327 0.356	0.138 0.703	0.879 0.001	0.851 0.002	0.235 0.513	0.673 0.033	0.765 0.010	-0.364 0.301	0.825 0.003
Gd	0.248 0.490	0.032 0.929	0.342 0.333	0.148 0.682	0.859 0.001	0.828 0.003	0.278 0.437	0.640 0.046	0.737 0.015	-0.310 0.384	0.839 0.002
Tb	0.286 0.424	0.066 0.855	0.318 0.371	0.131 0.719	0.865 0.001	0.835 0.003	0.268 0.454	0.653 0.041	0.755 0.012	-0.330 0.352	0.813 0.004
Dy	0.341 0.335	0.137 0.706	0.319 0.369	0.122 0.737	0.888 0.001	0.859 0.001	0.238 0.509	0.678 0.031	0.785 0.007	-0.369 0.295	0.807 0.005
Ho	0.415 0.233	0.179 0.621	0.245 0.495	0.054 0.882	0.919 0.000	0.896 0.000	0.237 0.509	0.734 0.016	0.834 0.003	-0.416 0.232	0.753 0.012
Er	0.485 0.155	0.241 0.503	0.229 0.524	0.040 0.912	0.920 0.000	0.897 0.000	0.177 0.624	0.742 0.014	0.853 0.002	-0.443 0.200	0.720 0.019
Tm	0.591 0.072	0.273 0.446	0.184 0.611	0.005 0.990	0.915 0.000	0.895 0.000	0.083 0.819	0.751 0.012	0.876 0.001	-0.471 0.169	0.661 0.037
Yb	0.582 0.078	0.292 0.413	0.147 0.686	-0.027 0.941	0.915 0.000	0.895 0.000	0.105 0.773	0.747 0.013	0.888 0.001	-0.463 0.178	0.625 0.053
Lu	0.547 0.102	0.225 0.533	0.183 0.614	0.009 0.981	0.908 0.000	0.887 0.001	0.110 0.761	0.728 0.017	0.868 0.001	-0.436 0.208	0.668 0.035
Y	0.457 0.184	0.214 0.552	0.250 0.485	0.061 0.867	0.914 0.000	0.890 0.001	0.190 0.598	0.728 0.017	0.838 0.002	-0.429 0.216	0.741 0.014
Ag	-0.464 0.177	-0.214 0.553	-0.427 0.218	-0.481 0.160	-0.467 0.174	-0.445 0.197	0.189 0.601	-0.351 0.320	-0.476 0.164	-0.058 0.874	-0.332 0.349
Au	0.351 0.320	-0.300 0.399	0.586 0.075	0.435 0.210	0.471 0.170	0.442 0.201	-0.317 0.372	0.283 0.427	0.341 0.335	-0.164 0.652	0.839 0.002
Pt	0.117 0.747	-0.217 0.548	0.708 0.022	0.574 0.083	0.280 0.434	0.239 0.506	-0.294 0.410	0.056 0.877	0.148 0.684	-0.022 0.952	0.814 0.004
Pd	-0.040 0.912	-0.111 0.760	0.665 0.036	0.628 0.052	0.071 0.845	0.018 0.960	-0.109 0.764	-0.229 0.525	-0.054 0.882	-0.003 0.994	0.570 0.086
	W	Co	Ni	Cu	Zn	Cd	Hg	Ga	Tl	Ge	Sn
Co	0.139 0.702										
Ni	-0.042 0.909	0.347 0.326									
Cu	0.291 0.415	-0.125 0.731	0.516 0.127								
Zn	0.272 0.447	0.889 0.001	0.360 0.308	-0.135 0.710							
Cd	-0.511 0.131	-0.230 0.522	0.238 0.508	-0.246 0.493	-0.388 0.268						
Hg	0.295 0.408	0.259 0.469	0.766 0.010	0.547 0.102	0.227 0.529	0.258 0.471					
Ga	-0.643 0.045	-0.160 0.659	-0.109 0.765	-0.733 0.016	-0.120 0.741	0.505 0.136	-0.438 0.205				
Tl	-0.244 0.497	-0.012 0.974	-0.326 0.358	0.002 0.997	-0.284 0.426	-0.167 0.645	-0.175 0.629	-0.103 0.777			
Ge	0.176 0.627	-0.039 0.915	-0.569 0.086	-0.538 0.109	0.004 0.991	-0.300 0.399	-0.464 0.177	0.350 0.322	0.269 0.453		
Sn	0.581 0.078	0.340 0.336	0.086 0.813	0.155 0.668	0.150 0.680	-0.015 0.967	0.433 0.211	-0.375 0.286	0.015 0.966	0.280 0.434	

Pb	0.297 0.405	-0.232 0.519	0.401 0.251	0.780 0.008	-0.104 0.775	-0.144 0.691	0.496 0.145	-0.669 0.034	-0.199 0.581	-0.728 0.017	-0.216 0.549
As	-0.438 0.205	0.016 0.965	-0.354 0.316	-0.198 0.584	-0.234 0.515	-0.057 0.876	-0.296 0.407	0.098 0.788	0.952 0.000	0.211 0.559	-0.201 0.578
Sb	-0.565 0.089	0.356 0.313	-0.140 0.700	-0.372 0.289	0.122 0.737	0.013 0.971	-0.223 0.536	0.327 0.356	0.756 0.011	0.307 0.387	-0.089 0.807
Bi	-0.161 0.657	0.124 0.732	-0.274 0.444	-0.001 0.999	-0.159 0.662	-0.226 0.529	-0.173 0.633	-0.126 0.729	0.968 0.000	0.266 0.458	0.095 0.793
S	0.316 0.373	-0.622 0.055	-0.203 0.574	0.551 0.099	-0.454 0.187	-0.326 0.358	-0.080 0.826	-0.517 0.126	-0.040 0.913	-0.326 0.358	-0.294 0.410
Se	*	*	*	*	*	*	*	*	*	*	*
Te	-0.347 0.326	-0.312 0.381	0.369 0.294	0.411 0.238	-0.300 0.400	0.176 0.628	0.358 0.310	-0.085 0.815	0.275 0.442	-0.406 0.245	-0.461 0.180
Th	-0.579 0.080	-0.357 0.311	-0.034 0.926	-0.543 0.105	-0.209 0.563	0.477 0.163	-0.435 0.209	0.883 0.001	-0.339 0.337	0.051 0.889	-0.632 0.050
U	0.348 0.324	0.016 0.965	0.341 0.335	0.880 0.001	-0.091 0.803	-0.191 0.596	0.528 0.117	-0.875 0.001	0.001 0.998	-0.611 0.061	0.274 0.444
La	-0.699 0.025	-0.345 0.329	-0.096 0.792	-0.144 0.691	-0.288 0.420	0.261 0.466	-0.342 0.333	0.320 0.368	0.035 0.923	-0.454 0.187	-0.919 0.000
Ce	-0.575 0.082	-0.629 0.051	-0.150 0.680	-0.218 0.545	-0.492 0.149	0.481 0.160	-0.320 0.367	0.471 0.170	-0.227 0.528	-0.357 0.311	-0.797 0.006
Pr	-0.782 0.007	-0.405 0.246	-0.135 0.710	-0.230 0.522	-0.376 0.284	0.370 0.293	-0.363 0.303	0.443 0.200	0.114 0.754	-0.362 0.304	-0.892 0.001
Nd	-0.796 0.006	-0.388 0.268	-0.108 0.767	-0.230 0.523	-0.353 0.317	0.359 0.309	-0.355 0.315	0.462 0.179	0.122 0.737	-0.348 0.325	-0.903 0.000
Pm	*	*	*	*	*	*	*	*	*	*	*
Sm	-0.789 0.007	-0.408 0.241	-0.098 0.788	-0.232 0.518	-0.340 0.337	0.360 0.307	-0.356 0.312	0.482 0.158	0.038 0.917	-0.343 0.332	-0.911 0.000
Eu	-0.826 0.003	-0.413 0.236	-0.100 0.783	-0.247 0.491	-0.355 0.314	0.356 0.313	-0.404 0.247	0.536 0.110	0.062 0.865	-0.297 0.404	-0.909 0.000
Gd	-0.827 0.003	-0.351 0.320	-0.044 0.905	-0.223 0.536	-0.295 0.407	0.327 0.356	-0.360 0.308	0.512 0.130	0.089 0.806	-0.318 0.370	-0.919 0.000
Tb	-0.817 0.004	-0.391 0.264	-0.075 0.836	-0.234 0.516	-0.334 0.346	0.334 0.345	-0.378 0.281	0.521 0.123	0.106 0.770	-0.300 0.399	-0.921 0.000
Dy	-0.821 0.004	-0.421 0.226	-0.085 0.816	-0.235 0.514	-0.366 0.298	0.346 0.328	-0.419 0.228	0.549 0.100	0.075 0.836	-0.293 0.412	-0.916 0.000
Ho	-0.823 0.003	-0.474 0.167	-0.142 0.696	-0.271 0.448	-0.411 0.238	0.348 0.325	-0.469 0.172	0.595 0.070	0.086 0.813	-0.216 0.548	-0.899 0.000
Er	-0.786 0.007	-0.532 0.113	-0.170 0.638	-0.274 0.444	-0.458 0.183	0.362 0.304	-0.485 0.156	0.601 0.066	0.060 0.869	-0.204 0.572	-0.888 0.001
Tm	-0.720 0.019	-0.614 0.059	-0.239 0.506	-0.292 0.412	-0.507 0.135	0.361 0.306	-0.509 0.133	0.601 0.066	0.002 0.996	-0.155 0.670	-0.858 0.001
Yb	-0.709 0.022	-0.618 0.057	-0.274 0.444	-0.296 0.406	-0.503 0.138	0.308 0.387	-0.548 0.101	0.597 0.068	0.029 0.938	-0.111 0.761	-0.862 0.001
Lu	-0.719 0.019	-0.595 0.070	-0.259 0.469	-0.291 0.414	-0.476 0.164	0.310 0.383	-0.519 0.124	0.575 0.082	0.021 0.954	-0.146 0.687	-0.882 0.001
Y	-0.795 0.006	-0.511 0.131	-0.159 0.662	-0.267 0.455	-0.442 0.201	0.359 0.309	-0.475 0.166	0.588 0.074	0.064 0.860	-0.224 0.533	-0.896 0.000

Ag	0.334 0.345	0.823 0.003	0.144 0.692	-0.349 0.323	0.805 0.005	-0.234 0.516	0.099 0.785	0.048 0.895	-0.229 0.524	0.375 0.286	0.512 0.130
Au	-0.396 0.258	-0.327 0.356	0.083 0.820	-0.092 0.800	-0.189 0.601	0.505 0.136	0.082 0.822	0.183 0.612	-0.425 0.221	-0.579 0.079	-0.600 0.067
Pt	-0.281 0.432	-0.191 0.596	0.242 0.500	0.055 0.880	-0.124 0.733	0.466 0.175	0.227 0.528	0.010 0.978	-0.312 0.380	-0.753 0.012	-0.563 0.090
Pd	-0.200 0.579	-0.032 0.931	-0.176 0.626	0.123 0.735	-0.081 0.824	-0.090 0.804	-0.339 0.338	-0.231 0.521	-0.168 0.643	-0.531 0.114	-0.416 0.232
	Pb	As	Sb	Bi	S	Se	Te	Th	U	La	Ce
As	-0.280 0.434										
Sb	-0.575 0.082	0.845 0.002									
Bi	-0.247 0.492	0.923 0.000	0.765 0.010								
S	0.714 0.020	-0.113 0.756	-0.543 0.105	-0.070 0.848							
Se	*	*	*	*	*						
Te	0.564 0.090	0.268 0.455	0.075 0.836	0.112 0.758	0.202 0.576	*					
Th	-0.295 0.409	-0.119 0.743	-0.026 0.944	-0.379 0.280	-0.174 0.630	*	0.073				
U	0.764 0.010	-0.189 0.601	-0.395 0.258	-0.020 0.956	0.476 0.164	*	0.305	-0.691 0.027			
La	0.244 0.497	0.253 0.480	0.108 0.766	-0.080 0.827	0.234 0.515	*	0.522	0.565	-0.120		
Ce	0.183 0.613	-0.020 0.956	-0.171 0.636	-0.332 0.348	0.337 0.341	*	0.327	0.738 0.015	-0.262	0.855 0.002	
Pr	0.119 0.743	0.340 0.337	0.210 0.561	-0.006 0.987	0.162 0.654	*	0.511	0.627 0.131	-0.236	0.980 0.000	0.882 0.001
Nd	0.109 0.765	0.349 0.323	0.235 0.514	0.003 0.994	0.138 0.703	*	0.530	0.637 0.115	-0.255	0.976 0.000	0.869 0.001
Pm	*	*	*	*	*	*	*	*	*	*	*
Sm	0.110 0.761	0.266 0.457	0.178 0.622	-0.086 0.813	0.144 0.691	*	0.507	0.670 0.134	-0.267	0.974 0.000	0.894 0.000
Eu	0.049 0.894	0.289 0.417	0.219 0.544	-0.054 0.882	0.113 0.756	*	0.480	0.704 0.160	-0.310	0.957 0.000	0.880 0.001
Gd	0.075 0.837	0.316 0.373	0.256 0.476	-0.025 0.944	0.083 0.820	*	0.533	0.677 0.112	-0.290	0.961 0.000	0.842 0.002
Tb	0.070 0.849	0.333 0.346	0.251 0.484	-0.006 0.987	0.113 0.756	*	0.522	0.687 0.122	-0.309	0.958 0.000	0.860 0.001
Dy	0.047 0.897	0.302 0.397	0.220 0.542	-0.028 0.938	0.125 0.730	*	0.477	0.724 0.164	-0.321	0.948 0.000	0.875 0.001
Ho	-0.016 0.966	0.309 0.385	0.231 0.521	-0.017 0.964	0.131 0.718	*	0.426	0.748 0.220	-0.380	0.916 0.000	0.882 0.001
Er	-0.011 0.976	0.280 0.434	0.178 0.623	-0.036 0.920	0.181 0.616	*	0.389	0.768 0.266	-0.393	0.897 0.000	0.908 0.000

Tm	-0.018 0.960	0.214 0.553	0.097 0.790	-0.095 0.794	0.247 0.491	*	0.318 0.370	0.776 0.008	-0.418 0.229	0.855 0.002	0.935 0.000
Yb	-0.038 0.917	0.236 0.512	0.117 0.748	-0.066 0.856	0.261 0.467	*	0.300 0.400	0.763 0.010	-0.434 0.211	0.841 0.002	0.915 0.000
Lu	-0.006 0.987	0.234 0.516	0.119 0.744	-0.084 0.817	0.255 0.478	*	0.338 0.340	0.748 0.013	-0.409 0.240	0.874 0.001	0.926 0.000
Y	0.002 0.996	0.286 0.423	0.186 0.606	-0.035 0.924	0.172 0.634	*	0.407 0.243	0.758 0.011	-0.377 0.283	0.913 0.000	0.905 0.000
Ag	-0.477 0.163	-0.248 0.491	0.134 0.713	-0.118 0.746	-0.717 0.020	*	-0.530 0.115	-0.182 0.614	-0.227 0.528	-0.582 0.077	-0.685 0.029
Au	0.396 0.257	-0.251 0.484	-0.312 0.379	-0.560 0.092	0.202 0.576	*	0.417 0.231	0.461 0.180	0.029 0.936	0.756 0.011	0.814 0.004
Pt	0.575 0.082	-0.157 0.666	-0.316 0.373	-0.404 0.246	0.245 0.495	*	0.526 0.118	0.339 0.338	0.194 0.592	0.733 0.016	0.698 0.025
Pd	0.345 0.330	-0.087 0.810	-0.242 0.501	-0.207 0.565	0.322 0.365	*	0.058 0.873	0.053 0.885	0.390 0.265	0.583 0.077	0.369 0.295
Nd	Pr 0.998 0.000	Nd	Pm	Sm	Eu	Gd	Tb	Dy	Ho	Er	Tm
Pm	*	*									
Sm	0.993 0.000	0.994 0.000	*								
Eu	0.985 0.000	0.990 0.000	*	0.995 0.000							
Gd	0.982 0.000	0.990 0.000	*	0.991 0.000	0.995 0.000						
Tb	0.986 0.000	0.993 0.000	*	0.991 0.000	0.996 0.000	0.998 0.000					
Dy	0.978 0.000	0.984 0.000	*	0.985 0.000	0.996 0.000	0.992 0.000	0.996 0.000				
Ho	0.962 0.000	0.967 0.000	*	0.972 0.000	0.989 0.000	0.976 0.000	0.985 0.000	0.994 0.000			
Er	0.948 0.000	0.951 0.000	*	0.957 0.000	0.974 0.000	0.954 0.000	0.968 0.000	0.983 0.000	0.995 0.000		
Tm	0.912 0.000	0.911 0.000	*	0.925 0.000	0.941 0.000	0.908 0.000	0.928 0.000	0.947 0.000	0.971 0.000	0.988 0.000	
Yb	0.898 0.000	0.898 0.000	*	0.912 0.000	0.931 0.000	0.898 0.000	0.919 0.000	0.938 0.000	0.967 0.000	0.984 0.000	0.998 0.000
Lu	0.923 0.000	0.923 0.000	*	0.939 0.000	0.951 0.000	0.922 0.000	0.939 0.000	0.953 0.000	0.975 0.000	0.987 0.000	0.996 0.000
Y	0.958 0.000	0.962 0.000	*	0.966 0.000	0.982 0.000	0.965 0.000	0.977 0.000	0.989 0.000	0.998 0.000	0.999 0.000	0.983 0.000
Ag	-0.618 0.057	-0.603 0.065	*	-0.592 0.071	-0.583 0.077	-0.550 0.100	-0.583 0.077	-0.591 0.072	-0.608 0.062	-0.643 0.045	-0.674 0.033
Au	0.722 0.018	0.706 0.022	*	0.743 0.014	0.683 0.029	0.670 0.034	0.660 0.038	0.641 0.046	0.604 0.064	0.600 0.067	0.609 0.062
Pt	0.671 0.034	0.654 0.040	*	0.657 0.039	0.591 0.072	0.603 0.065	0.595 0.069	0.571 0.085	0.503 0.138	0.497 0.144	0.470 0.171

Pd	0.451	0.422	*	0.425	0.399	0.390	0.368	0.384	0.328	0.309	0.273
	0.191	0.225	*	0.221	0.253	0.265	0.295	0.274	0.355	0.385	0.446
	Yb	Lu	Y	Ag	Au	Pt					
Lu	0.997										
	0.000										
Y	0.977	0.983									
	0.000	0.000									
Ag	-0.670	-0.666	-0.635								
	0.034	0.035	0.048								
Au	0.569	0.619	0.613	-0.437							
	0.086	0.056	0.059	0.207							
Pt	0.421	0.470	0.516	-0.417	0.902						
	0.226	0.170	0.127	0.230	0.000						
Pd	0.261	0.291	0.331	-0.214	0.463	0.505					
	0.467	0.415	0.350	0.553	0.178	0.136					

The * symbol in the correlation matrix means that the variable (chemical element) either has no values or a constant one.

Bibliography

- Agard, P., P. Yamato, L. Jolivet, and E. Burov (2009). “Exhumation of oceanic blueschists and eclogites in subduction zones: Timing and mechanisms”. In: *Earth–Science Reviews* 92, pp. 53–79.
- Akasaka, M., M. Sakakibara, and K. Togari (1988). “Piemontite from the Manganiferous Hematite Ore Deposits in the Tokoro Belt, Hokkaido, Japan”. In: *Mineralogy and Petrology* 38, pp. 105–116.
- Altherr, R., C. Soder, S. Panienka, D. Peters, and H.-P. Meyer (2013). “Pink manganian phengite in a high P/T metaconglomerate from northern Syros (Cyclades, Greece)”. In: *Contributions in Mineralogy and Petrology* 166, pp. 1323–1334.
- Aubouin, J. (1959). “Contribution a l’etude geologique de la Grece septentrionale, les confins de l’Epire et de la Thessalie”. In: *Annales Géologiques des Pays Helléniques* 10.
- Aubouin, J., X. Le Pichon, E. Winterer, and M. Bonneau (1977). *Les Hellenides dans l’optiques de le tectonique des plaques*.
- Barker, A. J. (2014). *A Key for Identification of Rock-forming Minerals in Thin-Section*. CRC Press.
- Baturin, G. N. (1988). *The Geochemistry of Manganese and Manganese Nodules in the Ocean*. Sedimentary and Petroleum Geology. D. Reidel Publishing Company.
- Baziotis, I., A. Proyer, and E. Mposkos (2009). “High–pressure/low–temperature metamorphism of basalts in Lavrion (Greece): implications for the preservation of peak metamorphic assemblages in blueschists and greenschists”. In: *European Journal of Mineralogy* 21.1, pp. 133–148.
- Baziotis, I., A. Proyer, E. Mposkos, B. Windley F., and I. Boukouvala (2019). “Exhumation of the high–pressure northwestern Cyclades, Aegean: New P–T constraints, and geodynamic evolution”. In: *Lithos* 324–325, pp. 439–453.
- Bennett, M. A. (1987). “Genesis and diagenesis of the Cambrian manganese deposits, North Wales”. In: *Geological Journal* 22, pp. 7–18.
- Berezhnaya, E. D., A. V. Dubinin, M. N. Rimskaya-Korsakova, and T. H. Safin (2018). “Accumulation of Platinum Group Elements in Hydrogenous Fe–Mn Crust and Nodules from the Southern Atlantic Ocean”. In: *Minerals* 8.7, pp. 1–20.
- Bhatia, M. R. and K. A. W. Crook (1986). “Trace element characteristics of graywackes and tectonic setting discrimination of sedimentary basins”. In: *Contributions to Mineralogy and Petrology* 92, pp. 181–193.
- Blencoe, J. G., C. V. Guidotti, and F. P. Sassi (1994). “The paragonite–muscovite solvus: II. Numerical geothermometers for natural, quasibinary paragonite–muscovite pairs”. In: *Geochimica et Cosmochimica Acta* 58.10, pp. 442–470.
- Bonatti, E. and T. Kraemer and H. Rydell (1972). “Classification and Genesis of Submarine Iron–Manganese Deposits”. In: *Office for International Decade of Ocean Exploration*.
- Bonazzi, P. and S. Menchetti (2004). “Manganese in Monoclinic Members of the Epidote Group: Piemontite and Related Minerals”. In: *Epidotes*. Ed. by A. Liebscher and G. Franz. Vol. 56. Reviews in Mineralogy & Geochemistry. Mineralogical Society of America, Geochemical Society, pp. 495–552.
- Bortolotti, V. and G. Principi (2005). “Tethyan ophiolites and Pangea break–up”. In: *The Island Arc* 14, pp. 442–470.
- Brown, P., E. J. Essene, and D. R. Peacor (1978). “The Mineralogy and Petrology of Manganese–Rich Rocks From St. Marcel, Piedmont, Italy”. In: *Contributions to Mineralogy and Petrology* 67, pp. 227–232.
- Brun, J.-P. and C. Faccenna (2008). “Exhumation of high-pressure rocks driven by slab rollback”. In: *Earth and Planetary Science Letters* 272, pp. 1–7.
- Brunn, J. H. (1956). “Contribution a l’etude geologique du Pinde septentrional et d’une partie de la Macedoine centrale”. In: *Annales Géologiques des Pays Helléniques* 7, pp. 1–358.
- (1960). “Les zones helléniques internes et leur extension. Réflexions sur l’orogénèse alpine”. In: *Bulletin de la Société géologique de France* 2, pp. 470–486.
- Brusnitsyn, A. I. (2006). “Mineralogy and Metamorphism Conditions of Manganese Ore at the South Faizulino Deposit, the Southern Urals, Russia”. In: *Geology of Ore Deposits* 48.3, pp. 193–214.
- (2010). “Mineralogy of Metamorphosed Manganese Deposits of the South Urals”. In: *Geology of Ore Deposits* 52.7, pp. 551–565.
- Brusnitsyn, A. I. and I. G. Zhukov (2012). “Manganese deposits of the Devonian Magnitogorsk palaeovolcanic belt (Southern Urals, Russia)”. In: *Ore Geology Reviews* 47, pp. 42–58.
- Burns, R. G. (2005). *Mineralogical Applications of Crystal Field Theory*. 2nd ed. Cambridge Topics in Mineral Physics and Chemistry. Cambridge University Press.

- Cannon, W. F., B. E. Kimball, and L. A. Corathers (2017). "Manganese (Professional Paper 1802-L)". In: ed. by K. J. Schulz, Jr. J. H. DeYoung, R. R. Seal II, and D. C. Bradley. *Critical Mineral Resources of the United States – Economic and Environmental Geology and Prospects for Future Supply*. U.S. Department of the Interior, U.S. Geological Survey.
- Cardarelli, F. (2017). *Materials Handbook: A Concise Desktop Reference*. 3rd ed. Springer.
- Choi, J. H. and Y. Harita (1992). "Geochemistry and Depositional Environment of Mn Oxide Deposits in the Tokoro Belt, Northeastern Hokkaido, Japan". In: *Economic Geology* 87, pp. 1265–1274.
- Chrysanthaki, A. I. and E. Baltatzis (2003). "Geochemistry and depositional environment of ferromanganoan metasediments on the Island of Kythnos, Cyclades, Greece". In: *Neues Jahrbuch für Mineralogie - Abhandlungen* 1, pp. 1–17.
- Coombs, D. S., M. Dowse, R. Grapes, Y. Kawachi, and B. Roser (1985). "Geochemistry and origin of piemontite-bearing and associated manganiferous schists from Arrow Junction, Western Otago, New Zealand". In: *Chemical Geology* 48, pp. 57–78.
- Corathers, L. A. and J. F. Machamer (2006). "Manganese". In: ed. by J. E. Kogel, N. C. Trivedi, J. M. Barker, and S. T. Krukowski. 7th ed. *Industrial Minerals and Rocks Commodities, Markets, and Uses*. Society for Mining, Metallurgy, and Exploration, Inc.
- Crerar, D. A., J. Namson, M. So Chyi, L. Williams, and M. D. Feigenso (1982). "Manganiferous Cherts of the Franciscan Assemblage I: General Geology, Ancient and Modern Analogues and Implications for Hydrothermal Convection at Oceanic Spreading Centers". In: *Economic Geology* 77.3, pp. 519–540.
- Sengör, A. M. C. (1989). "The Tethyside Orogenic System: An Introduction". In: *Tectonic Evolution of the Tethyan Region*. Ed. by D. G. Gee and R. A. Stephenson. Vol. 259. NATO Science Series: C Mathematical and Physical Sciences. Kluwer Academic Publishers, pp. 1–22.
- Dasgupta, S., H. Banerjee, M. Fukuoka, P. K. Bhattacharya, and S. Roy (1990). "Petrogenesis of Metamorphosed Manganese Deposits and the Nature of the Precursor Sediments". In: *Ore Geology Reviews* 5, pp. 359–384.
- Dasgupta, S., P. Sengupta, P. K. Bhattacharya, M. Mukherjee, M. Fukuoka, H. Banerjee, and S. Roy (1989). "Mineral Reactions in Manganese Oxide Rocks: P–T–X Phase Relations". In: *Economic Geology* 84, pp. 434–443.
- Decourt, J. (1972). "The Canadian cordillera, the Hellenides and the sea–floor spreading theory". In: *Canadian Journal of Earth Sciences* 9, pp. 709–743.
- Dewey, J. F., W. C. Pitman, W. B. F. Ryan, and J. Bonnin (1973). "Plate tectonics and the evolution of the Alpine system". In: *Geological Society of America Bulletin* 84.
- Dilek, Y. and H. Furnes (2019). "Tethyan ophiolites and Tethyan seaways". In: *Journal of the Geological Society* 272, pp. 899–912.
- Dollace, W. A. (1969). "Crystal structure and cation ordering of piemontite". In: *The American Mineralogist* 54, pp. 710–717.
- Fitzgerald, C. E. and K. M. Gillis (2006). "Hydrothermal manganese oxide deposits from Baby Bare seamount in the Northeast Pacific Ocean". In: *Marine Geology* 225, pp. 145–156.
- Flohr, M. J. K. (1992). "Geochemistry and Origin of the Bald Knob Manganese Deposit, North Carolina". In: *Economic Geology* 87, pp. 2023–2040.
- Galanopoulos, E. and C. Charmatzis (2008). *Petrological–mineralogical study of manganoan metasedimentary horizons in the Varnavas area, Attica, and comparisons with S. Evvia and Andros Islands (in greek)*. National and Kapodistrian University of Athens.
- Gessner, K., U. Ring, and T. Gungör (2011). *Field Guide to Samos and Menderes Massif: Along–Strike Variations in the Mediterranean Tethyan Orogen*. Vol. 23. Field Guide. The Geological Society of America.
- Ghose, S., M. Kersten, K. Langer, G. Rossi, and L. Ungaretti (1986). "Crystal Field Spectra and Jahn Teller Effect of Mn³⁺ in Clinopyroxene and Clinoamphiboles from India". In: *Physics and Chemistry of Minerals* 13, pp. 291–305.
- Graedel, T. E., E. M. Harper, N. T. Nassar, P. Nuss, and B. K. Reck (2015). "Criticality of metals and metalloids". In: *Proceeding of the National Academy of Sciences* 112.14, pp. 4257–4262.
- Grapes, R. H. and S. Hashimoto (1978). "Manganiferous schists and Their Origin, Hidaka Mountains, Hokkaido, Japan". In: *Contributions to Mineralogy and Petrology* 68, pp. 23–35.
- Gromet, L. P., R. F. Dymek, L. A. Haskin, and R. L. Korotev (1984). "The «North American shale composite»: Its compilation, major and trace element characteristics". In: *Geochimica and Cosmochimica Acta* 48, pp. 2469–2482.
- Guan, Y., X. Sun, Y. Ren, and X. Jiang (2017). "Mineralogy, geochemistry and genesis of the polymetallic crusts and nodules from the South China Sea". In: *Ore Geology Reviews* 89, pp. 206–227.
- Hein, J. R., A. Koschinsky, and T. Kuhn (2020). "Deep–ocean polymetallic nodules as a resource for critical materials". In: *Nature Reviews Earth & Environment* 1, pp. 158–169.
- Hein, J. R., M. G. Stamatakis, and J. S. Dowling (2000). "Trace metal–rich Quaternary hydrothermal manganese oxide and barite deposit, Milos Island, Greece". In: *Transactions of the Institution of Mining and Metallurgy; Section B: Applied earth science* 109, pp. 67–79.
- Hein, R. J. and K. Mizell (2013). "Hydrothermal systems and mineralization of volcanic arcs: Comparison of West Pacific and Mediterranean arcs". In: *Geological Setting, Mineral Resources and ancient works of Samos and adjacent islands of the Aegean Sea*.

- Hinsbergen, D. J. J. van, T. H. Torsvik, S. M. Schmid, L. C. Mañenco, M. Maffione, R. L. M. Vissers, D. Guürer, and W. Spakman (2020). "Orogenic architecture of the Mediterranean region and kinematic reconstruction of its tectonic evolution since the Triassic". In: *Gondwana Research* 81, pp. 79–229.
- Hori, F. (1954). "On the diadochic substitution in silicates". In: *Mineralogical Magazine* 1.2, pp. 109–125.
- Huet, B., L. Labrousse, P. Monié, B. Malvoisin, and L. Jolivet (2014). "Coupled phengite ^{40}Ar – ^{39}Ar geochronology and thermobarometry: P–T–t evolution of Andros Island (Cyclades, Greece)". In: *Geological Magazine* 152.4, pp. 1–17.
- Jacobschagen, V., ed. (1986). *Geologie von Griechenland*. Borntraeger.
- Janoušek, V., C. M. Farrow, and V. Erban (2006). "Interpretation of Whole-rock Geochemical Data in Igneous Geochemistry: Introducing Geochemical Data Toolkit (GCDkit)". In: *Journal of Petrology* 303, pp. 1255–1259.
- Jolivet, L. and J.-P. Brun (2010). "Cenozoic geodynamic evolution of the Aegean". In: *International Journal of Earth Sciences* 99, pp. 109–138.
- Jolivet, L., C. Faccenna, B. Goffé, E. Burov, and P. Agard (2003). "Subduction tectonics and exhumation of high-pressure metamorphic rocks in the Mediterranean Orogens". In: *American Journal of Science* 303, pp. 353–409.
- Jolivet, L., C. Faccenna, B. Huet, L. Labrousse, L. Le Pourhiet, O. Lacombe, E. Lecomte, E. Burov, Y. Denèle, J.-P. Brun, M. Philippon, A. Paul, G. Salaün, H. Karabulut, C. Piromallo, P. Monié, F. Gueydan, A. I. Okay, R. Oberhänsli, A. Pourteau, R. Augier, L. Gadenne, and O. Driussi (2013). "Aegean tectonics: Strain localisation, slab tearing and trench retreat". In: *Tectonophysics* 597–598, pp. 1–33.
- Josso, P., E. Pelleret, O. Pourret, Y. Fouquet, J. Etoubleau, S. Cheron, and C. Bollinger (2017). "A new discrimination scheme for oceanic ferromanganese deposits using high field strength and rare earth elements". In: *Ore Geology Reviews* 87, pp. 3–15.
- Katsikatos, G. (1976). "La structure tectonique de l'Attique et de l'île d'Eubée". In: *Bulletin de la Société géologique de France* 19, pp. 75–80.
- (1993). *Geological Map of Greece in scale 1:50000, Eretria Sheet*. Institute of Geology and Mineral Exploration, Greece.
- (2002). *Geological Map of Greece in scale 1:50000, Kifissia Sheet*. Institute of Geology and Mineral Exploration, Greece.
- Keskinen, M. and J. G. Liou (1987). "Stability relations of Mn–Fe–Al piemontite". In: *Journal of Metamorphic Petrology* 5, pp. 495–507.
- Kober, L. (1929). *Beitrage zur Geologie von Attica*.
- Koukouvelas, I. K. (2019). *Geology of Greece (in greek)*. Liberal Books.
- Kuleshov, V. (2017). *Isotope Geochemistry: The Origin and Formation of Manganese Rocks and Ores*. Ed. by J. B. Maynard. Elsevier.
- Langer, K., E. Tillmanns, M. Kersten, H. Almen, and R. K. Arni (2002). "The crystal chemistry of Mn³ in the clino- and orthoisoite structure types, Ca₂Mn³⁺[OH | O | SiO₄ | Si₂O₇]: A structural and spectroscopic study of some natural piemontites and «thulites» and their synthetic equivalents". In: *Zeitschrift für Kristallographie* 217, pp. 563–580.
- Lekkas, S. and S. Lozios (2000). "Tectonic structure of Mt. Hymittos". In: *Annales Géologiques des Pays Helléniques* 38, pp. 47–62.
- Lepsius, R. (1893). *Geologie von Attica. Ein Beitrage zur Lehre von Metamorphismus der Gesteine*.
- Liao, J., X. Sun, Z. Wu, R. Sa, Y. Guan, Y. Lu, D. Li, Y. Liu, Y. Deng, and Y. Pan (2019). "Fe–Mn (oxyhydr)oxides as an indicator of REY enrichment in deep-sea sediments from the central North Pacific". In: *Ore Geology Reviews* 112.
- Lozios, S. (1993). *Structural Analysis of the Metamorphosed Formations of NE Attica (in greek)*.
- Lozios, S., K. Soukis, and V. Antoniou (2019). "A guide to lithostratigraphy and structural inventory of the Cycladic Blueschist Unit rocks of NE Attica (Greece)". In: *Journal of the VIRTUAL EXPLORER* 50, pp. 1–30.
- MacKenzie, W. S., A. E. Adams, and K. H. Brodie (2017). *Rocks and Minerals in Thin Section*. 2nd ed. CRC Press.
- Marino, E., F. J. González, L. Somoza, R. Lunar, L. Ortega, J. T. Vázquez, J. Reyes, and E. Bellido (2017). "Strategic and rare elements in Cretaceous–Cenozoic cobalt-rich ferromanganese crusts from seamounts in the Canary Island Seamount Province (northeastern tropical Atlantic)". In: *Ore Geology Reviews* 87, pp. 41–61.
- Marinos, G. and W. E. Petrascheck (1956). *Lavrion: geological and geophysical research*. Institute for Geology and Subsurface Research.
- Maynard, J. B. (2014). "Manganiferous Sediments, Rocks and Ores". In: ed. by K. Turekian and H. Holland. 2nd ed. Treatise on Geochemistry. Elsevier.
- Melfos, V. and P. Voudouris (2017). "Cenozoic metallogeny of Greece and potential for precious, critical and rare metals exploration". In: *Ore Geology Reviews* 89, pp. 1030–1057.
- Murray, R. W., M. R. Buchholtz ten Brink, H. J. Brumsack, D. C. Gerlach, and G. P. Russ III (1991). "Rare earth elements in Japan Sea sediments and diagenetic behavior of Ce/Ce*: Results from ODP Leg 127". In: *Geochimica et Cosmochimica Acta* 55.9, pp. 2453–2466.
- Murray, R. W., M. R. Buchholtz ten Brink, D. L. Jones, D. C. Gerlach, and G. P. Russ III (1990). "Rare earth elements as indicators of different marine depositional environments in chert and shale". In: *Geology* 18.3, pp. 268–271.

- Nath, B. N., W. L. Plüger, and I. Roelandts (1997). "Geochemical constraints on the hydrothermal origin of ferromanganese encrustations from the Rodriguez Triple Junction, Indian Ocean". In: *Manganese Mineralization: Geochemistry and Mineralogy of Terrestrial and Marine Deposits*. Ed. by K. Nicholson, J. R. Hein, S. Dasgupta, and B. Buhn. Vol. 119. Special Publications. The Geological Society, pp. 199–212.
- Nicholson, K. (1992). "Contrasting Mineralogical–Geochemical Signatures of Manganese Oxides: Guides to Metallogenesis". In: *Economic Geology* 87, pp. 1253–1264.
- Nirta, G., G. Moratti, L. Piccardi, D. Montanari, N. Carras, R. Catanzariti, M. Chiari, and M. Marcuzzi (2018). "From obduction to continental collision: new data from Central Greece". In: *Geological Magazine* 155.2, pp. 377–421.
- Ostwald, J. (1988). "Mineralogy of the Groote Eylandt manganese oxides: A review". In: *Ore Geology Reviews* 4, pp. 3–45.
- Panagos, A. G. and S. P. Varnavas (1984). "One the Genesis of Some Manganese Deposits from Eastern Greece". In: ed. by A. Wauschkuhn, C. Kluth, and R. A. Zimmermann. *Syngeneses and Epigenesis in the Formation of Mineral Deposits*. Springer–Verlag.
- Papanikolaou, D. (1984). "The three metamorphic belts of the Hellenides: A review and a kinematic interpretation". In: *The geological evolution of the Eastern Mediterranean*. Ed. by J. E. Dixon and A. H. F. Robertson. Vol. 17. Geological Society of London Special Publication. Geological Society of London, pp. 551–561.
- (1987). "Tectonic evolution of the Cycladic blueschist belt (Aegean Sea, Greece)". In: ed. by H. C. Helgeson. *Chemical transport in metasomatic processes*. Springer, pp. 429–450.
- (1997). "The tectonostratigraphic terranes of the Hellenides". In: *Annales Géologiques de Pays Hellénique* 37, pp. 495–514.
- (2009). "Timing of tectonic emplacement of the ophiolites and terrane paleogeography in the Hellenides". In: *Lithos* 108, pp. 262–280.
- (2013). "Tectonostratigraphic models of the Alpine terranes and subduction history of the Hellenides". In: *Tectonophysics* 595–596, pp. 1–24.
- (2015). *Geology of Greece (in greek)*. Patakis Publications.
- Passchier, C. W. and R. A. J. Trouw (2005). *Microtectonics*. 2nd ed. Springer.
- Pattan, J. N., G. Parthiban, A. Amonkar, S. A. Shaikh, and S. J. Sankar (2017). "Trace elements in ferromanganese nodules from the central indian ocean basin". In: *Marine Georesources & Geotechnology* 35.8, pp. 1147–1157.
- Pelleter, E., Y. Fouquet, J. Etoubleau, S. Cheron, S. Labanieh, P. Josso, C. Bollinger, and J. Langlade (2017). "Ni–Cu–Co-rich hydrothermal manganese mineralization in the Wallis and Futuna back–arc environment (SW Pacific)". In: *Ore Geology Reviews* 87, pp. 126–146.
- Perraki, M. and E. Mposkos (2001). "New constraints for the Alpine HP metamorphism of the Ios Basement, Cyclades, Greece". In: *Bulletin of the Geological Society of Greece* 34.3, pp. 977–984.
- Philippson, A. (1898). "La tectonique de l'Égée (Grèce, Mer Egée, Asie Mineure Occidentale)". In: *Annales de Géographie* 32, pp. 112–141.
- Pichler, H., C. Schmitt-Riegraf, and L. Hoke (1997). *Rock-forming Minerals in Thin Section*. Chapman & Hall.
- Pirajno, F. (2009). *Hydrothermal Processes and Mineral Systems*. Springer, Geological Survey of Western Australia.
- Polgari, M., J. R. Hein, T. Vigh, M. Scabó-Drubina, I. Fórizs, L. Bíró, A. Müller, and A. L. Tóth (2012). "Microbial processes and the origin of the Úrkút manganese deposit, Hungary". In: *Ore Geology Reviews* 47, pp. 87–109.
- Post, J. E. (1999). "Manganese oxide minerals: Crystal structures and economic and environmental significance". In: *Proceedings of the National Academy of Sciences of the USA* 96, pp. 3447–3454.
- Pracejus, B. (2015). *The Ore Minerals under the Microscope: An Optical Guide*. 2nd ed. Elsevier.
- Puertas, F., M. Teresa Blanco, and T. Vazquez (1989). "Manganese substitutions into the portland cement clinker phases". In: *Materiales de Construcción* 39.214, pp. 19–30.
- Reinecke, T. (1982). "Cymrite and Celsian in Manganese–Rich Metamorphic Rocks from Andros Island/Greece". In: *Contributions to Mineralogy and Petrology* 79, pp. 333–336.
- (1986). "Phase relationships of sursassite and other Mn–silicates in highly oxidized low-grade, high-pressure metamorphic rocks from Evvia and Andros Islands, Greece". In: *Contributions to Mineralogy and Petrology* 94, pp. 110–126.
- (1987). "Manganoan deerite and calderitic garnet from high–pressure metamorphic Fe–Mn-rich quartzites on Andros Island, Greece". In: *Mineralogical Magazine* 51, pp. 247–251.
- Reinecke, T., M. Okrusch, and P. Richter (1985). "Geochemistry of ferromanganoan metasediments from the Island of Andros, Cycladic Blueschist Belt, Greece". In: *Chemical Geology* 53, pp. 249–278.
- Reykhart, L. Y. and N. A. Shulga (2019). "Fe–Mn nodule morphotypes from the NE Clarion–Clipperton Fracture Zone, Pacific Ocean: Comparison of mineralogy, geochemistry and genesis". In: *Ore Geology Reviews* 110.
- Ring, U., J. Glodny, T. Will, and S. Thompson (2010). "The Hellenic Subduction System: High–Pressure Metamorphism, Exhumation, Normal Faulting, and Large–Scale Extension". In: *Annual Review of Earth and Planetary Sciences* 38, pp. 45–76.
- Rodríguez-Díaz, A. A., C. Canet, R. E. Villanueva-Estrada, E. Chacón, F. Gervilla, F. Velasco-Tapia, E. M. Cruz-Gámez, E. González-Partida, R. Casas-García, C. Linares-López, and D. Pérez-Zárate (2018). "Recent Mn–Ag deposits in coastal hydrothermal springs in the Baja California Peninsula, Mexico". In: *Mineralium Deposita*.

- Roy, S. (1968). "Mineralogy of the Different Genetic Types of Manganese Deposits". In: *Economic Geology* 63, pp. 760–786.
- (1992). "Environments and Processes of Manganese Deposition". In: *Economic Geology* 87, pp. 1218–1236.
- (2006). "Sedimentary manganese metallogenesis in response to the evolution of the Earth system". In: *Earth Science Reviews* 77, pp. 273–305.
- Rudnick, R. L. and S. Gao (2014). "Composition of the Continental Crust". In: *Treatise on Geochemistry*. Ed. by H. D. Holland and K. K. Turekian. 2nd ed. Elsevier.
- Salas, R. Del Rio, J. Ruiz, L. Ochoa-Landín, O. Noriega, F. Barra, D. Meza-Figueroa, and F. Paz-Moreno (2008). "Geology, Geochemistry and Re–Os systematics of manganese deposits from the Santa Rosalía Basin and adjacent areas in Baja California Sur, México". In: *Mineralium Deposita* 43, pp. 467–482.
- Sarbas, B. and W. Topper (1993). *Mn Manganese A2 Natural Occurrence. Minerals*. Ed. by R. Ditz. Gmelin Handbook of Inorganic and Organometallic Chemistry. Springer–Verlag.
- Scheffer, C., O. Vanderhaeghe, P. Lanari, A. Tarantola, L. Ponthus, A. Photiades, and L. France (2016). "Syn- to post-orogenic exhumation of metamorphic nappes: Structure and thermobarometry of the western Attic–Cycladic metamorphic complex (Lavrion, Greece)". In: *Journal of Geodynamics* 96, pp. 174–193.
- Schmid, S. M., D. Bernoulli, B. Fügenschum, L. Matenco, S. Schefer, R. Schuster, M. Tischler, and K. Ustaszewski (2008). "The Alpine–Carpathian–Dinaridic orogenic system: correlation and evolution of tectonic units". In: *Swiss Journal of Geosciences* 101, pp. 139–183.
- (2020). "Tectonic units of the Alpine collision zone between Eastern Alps and western Turkey". In: *Gondwana Research* 78, pp. 308–374.
- Schreyer, W., A.-M. Franolet, and K. Abrahan (1986). "A miscibility gap in trioctahedral Mn–Mg–Fe chlorites: Evidence from the Lienne Valley manganese deposit, Ardennes, Belgium". In: *Contributions to Mineralogy and Petrology* 94, pp. 333–342.
- Shaked, Y., D. Avigad, and Z. Garfunkel (2000). "Alpine high–pressure metamorphism at the Almyropotamos window (southern Evia, Greece)". In: *Geological Magazine* 137.4, pp. 367–380.
- Sinisi, R., G. Mongelli, F. Perri, and G. Rizzo (2018). "The braunite (3Mn₂O₃·MnSiO₃)–rich mineralization in the metasedimentary succession from southern Apennines (Italy): Genesis constraints". In: *Ore Geology Reviews* 94, pp. 4–11.
- Smith, G., U. Hålenius, H. Annersten, and L. Ackermann (1983). "Optical and Mössbauer spectra of manganese–bearing phlogopites: Fe_{IV}³⁺–Mn_V²⁺ pair absorption as the origin of reverse pleochroism". In: *American Mineralogist* 68, pp. 759–768.
- Spanos, D. G. (2012). *Geodynamic Evolution of Attica (in greek)*.
- Stampfli, G. M. and G. D. Borel (2002). "A plate tectonic model for the Paleozoic and Mesozoic constrained by dynamic plate boundaries and restored synthetic oceanic isochrons". In: *Earth and Planetary Science Letters* 196, pp. 17–33.
- Stampfli, G. M. and H. W. Kozur (2006). "Europe from the Variscan to the Alpine cycles". In: *European Lithosphere Dynamics*. Ed. by D. G. Gee and R. A. Stephenson. Vol. 32. Memoirs. The Geological Society of London, pp. 57–82.
- Stouraiti, C., S. Lozios, K. Soukis, H. Downes, and A. Carter (2020). "Geochemical and geological evidence for a Triassic transition from subduction- to rift-related volcanic activity in the Cycladic Blueschist Unit in Attica (Greece)". In: EGU General Assembly 2020.
- Taylor, S. R. and S. M. McLennan (1985). *The Continental Crust: Its Composition and Evolution*. Blackwell.
- (2008). *Planetary Crusts: Their Composition, origin and Evolution*. Vol. 10. Cambridge Planetary Science. Cambridge University Press.
- Usui, A. and G. P. Glasby (1998). "Submarine hydrothermal manganese deposits in the Izu–Bonin–Mariana arc: An overview". In: *The Island Arc* 7, pp. 422–431.
- Varentsov, I. M. (1996). *Manganese Ores of Supergene Zone: Geochemistry of Formation*. Solid Earth Sciences Library. Springer Netherlands.
- Vereshchagin, O. S., E. N. Perova, A. I. Brusnitsyn, V. B. Ershova, A. K. Khudoley, V. V. Shilovskikh, and E. V. Molchanova (2019). "Ferro–manganese nodules from the Kara Sea: Mineralogy, geochemistry and genesis". In: *Ore Geology Reviews* 106, pp. 192–204.
- Šalák, A. and M. Selecká (2012). *Manganese in Powder Metallurgy Steels*. Springer.
- White, R. W., E. Powell, and T. E. Johnson (2014). "The effect of Mn on mineral stability in metapelites revisited: new a–x relations for manganese–bearing minerals". In: *Journal of Metamorphic Petrology* 32, pp. 809–828.
- Xiao, J., J. He, H. Yang, and C. Wu (2017). "Comparison between Datangpo–type manganese ores and modern marine ferromanganese oxyhydroxide precipitates based on rare earth elements". In: *Ore Geology Reviews* 89, pp. 290–308.
- Zhang, Z., Y. Du, L. Gao Lianfeng, Y. Zhang, G. Shi, C. Liu, P. Zhang, and X. Duan (2012). "Enrichment of REEs in polymetallic nodules and crusts and its potential for exploitation". In: *Journal of Rare Earths* 30.6.